HABILITATION THESIS

Processes and materials in electrochemical energy systems

Assoc. Prof. Dr. Andrea Kellenberger

Politehnica University Timisoara
Faculty of Industrial Chemistry and Environmental Engineering

2017

Table of Contents

Abstract ***3***

Rezumat ***6***

PART I. Main scientific, professional and academic achievements ***9***

Section I. Scientific achievements ***9***

Section II. Professional and academic achievements ***11***

1. Contributions on the electrocatalysis of hydrogen evolution reaction ***14***

1.1. Background **14**

1.2. HER catalysis by proton carriers **18**

1.2.1. Catalytic enhancement of HER on copper electrode 19

1.2.2. Catalytic enhancement of HER on gold electrode 27

1.2.3. Catalytic enhancement of HER on platinum electrode 35

1.3. Conclusions **41**

2. Contributions on the electrochemical synthesis of polyaniline nanofibers ***44***

2.1. Background **44**

2.2. Influence of synthesis conditions on the structure, morphology and electrochemical properties of polyaniline films **46**

2.2.1. Effect of acid concentration and monomer/acid ratio 47

2.2.2. Effect of scan rate 53

2.2.3. Effect of temperature 60

2.2.4. Effect of substrate 67

2.3. Applications of electrochemically synthesized polyaniline films **71**

2.3.1. Electrochemical sensors 71

2.3.2. Adsorption of dyes 76

2.4. Conclusions **80**

3. Contributions on the study of charge transport mechanism in conducting polymer films ***81***

3.1. Background **81**

3.2. Charge transport mechanism in polyanilines **84**

3.2.1. Charged states in electrochemically prepared polyanilines and copolymers 86

3.2.2. Charged states in “linear” polyanilines 91

3.3. Charge transport mechanism in polythiophenes **96**

3.3.1. Charged states in poly(3-alkylthiophenes) 98

3.3.2. Charged states in functionalized poly(3-alkylthiophenes) 101

3.4. Conclusions **107**

PART II. Carrier evolution and development plan ***108***

References ***112***

List of Figures ***133***

List of Tables ***138***

Abstract

The present habilitation thesis entitled "Processes and materials in electrochemical energy systems" is a synthesis of the research activities carried out by the candidate after obtaining the scientific title of Doctor in Chemical engineering in 2004. The main research directions are the electrocatalysis of hydrogen evolution reaction and the electrochemical synthesis of conducting polymer films and the study of charge transport mechanism within such films.

The thesis consists of two parts, the first part presenting the main scientific, professional and academic achievements, and the second part contains the plans for evolution and further development of the research and university career.

Part I of the thesis is divided into two sections, of which ***Section I*** presents the main scientific achievements in the research fields approached, based on the original results published in 14 selected ISI papers, and Section II presents the main professional and academic achievements between 2004 and present. These include the publication of 29 articles in ISI-indexed journals (*h*-index 11) and 2 books, 1 patent, 3 research projects as principal investigator, member in the research team of 10 research projects, from which 1 international project, and respectively member in the target group of 3 POSDRU projects. ***Section II*** briefly outlines the main professional and academic achievements after obtaining the title of Doctor. The professional development involved the advancement from the position of assistant to assistant professor in 2005, respectively associate professor in 2008. From this position I have won two grants for equipping and modernizing the laboratories of Electrochemistry and General Chemistry. I was also involved in 3 POSDRU projects: Development and implementation of master programs in micro- and nanomaterials, Increasing the attractiveness and performance of doctoral and post-doctoral training programs for researchers in engineering sciences and Doctoral School in support of research in European context, of which the last project was specifically devoted to potential doctoral advisors and contributed to my training as a future doctoral supervisor through active involvement in coordinating a doctoral student.

The main scientific achievements are presented, divided in 3 chapters corresponding to the main research directions approached, namely Contributions on the electrocatalysis of hydrogen evolution reaction, Contributions on the electrochemical synthesis of nanostructured polyaniline, respectively Contributions on the charge transport mechanism in conducting polymer films.

Chapter 1 presents a continuation of the research carried out during the PhD thesis, being one of the research directions initiated in the Laboratory for Electrochemistry, Corrosion and Electrochemical Engineering, which led to the elaboration of 2 PhD theses and the publication of 4 articles in ISI ranked journals, to which the candidate is a co-author. The investigations aimed at accelerating the hydrogen evolution reaction by using electrocatalysts added in the solution. These catalysts, also called proton carriers, have the ability to increase the proton concentration in the double electric layer from the metal-solution interface by transporting the protons from the bulk of the solution to the interface. The results obtained have shown that the catalytic effect of the proton carriers is manifested for both electrode materials with high hydrogen overpotential, such as copper, but, more important from a practical point of view, even in the case of metals with low hydrogen overpotential, namely gold and platinum. Various aromatic or aliphatic amines were investigated as proton carriers, since the ability to carry protons is given by the lone pair of electrons of the nitrogen atom. The results obtained showed that the catalytic effect of the amines on the hydrogen evolution reaction can be explained based on their molecular parameters obtained by modeling, the most important being the dipole moment and the surface coverage degree. Thus, the most pronounced catalytic effect was obtained in the case of amines with a low surface coverage, which is equivalent to a larger number of molecules present at the interface, so an increased proton concentration, and respectively for a large dipole moment, which indicates a favorable orientation of the molecules at the interface, namely with the nitrogen atom and the attached proton directed towards the metal, where the charge transfer is greatly facilitated.

Chapter 2 describes one of the research directions initiated by the candidate in collaboration with the Institute of Chemistry of the Romanian Academy, which led to the elaboration of one PhD thesis and 5 articles in ISI ranked journals where the candidate is the principal author or co-author, part of the results being obtained within the framework of a Partnership research project coordinated by the candidate as partner responsible. The aim of the research was to investigate the influence of working conditions on the electrochemical synthesis of nanostructured polyaniline, namely the influence of acid concentration and the monomer / acid molar ratio, as well as the influence of scan rate, temperature and substrate. The results obtained have shown that polyaniline nanofibers can be obtained by electrochemical synthesis on different electrode materials under specific conditions of each substrate. It has been also found that capacitance values, which indicate the ability of polyaniline films to store electrical charges, are much higher for nanostructured polyaniline films as compared to those with granular structure. It has been also demonstrated the use of conductive polymer films in various applications, such as the development of dopamine biosensors and the adsorption of azo-dye pollutants.

Chapter 3 refers to the results obtained in collaboration with the Center of Spectroelectrochemistry of the Leibniz Institute of Solid State and Materials Research in Dresden, Germany, during 5 post-doctoral research stages and subject to 5 papers published in ISI indexed journals to which the candidate is the main author or co-author. The researches carried out have studied the charge transport mechanism in conductive polymer films such as polyaniline and polythiophene. For this purpose, spectroelectrochemical methods were used *in situ*, which allow the simultaneous recording of spectra during a cyclic voltammogram, which is equivalent to the real-time generation of spectra for various intermediates resulting from the electrochemical oxidation of conductive polymers. The combined application of several such techniques, such as infrared spectroscopy, electron spin resonance spectroscopy, and ultraviolet and visible spectroscopy, allows the differentiation of paramagnetic and diamagnetic species and the unambiguous assignment of adsorption bands to various charge carriers, such as polarons, bipolarons or polaron pairs. The results obtained have shown that in the case of polyaniline phenazine-like structures play an important role in the formation and stabilization of the charge carriers. In the case of substituted polythiophene derivatives, it has been shown that polarons and polaron pairs are the main charge carriers at low doping levels, respectively, bipolarons and polaron pairs at high doping levels.

Part II of the habilitation thesis includes plans for career evolution and development. The main future research directions are presented as a continuation of the actual research interest. Thus, based on the research and expertise in electrocatalysis of hydrogen evolution reaction, our research group is partner in a HORIZON 2020 proposal submitted in 2017: *Novel modular stack design for high pressure PEM water electrolyzer technology with wide operation range and reduced cost* – **PRETZEL**. The trends in my future research work will be focused on (i) development of new electrocatalysts for hydrogen evolution reaction; (ii) development of new biosensors using carbon based materials such as conducting polymers and carbon nanotubes and (iii) development of supercapacitors for electrochemical energy storage using conducting polymers.

Rezumat

Teza de abilitare intitulată „Procese şi materiale în sisteme electrochimice de energie" reprezintă sinteza activităţilor de cercetare desfăşurate de candidată după obţinerea titlului ştiinţific de Doctor în Inginerie Chimică, în anul 2004. Principala tematică de cercetare o reprezintă electrocataliza reacţiei de degajare a hidrogenului şi sinteza electrochimică a polimerilor conductori şi studiul mecanismului de transport de sarcină în filmele de polimeri conductori.

Teza este structurată pe două părţi, în prima parte fiind prezentate principalele realizări ştiinţifice, profesionale şi academice, iar în partea a doua fiind prezentate planurile de evoluţie şi dezvoltare ulterioară a carierei de cercetare şi universitare.

Partea I este împărţită în două secţiuni, dintre care ***Secţiunea I*** prezintă principalele realizări ştiinţifice în domeniile de cercetare abordate, bazate pe rezultatele originale publicate în cele 14 lucrări ISI selectate, iar Secţiunea II prezintă principalele realizări profesionale şi academice în perioada 2004 – prezent. Acestea includ publicarea a 25 de articole în reviste indexate ISI (*h*-index 11) şi 2 cărţi, 1 brevet de invenţie, 3 proiecte de cercetare în calitate de director, participarea ca membru în echipa de cercetare la 10 proiecte, dintre care unul internaţional, respectiv ca membru în grupul ţintă în 3 proiecte POSDRU. ***Secţiunea II*** prezintă succint principalele realizări profesionale şi academice după obţinerea titlului de doctor. Evoluţia profesională a implicat avansarea din poziţia de asistent pe poziţia de şef de lucrări în anul 2005 respectiv conferenţiar în anul 2008. Din această poziţie am câştigat două granturi pentru dotarea şi modernizarea laboratoarelor de Electrochimie şi Chimie generală. De asemenea, am fost implicată în 3 proiecte POSDRU: Elaborarea şi implementarea programelor de master în domeniul micro- şi nanomaterialelor (MASTERMAT), Creşterea atractivităţii şi performanţei programelor de formare doctorală şi post-doctorală pentru cercetători în ştiinţe inginereşti (ATRACTING) şi Şcoala doctorală în sprijinul cercetării în context european, dintre care ultimul proiect a fost în mod special dedicat cadrelor didactice şi cercetătorilor potenţiali conducători de doctorat şi care a contribuit la formarea mea ca viitor conducător de doctorat prin implicarea activă în coordonarea unui student doctorand.

Principalele realizări ştiinţifice sînt prezentate sub forma a 3 capitole corespunzătoare direcţiilor de cercetare abordate, şi anume Contribuţii la electrocataliza reacţiei de degajare a hidrogenului, Contribuţii la sinteza electrochimică a polianilinei nanostructurate, respectiv Contribuţii la studiul mecanismului de transport de sarcină în polimeri conductori.

Capitolul 1 prezintă o continuare a cercetărilor întreprinse în cadrul tezei de doctorat, fiind una din direcţiile de cercetare iniţiate în Laboratorul de electrochimie, Coroziune şi Industrii electrochimice, care a dus la elaborarea a două teze de doctorat şi publicarea a 4 articole în reviste cotate ISI, la care candidata este co-autor. Cercetările efectuate au avut drept scop accelerarea reacţiei de degajare a hidrogenului prin utilizarea unor electrocatalizatori sub formă de adaosuri în soluţie. Aceşti catalizatori, denumiţi şi vectori de protoni, au capacitatea de a creşte concentraţia protonilor în dublul strat electric de la interfaţa metal-soluţie prin transportul protonilor din masa soluţiei la interfaţă. Rezultatele obţinute au demonstrat că efectul catalitic al vectorilor de protoni se manifestă atât în cazul materialelor de electrod pe care suprapotenţialul de degajare al hidrogenului este crescut, cum ar fi cupru, dar, cu mult mai important din punct de vedere practic, chiar şi în cazul metalelor pe care suprapotenţialul de degajare a hidrogenului este scăzut, şi anume aur şi platină. Drept vectori de protoni au fost alese diverse amine aromatice sau alifatice, având în vedere că abilitatea de a transporta protoni este dată de perechea de electroni neparticipanţi ai azotului. Rezultatele obţinute au arătat că efectul catalitic al aminelor asupra reacţiei de degajare a hidrogenului poate fi explicat pe baza parametrilor moleculari obţinuţi prin modelare, cei mai importanţi fiind momentul dipol şi suprafaţa de acoperire. Astfel, efectul catalitic cel mai pronunţat a fost obţinut în cazul aminelor cu o suprafaţă de acoperire cât mai redusă, ceea ce echivalează cu un număr mai mare de molecule prezente la interfaţă, deci o concentraţie crescută de protoni, respectiv pentru un moment dipol cât mai ridicat, care indică o orientare favorabilă a moleculelor la interfată, şi anume cu atomul de azot şi protonul ataşat orientate înspre metal, poziţie în care transferul de sarcină este mult facilitat.

Capitolul 2 descrie una din direcţiile de cercetare iniţiate de candidată în colaborare cu Institutul de Chimie Timişoara la Academiei Române, care a dus la elaborarea unei teze de doctorat şi 5 articole în reviste cotate ISI la care candidata este autor principal sau co-autor, o parte a rezultatelor fiind obţinute în cadul unui proiect de cercetare de tip Parteneriate, coordonat de către candidată în calitate de responsabil partener. Cercetările efectuate au urmărit influenţa condiţiilor de lucru asupra sintezei electrochimice a nanofirelor de polianilină, şi anume influenţa concentraţiei de acid şi a raportului molar monomer/acid, precum şi influenţa vitezei de scanare, a temperaturii şi a substratului. Rezultatele obţinute au demonstrat că nanofirele de polianilină pot fi obţinute prin metode electrochimice de sinteză, pe diferite materiale de electrod, în condiţii de lucru specifice fiecărui substrat. S-a constatat de asemenea, că valorile capacităţii, care indică abilitatea filmelor de polianilină de a stoca sarcini electrice, sînt mult mai ridicate în cazul filmelor cu o structură nanofibrilară comparativ cu cele cu structură granulară. De asemenea, s-a demonstrat posibilitatea utilizării filmelor de polimeri conductori în diverse aplicaţii, cum ar fi dezvoltarea

unor biosenzori pentru dopamină, respectiv pentru adsorbţia unor poluanţi de tipul coloranţilor azoici.

Capitolul 3 face referire la rezultatele obţinute în colaborare cu Centrul de Spectroelectrochimie al Institutului de cercetare a stării solide şi materialelor din Dresda, Germania, de-a lungul a 5 stagii de cercetare post-doctorală şi care fac obiectul a 5 lucrări publicate în reviste indexate ISI la care candidata este autor principal sau co-autor. Cercetările efectuate au urmărit studiul mecanismului de transport de sarcină în polimeri conductori de tipul polianilinei şi politiofenului. În acest scop au fost utilizate metode spectroelectrochimice *in situ*, care permit înregistrarea simultană a spectrelor în timpul unei voltamograme ciclice, ceea ce echivalează cu obţinerea în timp real a spectrelor pentru diverşi intermediari rezultaţi în timpul oxidării electrochimice a polimerilor conductori. Aplicarea combinată a mai multor astfel de tehnici, cum sînt spectroscopia în infraroşu, spectroscopia de rezonanţă electronică de spin, respectiv spectroscopia în ultraviolet şi vizibil permite diferenţierea speciilor paramagnetice şi diamagnetice şi atribuirea univocă a benzilor de adsorbţie diverşilor purtători de sarcină ce pot fi polaroni, bipolaroni sau perechi de polaroni. Rezultatele obţinute au demonstrat că în cazul polianilinei nucleele de tip fenazină joacă un rol important în formarea şi stabilizarea purtătorilor de sarcină. În cazul derivaţilor substituiţi ai politiofenului a fost pusă în evidenţă existenţa simultană a polaronilor şi perechilor de polaroni, respectiv a bipolaronilor şi perechilor de polaroni în funcţie de creşterea gradului de oxidare/dopare.

Partea a II-a a tezei de abilitare cuprinde planurile pentru evoluţia şi dezvoltarea carierei. Sînt prezentate principalele direcţii viitoare de cercetare, ca o continuare a direcţiilor actuale. Astfel, ca urmare a cercetărilor şi expertizei în electrocataliza reacţiei de degajare a hidrogenului, grupul nostru de cercetare este partener într-o propunere HORIZON 2020 depusă în 2017: *Novel modular stack design for high pressure PEM water electrolyzer technology with wide operation range and reduced cost* – **PRETZEL**. Tendinţele de viitor abordate în munca de cercetare vor fi concentrate în principal pe: (i) dezvoltarea de noi materiale electrocatalitice pentru reacţia de degajare a hidrogenului; (ii) dezvoltarea de noi biosenzori folosind materiale pe bază de carbon cum ar fi polimerii conductori şi nanotuburile de carbon şi (iii) dezvoltarea de supercapacitori pentru stocarea energiei electrochimice utilizând polimeri conductori.

PART I. Main scientific, professional and academic achievements

Section I. Scientific achievements

This habilitation thesis summarizes my activity after defending the PhD thesis in July 2004 and receiving the scientific title of Doctor in the field of Chemical Engineering on the basis of Order no. 4450 dated 02.08.2004 issued by the Ministry of Education and Research.

The scientific and research activity begins in the *Laboratory of Electrochemistry, Corrosion and Electrochemical Engineering* with the development, characterization and practical applications of skeleton nickel electrocatalysts [1-4]. This kind of electrode materials have been used for the hydrogen evolution reaction and as cathodes in direct methanol-air and respectively hydrogen-oxygen fuel cells. These results were obtained as part of the PhD thesis in collaboration with the *University of Applied Sciences Gelsenkirchen, Germany* and within the framework of Romanian excellence research projects (Grant A 40535/2003, 32940/2004 and 2005: Methanol-air fuel cells with skeleton nickel electrodes and Grant A 226/2006 and 76/2007: H_2-O_2 (air) fuel cells with anion exchange membrane and electrodes based on non-noble metals).

In the present my research interest continues the topics started during the PhD thesis and are oriented towards applied electrochemistry with special emphasis on the electrocatalysis of hydrogen evolution reaction and the electrochemical synthesis and characterization of conducting polymer films for the development of electroactive coatings and electrochemical sensors.

The entire research activity is reflected in 29 papers published in ISI ranked journals (*h*-index 11), 1 national patent, 3 research grants as project leader, member in 1 international and 9 national research projects, 2 books.

The scientific achievements presented in this habilitation thesis refer to ***14 selected papers*** that illustrate the two major research directions followed after defending the PhD thesis, namely the electrocatalysis of hydrogen evolution reaction and the electrochemical synthesis of conducting polymer films and the study of charge transport mechanism within such films. The first research direction was initiated in our Electrochemistry group and includes the development of electrocatalytic active films [1-4] and/or electrocatalytic enhancement of the hydrogen evolution reaction [5-8], one of the most intensively studied electrochemical reactions due to its importance in practical applications such as water electrolysis, chlor-alkali

electrolysis and electrochemical reduction of organic compounds. The results obtained within this direction are subject of ***4 research papers*** and lead to the elaboration of two PhD thesis and several diploma works and dissertation thesis, as well as an international research project ***BS ERA-NET 7-046/2011***: Hydrogen production from black sea water by sulfide driven fuel cells.

The second research direction was initiated in collaboration with the *Institute of Chemistry Timisoara of the Romanian Academy* and focuses on the electrochemical synthesis and properties of conducting polymer films [9-13]. Some of the research activities were carried out in the frame of a national project ***PN II Partnership 72-171/2008*** entitled "Microporous polyaniline sensors functionalized with pendant groups, innovative material for use in identification and control of Parkinson's disease" funded by the Romanian Ministry of Education, Research, Youth and Sports between 2008-2011, for which I was partner responsible. Within this project polyaniline films functionalized with boronic acid groups were used to develop microporous biosensors for dopamine detection. The obtained results are subject of ***5 research papers***, 1 PhD thesis and several diploma works and dissertation thesis.

The research activities in the field of conducting polymers were continued by initiating a new collaboration with the *Center of Spectroelectrochemistry of the Leibniz Institute for Solid State and Materials Research Dresden, Germany* to study the charge transport mechanism in conducting polymers by means of spectroelectrochemical methods [14-18]. The results of this cooperation were a number of 5 post-doctoral research stages at *Leibniz Institute for Solid State and Materials Research Dresden, Germany* (2005, 2006, 2007, 2009 and 2011) and ***5 research papers***.

One of the newest research activities related to conducting polymers is their use in the development of flexible electrodes for solar cells and it was part of a research project ***PN II Ideas 77/2013*** for which I was project manager, entitled "New fabrication concept of silver nanowire/polyaniline transparent, conductive and flexible electrodes for solar cells". The project was funded by the Executive Agency for Higher Education, Research, Development and Innovation, subordinated to the Ministry of National Education between 2013-2016 and aimed to develop transparent, conductive and flexible electrodes for solar cells based on silver nanowire/polyaniline hybrid materials and to offer a new technical solution to decrease the sheet resistance of the silver nanowires embedded in the polymer matrix [19-21]. The results obtained within this project are subject of 1 national patent application, ***3 research papers*** and some diploma works and dissertation thesis.

Section II. Professional and academic achievements

The main professional and academic achievements of the candidate in the last 12 years, in the period 2004 -2016, after defending the PhD thesis and receiving the PhD title, are represented by the promotion from the position of assistant in 2004 to assistant professor in 2005 and associated professor in 2008. From this position I have taught the disciplines of Electrochemistry and Corrosion Protection, Electrochemical Processes, Chemistry and General Chemistry.

In my teaching activity with the students I was constantly preoccupied to improve the content of my lectures and laboratory works to keep up with the newest trends in electrochemistry. The lectures are appreciated by the students as clear, with an accessible content and an appropriate scientific level. I have tried to apply modern education methods, using multimedia techniques in the teaching. I was encouraging and offering support to students in the use of specialized software to represent and analyze experimental results obtained during the laboratory works. I participated actively in upgrading and equipping laboratories with specific equipment intended for teaching purposes. Thus, I won by competition two projects to equip undergraduate laboratories financed by Politehnica University Timisoara, namely: Laboratory of Electrochemistry, as a team member and General Chemistry Laboratory, as project manager. I have conducted over 20 diploma works and dissertations, and been actively involved in the supervision of 3 PhD students.

I was member of the Senate of Politehnica University Timisoara, member of the Faculty Council and member of the Department Council.

Starting from 2010 I was involved as long term expert and / or member of the target group in the following 3 POSDRU projects:

POSDRU/86/1.2/S/58146 University for future, DMI. Quality in Higher Education, between 2010-2013, title: *Development and implementation of Master program in the field of micro-and nanomaterials – MASTERMAT*. In the first stage of the project I was involved in the analysis of master programs in the field of micro- and nanomaterials from UE countries and I elaborated the content and Syllabus for the courses of Solid State Electrochemistry and Nanomaterials with electrical, optical and magnetic properties. This courses are compatible with similar or neighbouring courses taught at University of Cambridge, Ecolle Polytechnique de Bruxelles, Ulm University, Graz University of Technology and University of Copenhagen. As a result we have published 1 book: Solid State Electrochemistry, A. Kellenberger, N. Vaszilcsin, Ed. Politehnica, Timisoara, 2013, ISBN 978-606-554-563-2. After starting the Micro- and nanomaterials Master program at the Politehnica University Timisoara, I have taught the discipline of Solid State Electrochemistry (lecture and laboratory works) and I have planned and conducted a dissertation thesis entitled

"Electrochemical synthesis of polyaniline nanofibers applied in hydrogen evolution reaction". As a result, we have published an ISI indexed paper [12].

POSDRU/21/1.5/G/13798 Better Doctoral Programs, DMI. Doctoral and Postdoctoral programs in support of research, between 2010-2012, title: *Doctoral School in support of research in the European context*, member of the target group. This project was intended to support teachers and researchers having the PhD title and aiming to become PhD advisors. I was involved in advising one PhD student including: (i) advising the PhD student in writing his research reports; (ii) advising the PhD student in completing his thesis; (iii) writing and publishing scientific papers in collaboration with the PhD student. As a result we have published three ISI indexed papers [5,6,47]. In the frame of this project I have participated to an international conference: Journées d'Electrochimie 2011, Grenoble, France, 04-08 July 2011 with a poster and I have attended a 2 month research stage at Leibniz Institute for Solid State and Materials Research Dresden between 18.04.2011 – 18.06.2011. As a result of the aforementioned research stage I have published one ISI indexed paper [18].

POSDRU 159/1.5/S/137070 Support for doctoral candidates and postdoctoral researchers, DMI. Doctoral and Postdoctoral programs in support of research, between 2014-2015, title: *Increasing the attractiveness and performance of doctoral and postdoctoral training programs for researchers in engineering sciences – ATRACTING*. In the frame of this project I was responsible with the organization of a thematic workshop for PhD students and postdoctoral researchers, entitled: "*Advanced electrochemical techniques for characterization of electrode materials with applications in energy and environment*" which was held over 4 days and it was attended by 10 participants. My attribution included the elaboration of handout documents for the workshop, as well as 2 lectures on *Linear and cyclic voltammetry. Application in the synthesis of nanomaterials used for supercapacitors* and *Electrochemical impedance spectroscopy. Applications in the study of fuel cells* and also 2 hands-on trainings on *Reversible / irreversible electrochemical reactions studied by cyclic voltammetry* and *Study of electrode reactions and materials by electrochemical impedance spectroscopy*.

In addition to the aforementioned achievements, I was co-chairperson of two of the sections of 1st *Regional Symposium of Electrochemistry South-East Europe*, Croatia 2008 and of *3rd Regional Symposium of Electrochemistry South-East Europe* Bucharest, 13 -17 May 2012 and secretary of the section of Physical Chemistry and Electrochemistry of the *International Conference of Chemistry and Chemical Engineering*, Timisoara, 27-28 May, 2010.

I am member of 2 professional associations: Chemical Society from Romania and International Society of Electrochemistry.

I have participated as reviewer in peer-review process for ISI journals such as: *International Journal of Hydrogen Energy, Synthetic Metals, Chemical Papers, Journal of Alloys and Compounds, Chemical Bulletin of the University Politehnica of Timisoara*, as evaluator for research projects, as member in the advisory committee of 14 PhD students and as a member in the PhD juries of the following thesis:

- Anamaria DABICI, *Oxide materials with photocatalytic activity used for mineralization of dyes from wastewaters*, Politehnica University Timisoara, Faculty of Industrial Chemistry and Environmental Engineering, 2011.
- Anamaria Simona BACIU, *Electrochemical detection of certain specific pollutants from water using nanostructured graphite-based composite electrode materials*, Politehnica University Timisoara, Faculty of Industrial Chemistry and Environmental Engineering, 2012.
- Ştefan Dănică NOVACONI, *Contributions on the development of photoelectrochemical cells based on nanostructured titanium dioxide and dye*, Politehnica University Timisoara, Faculty of Industrial Chemistry and Environmental Engineering, 2013.

1. Contributions on the electrocatalysis of hydrogen evolution reaction

The results presented within this chapter have been obtained in the frame of an international research project **BS ERA-NET 7-046/2011**: "*Hydrogen production from black sea water by sulfide driven fuel cells*" and also as part of two POSDRU projects: **POSDRU/21/1.5/G/13798** *Doctoral school in support of research in the European context* and **POSDRU 159/1.5/S/137070** *Increasing the attractiveness and performance of doctoral and postdoctoral training programms for researchers in engineering sciences – ATRACTING* where I was involved in advising two PhD students.

The results have been published in 4 ISI indexed papers, as follows:

- C.C. Vaduva, N. Vaszilcsin, **A. Kellenberger**, M. Medeleanu, Catalytic enhancement of hydrogen evolution reaction on copper in the presence of benzylamine, *International Journal of Hydrogen Energy* 36 (2011) 6994-7001.
- C.C. Vaduva, N. Vaszilcsin, **A. Kellenberger**, Aromatic amines as proton carriers for catalytic enhancement of hydrogen evolution reaction on copper in acid solutions, *International Journal of Hydrogen Energy* 37 (2012) 12089-12096.
- R. Cretu, **A. Kellenberger**, N. Vaszilcsin, Enhancement of hydrogen evolution reaction on platinum cathode by proton carriers, *International Journal of Hydrogen Energy* 38 (2013) 11685-11694.
- R. Cretu, **A. Kellenberger**, M. Medeleanu, N. Vaszilcsin, Cathodic Hydrogen Evolution Reaction on Gold Catalyzed by Proton-Carriers, *International Journal of Electrochemical Science* 9 (2014) 4465-4477.

1.1. Background

The concept of ecologically clean hydrogen energy started to develop during the mid of 70's, as a response of the scientific community to the impending environmental disaster. Utilizing hydrogen does not produce any harmful effluents, nor does it produce CO_2. It is evident that using hydrogen as an energy carrier automatically solves, in principle, the global problem of the greenhouse effect. The concept of hydrogen economy has been completed by the mid of the 80's and it comprises [22]:

- hydrogen production from water using non-renewable energy sources (coal, atomic energy, thermonuclear energy) and renewable energy sources (sun, hydro, wind, currents, tides, biomass).
- hydrogen delivery, transportation and storage.
- hydrogen utilization in industry, transport (land, water and air) and home.
- problems of material reliability and system safety.

Concerning hydrogen production, one of the main energy sources is coal and hydrocarbons from natural gas and oil. Hydrogen can be obtained with low costs by coal gasification, steam reforming, partial oxidation and autothermal reforming, but besides hydrogen, huge amounts of carbon dioxide are also produced. For example, if hydrogen is obtained by steam reforming of methane, for each ton of H_2 an amount of 5.5 tons of CO_2 are released in the atmosphere [23]. Moreover, in coal gasification technology, 11 tons of CO_2 are emitted in environment for 1 ton of H_2 obtained [24]. The second energy source is water and hydrogen can be obtained by electrolysis, thermolysis or photocatalytic water splitting. Although water splitting by electrolysis is a green procedure, it is limited by important electric energy consumption and it is applicable particularly in areas where clean, inexpensive electricity is available. As a matter of fact, statistical data from 2007 reveal that 96% of hydrogen was obtained from fossil fuels and only 4% by electrolysis. So it seems to be enough potential to improve water electrolysis.

Water electrolysis was performed for the first time in 1800 by William Nicholson and Anthony Carlisle, who used the battery invented by Volta. Water electrolysis implies oxygen evolution reaction (OER) at the anode, with a standard potential of 1.23 V and hydrogen evolution reaction (HER) at the cathode with a standard potential of 0V at pH = 0, according to equations (1) and (2). The overall decomposition reaction of water proceeds according to equation (3) and requires a cell voltage of 1.23 V. However, electrolysis will not generally proceed at these voltages, as the electrical input must overcome the ohmic resistance and the electrode overpotential, as seen in equation (4). In order to reduce energy consumption for water electrolysis these two terms needs to be minimized.

A(+): $2\ H_2O \rightarrow O_2 + 4\ H^+ + 4e^-$ $E_o = 1.23$ V (1)

C(−): $2\ H^+ + 2e^- \rightarrow H_2$ $E_o = 0$ V (2)

Global: $2\ H_2O \rightarrow 2\ H_2 + O_2$ $\Delta E_o = 1.23$ V (3)

$\Delta E_{cell} = \Delta E_o + IR_{cell} + \Sigma\eta$ (4)

The first term refers to the total ohmic series resistance of the cell including external circuit resistances and connections at the anode and cathode, the electrolyte and membrane resistance, and also resistances coming from partial coverage of the anode and cathode with oxygen and respectively hydrogen bubbles. This term can be minimized by operating the electrolysis at high temperatures and pressures, by using high conductivity electrolytes and by decreasing wire length, increasing cross-section and using more conductive wire materials and also by zero-gap geometry electrolysis cells. Pure water is a very poor electric conductor and, for this reason, is difficult to electrolyze. Electrolysis may be conducted in acidic or alkaline solution, but alkaline electrolysis has been developed commercially because the electrode materials are cheaper and less susceptible to corrosion compared to those required for acid electrolytes. Important progress has been achieved since the development of proton exchange membrane (PEM) water electrolyzers consisting of a thin proton-conducting membrane which acts as solid electrolyte. On each side of the membrane thin layers of electrocatalysts are coated, acting as anode for oxygen evolution reaction and respectively cathode for hydrogen evolution reaction. Electrolyzers based on this concept can operate at

higher pressures than conventional electrolyzers and also at much higher current densities because they provide a compact system design (zero-gap geometry) and therefore minimize the ohmic losses [25-27].

The second term refers to the sum of the overpotentials including the activation overpotential at the two electrodes and the concentration overpotential due to the mass transport of the gaseous products away from the anode and cathode surfaces. The ways to reduce the overpotential can be deduced from electrode kinetics, described by the Butler-Volmer equation, which gives the dependence of the current density on the potential, according to equation (5).

$$i = i_o\left(e^{\alpha f\eta} - e^{-(1-\alpha) f\eta}\right) \qquad \text{Butler-Volmer equation} \qquad (5)$$

where $f = zF/RT$

This equation can be simplified, for example at very large cathodic overpotentials the first term can be neglected and the relationship can be written as the Tafel equation which gives a linear dependence between overpotential and the logarithm of current density.

$$\eta = 2.303\frac{RT}{(1-\alpha)F}\log i_o - 2.303\frac{RT}{(1-\alpha)F}\log|i| \qquad \text{Tafel equation} \qquad (6)$$

or $\eta = a + b\cdot\log|i|$

Tafel equation shows that overpotential can be minimized by using electrocatalysts which enhance the rate of the electrode reaction in two ways: (i) by providing higher values of the exchange current density i_o, without changing the reaction mechanism or (ii) by decreasing the slope of the equation, which means an increase of the charge transfer coefficient $1 - \alpha$, so a change of the reaction mechanism. The two ways an electrocatalyst can decrease the overpotential at high current densities are illustrated in Figure 1.

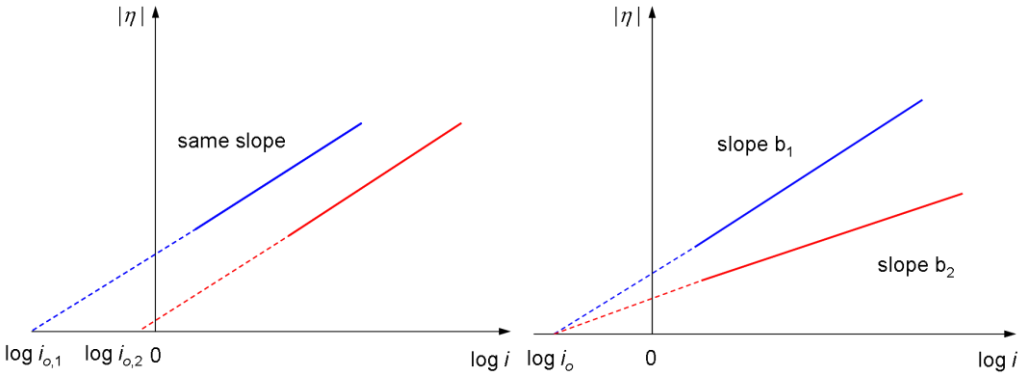

Figure 1. Electrocatalytic enhancement of electrode reactions without mechanism change (left) and by changing the mechanism (right).

The electrocatalysts enhance the electron transfer between the electrode and the reactants and they may act at the electrode surface or may be the electrode surface itself.

Catalytic enhancement of the HER is one of the best available ways to increase the efficiency of the water electrolysis process, which can be achieved on one hand by using electroactive materials and modified electrodes for HER, and on the other hand, by introducing additives in the electrolyte solution as proton carriers.

The mechanism of hydrogen evolution reaction is a combination of three reaction steps. The first step is always the electrochemical hydrogen adsorption or Volmer reaction. The second step is hydrogen desorption and it can proceed either electrochemically according to the Heyrovsky reaction or chemically according to the Tafel reaction. Based on the two possibilities for hydrogen desorption, two mechanisms have been proposed: the Volmer-Tafel mechanism and the Volmer-Heyrovsky mechanism. In acid media, the Volmer and Heyrovsky reactions are given by equation (7) and (8).

$$M + H_3O^+ + e^- \underset{k_{-1}}{\overset{k_1}{\rightleftharpoons}} MH_{ads} + H_2O \qquad \text{Volmer reaction / acid media} \qquad (7)$$

$$MH_{ads} + H_3O^+ + e^- \underset{k_{-2}}{\overset{k_2}{\rightleftharpoons}} H_2 + M + H_2O \qquad \text{Heyrovsky reaction / acid media} \qquad (8)$$

In alkaline media the Volmer and Heyrovsky reactions are given by equations (9) and (10).

$$M + H_2O + e^- \underset{k_{-1}}{\overset{k_1}{\rightleftharpoons}} MH_{ads} + OH^- \qquad \text{Volmer reaction / alkaline media} \qquad (9)$$

$$MH_{ads} + H_2O + e^- \underset{k_{-2}}{\overset{k_2}{\rightleftharpoons}} H_2 + M + OH^- \qquad \text{Heyrovsky reaction / alkaline media} \qquad (10)$$

The Tafel reaction is pH independent and it is given by equation (11).

$$MH_{ads} + MH_{ads} \underset{k_{-3}}{\overset{k_3}{\rightleftharpoons}} 2M + H_2 \qquad \text{Tafel reaction} \qquad (11)$$

If the electrocatalyst is the electrode material itself, then the Trasatti's volcano curve [28] can be used to estimate its electrocatalytic activity. The volcano curve is a plot of the reaction rate, expressed as logarithm of the exchange current density, versus the hydrogen adsorption energy. It shows that if the hydrogen adsorption energy is too low, than the rate of adsorption is slow and becomes the rate determining step. If it is too high, the overall reaction rate is limited by the desorption step. The maximum rate is observed for platinum group metals, with intermediate values of hydrogen adsorption energies.

Although platinum group metals present the highest activity for HER, the high costs associated with the electrocatalyst development have promoted researches to reduce platinum loadings or to replace platinum with other metals, less expensive but with comparable electrocatalytic properties [29,30]. Electroactive cathodes based on platinum group metals were realized by depositing a thin film [31,32] on common metals, so that the costs of cathodes used for water electrolysis were substantially reduced. As replacement for platinum, nickel has been extensively studied due to its good corrosion resistance in alkaline media. Recent trends in research include the study of nickel nanoparticles supported on carbon nanofibers and graphenes as effective electrocatalysts for hydrogen evolution reaction [33-

35]. However, in acid electrolytes only noble metals, and in particular platinum metals, are resistant under unpolarized conditions and can be used as electrode materials for hydrogen evolution [36]. Independently on the electrocatalyst which is used, a further decrease of the overpotential of HER can be achieved by increasing the real surface area of the electrode and/or by increasing the intrinsic activity of the electrode material, which can be achieved by alloying and/or doping with transitional metals. Recent advances in the development of efficient electrocatalyst for HER using low cost and earth abundant materials include the use of transitional metal sulfides [37-40], phosphides [41-43] and carbides [44-46] and even metal-free catalyst based on graphene composites [47].

1.2. HER catalysis by proton carriers

Another way to reduce the overpotential of HER is by using electrocatalysts in the solution. The electrocatalysts in the solution are compounds that are able to increase the concentration of protons in the electric double layer at the interface, by transporting protons from the bulk to the interface, therefore they are called proton carriers. Example of such proton carriers are amines, and their catalytic activity is caused by the lone electron pair of the nitrogen atom.

The catalytic enhancement of HER by proton carriers is scarcely reported in the literature. Such a pseudo–homogeneous catalytic effect was reported for the first time on the dropping mercury electrode, since the HER overpotential on mercury has very high values and a catalytic effect is easier to observe [48]. Different catalysts have been studied, such as peptides and proteins [49-51] and their action has been interpreted as a mediated proton transfer from the solution to the mercury cathode [52]. Frumkin also observed a depolarization of the polarographic waves of hydrogen evolution on mercury in the presence of amines [53]. He proposed a two-step mechanism by which, in the first step the protonated amine participates directly in the HER, by a reversible charge transfer process:

$$CAT - H^+ + e^- \longleftrightarrow [CAT - H]$$

The second step is irreversible and leads to the formation and release of hydrogen molecule and regeneration of the amine molecule which is released in the bulk of solution and can be again protonated:

$$2[CAT - H] \longrightarrow H_2 + CAT$$

In this mechanism, the protonated amine, the reaction intermediate and the amine are temporarily adsorbed at the metal–electrolyte solution interface, so that the process takes place through an adsorption – re-sorption mechanism [53].

Such catalyst molecules behave as a proton carrier because they transport protons from the solution bulk into the electric double layer at the metal – electrolyte solution interface. A molecule is able to act as a proton carrier if it has lone electron pairs in the valance layer, where the protons can attach. This condition is fulfilled if nitrogen, oxygen, phosphorus and/or sulfur atoms are present in the molecular structure of the catalyst [52]. Noteworthy in this way, is the catalytic effect of famotidine, an organic compound which contains nitrogen,

sulfur and oxygen atoms in the molecule [54]. The catalytic effect of sulfur compounds (thiourea and N–substituted thioureas) on the HER on mercury electrodes was also studied [55]. However, it has been found that thiourea does not have a catalytic effect for HER on silver electrode in acid media, but only in neutral solutions. This has been explained in terms of hydrogen bonds formed between the nitrogen atom and the water molecules, thus mediating the proton discharge [56].

1.2.1. Catalytic enhancement of HER on copper electrode

Copper is not commonly used as such as electrode material for hydrogen evolution reaction. In fact, the catalytic enhancement of HER on copper has been observed in our research group during studies on the cathodic copper deposition using several aromatic amines as leveling agents [57]. It has been found that benzylamine acts as inhibitor for copper deposition and, in the same time as accelerator for HER.

In our studies we have evidenced the catalytic effect of benzylamine for HER on a copper electrode. Electrochemical measurements were carried out with a PAR 2273 potentiosta-galvanostat, using a conventional three-electrode, one compartment glass cell, with the working electrode made of Cu (99.99% Cu) with a surface of 0.5 cm^2. Two graphite rods were used as counter electrode and saturated calomel electrode (SCE) as reference electrode.

Steady-state polarization curves were recorded potentiostatically at low scan rate (2.5 mV s^{-1}) from 1 mol L^{-1} H_2SO_4 solution in the absence and respectively in the presence of different concentrations of benzylamine (BA) and the corresponding Tafel plots were represented, as seen in Figure 2.

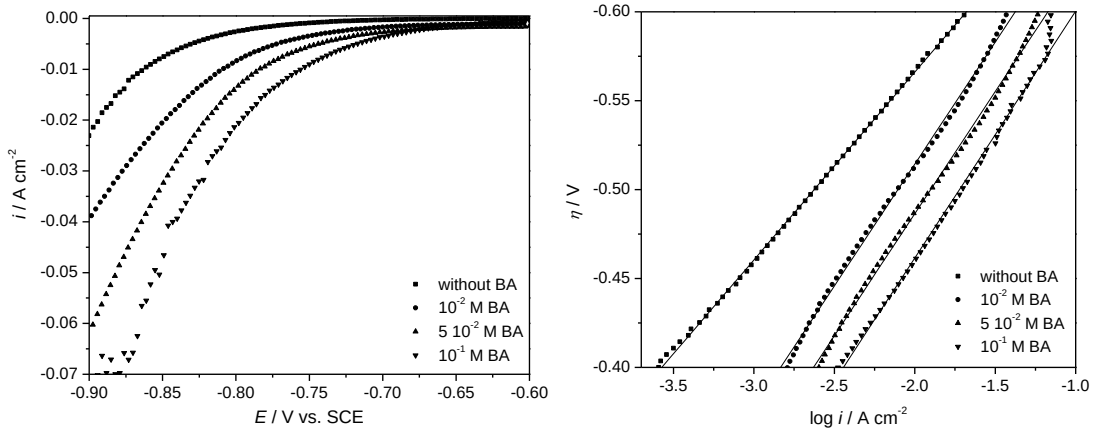

Figure 2. Steady-state polarization curves (left) and Tafel plots (right) for hydrogen evolution reaction on copper electrode in 1 mol L^{-1} H_2SO_4 solution in the absence and presence of various concentrations of benzylamine.

The presence of BA in the electrolyte solution induces a decrease of the overpotential for HER, proportional to the concentration of BA in the solution. The decrease of overpotential

at a current density of 200 A m^{-2} is about 45, 70 and respectively 100 mV for concentration of BA of 10^{-2}, 5 10^{-2} and respectively 10^{-1} mol L^{-1}.

Based on the Tafel plots the kinetic parameters (Tafel slope *b*, charge transfer coefficient $1-\alpha$ and exchange current density i_o) have been determined in dependence of the BA concentration and are given in Table 1.

Table 1. Kinetic parameters for HER on copper electrode at various concentration of BA.

BA [mol L^{-1}]	*b* [mV dec^{-1}]	$1-\alpha$	i_o [A cm^{-2}]
0	–106	0.56	4.4×10^{-8}
10^{-2}	–137	0.43	1.8×10^{-6}
5 10^{-2}	–137	0.43	2.9×10^{-6}
10^{-1}	–139	0.42	4.8×10^{-6}

The value of the Tafel slope on copper without benzylamine is –106 mV $decade^{-1}$. This value is slightly lower than the theoretical value of –118 mV $decade^{-1}$ predicted for the HER mechanism in acidic media, if the Volmer reaction is the rate determining step [58]. When BA is added to the electrolyte solution, the value of the Tafel slope increases to –137 mV $decade^{-1}$ and remains almost constant, independently on the concentration of BA. The increase in the absolute value of the Tafel slope is a consequence of the decrease of the cathodic charge transfer coefficient $1-\alpha$. The second electrochemical parameter which gives information about the electrocatalytic activity is the exchange current density i_o. Considering the values of the exchange current density given in Table 1, it can be observed that for copper, in the absence of BA, the value is very low and comparable to those reported in the literature [58]. In the presence of BA, the values of the exchange current density show an important increase, directly proportional to the concentration of BA. The highest value obtained is two orders of magnitude higher than the exchange current density on copper without BA. It can be therefore concluded, that the overall effect of BA is to accelerate the HER without changing the reaction mechanism, but by increasing the exchange current density, which compensates the decrease of the cathodic transfer coefficient.

The catalytic activity of BA on the HER on copper electrode was also investigated as a function of temperature and the HER activation energy was calculated both in the absence and presence of BA. Steady–state polarization curves and the corresponding Tafel plots at different temperatures, from 1 M sulfuric acid solution with 5 10^{-2} mol L^{-1} BA are shown in Figure 3.

According to the general theory for the HER mechanism, the temperature influences the HER overpotential in two ways. On one hand, the temperature increase leads to a slight increase in the value of the Tafel slope, meaning an enlargement of the HER overpotential. However, this effect is less important and it is overcome by the pronounced increase of the exchange current density. Therefore, the overall effect of temperature on the HER is to decrease the overpotential. The experimental polarization curves from Fig. 3 indicate a decrease of the HER overpotential of about 150 mV when increasing the temperature from 288 to 328 K.

The kinetic parameters for the HER as function of temperature determined from the Tafel plots are given in Table 2.

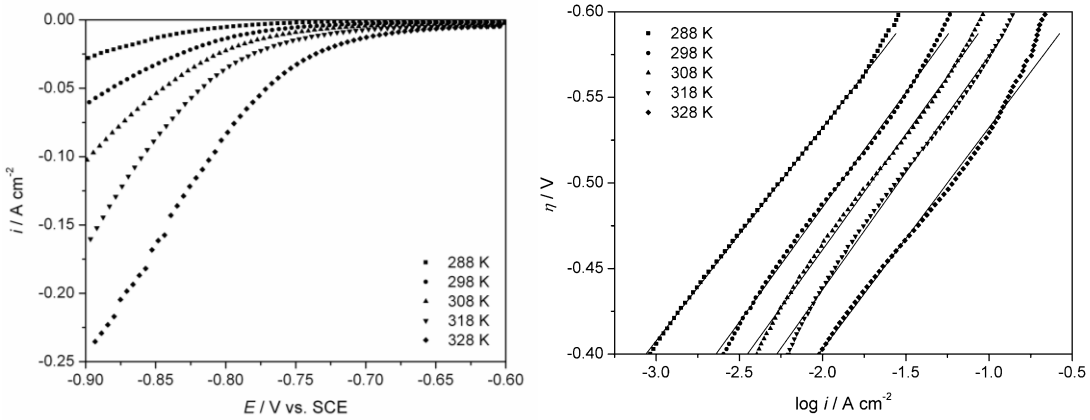

Figure 3. Steady-state polarization curves (left) and Tafel plots (right) for hydrogen evolution reaction on copper electrode in 1 mol L^{-1} H_2SO_4 solution with 5 10^{-2} mol L^{-1} benzylamine at different temperatures.

The dependence of exchange current density on temperature was used to construct Arrhenius plots and to calculate the activation energy for HER according to relation (12):

$$E_a = -2.303 \cdot R \frac{\partial(\log i_o)}{\partial(T^{-1})} \qquad (12)$$

Activation energies of 94.6 kJ mol^{-1} and 33.0 kJ mol^{-1} have been obtained for HER in 1 mol L^{-1} H_2SO_4 solution without BA and with 5 10^{-2} mol L^{-1} BA. The threefold decrease of the value of activation energy is a supplementary evidence of the catalytic effect of BA on HER.

Table 2. Kinetic parameters for HER on copper electrode at different temperatures in 1 mol L^{-1} H_2SO_4 solution without / with 5 10^{-2} mol L^{-1} BA.

T [K]	without BA			5 10^{-2} mol L^{-1} BA		
	b [mV dec^{-1}]	1–α	i_o [A cm^{-2}]	b [mV dec^{-1}]	1–α	i_o [A cm^{-2}]
298	–105	0.56	4.4×10^{-8}	–137	0.43	2.9×10^{-6}
308	–109	0.54	7.1×10^{-8}	–135	0.44	3.8×10^{-6}
318	–117	0.50	2.7×10^{-7}	–137	0.43	6.3×10^{-6}
328	–118	0.50	6.8×10^{-7}	–130	0.46	7.8×10^{-6}

The catalytic effect of BA was further investigated by electrochemical impedance spectroscopy (EIS). Impedance measurements were performed in the frequency range from 0.1 Hz to 100 kHz with AC voltage amplitude of 10 mV. Complex plane (Nyquist) and phase angle (Bode) plots obtained in 1 mol L^{-1} H_2SO_4 solution in the absence and respectively in the presence of different concentrations of BA are given in Figure 4.

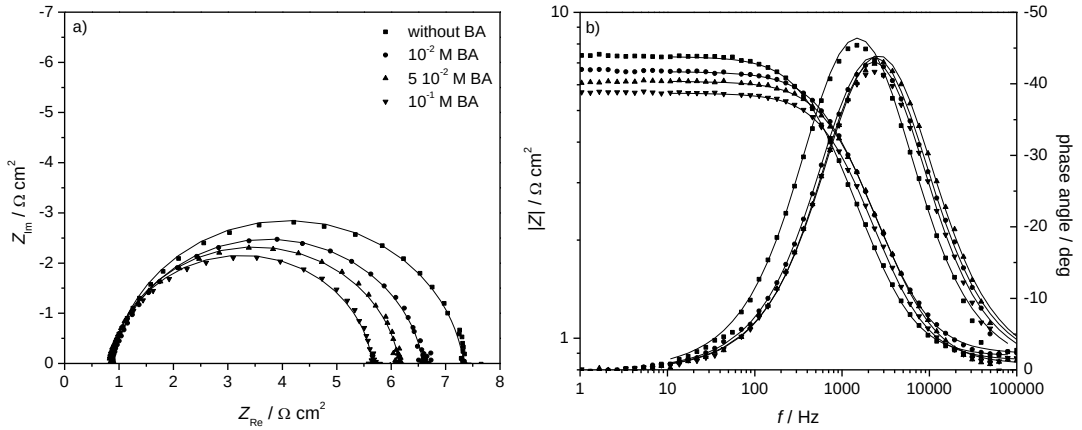

Figure 4. Experimental Nyquist (a) and Bode (b) plots at E = –0.75 V, for HER on copper in 1 mol L^{-1} H_2SO_4 solution in the absence and presence of various concentrations of benzylamine.

The shape of the Nyquist and Bode plots is similar both in the absence and presence of BA, characterized by a slightly depressed semicircle related to the charge transfer step and by the presence of only one time constant, indicating that HER proceeds according to the same mechanism in both cases. The addition of BA has the effect of decreasing the charge transfer resistance, as evidenced by the decrease of the semicircle radius when the concentration of BA increases.

An electrical equivalent circuit (EEC) with one time constant has been proposed to model the impedance data. The EEC contains the solution resistance R_S in series with a parallel connection of the double layer capacitance C_{dl} and the charge transfer resistance R_{ct}. The impedance response of solid electrodes is usually described more accurately if the double layer capacitance is replaced by a constant phase element CPE, characterized by two parameters: T which is related to the double layer capacitance and n which is an exponent between 0 and 1 describing the constant phase angle of the CPE.

Table 3. Experimental values and standard errors for the EEC parameters related to HER on copper in 1 mol L^{-1} H_2SO_4 in the presence of different concentrations of BA.

BA [mol L^{-1}]	R_S [Ω cm^2]	R_{ct} [Ω cm^2]	C_{dl} [F cm^{-2}]	Chi^2
0	0.9 (0.88%)	6.5 (0.86%)	4.30×10^{-5}	3.2×10^{-3}
10^{-2}	0.9 (0.77%)	5.7 (0.71%)	2.91×10^{-5}	2.5×10^{-3}
$5\ 10^{-2}$	0.8 (0.87%)	5.3 (0.77%)	2.72×10^{-5}	3.0×10^{-3}
10^{-1}	0.9 (0.94%)	4.8 (0.89%)	3.33×10^{-5}	4.2×10^{-3}

The experimental EIS data were fitted by a complex non–linear least squares (CNLS) Levenberg–Marquard procedure using ZView 3.0, a Scribner Associates Inc. Software. The values of double layer capacitance and charge transfer resistance were determined by

modeling the experimental EIS data to the electrical equivalent circuit and they are given in Table 3.

The values of the double layer capacitance decrease with increasing concentrations of BA, showing that BA adsorbs on the copper–electrolyte solution interface. The values of the charge transfer resistance decrease proportionally with the BA concentration, meaning that HER takes place easier in the presence of BA.

We suppose that the mechanism of HER implies both hydrogen discharge from benzylammonium ions according to equation (13) as well as hydrogen discharge from hydronium ions, reaction (14).

$$C_6H_5-CH_2-NH_3^+ + e^- \longrightarrow H_{ads} + C_6H_5-CH_2-NH_2 \quad (13)$$

$$H_3O^+ + e^- \longrightarrow H_{ads} + H_2O \quad (14)$$

The EIS results demonstrate that BA directly participates in the HER mechanism, by transporting protons from the bulk of the solution to the interface, although a clear distinction between the two charge transfer steps was not possible, probably due to similar time constants.

To establish the reasons for the increase of exchange current density in the presence of benzylamine, molecular parameters such as dipole moment and molecular coverage area have been computed. The orientation of the dipole moment of protonated benzylamine molecule is shown in Figure 5 and the obtained value is 9.856 D. The surface coverage area is 52.26 Å. The large value of the dipole moment determines a strong adsorption of benzylammonium molecules at the interface and also a preferential orientation, with the ammonium group towards the metal, which is the most favorable position for the charge transfer reaction to take place. So, in the presence of BA the concentration of $–NH_3^+$ groups at the interface is high, probably much higher than the concentration of H_3O^+ ions in the absence of BA and this explains the enhancement of HER by increasing the exchange current density.

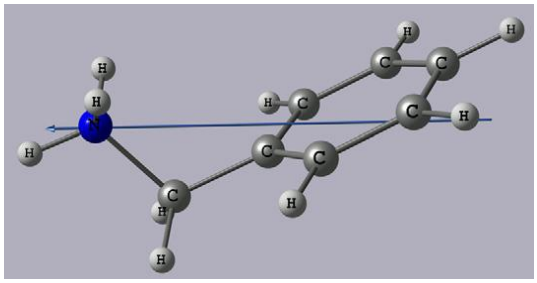

Figure 5. Molecular dipole moment (arrow) of protonated benzylamine molecule.

As a conclusion, the catalytic effect of BA on HER on copper has been evidenced by different electrochemical techniques. Steady-state polarization curves showed that BA (10^{-1} mol L^{-1}) depresses the overpotential of HER on copper by 100 mV at a current density of 200 A m^{-2}. Also, the kinetic parameters for HER on copper are enhanced in the presence of BA.

The exchange current density increases by two orders of magnitude and the activation energy decreases three times in the presence of BA (10^{-1} mol L^{-1}). Impedance measurements indicate that BA adsorbs on the copper–electrolyte solution interface as seen from the decrease of double layer capacitance in the presence of BA. Also, the charge transfer resistance values decrease proportionally with the BA concentration, confirming a direct participation of BA in HER. Quantum calculation showed that the catalytic effect of BA can be explained in terms of a strong adsorption of benzylammonium ions at the electrode–electrolyte interface and of a favorable orientation of the cation with the $-N^{+}H_3$ group toward the electrode's surface.

The promising results obtained with benzylamine have determined to extend the studies on the catalytic effect of other aromatic amines. A series of aniline derivatives has been selected, with the chemical structure given in Figure 6.

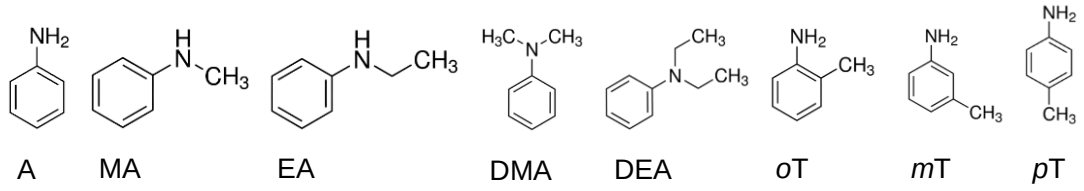

Figure 6. Chemical structure of aniline derivatives used as proton carriers for HER on copper.

Steady-state polarization curves for HER were recorded potentiostatically in 0.5 mol L^{-1} H_2SO_4 solution, in the absence and respectively in the presence of the selected aromatic amines at different concentrations, 10^{-4}, 5 10^{-4}, 10^{-3} and 5 10^{-3} mol L^{-1}. Measurements were also made at different temperatures (298, 308, 318 and 328 K) to determine the temperature dependence of the kinetic parameters and to calculate the activation energy of HER.

The steady-state polarization curves and the corresponding Tafel plots obtained in 0.5 mol L^{-1} H_2SO_4 solution in the presence of 10^{-4} mol L^{-1} of different aniline derivatives are given in Figure 7 and 8.

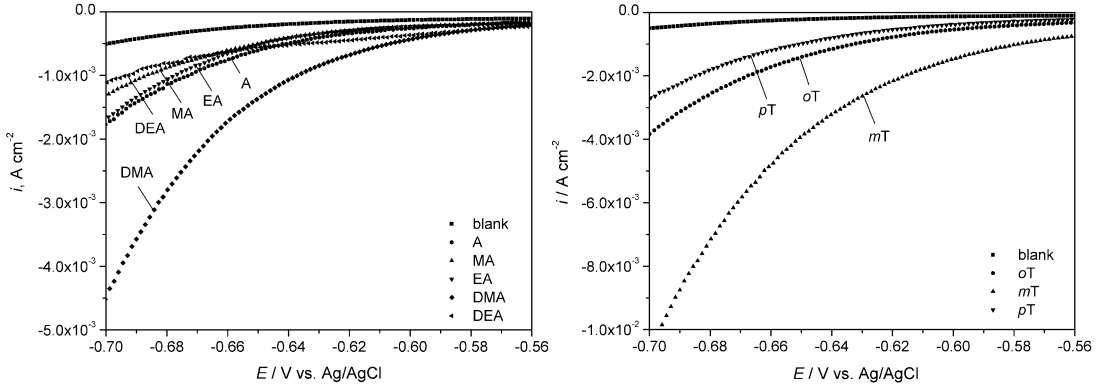

Figure 7. Steady-state polarization curves for hydrogen evolution reaction on copper electrode in 0.5 mol L^{-1} H_2SO_4 solution with 10^{-4} mol L^{-1} of different aniline derivatives.

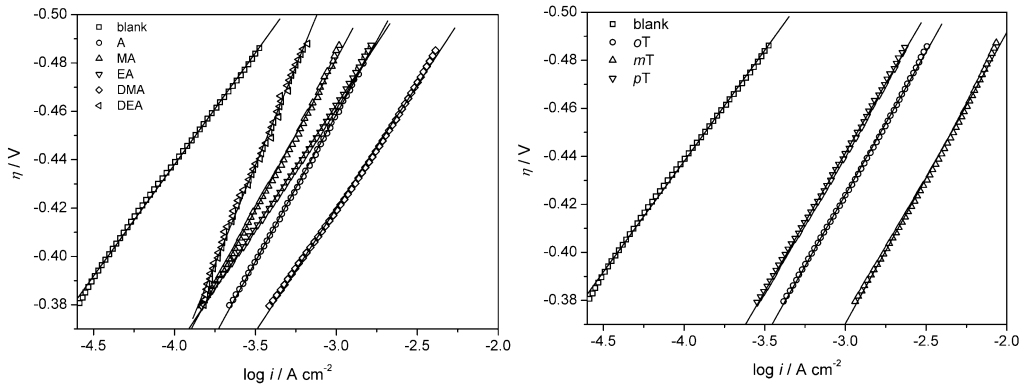

Figure 8. Tafel plots for hydrogen evolution reaction on copper electrode in 0.5 mol L^{-1} H_2SO_4 solution with 10^{-4} mol L^{-1} of different aniline derivatives.

It is obvious that all the aromatic amines induced a decrease of the overpotential for HER, the strongest effects being observed for toluidines and DMA. The depolarization observed on the linear polarization curves is considerably influenced by the nature of amines, suggesting a strong dependence between amines structure and catalytic effect.

Based on the Tafel plots the kinetic parameters have been evaluated for all the amines at the lowest concentration and are given in Table 4.

Table 4. Kinetic parameters for HER on copper electrode in 0.5 mol L^{-1} H_2SO_4 solution and 10^{-4} mol L^{-1} of different aromatic amines.

Added amines	- b [mV decade^{-1}]	1-α	i_o [A m^{-2}]
Blank	92	0.64	2.0×10^{-5}
A	122	0.48	2.9×10^{-3}
MA	125	0.47	6.5×10^{-4}
EA	102	0.58	6.8×10^{-4}
DMA	103	0.58	7.6×10^{-4}
DEA	164	0.40	1.9×10^{-3}
*o*T	119	0.50	2.7×10^{-3}
*m*T	121	0.50	2.8×10^{-3}
*p*T	114	0.51	1.5×10^{-3}

It can be observed that the Tafel slope value is ranging between 100 – 125 mV decade^{-1} in the presence of amines, indicating that they are catalysts which act on the HER without changing the mechanism, only increasing the exchange current density. A higher value of the slope is obtained in case DEA, with two voluminous ethyl substituents at the nitrogen atom.

The cathodic charge transfer coefficient decreases in the presence of amines, because the distance along reaction coordinate between metal and activated states is greater for aryl-ammonium ions than for hydronium ions, considering the different dimensions of the two ions. The decrease of 1-α is kinetically unfavorable but this effect is compensated by the

large increase of the exchange current density, resulting in an overall effect of HER enhancement. It should be also noted that the increase of i_o is more pronounced than the decrease of 1-α.

The way amines act on HER kinetics is rather complex, since the catalytic activity depends not only on concentration and molecular properties, but also on the surface coverage degree and energetic aspects related to amines adsorption on the electrode-electrolyte interface. Low molecular volume amines, such as aniline, can provide a higher concentration of aryl-ammonium ions at the interface, at least at concentrations corresponding to a surface coverage degree of 1. The experimental results confirm that the addition of aniline increases the exchange current density by two orders of magnitude. The effect is less pronounced for the *N*-substituted derivatives of aniline, excepting DEA, where the adsorption is influenced by the steric effects of the ethyl groups. A similar influence to that of aniline is observed for *p*T, explained by the fact that the amino group is not shielded by any substituent, however the methyl- group, due to its inductive electronic effect, decrease the molecular dipole moment, having as a consequence the diminution of exchange current density. Additionally, the surface coverage of *p*T molecule (perpendicularly on the dipole moment) is the same as that of aniline. A pronounced effect on the exchange current density is observed also for *m*T and *o*T. This could be explained in terms of different adsorption energy values and also due to the electron-releasing inductive effect of methyl groups which are now closer to the reaction center.

The catalytic effect of the proton carrier amines has been also confirmed by electrochemical impedance spectroscopy. EIS spectra, shown in Figure 9 were recorded at – 0.7 V vs. Ag/AgCl and modeled by a simple electrical equivalent circuit, presented as inset in Figure 9.

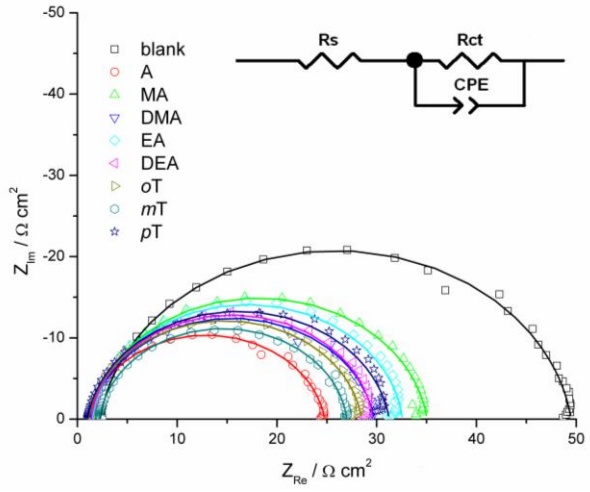

Figure 9. Complex plane plots for HER on copper in 0.5 mol L^{-1} H_2SO_4 in the presence of 10^{-4} mol L^{-1} aromatic amines. Inset: electrical equivalent circuit used to model impedance data.

The Nyquist plots show the presence of a slightly depressed semicircle related to the charge transfer step, with the diameter of the semicircle depending on the nature of the aromatic amines. All the experimental data were fitted by a CNLS procedure to the electrical

equivalent circuit and the corresponding values of the circuit elements are given in Table 5, together with the standard errors and the goodness of fit expressed by the Chi-squared value and the double layer capacitance values.

Table 5. Charge transfer resistance for HER on copper in 0.5 mol L^{-1} H_2SO_4 in the presence of 10^{-4} mol L^{-1} amines.

Parameter	blank	A	MA	EA	DMA	DEA	*o*T	*m*T	*p*T
R_{ct} [Ω cm^2]	47.2	23.6	33.7	28.4	31.1	28.2	27.4	24.8	30.2
$C_{dl} \times 10^5$ [F cm^{-2}]	2.14	4.26	3.37	3.26	2.94	3.23	4.12	4.13	3.77

The experimental values of the EEC elements obtained by modeling the impedance data point out to the catalytic effect of aromatic amines. Although the amines are adsorbed in the inner Helmholtz layer, only slight changes in the double layer capacitance can be noticed, probably due to the low concentrations. The strongest effect is observed in regard with the charge transfer resistance. Generally, the addition of aromatic amines leads to a decrease of the charge transfer resistance, compared to that obtained in the blank solution, showing that HER is enhanced in the presence of aromatic amines. Because the EIS plots show the presence of only one time constant it is assumed that the HER mechanism does not change in the presence of amines. The protonated amines act as "protons carriers" accelerating the HER. The charge transfer resistance decreases in the order: blank > MA > DMA > *p*T > EA > DEA > *o*T > A > *m*T, which is in very good agreement with the order of exchange current density values.

As a conclusion, the catalytic effect of several aromatic amines on HER on copper has been evidenced by different electrochemical techniques. Steady-state polarization curves showed an important depolarization for the HER on copper for all the studied amines. Also, the kinetic parameters for HER on copper are enhanced in the presence of aromatic amines. The exchange current density increases by two orders of magnitude even at low concentrations of added amines. Impedance measurements confirm that the investigated aromatic amines directly participate in the HER mechanism and decrease the charge transfer resistance values.

1.2.2. Catalytic enhancement of HER on gold electrode

The catalytic effect of aromatic amines has been evidenced on metals with high overpotential for HER, such as mercury and copper, but these metals can not be used as electrode materials for hydrogen production by water electrolysis. As a consequence, the catalytic effect of aromatic amines has been disregarded for a long time as a practical method to reduce HER overpotential. The aim of our investigation was to prove that the catalytic effect of amines is still observable for metals with low HER overpotential, such as gold and platinum.

Gold shows a moderate to low overpotential for HER and according to the *volcano plot* for HER the strength of Au–H bond is lower than that of Pt–H bond, with a value close to that of iron group metals [28] which suggest that gold should provide a similar catalytical effect on the recombination of hydrogen atoms. The lower strength of Au–H bond makes gold an

interesting partner in the development of bifunctional catalysts with catalytic activity for both charge transfer reaction and chemical/electrochemical hydrogen desorption.

In our studies, several aliphatic and aromatic amines have been tested as electrocatalysts in the solution for HER on gold electrode: methylamine, *DL*-1-phenylethylamine, aniline, N-methylaniline, 2-biphenylylamine, 3-chloroaniline, 4-chloroaniline and ammonium sulphate, with the corresponding chemical structures shown in Figure 10.

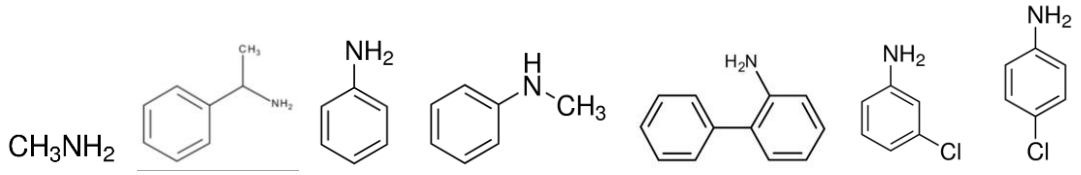

Figure 10. Chemical structure of aliphatic/aromatic amines used as proton carriers for HER on gold.

Linear voltammograms were recorded from 0.5 mol L^{-1} H_2SO_4 solution and 10^{-3} mol L^{-1} added amine with a PAR 2273 potentiostat-galvanostat. The electrochemical measurements were carried out in a standard three-electrode configuration, using a gold working electrode (ϕ = 1.6 mm, A = 0.02 cm^2), a platinum sieve as counterelectrode and Ag/AgCl (sat) as reference electrode. Examples of linear voltammograms obtained on the gold electrode are given in Figure 11.

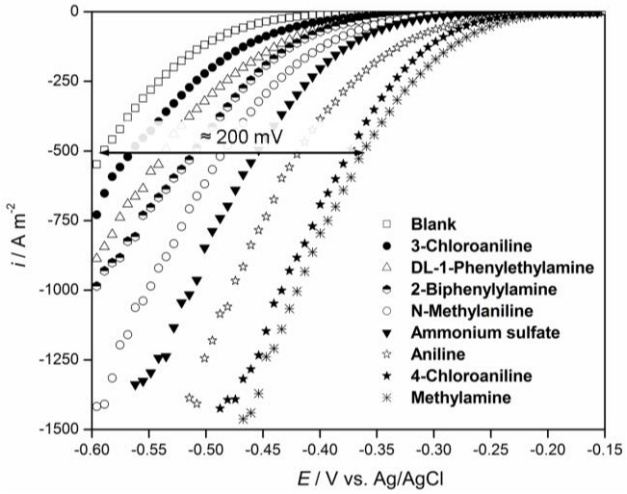

Figure 11. Linear voltammograms on gold electrode in 0.5 mol L^{-1} H_2SO_4 solution at 25°C, concentration of amines: 10^{-3} mol L^{-1}, scan rate: 10 mV s^{-1}.

It can be observed that all the tested amines show some catalytic effect, by decreasing the potential needed for hydrogen evolution at a constant current density. The most significant effect, of about 200 mV decrease of the overpotential, has been observed for aniline, 4-chloroaniline and methylamine, therefore these three amines were selected for further studies regarding the effect of concentration and temperature on the kinetic parameters of HER.

Linear voltammograms have been obtained at different concentrations of the amines, between 10^{-6} and 10^{-3} mol L^{-1} and different temperatures, between 298 and 328 K. A selection of such curves is given in Figure 12.

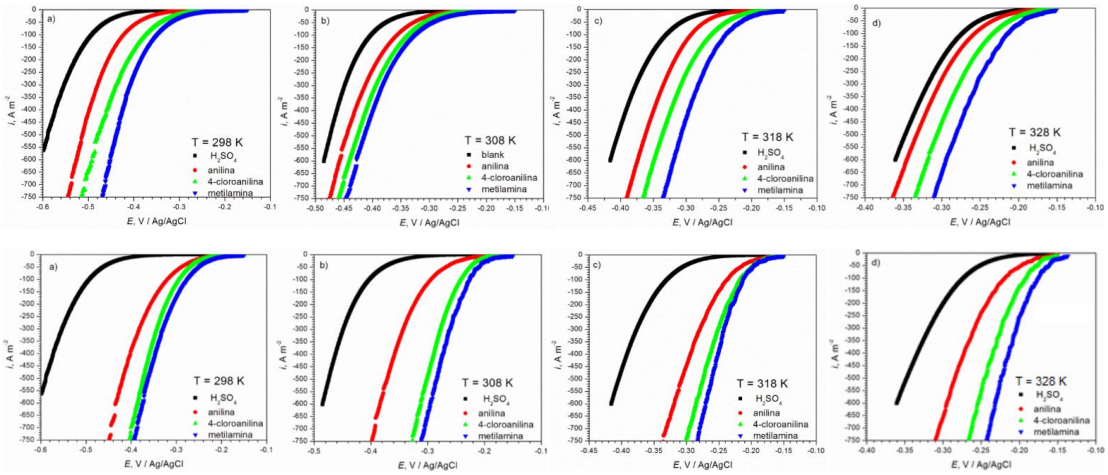

Figure 12. Linear polarization curves for HER on gold in 0.5 mol L^{-1} H_2SO_4 at different temperatures for a concentration of the selected amines of 10^{-6} mol L^{-1} (upper row) and 10^{-3} mol L^{-1} (lower row).

The highest depolarization is observed for methylamine, followed by 4-chloroaniline and aniline, due to important structural differences between these three amines. This enables us to correlate the catalytic properties with their molecular parameters.

The kinetic parameters for HER have been determined based on the Tafel plots shown in Figure 13 and the values of exchange current density i_o and cathodic charge transfer coefficient 1-α are given in Table 6.

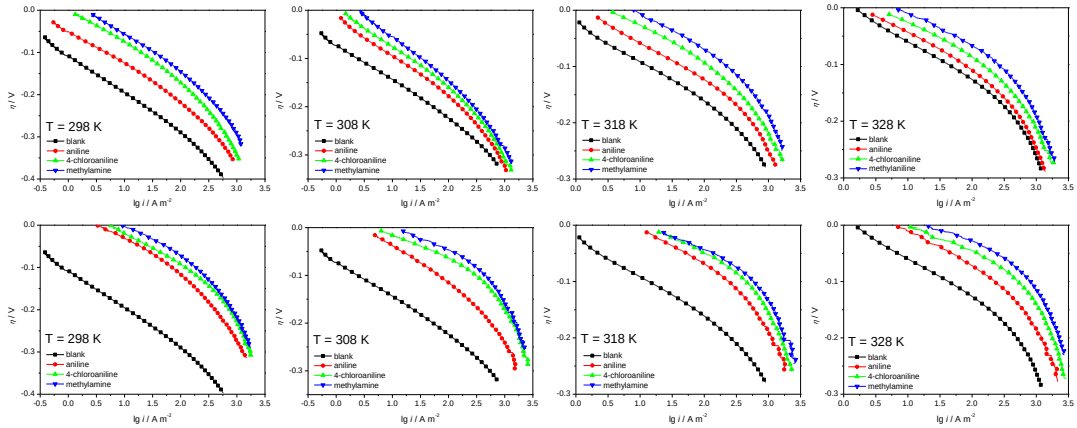

Figure 13. Tafel plots for HER on gold electrode in 0.5 mol L^{-1} H_2SO_4 at different temperatures for a concentration of the selected amines of 10^{-6} mol L^{-1} (upper row) and 10^{-3} mol L^{-1} (lower row).

As observed by other authors [59] the Tafel plots on gold in sulfuric acid present two distinct slopes, of about 30 and respectively 120 mV, depending on the overpotential. The lower slope, observed at low overpotentials corresponds to HER controlled by desorption of the hydrogen atoms, while the larger slope is due to the mechanism in which the charge transfer is the slow step of the overall cathodic process. The kinetic parameters that characterize the charge transfer step have been determined in the region of high overpotentials.

Table 6. Kinetic parameters for HER on gold electrode in 0.5 mol L^{-1} H_2SO_4 solution in the presence of amines at different concentrations and temperatures.

c	T	$-b$ [mV dec^{-1}]			$1-\alpha$			i_o [A m^{-2}]		
[mol L^{-1}]	[K]	AH^+	$ClAH^+$	MAH^+	AH^+	$ClAH^+$	MAH^+	AH^+	$ClAH^+$	MAH^+
10^{-6}	298	123	135	141	0.48	0.44	0.42	1.71	5.3	**10.8**
	308	130	150	151	0.47	0.41	0.40	4.67	10.6	**13.3**
	318	154	161	164	0.41	0.39	0.38	26.50	43.7	**71.5**
	328	162	172	183	0.40	0.38	0.36	33.79	58.6	**91.2**
10^{-5}	298	123	139	153	0.48	0.43	0.39	3.48	11.4	**17.9**
	308	134	144	163	0.46	0.42	0.39	6.54	29.0	**54.4**
	318	154	169	187	0.41	0.37	0.34	32.89	76.8	**133.1**
	328	180	185	201	0.36	0.35	0.32	50.12	95.0	**146.1**
10^{-4}	298	133	145	159	0.44	0.41	0.37	8.00	20.5	**33.3**
	308	142	167	171	0.43	0.37	0.36	11.25	66.4	**94.4**
	318	161	184	199	0.39	0.34	0.32	51.30	116.7	**160.9**
	328	183	193	211	0.36	0.34	0.31	60.04	131.0	**193.0**
10^{-3}	298	148	165	181	0.40	0.36	0.33	17.78	44.1	**64.1**
	308	155	173	185	0.39	0.35	0.33	27.74	98.2	**141.3**
	318	171	196	205	0.37	0.32	0.31	75.74	155.3	**214.2**
	328	186	210	216	0.35	0.31	0.30	94.41	207.1	**296.7**

The main effect of the amines is to decrease the charge transfer coefficient $1-\alpha$ and to increase the exchange current density i_o. This two effects are proportional to the increase of concentration and temperature. The charge transfer coefficient decreases in the order $MAH^+ < ClAH^+ < AH^+$ and the exchange current density increases in the same order.

According to the Butler-Volmer equation, a low charge transfer coefficient $1-\alpha$ is unfavorable for HER kinetics, because only a smaller fraction of the interfacial potential is used in activating the reactants to the top of the free energy barrier. In terms of reaction coordinates, a lower value of $1-\alpha$ means that the reaction plane is farther away from the metal surface. This happens if more voluminous ions than hydronium ions are involved in the charge transfer reaction, like alkyl-ammonium or aryl-ammonium cations, which for steric reasons cannot approach as close to the metal surface as hydronium ions.

The decrease of $1-\alpha$ is compensated by the significant increase of the exchange current density i_o due to the adsorption of protonated amines on the cathode surface, leading to a higher concentration of proton carriers which can be discharged. As a result, the overall effect of amines is to accelerate HER.

The catalytic effect of the amines was explained based on their molecular parameters which have been determined by quantum calculations and are presented in Table 7. The orientation of the dipole moment is also shown in Figure 14.

Table 7. Molecular parameters of protonated amines.

Compound	No of atoms	Molecular volume [Å^3]	Dipole moment [D]	Molecular coverage area [Å^2]
Phenylammonium, AH^+	15	95.3	7.12	30.9
4-Chlorphenylammonium, $ClAH^+$	15	108.6	12.31	30.9
Methyl-ammonium, MAH^+	8	36.1	2.22	21.5

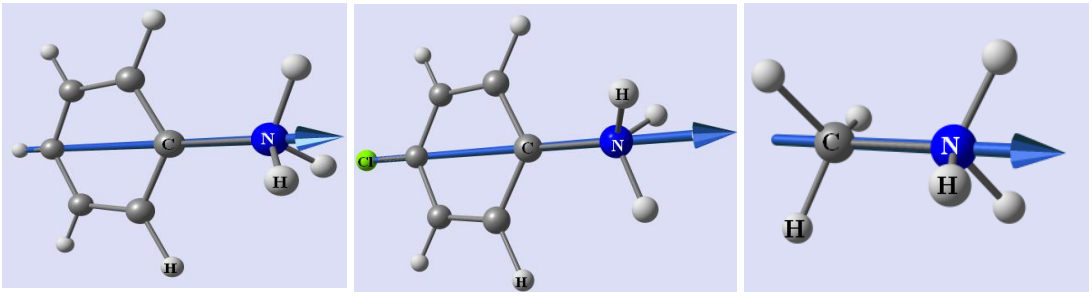

Figure 14. Molecular dipole moment (arrow) of protonated aniline, 4-chloro-aniline and methylamine.

The kinetic parameters for HER are correlated to the dipole moment and molecular coverage area of the protonated molecules. MAH^+ with the lowest dipole moment is less attracted to the cathode surface and it shows the lowest value of $1–\alpha$, but because it has the lowest coverage area, a higher number of MAH^+ molecules can be adsorbed on the cathode surface, providing a higher concentration of hydronium ions at the interface, which consequently leads to a higher exchange current density.

In case of phenylammonium and 4-chlor phenylammonium cations, the coverage areas are the same, but the molecular dipole moments differ because the Cl atom has an electron-withdrawing inductive effect and this produces a higher charge separation in $ClAH^+$ than in AH^+. As a result, the orientation of $ClAH^+$ dipoles on the electrode surface will be more ordered and a higher number of $ClAH^+$ molecules will be adsorbed on the electrode surface, leading to a higher concentration of the electroactive species and a higher value of the exchange current density.

It is well known that exchange current density i_o is directly proportional to the concentration of electroactive ions at the interface, according to relation (15) [60].

$$i_o = F \cdot c_{Ox} \cdot k_c \exp\left(-\frac{E_a}{RT}\right) \qquad (15)$$

where c_{Ox} is the concentration of the electroactive particles, k_c – rate constant of the cathodic process, E_a – activation energy.

In the absence of protonated amines, the exchange current density will be determined only by the hydronium ions concentration, provided that the rate determining step is the charge transfer:

$$i_{o(b)} = F \cdot c_{H_3O^+(b)} \cdot k_{c(b)} \exp\left(-\frac{E_{a(b)}}{RT}\right) \quad (16)$$

where $i_{o(b)}$ is the exchange current density, $c_{H_3O^+(b)}$ - hydronium concentration, $k_{c(b)}$ - rate constant of cathodic reduction of hydronium ions, $E_{a(b)}$ – activation energy (all referred to the blank solution).

In the presence of protonated amines, the concentration of hydronium ions increases with $c_{H_3O^+(a)}$ due to the hydrolysis of ammonium ions. It must be taken into account that the discharge of ammonium ions itself may also occur on the cathode. In this case, the global exchange current density will be:

$$i_o = F \cdot \left[c_{H_3O^+(b)} + c_{H_3O^+(a)}\right] \cdot k_{c(H_3O^+)} \exp\left(-\frac{E_{a(H_3O^+)}}{RT}\right) + F \cdot c_{RH^+} \cdot k_{RH^+} \exp\left(-\frac{E_{a(RH^+)}}{RT}\right) \quad (17)$$

where RH^+ represents the protonated forms of the studied amines AH^+, $ClAH^+$ and respectively MAH^+.

According to literature data, cathodic surface coverage with these species is high even at low concentrations, reason for which the exchange current density increases significantly in the presence of amines. Since it is difficult to separate the amines contribution to the increase of the hydronium ion concentration, a global relationship can be used:

$$i_o = F \cdot c^*_{H_3O^+} \cdot k^*_c \exp\left(-\frac{E^*_a}{RT}\right) \quad (18)$$

where $c^*_{H_3O^+}$, k^*_c and E^*_a represent apparent values.

The effect of amines on HER has been confirmed by electrochemical impedance spectroscopy. Impedance spectra were recorded at an overpotential of -200 mV, at different temperatures and different concentrations of the amines.

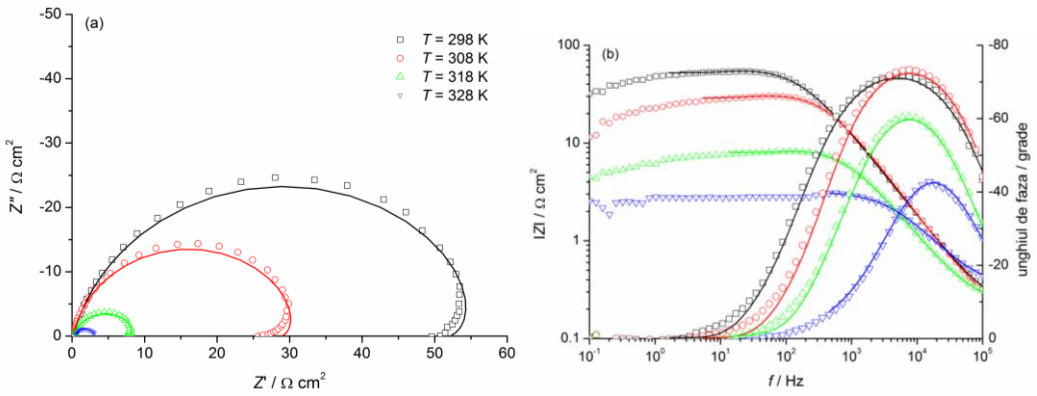

Figure 15. Complex plane and Bode plots plots for HER on gold in 0.5 mol L^{-1} H_2SO_4 at η = -200 mV.

The shape of the Nyquist diagrams in the blank (Figure 15) at low temperatures corresponds to a high frequency semicircle assigned to the charge transfer process, followed by a low frequency inductive loop characteristic to adsorption / desorption processes. At higher temperatures the inductive loop disappears and a single semicircle can be observed. This behavior was also observed by linear voltammetry, where the Tafel plots showed two different slopes. At low temperatures the overpotential of -200 mV is in the region of low Tafel slopes, where HER kinetics is controlled by desorption of atomic hydrogen, hence the inductive loop in the impedance plots. At higher temperatures, the overpotential of -200 mV corresponds to the region where HER is controlled by the charge transfer step, so the shape of the Nyquist plot changes to a single semicircle.

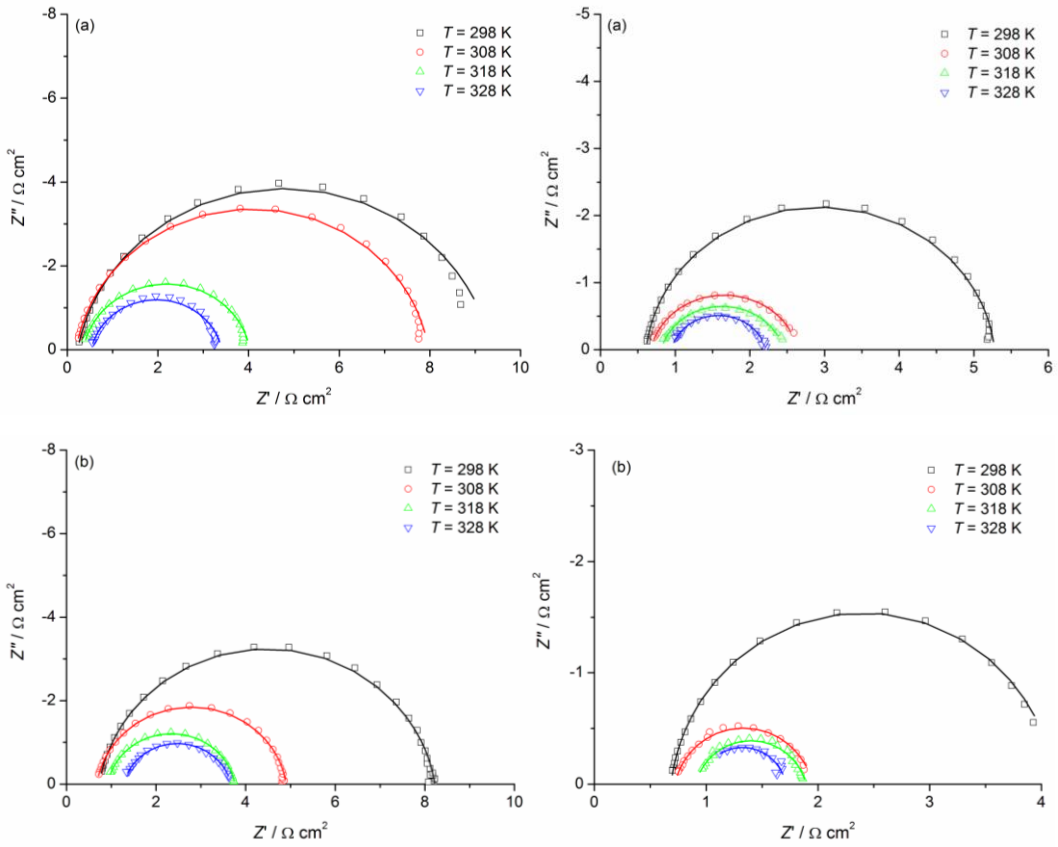

Figure 16. Complex plane plots for HER on gold in 0.5 mol L^{-1} H_2SO_4 at η = -200 mV in the presence of AH^+ and $4ClAH^+$ at concentrations of 10^{-6} mol L^{-1} (upper row) and 10^{-3} mol L^{-1} (lower row).

In the presence of amines all the Nyquist plots (Figure 16) show a single semicircle whose diameter decreases with increasing concentration and temperature and its value corresponds to the charge transfer resistance. In the presence of methylamine the catalytic effect on HER is very intense, so at the overpotential of -200 mV vigorous hydrogen release takes place and the impedance diagrams are quite distorted and more difficult to model.

Figure 17 shows the equivalent circuit which has been used to model the process in blank solution, to account for charge transfer process at high frequencies and hydrogen desorption at low frequencies, and the equivalent circuit which was proper in the presence of amines.

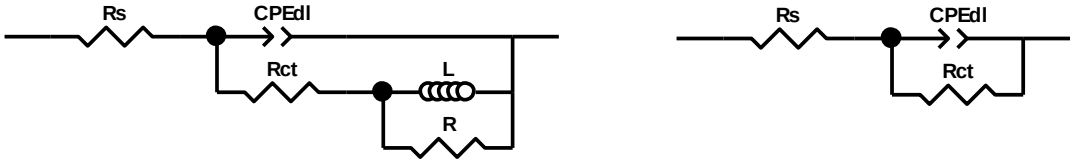

Figure 17. Electrical equivalent circuits used to model impedance data for HER on gold in the absence of proton carriers (left) and in the presence of proton carriers (right).

The results obtained by electrochemical impedance spectroscopy are consistent with those derived from the Tafel plots and from molecular modeling. The parameter which describes the catalytic effect of investigated amines is the charge transfer resistance, whose values are given in Table 8 for different temperatures and amine concentrations.

Table 8. Values of the charge transfer resistance for HER on gold in 0.5 mol L^{-1} H_2SO_4 at η = -200 mV in the presence of amines at different concentrations and temperatures.

Amine	Conc.	R_{ct} [Ω cm^2]			
	[mol L^{-1}]	T_1 = 298 K	T_2 = 308 K	T_3 = 318 K	T_4 = 328 K
blank	0	52.3 (0.9 %)	28.4 (1.2 %)	7.8 (0.9 %)	2.9 (0.9 %)
AH^+	10^{-6}	9.1 (0.5 %)	7.8 (0.3 %)	3.7 (0.4 %)	2.9 (0.9 %)
	10^{-3}	7.5 (0.4 %)	4.2 (0.3 %)	2.9 (0.8 %)	2.4 (1.3 %)
$4ClAH^+$	10^{-6}	4.7 (0.4 %)	1.9 (0.8 %)	1.6 (2.3 %)	1.3 (3.2 %)
	10^{-3}	3.4 (0.8 %)	1.2 (1.9 %)	1.0 (1.9 %)	0.8 (4.6 %)
MAH^+	10^{-6}	1.4 (1.4 %)	1.3 (1.3 %)	0.6 (3.4 %)	0.5 (5.9 %)
	10^{-3}	0.6 (3.0 %)	0.4 (8.5 %)	0.4 (5.8 %)	–

As expected, the charge transfer resistance shows an important decrease at high temperatures, both in the absence and presence of amines. The strongest catalytic effect is observed at room temperature, as indicated by the 100 fold decrease of the charge transfer resistance upon addition of methylamine. The catalytic effect increases in the order: $AH^+ < ClAH^+ < MAH^+$, according to Figure 18, similar to the order of exchange current densities and consistent with the coverage degree and dipole moment obtained by molecular modeling.

In conclusion, the catalytic effect of some aromatic / aliphatic amines on HER on gold has been evidenced by different electrochemical techniques. Steady-state polarization curves showed that even low concentrations of amines (10^{-4} to 10^{-3} mol L^{-1}) still produce a significant depolarization of HER, of about 200 mV at 200 A m^{-2}. Also, the kinetic parameters for HER on gold are enhanced in the presence of amines. The exchange current density increases by two orders of magnitude and the activation energy decreases three times in the presence of amines (10^{-3} mol L^{-1}). Impedance measurements confirm that the amines

directly participate in the HER mechanism on gold and decrease the charge transfer resistance values. Quantum calculation showed that the catalytic effect of amines on HER on gold can be explained in terms of molecular coverage area and adsorption of protonated amines at the gold–electrolyte interface.

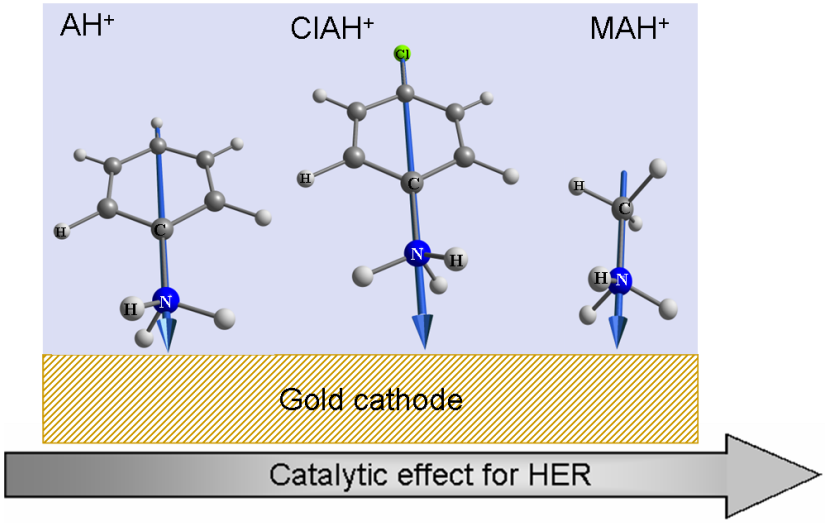

Figure 18. Catalytic effect of aniline, 4-chloro-aniline and methylamine on HER on gold electrode.

1.2.3. Catalytic enhancement of HER on platinum electrode

Platinum is the best electrocatalytic material for HER but due to its high price, methods have been searched to reduce the costs associated with electrocatalyst development for water electrolysis. State of the art in today's proton exchange membrane electrolyzers is the use of low and ultra-low (2 - 0.5 mg/cm^2) platinum loadings, usually platinum nanoparticle catalysts [61-63].

Our studies focused on the use of proton carriers, which are catalysts in the solution, to further increase the rate of HER. Although the overpotential of HER on platinum is very low, our results have shown that the catalytic effect of proton carriers can still be observed on platinum. We have selected benzylamine (BA) and aniline (A).

Linear voltammograms were recorded from 0.5 mol L^{-1} H_2SO_4 solution with amine concentrations between 10^{-5} and 10^{-2} mol L^{-1} using a PAR 2273 potentiostat-galvanostat. The electrochemical measurements were carried out in a standard three-electrode configuration, using a platinum working electrode (ϕ = 1.6 mm, A = 0.02 cm^2), a platinum sieve as counterelectrode and Ag/AgCl (sat) as reference electrode. Examples of linear voltammograms obtained on the platinum electrode are given in Figure 20.

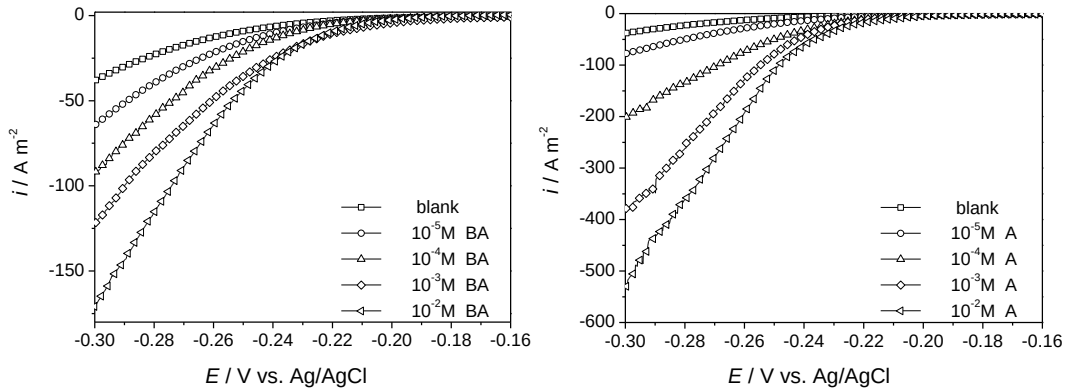

Figure 19. Linear voltammograms for HER on platinum electrode in 0.5 mol L^{-1} at 25°C and different concentrations of benzylamine (left) and aniline (right). Scan rate 5 mV s^{-1}.

The catalytic effect depends on amine concentration. It can be observed that at highest concentration, the presence of aromatic amines induces a decrease of the overpotential of about 50 mV for benzylamine and about 70 mV for aniline. A measure of the catalytic effect is the current density at a certain potential value. It is interesting to observe that at low concentrations both amines have a similar catalytic effect but at high concentrations aniline has a much stronger catalytic effect than benzylamine.

More conclusive information about the catalytic effect is given by the kinetic parameters (Tafel slope, exchange current density and transfer coefficient) derived from the Tafel plots. The values of kinetic parameters are given in Table 9 for the blank solution and in Table 10 in the presence of proton carriers.

Table 9. Kinetic parameters for HER on platinum electrode in 0.5 mol L^{-1} H_2SO_4 solution.

T [K]	b [mV dec^{-1}]	1-α	i_o [A m^{-2}]
298	87	0.68	2.95
308	101	0.58	7.58
318	122	0.48	25.1
328	130	0.45	28.8

In the presence of benzylamine and aniline, it can be observed that the kinetics is still controlled by the charge transfer step and the temperature increase affects to a great extent the exchange current density which is a measure of hydrogen evolution reaction rate.

At low concentration, the values of exchange current density are closed, indicating a similar catalytic effect. This can be explained considering the dipole moment of protonated molecules. In both cases a high dipole moment of 9.44 D for BAH^+ and of 7.46 D for AH^+ ensures a similar concentration of proton carriers at the interface in a favorable position for charge transfer.

Table 10. Kinetic parameters for HER on platinum electrode in 0.5 mol L^{-1} H_2SO_4 solution in the presence of benzylamine and aniline at different concentrations and temperatures.

T [K]	*Benzylamine* 10^{-5} mol L^{-1}			*Benzylamine* 10^{-2} mol L^{-1}		
	b [mV dec^{-1}]	1-α	i_o [A m^{-2}]	b [mV dec^{-1}]	1-α	i_o [A m^{-2}]
298	88	0.66	5.75	103	0.57	22.9
308	109	0.54	21.9	119	0.49	41.7
318	129	0.46	32.5	129	0.45	51.3
328	141	0.45	34.7	140	0.42	66.1
T [K]	*Aniline* 10^{-5} mol L^{-1}			*Aniline* 10^{-2} mol L^{-1}		
	b [mV dec^{-1}]	1-α	i_o [A m^{-2}]	b [mV dec^{-1}]	1-α	i_o [A m^{-2}]
298	94	0.63	6.9	110	0.54	67.6
308	100	0.59	11.0	126	0.47	128.8
318	121	0.45	28.2	147	0.40	169.8
328	136	0.43	40.7	168	0.35	239.9

At high concentrations, when the coverage degree of the electrode surface tends to be 1, the concentration of the proton carriers at the interface becomes inversely proportional to their molecular surface coverage, which is defined as the maximum cross section area of the molecule, perpendicular to the dipole moment. Due to different orientation of the dipole moment, the surface coverage of the adsorbed phenylammonium cation is about 28 Å and that of benzylammonium is about 52 Å. For a low molecular surface coverage we have a larger number of adsorbed molecules, therefore a higher concentration of protons at the interface and hence a higher reaction rate.

Electrochemical impedance spectroscopy is a powerful method very often used to elucidate the HER mechanism. It is well known that HER proceeds through three steps: electrochemical adsorption – the Volmer reaction, and two possible desorption steps: electrochemical desorption – the Heyrovsky reaction and chemical desorption – the Tafel reaction. The equivalent electrical circuit (EEC) proposed by Armstrong and Henderson [64] to model the impedance of HER, shown in fig. 9a, is a two-time constant model that predicts the appearance of two depressed semicircles on the complex plane plots. The high frequency semicircle (C_{dl}-R_{ct}) is related to the charge transfer kinetics and the low frequency semicircle (C_p-R_p) is associated with hydrogen adsorption. When hydrogen evolution is accompanied by H absorption, which may take place either by a two-step (indirect) or by a direct absorption mechanism, the equivalent electrical circuit is changed by the addition of a new branch, in parallel with C_p consisting of (R_{ab} – W), related to the absorption resistance and the H diffusion effects, according to the model proposed by Lasia [65] and presented in fig. 9b. The complex plane impedance plots reveal the presence of three semicircles, corresponding to charge transfer resistance, R_{ct}, absorption resistance, R_{ab}, and adsorption resistance, R_p, together with H diffusion effects (part of a straight line at 45°). A complete mathematical description of these models is given by Lasia [65,66] and the faradaic impedance of HER for the circuits in Figure 21(a) and 21(b) is given by equations (19) and (20):

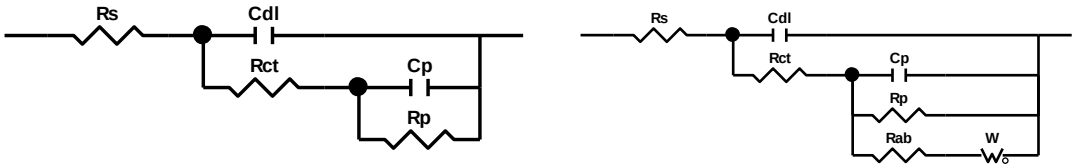

Figure 20. Equivalent electrical circuits for HER without absorption (a) and HER with indirect absorption (b).

$$\hat{Z} = R_{ct} + \frac{1}{j\omega C_p + \frac{1}{R_p}} \tag{19}$$

$$\hat{Z} = R_{ct} + \frac{1}{j\omega C_p + \frac{1}{R_p} + \frac{1}{R_{ab} + \hat{Z}_W}} \tag{20}$$

The Warburg diffusion element is defined by equation (21):

$$Z_W = (R_d(j\omega\tau_d)^{-p}) \coth (j\omega\tau_d)^p \tag{21}$$

where R_d is the diffusion resistance and τ_d is the diffusion time constant.

Electrochemical impedance measurements carried out in the absence and presence of aniline and benzylamine have shown that hydrogen evolution reaction on Pt takes place according to a mechanism dependent on the electrode potential. At low overpotentials hydrogen evolution together with H absorption is observed and the complex plane plots reveal the existence of three semicircles. For the blank solution, as the overpotential is increased to more negative values, the semicircle corresponding to H absorption gradually diminishes and finally disappears around η = - 55 mV (E = -0.26 V) indicating that the absorption is very fast. The complex plane plots change to only two semicircles corresponding to charge transfer and hydrogen adsorption. However, the impedance spectra at higher overpotentials are quite distorted especially in the low frequency region due to vigorous hydrogen evolution.

EIS spectra measured on platinum in H_2SO_4 solution in the absence of amines are given in Figure 22 for two different overpotentials. At low overpotentials three semicircles are observed, corresponding to three time constants. The radius of the semicircles is potential dependent, indicated they can all be related to the HER mechanism.

In the presence of low concentrations of BA (Figure 23a) the complex plane plots are similar to those measured in the blank sulfuric acid solution, but the semicircle related to absorption start to disappear at less negative overpotentials (η = -35 mV). At high BA concentration (Figure 23b) the semicircle related to absorption is visible only at η = -15 mV.

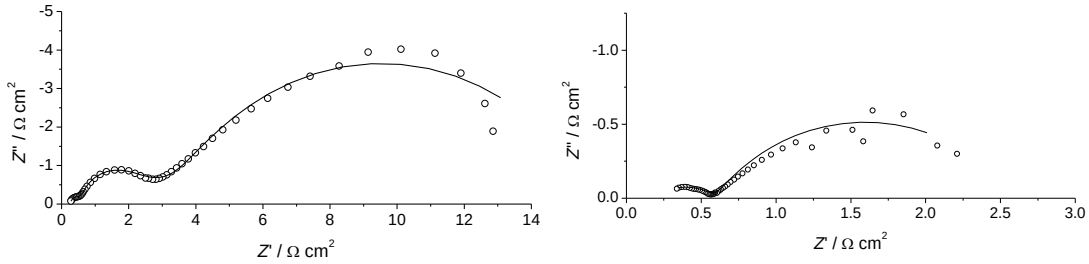

Figure 21. Complex plane plots for HER in blank 0.5 mol L^{-1} H_2SO_4 solution, η = -15 mV (a) and η = -45 mV (b). Open symbols are experimental data and continuous line is simulated by CNLS fitting.

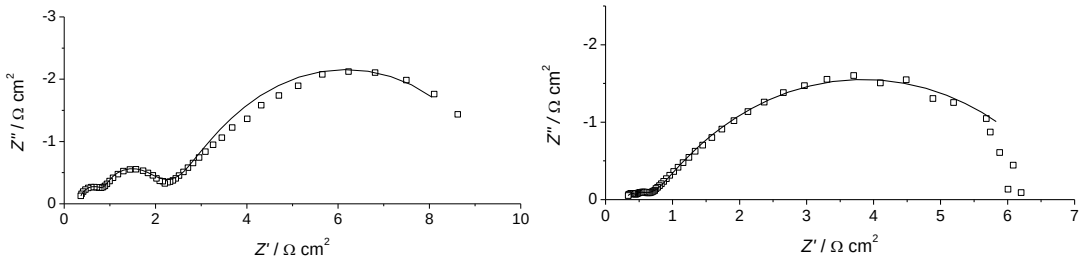

Figure 22. Complex plane plots for HER in 0.5 mol L^{-1} H_2SO_4 solution with 10^{-5} mol L^{-1} BA (a) and 10^{-2} mol L^{-1} BA, η = -15 mV. Open symbols are experimental data and continuous line is simulated by CNLS fitting.

The phase angle plots are more sensitive in the detection of time constants than complex plane plots. Figures 24-26 show the phase angle plots for HER at various overpotentials in blank sulfuric acid solution and at two different concentrations of benzylamine and respectively aniline. The existence of three relaxation time constants can be also observed in the phase angle plots, as indicated by the presence of three maxima. The high frequency time constant is related to charging/discharging of electrical double layer, the intermediate frequency time constant corresponds to absorption/desorption and the low frequency time constant to adsorption/desorption of hydrogen at the interface.

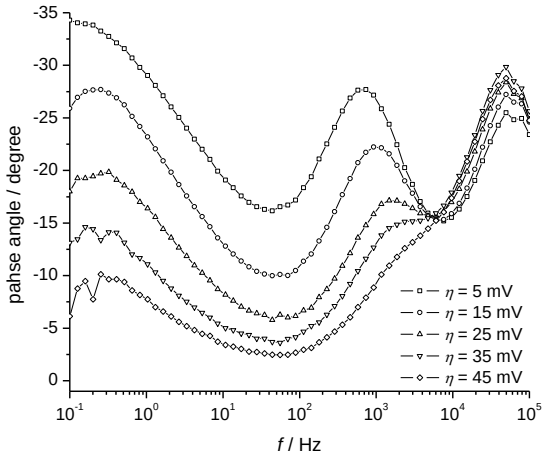

Figure 23. Phase angle plots for HER at increasing overpotentials in blank 0.5 mol L^{-1} H_2SO_4 solution.

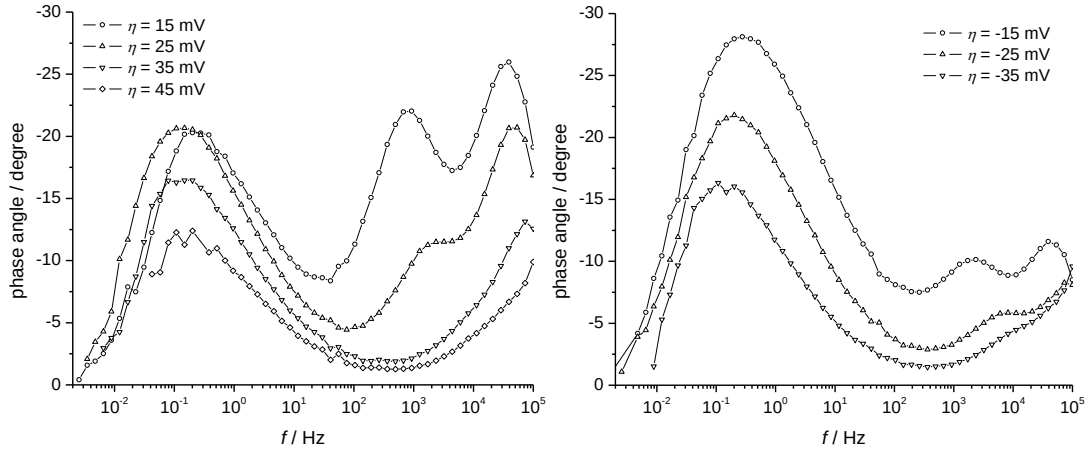

Figure 24. Phase angle plots for HER at increasing overpotentials in 0.5 mol L^{-1} H_2SO_4 solution with 10^{-5} mol L^{-1} BA (a) and 10^{-2} mol L^{-1} BA (b).

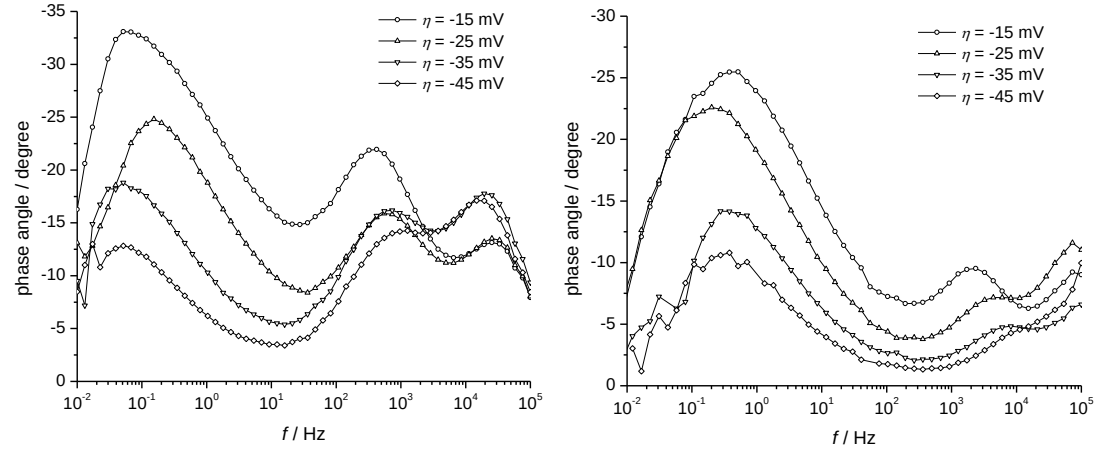

Figure 25. Phase angle plots for HER at increasing overpotentials in 0.5 mol L^{-1} H_2SO_4 solution with 10^{-5} mol L^{-1} A (a) and 10^{-2} mol L^{-1} A (b).

The frequency of the maximum related to the charge transfer process is around 5 10^4 Hz in the blank solution, 4 10^4 Hz in the presence of BA and 2 10^4 Hz in the presence of A. The H absorption is potential dependent, its frequency increases in the blank solution from 7 10^2 Hz at low overpotentials to 2 10^3 Hz at higher overpotentials and completely disappears at more negative overpotentials (over -55 mV), indicating that absorption becomes very fast. At low concentrations of BA, H absorption is still visible at low overpotentials and disappears around -35 mV. At high concentrations of BA and A, the phase angle plots are dominated by adsorption. The frequency of the maximum corresponding to adsorption is virtually independent on overpotential and amines concentration with a constant value around 0.2 Hz.

The electrochemical impedance spectra measured at low overpotentials have been modeled using the EEC given in Figure 21b. The results of the CNLS fitting are listed in Table 11 together with the calculated values of the time constants related to charge transfer τ_{ct}, absorption τ_{abs} and respectively adsorption τ_{ads}.

Table 11. EEC parameter values for HER at η = -25 V.

parameter	blank	10^{-5} BA	10^{-2} BA	10^{-5} A	10^{-2} A
R_S [Ω cm^2]	0.22	0.32	0.30	0.44	0.35
C_{dl} [F cm^{-2}]	1.32×10^{-5}	1.39×10^{-5}	1.84×10^{-5}	2.80×10^{-5}	1.49×10^{-5}
R_{ct} [Ω cm^2]	0.41	0.36	0.10	0.28	0.17
C_p [F cm^{-2}]	2.66×10^{-4}	2.90×10^{-4}	2.35×10^{-4}	4.43×10^{-4}	2.58×10^{-4}
R_p [Ω cm^2]	4.40	4.76	3.04	7.87	4.31
R_{ab} [Ω cm^2]	0.40	0.22	0.05	0.38	0.07
R_d [Ω cm^2]	1.05	0.98	0.43	1.86	0.44
τ_d [s]	0.129	0.253	0.121	0.296	0.065
p	0.32	0.32	0.31	0.33	0.29
χ^2	7.65×10^{-4}	2.08×10^{-3}	7.26×10^{-3}	8.60×10^{-4}	2.14×10^{-3}
τ_{ct} [ms]	5.4×10^{-3}	5.1×10^{-3}	1.8×10^{-3}	8.0×10^{-3}	2.5×10^{-3}
τ_{abs} [ms]	0.106	0.063	0.011	0.168	0.018
τ_{ads} [ms]	1.17	1.38	0.72	3.49	1.11

Analyzing the data from Table 11 it can be observed that the addition of benzylamine and aniline to the blank solution leads to a decrease of the charge transfer resistance. This effect is more pronounced as the concentration of amines increases, confirming that both BA and A have a catalytic effect on HER. Beside charge transfer resistance, resistances related to absorption and adsorption are also reduced in the presence of amines, due to a higher concentration of protons available at the interface. The time constant associated with the charge transfer process has values in the order of microseconds, indicating that charge transfer reaction takes place very fast. The lower values of τ_{ct} obtained for BA and A point to an acceleration of HER in the presence of amines.

In conclusion, the catalytic effect of aniline and benzylamine on HER on platinum has been evidenced using different electrochemical techniques. Linear polarization curves showed a reduction of the overpotential for HER of about 50 and 70 mV for benzylamine and respectively aniline at high concentrations (10^{-2} mol L^{-1}). The exchange current density has been found to increase in the presence of amines but a significant effect is observed only at high concentrations. Detailed analysis of impedance data indicated very fast charge transfer process in the presence of amine. The differences in the catalytic effect at high and low concentrations are explained by molecular modeling in terms of surface coverage area and adsorption of protonated amines at the platinum–electrolyte interface.

1.3. Conclusions

The catalytic enhancement of HER in the presence of catalysts added in the solution has been demonstrated using different electrochemical techniques such as linear sweep voltammetry and electrochemical impedance spectroscopy. These catalysts, also called proton carriers, have the ability to increase the proton concentration in the double electric layer from the metal-solution interface by transporting the protons from the bulk of the solution to the

interface. Aromatic and / or aliphatic amines can act as proton carriers and their catalytic activity is caused by the lone electron pair of the nitrogen atom.

The originality of our work is related to the following aspects:

(i) we have demonstrated based on the kinetic parameters derived from the Tafel plots and from electrochemical impedance data that the catalytic effect of the proton carriers is manifested for both electrode materials with high hydrogen overpotential, such as copper, but, more important from a practical point of view, even in the case of metals with low hydrogen overpotential, namely gold and platinum;

(ii) we have explained the catalytic effect of aromatic / aliphatic amines on the hydrogen evolution reaction based on their molecular parameters obtained by quantum calculation, the most important being the dipole moment and the surface coverage degree. Thus, the most pronounced catalytic effect was obtained in the case of amines with a low surface coverage, which is equivalent to a larger number of molecules present at the interface, so an increased proton concentration, and respectively for a large dipole moment, which indicates a favorable orientation of the molecules at the interface, namely with the nitrogen atom and the attached proton directed towards the metal, where the charge transfer is greatly facilitated.

(iii) we have proposed a more detailed mechanism of hydrogen evolution reaction in the presence of proton carriers, derived from the mechanism proposed by Stackelberg et al. [67-69] but taking into account also the direct discharge of hydronium ions.

According to the proposed mechanism, ammonium ions are formed as a result of amines protonation in the bulk of solution:

$$H_2N–R\ (aq) + H_3O^+(aq) \rightarrow H_3N^+–R(aq) + H_2O \qquad (22)$$

In the electric field between the electrodes, ammonium ions migrate towards cathode, where they adsorb on the electrode surface, with the nitrogen atoms oriented to the metal surface, according to the dipole moment, that is in a favorable position for charge transfer process:

$$H_3N^+–R(aq) \rightarrow H_3N^+–R(ads) \qquad (23)$$

Thereby, at the electrode-electrolyte solution interface, a high concentration of ammonium ions is reached. Taking into account that H–N bond energy in ammonium ions is lower than H-O bond in hydronium ions, it can be appreciated that at low current densities, where HER overpotential is not too large, the charge transfer occurs according to the reaction:

$$H_3N^+–R(ads) + e^- \rightarrow H(ads) + H_2N–R(ads) \qquad (24)$$

The recombination step of HER could occur chemically (Tafel step):

$$2H(ads) \rightarrow H_2(ads) \qquad (25)$$

or electrochemically (Heyrovsky step):

$$H_3N^+–R(ads) + H(ads) + e^- \rightarrow H_2(ads) + H_2N–R(ads) \qquad (26)$$

At higher current densities (elevated overpotential), hydronium ions discharge becomes possible:

$H_3O^+(ads) + e^- \rightarrow H(ads) + H_2O$ (27)

followed by Tafel (chemical) or Heyrovsky (electrochemical) desorption:

$H(ads) + H_3O^+(ads) + e^- \rightarrow H_2(ads) + H_2O$ (28)

The hydronium ions discharge has as a consequence a local pH increase of the solution adjacent to the cathode up to values that allow hydrolysis of ammonium ions:

$H_3N^+–R(ads) + H_2O \rightarrow H_2N–R(ads) + H_3O^+(ads)$ (29)

This reaction helps to keep the concentration of hydronium ions at high values. The neutral amines diffuse into the bulk solution where the re-protonation reaction (22) occurs. According to this mechanism and in contrary to Stackelberg's mechanism, the protonation of amines can not be the rate determining step of the cathodic process, even at high overpotentials.

The proposed mechanism of catalytic enhancement of HER in the presence of protonated aromatic amines is exemplified for the case of aniline as shown in Figure 19.

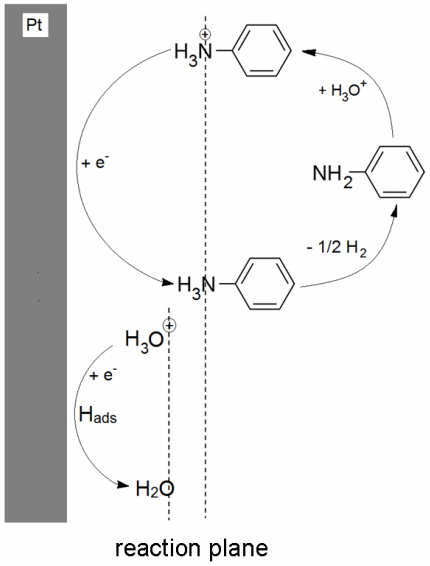

Figure 26. Mechanism of HER in the presence of proton carriers.

The presence of protonated aniline molecules at the interface increases the concentration of hydronium ions in the electric double layer. As a result, HER may proceed by discharge of anilinium cations at low current densities and low overpotentials and by direct discharge of hydronium ions at high current densities and high overpotentials. Since a high concentration of anilinium cations is available at the interface this will lead to the enhancement of HER. It is obvious that an important role in the orientation and adsorption of the protonated amine molecule at the electrode – electrolyte interface is played by its dipole moment, as it has been shown by correlations between the catalytic effect and the structure and molecular parameters of all the investigated amines.

2. Contributions on the electrochemical synthesis of polyaniline nanofibers

The results presented within this chapter were obtained in the frame of a research project **PN II Partnership 72-171/2008** entitled "*Microporous polyaniline sensors functionalized with pendant groups, innovative material for use in identification and control of Parkinson's disease*" funded by the Romanian Ministry of Education, Research, Youth and Sports between 2008-2011, for which I was partner responsible and also a **POSDRU/86/1.2/S/58146** project entitled: "*Development and implementation of Master program in the field of micro- and nanomaterials – MASTERMAT*".

The results have been published in 5 ISI indexed papers, as follows:

- N. Plesu, **A. Kellenberger**, M. Mihali, N. Vaszilcsin, Effect of temperature on the electrochemical synthesis and properties of polyaniline films, *Journal of Non-crystalline Solids* 356 (2010) 1081-1088.
- **A. Kellenberger**, N. Plesu, M. Tara Lunga Mihali, N. Vaszilcsin, Synthesis of polyaniline nanostructures by electrochemical deposition on niobium, *Polymer* 54 (2013) 3166-3174.
- **A. Kellenberger**, D. Ambros, N. Plesu, Scan rate dependent morphology of polyaniline films electrochemically deposited on nickel, *International Journal of Electrochemical Science* 9 (2014) 6821-6833.
- N. Plesu, **A. Kellenberger**, I. Taranu, B.O. Taranu, I. Popa, Impedimetric detection of dopamine on poly(3-aminophenyl boronic acid) modified skeleton nickel electrodes, *Reactive & Functional Polymers* 73 (2013) 772-778.
- M. Tara Lunga Mihali, N. Plesu, **A. Kellenberger**, G. Ilia, Adsorption of an Azo dye on polyaniline/niobium substrate, *International Journal of Electrochemical Science* 10 (2015) 7643-7659.

2.1. Background

Among electronically conducting polymers, polyaniline [70,71] is one of the representatives that has been intensively investigated due to its simple synthesis, stability at ambient conditions, unique electrochemical properties and a wide range of promising applications in the fabrication of electrochemical energy storage devices, electrochemical sensors and biosensors, electrochromic displays and anticorrosive coatings [72].

In the last years, the researches were focused on nanostructured conducting polymers, including nanostructured polyaniline, as a result of the increasing interest in nanoscience and nanotechnologies. The interest for this type of materials is very clearly evidenced in the mainstream publications. Thus, according to international databases Web of Science and Scopus, the first references in the literature on the synthesis of conducting polymers in the form of fibers and "microscopic" tubes occur in 1989. The study reports about the synthesis

of polypyrrole and poly-3-methylthiophene in a membrane with cylindrical pores having a diameter of 1 μm [73]. The same synthesis method was applied in 1993 to obtain micro- and nanofibers of polyaniline [74,75] with electrical conductivity values much higher than those of the amorphous polymer. In the forthcoming years there is a lack of publications on this subject, but beginning from 2002 the number of publications grow exponentially up to about 900 publications in the present.

The motivation of research regarding the synthesis and properties of polyaniline nanofibers is due to their potential applications in micro- and nanoelectronics and for the construction of sensors, biosensors and biomedical devices [76,77]. It is expected that nanostructured polyaniline will show net superior properties compared to amorphous polyaniline, or even unique properties. Several studies have recently shown that going down to nano-level dimensions, together with a marked increase of the specific surface area, can bring further improvement of several other properties like conductivity, processability and sensing properties.

Several methods have been proposed to synthesize polyaniline nanostructures, which can be divided in template methods and template free methods.

Template synthesis methods imply chemical oxidative polymerization and relay on the use of insoluble hard templates such as zeolites or polymer membranes with controlled pore size or soluble soft templates such as various molecules that are able to orient and guide the growth of nanofibers. Several macromolecules such as polymers, surfactants [78] and DNA molecules have been used. Although the dimensions and structure of polyaniline nanofibers can be easily controlled by the dimensions of the template, the disadvantage of this method is the need for subsequent removal of the template, which can destroy the nanostructures or may adversely affect essential properties, such as electrical conductivity. A particular case of the template synthesis is the chemical polymerization in the presence of small amounts of organic, inorganic or biologic nanofibers. In the presence of this nanoseeds, the polyaniline morphology change drastically from the usual granular / powder structure to nanostructure. Nanomaterials used for "seeding" are the most diverse, for example carbon nanotubes [79,80], polyaniline [81] nanofibers of emeraldine salt or vanadium oxide nanofibers [79].

Template free synthesis methods include chemical or electrochemical oxidative polymerization. Polyaniline has the ability to form spontaneously nanofibers during chemical oxidation of aniline, but the structure of the resulting product is strongly influenced by synthesis conditions, such as: monomer concentration, oxidant nature and concentration, acid nature and concentration, monomer/oxidant molar ratio, monomer/acid molar ratio, stirring or the way in which reactants are added. Experimental studies have shown that lower values of the aniline/oxidant molar ration lead to a less branched structure and longer polyaniline nanofibers with higher average diameter [82]. On the contrary, polyaniline nanofibers with small diameter have been obtained for a low addition rate of the oxidant [83]. The use of different oxidants may also induce improved properties of polyaniline nanofibers or decrease their diameter. The oxidant commonly used for the chemical synthesis of polyaniline is ammonium peroxydisulfate but it has been reported that in the presence of iron chloride as oxidant [84] nanofibers with a diameter of 20 nm have been obtained. Using potassium

biiodate as oxidant [85] leads to polyaniline nanofibers with a diameter of 90 nm and increased conductivity and using hydrogen peroxide as oxidant [86] results in polyaniline nanofibers with a diameter of 60-80 nm. A particular case of template free synthesis is the interfacial polymerization, when the reaction occurs at the interface between two immiscible phases, i.e. an organic phase which contain the dissolved monomer and an aqueous phase containing the dissolved oxidant [87-90]. Various organic solvents can be used, such as hexane, toluene, benzene, xylene, diethyl ether, carbon tetrachloride, chloroform, without affecting the diameter of the resulting polyaniline nanofibers. The diameter of the nanofibers can be controlled by the nature of the dopant, for example in the presence of hydrochloric acid the diameter of the nanofibers is 30 nm, whereas in the presence of perchloric acid the diameter increases to 120 nm [87,88]. Another important aspect in the formation and growth of nanofibers is the nucleation process [89]. Homogeneous nucleation leads to nanofibers, while heterogeneous nucleation leads to the formation of granular particles.

Despite the net advantage of chemical method in producing large scale quantities of polyaniline, the electrochemical methods play a significant role in the preparation and characterization of polyaniline nanofibers since they offer a very convenient and easy way to control the synthesis conditions, to tune a well-defined oxidation state and to study the electrochemical properties of polyaniline nanofibers. Nanostructured conducting homo- or copolymers of polyaniline have been obtained by template free electrochemical methods such as cyclic voltammetry [91-93], galvanostatic [94,95] or potentiostatic [96] methods, pulse galvanostatic or potentiostatic methods [97,98]. The results point out that the nanofibrilar morphology might be an intrinsic property of electrochemically synthesized polyaniline [96], however it is strongly affected by synthesis conditions. One of the factors reported to influence the morphology [98], as well as the diameter and length of nanofibers [93] is the scan rate in potentiodynamic methods. The mechanism of formation of polyaniline nanofibers involves two concurrent steps: the formation of nucleation centers and the one-directional growth of nanofibers [94]. The resulting polymer film has a layered structure, consisting in one compact, two-dimensional layer which is formed by the horizontal growth of the nucleation centers and a second loose layer composed of nanofibers formed by vertical growth [95,96].

2.2. Influence of synthesis conditions on the structure, morphology and electrochemical properties of polyaniline films

The synthesis method and processing conditions play an important role in tailoring polymer properties, i.e. morphology and as a consequence conductivity, which is one of the main properties of conducting polymers, particularly of polyaniline [99,100].

Different morphologies have been reported for polyaniline obtained by chemical oxidative synthesis depending on the molar ratio of oxidant to monomer [101]. Also, by changing the molar ratio of acid to monomer, nanoflakes, nanorods or nanospheres have been obtained in selenious acid [102] and respectively nanotubes, nanoflakes and nanofiber networks in

dichloroacetic acid [103]. Polyaniline nanofibers with diameters of 20-50 nm have been reported in the presence of soft templates such as polyethylene glycol [104]. It has been shown that acidity changes in the initial stages of polymerization also have an influence on polyaniline morphology obtained by interfacial polymerization, allowing a controlled synthesis of Pani micro/nanostructures [105]. Besides acidity, another factor that affects the size of polyaniline nanofibers obtained by interfacial polymerization is the polarity of the organic solvent [106].

The morphology obtained by means of electrochemical synthesis is less varied than with chemical oxidation methods due to the ease of controlling synthesis parameters. The main factors reported to affect the morphology in electrochemical synthesis are the nature of the doping anion [94], the electrode material [11,95], pH [107], scan rate in potentiodynamic deposition [93,108] and deposition time in potentiostatic deposition [109]. It has been found that varying the potential scan rate of only the first cycle from 100 to 2 mV s^{-1} induces changes from globular to fibrilar-like morphology [110], explained by different nucleation mechanisms. Frequently reported morphologies for electrochemical deposited polyaniline are nanofibers or nanofiber networks, as a consequence of the growth mechanism described as a two stages mechanism [95,96]. In the first stage, after the nucleation sites are deposited on the electrode surface, they tend to grow predominantly in the horizontal direction and form a compact 2D polyaniline layer. In the second stage, the polymerization takes place preferentially in the vertical direction and polyaniline nanofibers grow on the previously deposited compact layer and not directly on the bare electrode surface.

2.2.1. Effect of acid concentration and monomer/acid ratio

To study the effect of acid concentration and monomer/acid molar ratio, we have synthesized nanostructured polyaniline films on passivated niobium substrate by potentiodynamic method in 0.5 and 1 mol L^{-1} H_2SO_4 solution and different aniline / acid molar ratios.

The electrochemical polymerization of aniline was performed by cyclic voltammetry using an Autolab PGSTAT 302N. A standard three-electrode electrochemical cell was used, containing a working electrode made of Nb disc (A = 1 cm^2), two graphite rods as counter-electrodes and a saturated calomel electrode (SCE) as reference electrode. The electrochemical synthesis of polyaniline was carried out by cyclic voltammetry at a scan rate of 50 mV s^{-1} in two steps corresponding to initiation (I) and growth (G). In a first step the potential was cycled between 0.500 V and 1.200 V to initiate the polymerization process. In a second step, the potential range was limited between –0.350 and 0.800 V to avoid the overoxidation reactions of the polymer chain and to allow further growth of the polymer film. Pani samples were prepared at two different concentrations of the sulfuric acid solution (0.5 and 1 mol L^{-1}) and at aniline/acid ratio of 0.2, 0.4 and respectively 0.6. The number of initiation cycles was reduced from 5 to 2 for the last two samples, but the number of growth cycles remained constant for all the samples. An overview of the corresponding synthesis conditions is given in Table 12.

Table 12. Synthesis conditions and characteristics of the first anodic peak of Pani/Nb films obtained at different acid concentration and aniline/acid ratio.

Sample	H_2SO_4 [mol L^{-1}]	Aniline [mol L^{-1}]	molar ratio	no. of scans I/G	E^* [V]	i^* [mA cm^{-2}]	Q^* [mC cm^{-2}]
Pani/Nb/1	0.5	0.1	0.2	5/10	0.249	5.3	4.9
Pani/Nb/2	0.5	0.2	0.4	5/10	0.317	16.1	23.6
Pani/Nb/3	0.5	0.3	0.6	5/10	0.342	57.4	88.9
Pani/Nb/4	1	0.2	0.2	5/10	0.362	61.2	98.0
Pani/Nb/5	1	0.4	0.4	2/10	0.298	55.6	113.0
Pani/Nb/6	1	0.6	0.6	2/10	0.375	63.5	145.0

* values are given for the last cycle

It can be observed that increasing the aniline/acid molar ratio leads to an increase of the current density and charge associated with the first oxidation peak which is an indicator of the growth of the polymer film. This increase is more obvious at 0.5 mol L^{-1} acid concentration and less pronounced at 1 mol L^{-1} acid concentration. A more important effect is observed when the acid concentration changes from 0.5 to 1 mol L^{-1} and the aniline/acid molar ratio is kept constant.

Figure 27 shows representative examples of cyclic voltammograms for samples Pani/Nb/2 and Pani/Nb/5, obtained during the growth step in the two sulfuric acid solutions of different concentrations and the same aniline/acid molar ratio.

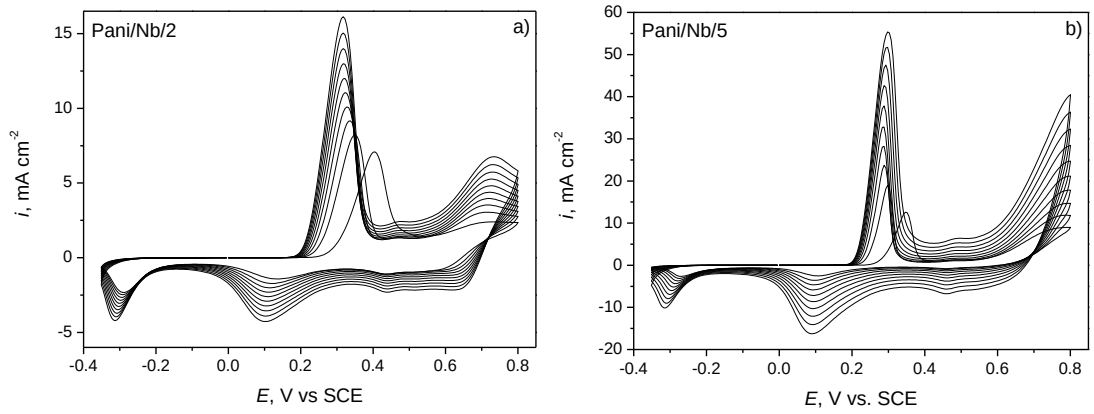

Figure 27. Potentiodynamic deposition of Pani/Nb samples from a solution of 0.2 mol L^{-1} aniline in 0.5 mol L^{-1} H_2SO_4 (a) and 0.4 mol L^{-1} aniline in 1 mol L^{-1} H_2SO_4 (b). Scan rate 50 mV s^{-1}.

The acid concentration plays an important role in determining the structure of the electrochemically obtained polyaniline films. This effect can be explained considering the two step mechanism of polyaniline deposition. In 0.5 mol L^{-1} sulfuric acid solution, the initiation step requires more time (a larger number of cycles) and the current densities are low. At low current densities only a small number of nucleation sites will form on the electrode surface. Since aniline concentration in the close vicinity of the electrode is sufficiently high, it is expected that the heterogeneous nucleation of polyaniline will be

favored so newly formed polyaniline molecules will preferably grow on the previously formed particles, leading to a branched structure with agglomerations of granular particles, as it will be discussed latter based on the SEM analysis. In 1 mol L^{-1} sulfuric acid solution, the number of cycles needed for the initiation step is reduced and also a marked increase in the current is observed. This means that in the initial stages of polymerization, a larger number of homogeneous nucleation sites are produced, which provide optimal conditions for the linear growth of the polyaniline nanofibers.

The redox behavior of Pani/Nb samples was studied by cyclic voltammetry in monomer free electrolyte solution. A classical behavior for conducting polyaniline is observed, as seen in Figure 28. The first anodic peak is roughly centered at 0.25 V for Pani/Nb/1, 0.32 V for Pani/Nb/2, 0.33 V for Pani/Nb/3, 0.37 V for Pani/Nb/4, 0.33 V for Pani/Nb/5 and 0.39 V for Pani/Nb/6. Its position shifts to higher potentials as the thickness of the polymer film increases.

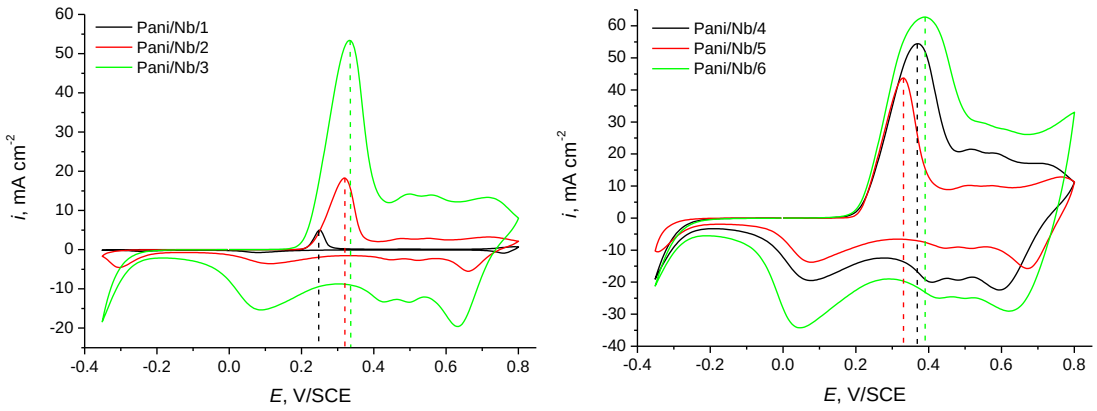

Figure 28. Cyclic voltammograms of Pani/Nb samples in monomer free 0.5 mol L^{-1} H_2SO_4 solution. Scan rate 50 mV s^{-1}.

The structure and morphology of the polyaniline films prepared on niobium were characterized by scanning electron microscopy (SEM) using a FEI INSPECT S electron microscope. Figure 29 gives the SEM images of the polyaniline films electrodeposited on niobium for different acid concentrations and aniline / acid ratios.

The structure and morphology of the polyaniline samples depend on the working conditions. In 0.5 mol L^{-1} H_2SO_4 solution the polyaniline films show a more granular structure and in 1 mol L^{-1} H_2SO_4 solution a fibrilar structure. Figure 29(a) and 29(b) show the morphology of polyaniline films deposited from 0.5 mol L^{-1} acid solution and low aniline / acid ratios. A very thin and smooth green polyaniline film was obtained under these conditions, but the SEM images reveal an inhomogeneous structure containing both granular and fibrilar features. The polyaniline deposit consists of two distinct layers: a compact 2D layer composed of globular structures with diameters between 100 and 200 nm very adherent to the electrode surface and a loosely bound layer. Figure 29(c) corresponds to a polyaniline sample obtained at higher aniline / acid ratios, therefore the thickness of the polyaniline film is larger

and the lowermost layer is not visible any more. The top layer is composed of short and highly branched nanofibers with diameters of about 100 nm combined with granular particles.

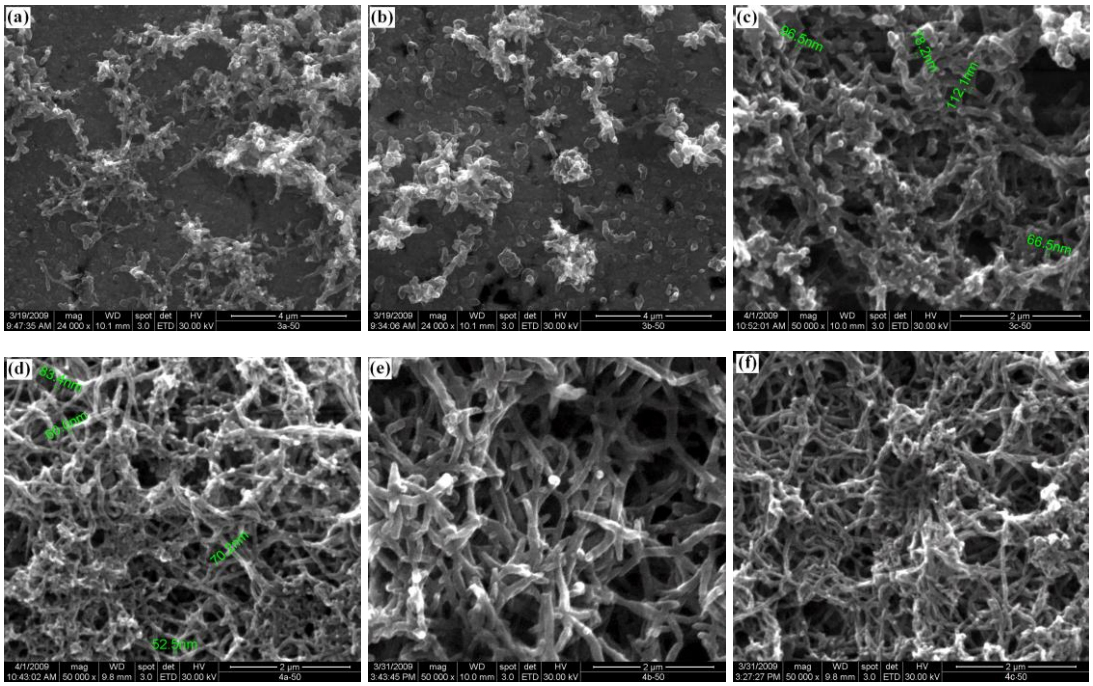

Figure 29. SEM images of polyaniline nanofibers electrodeposited on Nb by cyclic voltammetry in 0.5 mol L^{-1} H_2SO_4: (a) Pani/Nb/1, (b) Pani/Nb/2, (c) Pani/Nb/3 and in 1 mol L^{-1} H_2SO_4: (d) Pani/Nb/4, (e) Pani/Nb/5, (f) Pani/Nb/6.

Generally, the SEM micrographs for the polyaniline films obtained in 0.5 mol L^{-1} acid solution point out to a heterogeneous nucleation, leading to a prevalence of the granular particles and to a coral-like morphology. The concentration of aniline has little effect on the polyaniline structure, only the film thickness increases with increasing aniline concentration.

In 1 mol L^{-1} sulfuric acid solution the structure of polyaniline changes and the nanofibers are clearly distinguished. These results are consistent with those obtained for the chemical polymerization route, where the most important factor affecting the formation of polyaniline nanofibers is the acid concentration. It has been observed that lowering acid concentration the fraction of granular particles starts to increase and finally prevails over the nanofibers quantity in the final product [87]. Figure 29(d) shows an entangled network of nanofibers having a mean diameter of 70 nm. As it can be seen in the top right corner of the SEM image, most of the nanofibers have a large number of nodules which can act as nucleation sites for future fibers. As the aniline concentration is increased the polyaniline nanofibers in Figure 29(e) become well separated, less branched, with a smooth surface and a length more than 10 times higher than the diameter.

Some of the properties of electrochemically synthesized polyaniline films on Nb have been determined by electrochemical methods. Capacitance represents the ability of polyaniline to store electric charge. The mass specific capacitance of the polymer films was calculated as:

$$C_S = \frac{C}{m} \tag{30}$$

where C is the film capacitance determined by cyclic voltammetry and electrochemical impedance spectroscopy and m is the mass of deposited polyaniline, which was estimated assuming a current efficiency for the electropolymerization process of 100%, using Faraday's law of electrolysis:

$$m = \frac{(M_m + 0.5M_a)Q}{(2+0.5)F} \tag{31}$$

where M_m and M_a are the molar mass of aniline monomer (93.13 g mol^{-1}) and hydrogen sulfate (97 g mol^{-1}), Q is the deposition charge and F is the Faraday constant (F = 96485 C mol^{-1}).

A comparison of capacitance and mass specific capacitance values determined by cyclic voltammetry and impedance spectroscopy is given in Table 13.

Table 13. Capacitance values of Pani/Nb films determined from CV and EIS data.

Sample	Pani/Nb/1	Pani/Nb/2	Pani/Nb/3	Pani/Nb/4	Pani/Nb/5	Pani/Nb/6
C_{CV} [F cm^{-2}]	–	0.0458	0.161	0.244	0.143	0.267
C_{EIS}* [F cm^{-2}]	0.0067	0.0423	0.162	0.259	0.141	0.356
$C_{S,\,CV}$ [F g^{-1}]	–	125	80	154	174	117
$C_{S,\,EIS}$ [F g^{-1}]	113	115	80	164	172	156
δ [μm]	0.13	0.84	3.56	4.40	1.76	5.70

* capacitance values at E = 0.5 V.

It can be observed that all Pani samples showed high capacitance values. The capacitance values are correlated to the morphology of Pani films. Generally lower specific capacitances are obtained for less concentrated H_2SO_4 solutions, where the morphology of the deposited films is granular. For a higher concentration of the sulfuric acid solution, the morphology changes to nanofibrilar and the specific capacitances are higher than for granular Pani films.

Electrochemical impedance measurements were carried out in the frequency range from 10^4 Hz to 0.1 Hz and AC voltage amplitude of 10 mV, at several electrode potentials, placed in the region were the polyaniline films are in the conductive form. Typical examples of EIS spectra taken for the Pani films at an electrode potential of 0.4 V are given in Figure 30.

The shape of the complex plane impedance plots for Pani films depends on both polymer film thickness and morphology. As the thickness of the Pani films increases, the imaginary

impedance values decrease, indicating an increase of the low frequency capacitance, which was already observed for Pani [111] and substituted Pani derivatives [112]. For Pani films with a fibrilar morphology the Nyquist plots are characterized by the presence of a slightly deviated vertical line at low frequencies preceded by a small part with a slope of nearly 45° at intermediate frequencies.

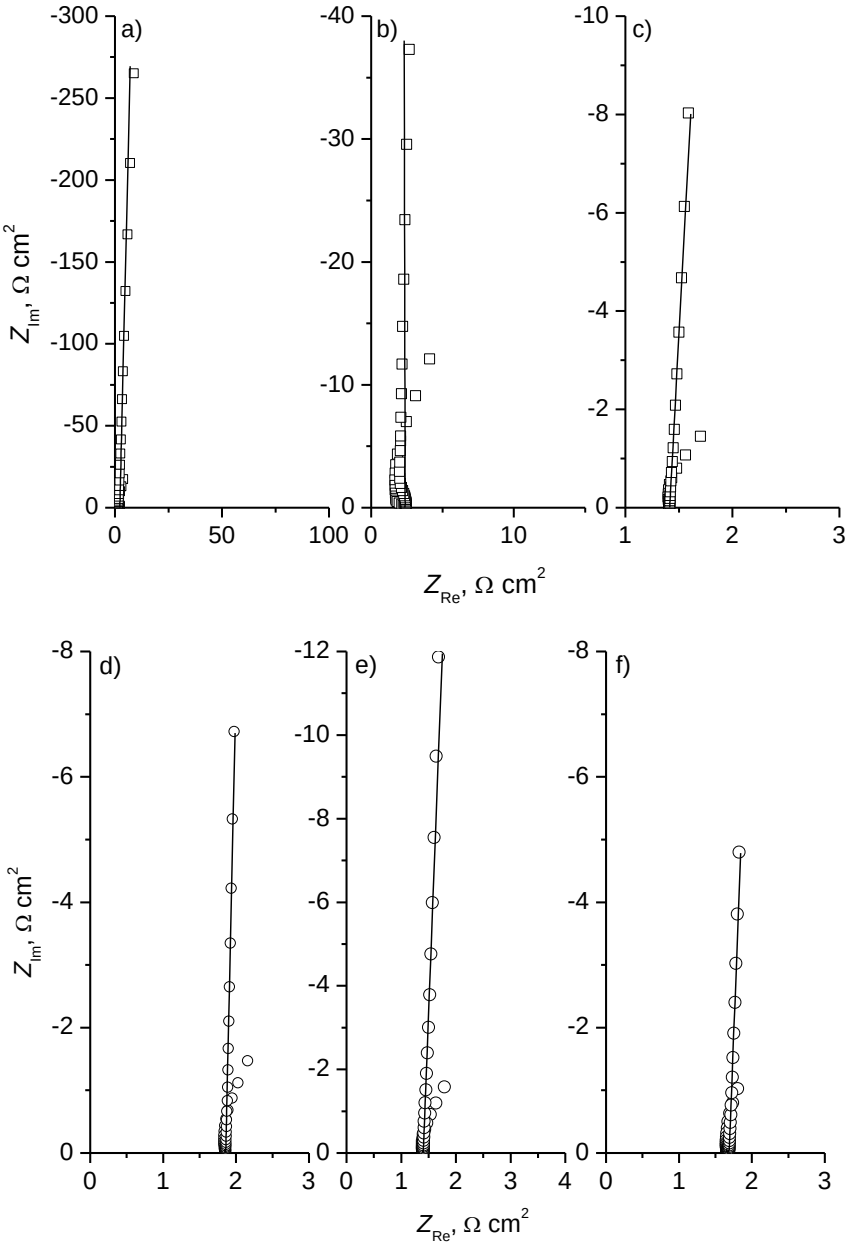

Figure 30. Complex plane plots of (a) Pani/Nb/1, (b) Pani/Nb/2, (c) Pani/Nb/3, (d) Pani/Nb/4, (e) Pani/Nb/5 and (f) Pani/Nb/6 films measured in 0.5 mol L^{-1} H_2SO_4 solution at E = 0.4 V.

Several equivalent electrical circuits have been proposed to describe the impedance of Pani films accounting for the processes that take place at the Pani/electrolyte interface and inside the Pani film. For oxidized Pani films it has been found that fast charge transfer and

counterions diffusion at the Pani/electrolyte interface are responsible for the high-frequency response and slow diffusion / migration of counterions inside the Pani layer is responsible for the low frequency response of Pani films [111, 113-115].

It can be observed that the diffusion resistance is correlated to Pani layer thickness and morphology. It has greater values for thin films Pani/Nb/1 and Pani/Nb/2, where a compact layer is formed on the metal surface and the ions motion inside the film is slower. It has much lower values for fibrilar Pani films where due to high porosity the electrolyte has an easier access inside the film. Pani/Nb/3 shows an intermediate behaviour, more close to fibrilar Pani since its structure is different from Pani/Nb/1 and Pani/Nb/2. The diffusional capacitances are directly related to the layer thickness and film morphology, as it can be seen in Figure 31.

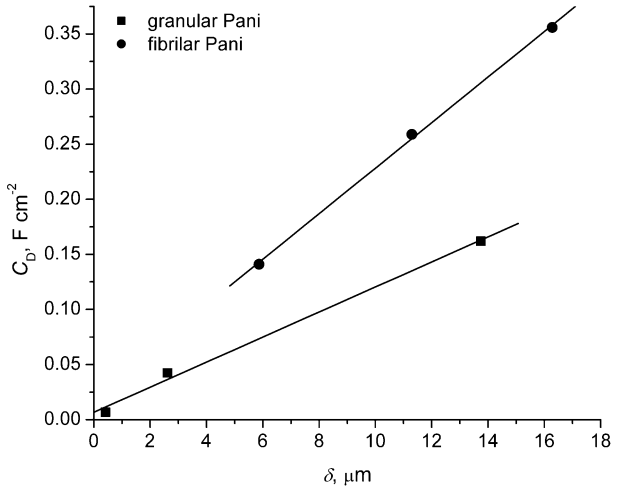

Figure 31. Dependence of the diffusional capacitance on film thickness for granular and fibrilar Pani films obtained on Nb.

For both granular and fibrilar Pani films, the capacitance increases linearly with the film thickness, but it is evident that fibrilar Pani films with similar thickness have a higher capacitance.

2.2.2. Effect of scan rate

We have studied the effect of potential scan rate on the morphology and properties of polyaniline films electrochemically deposited on nickel electrode. Polyaniline samples have been obtained by cyclic voltammetry at different scan rates of 10, 25, 50 and 100 mV s^{-1} from a solution of 0.1 mol L^{-1} aniline in 0.5 mol L^{-1} H_2SO_4. All measurements were performed in a conventional one-compartment, three-electrode electrochemical cell equipped with a nickel disc working electrode (A = 0.64 cm^2), two graphite rods as counter electrode and silver/silver chloride (Ag/AgCl) as reference electrode. The electrochemical deposition of polyaniline took place in two steps. In the first step, cyclic voltammograms were recorded in

a large potential window from –0.15 V to 1.25 V, corresponding to the induction or initiation of the polymerization reaction. In the next step, during the growth of the polymer film, the upper potential limit was shifted to a lower value of 0.85 V, to avoid the oxidative degradation reactions and consecutive cyclic voltammograms were taken in a narrower potential window. The prepared samples are denoted as Pani/Ni/10, Pani/Ni/25, Pani/Ni/50 and respectively Pani/Ni/100, indicating the scan rate applied in the potentiodynamic scan during the deposition of the polymer films. An overview of the corresponding synthesis conditions is given in Table 14.

Table 14. Synthesis conditions and characteristics of the first peak of Pani/Ni films obtained at different scan rates.

Sample	scan rate [mV s^{-1}]	no. of scans I/G	E_a* [V]	E_c* [V]	i_a* [mA cm^{-2}]	Q* [mC cm^{-2}]
Pani/Ni/10	10	3/3	0.290	0.077	16.5	117.1
Pani/Ni/25	25	3/4	0.275	0.070	16.8	41.6
Pani/Ni/50	50	3/9	0.258	0.055	17.3	21.7
Pani/Ni/100	100	3/13	0.258	0.052	16.0	11.9

* values are given for the last cycle.

A comparison of the last cycle recorded during the electrochemical deposition of Pani/Ni samples is given in Figure 32, together with the dependence of the charge corresponding to the first anodic peak versus the number of scans.

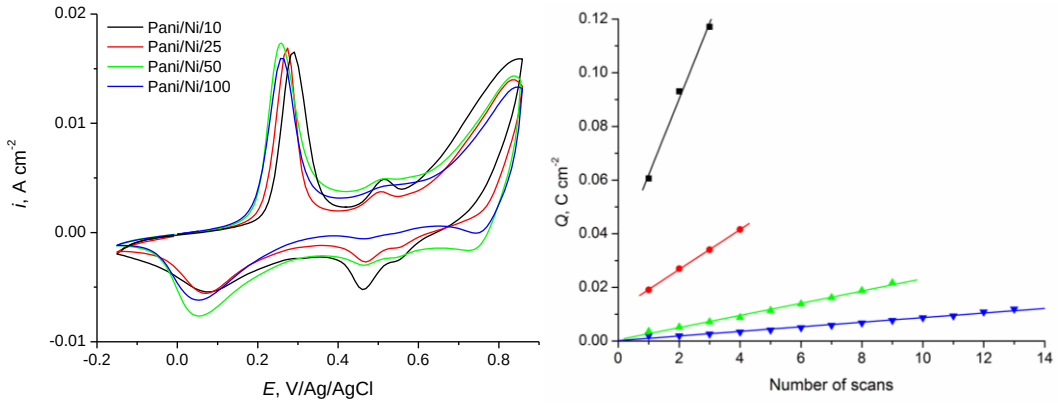

Figure 32. Potentiodynamic deposition of Pani/Ni samples from a solution of 0.1 mol L^{-1} aniline in 0.5 mol L^{-1} H_2SO_4. Last scan of the cyclic voltammograms (a) and dependence of the charge on the number of scans (b).

Typical CVs have been recorded during the growth of Pani films, characterized by the presence of two pairs of redox peaks corresponding to redox transitions from leucoemeraldine to emeraldine and from emeraldine to pernigraniline. Also, an intermediate pair of redox peaks is assigned to secondary degradation reactions. The potential peak of the first redox transition shifts slightly to more positive potentials as the scan rate decreases. It

can be also noticed that the intensity of the degradation peaks is more pronounced at lower scan rates.

The redox behavior of Pani/Ni samples was studied by cyclic voltammetry in monomer free electrolyte solution. A classical behavior for conducting polyaniline is observed, as seen in Figure 33. The first anodic peak is roughly centered at 0.38 V for Pani/Ni/10, at 0.34 V for Pani/Ni/25 and at 0.26 V for Pani/Ni/50 and Pani/Ni/100. Its position shifts to higher potentials as the thickness of the polymer film increases.

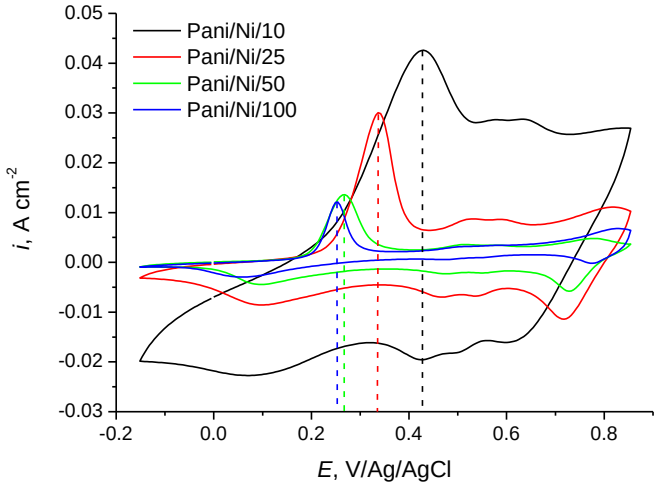

Figure 33. Cyclic voltammograms of Pani/Ni samples in monomer free 0.5 mol L^{-1} H_2SO_4 solution. Scan rate 50 mV s^{-1}.

The morphology and structure of the polyaniline films prepared on nickel were characterized by field emission scanning electron microscopy (FE-SEM) using a QUANTA FEG 250 scanning electron microscope. Figure 34 gives the FE-SEM images of the polyaniline films electrodeposited on nickel using different scan rates.

Polyaniline samples obtained at scan rates of 10, 25 and 50 mV s^{-1} show a porous, open, highly branched nanofibrilar structure, whereas samples obtained at 100 mV s^{-1} are composed of very short nanofibrils, almost completely merged with each other, resulting in a compact, stratified structure. For Pani/Ni/10 there is a high amount of long and smooth nanofibers while for Pani/Ni/50 some inclusions of granular polyaniline could be observed. The nanofiber network tends to be more compact and with less free-volume as the scan rate is increased. The average diameter and length of the nanofibers decrease with the potentiodynamic scan rate applied for deposition in the following order: **Pani/Ni/10** (140 nm / 1.35 μm) > **Pani/Ni/25** (100 nm / 1.06 μm) > **Pani/Ni/50** (90 nm / 0.72 μm). These results are consistent with literature data [93] and can be explained based on the mechanism of nucleation and growth of the polymer film. At low scan rates the number of nucleation sites generated at the surface of the nickel electrode is small, but their dimensions are bigger since the electrode is maintained for a longer time at the oxidation potential value. At higher scan rates the number of nucleation sites is higher, but their size is reduced. As a result a larger

number of nanofibers with smaller diameters will be obtained. Also, some of the nanofibers present nodules on their surface, which can act as nucleation sites for future fibers leading to a highly branched structure.

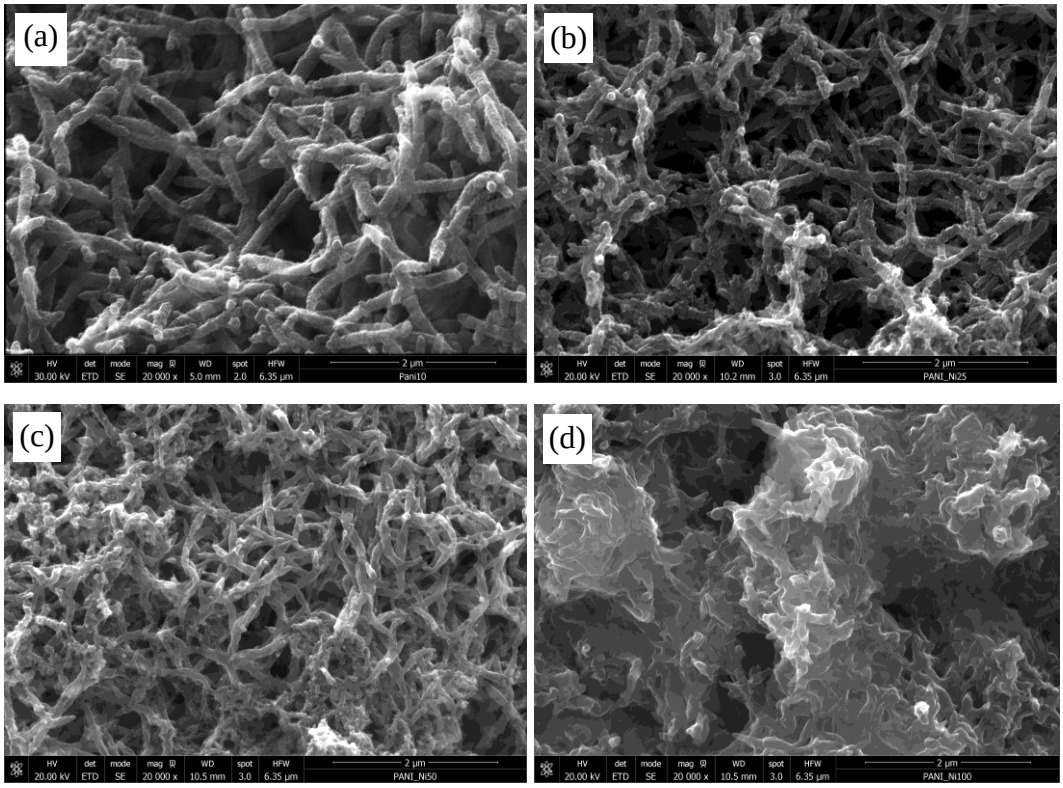

Figure 34. FE-SEM images of polyaniline films: Pani/Ni/10 (a), Pani/Ni/25 (b), Pani/Ni/50 (c) and Pani/Ni/100 (d).

The electrochemical properties of polyaniline nanofibers deposited on nickel were investigated by cyclic voltammetry and electrochemical impedance spectroscopy in monomer free H_2SO_4 solution. The mass specific capacitance was determined using equations (30) and (31).

A comparison of capacitance and mass specific capacitance values determined by cyclic voltammetry and impedance spectroscopy is given in Table 15.

Table 15. Capacitance values of Pani/Ni films determined from CV and EIS data.

Sample	Pani/Ni/10	Pani/Ni/25	Pani/Ni/50	Pani/Ni/100
C_{CV} [F cm^{-2}]	0.233	0.085	0.036	0.018
C_{EIS}^{*} [F cm^{-2}]	0.255	0.095	0.041	0.023
$C_{S,\,CV}$ [F g^{-1}]	655	715	585	490
$C_{S,\,EIS}$ [F g^{-1}]	717	799	666	626
δ [μm]	2.55	0.85	0.44	0.22

It can be observed that, as expected, the capacitance of Pani films increases proportionally to film thickness and mass of deposited Pani. However, when mass specific capacitance values are compared, the highest capacitance is obtained for Pani 25, and the lowest capacitance is obtained for Pani 100 due to different morphologies. The nanofibers' aspect ratio (L/D) varies in the order: Pani/Ni/25 (10.6) > Pani/Ni/10 (9.6) > Pani/Ni/50 (8.0) which might explain the highest capacitance and lowest resistance of Pani/Ni/25. It has been reported that high conductivities are obtained for branched Pani nanofibers with high aspect ratio, where charge carriers are free to move throughout the length of nanofibers and further extend to the branch regions, leading to an increased delocalization of charge [116]. The ability to transport charge carriers along the polymer backbone due to an extended conjugation length represents the intrachain conductivity, whereas the ability of carriers to hop between polymer chains represents the interchain conductivity.

Electrochemical impedance measurements were conducted to determine the effect of deposition scan rate on the charge transfer resistance and specific capacitance of synthesized polyaniline films. EIS measurements were carried out in the frequency range from 0.1 Hz to 100 kHz and AC voltage amplitude of 10 mV. For each spectrum 60 points were collected, with a logarithmic distribution of 10 points per decade. Figures 35-38 show impedance spectra of Pani/Ni samples at different electrode potentials in the range of 0.2 to 0.6 V.

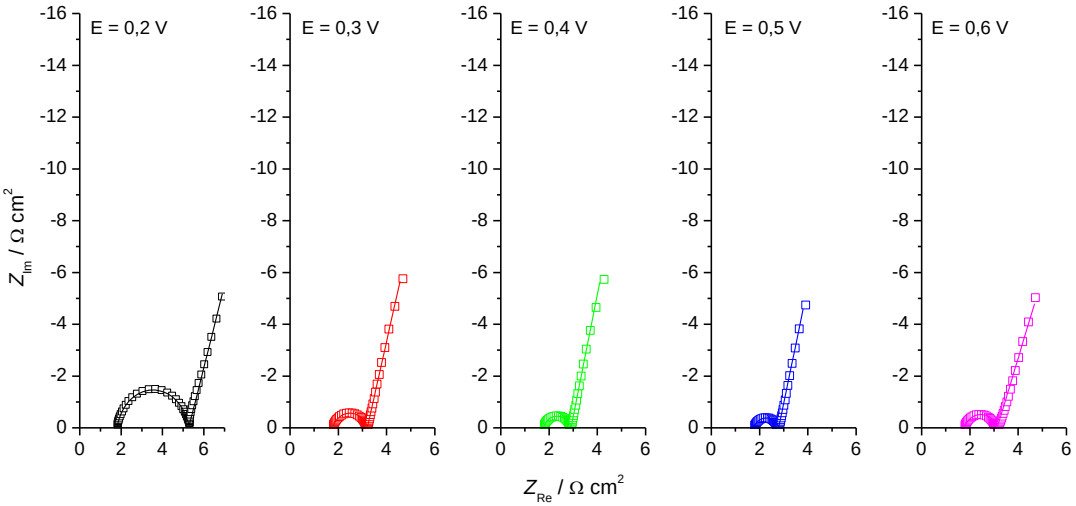

Figure 35. Complex plane plots of Pani/Ni/10 measured in 0.5 mol L^{-1} H_2SO_4 solution at different electrode potentials.

The impedance behavior in the potential window from 0.2 to 0.6 V is assumed to be a characteristic of Pani/electrolyte interface and of Pani layer pseudocapacitance [117,118]. The changes in impedance parameters were used to interpret processes taking place inside polyaniline and at the polyaniline/electrolyte interface as a consequence of morphology changes.

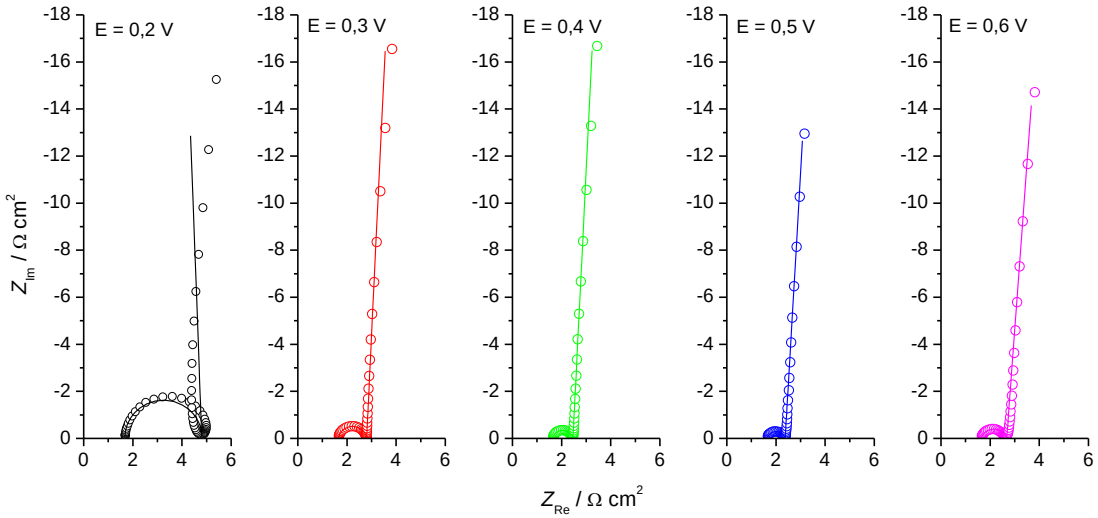

Figure 36. Complex plane plots of Pani/Ni/25 measured in 0.5 mol L^{-1} H_2SO_4 solution at different electrode potentials.

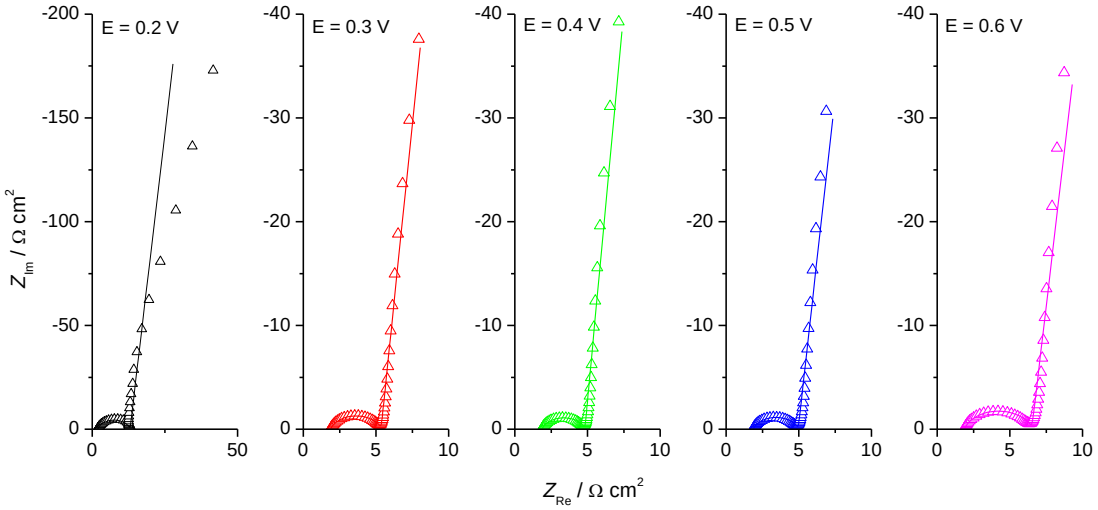

Figure 37. Complex plane plots of Pani/Ni/50 measured in 0.5 mol L^{-1} H_2SO_4 solution at different electrode potentials.

The shape of the complex plane plots depends on both polymer film thickness and morphology. For Pani/Ni/10, Pani/Ni/25 and Pani/Ni/50, with similar morphologies, the complex plane plots are characterized by the appearance of a high frequency semicircle followed by a near vertical line at low frequencies, at all investigated electrode potentials. The impedance response at high frequencies corresponds to the charge transfer at the polyaniline/electrolyte interface and low frequency response is dominated by the polyaniline film capacitance. As the film thickness decreases, the imaginary part of the impedance increases, indicating a decrease of the low frequency capacitance. The diameter of the high frequency semicircle is potential dependent decreasing up to potential of 0.4 – 0.5 V, in agreement with the transition from leucoemeraldine to the conductive emeraldine form of

Pani. A completely different behavior is observed for Pani/Ni/100, where an incomplete arc of a semicircle with larger diameter can be seen.

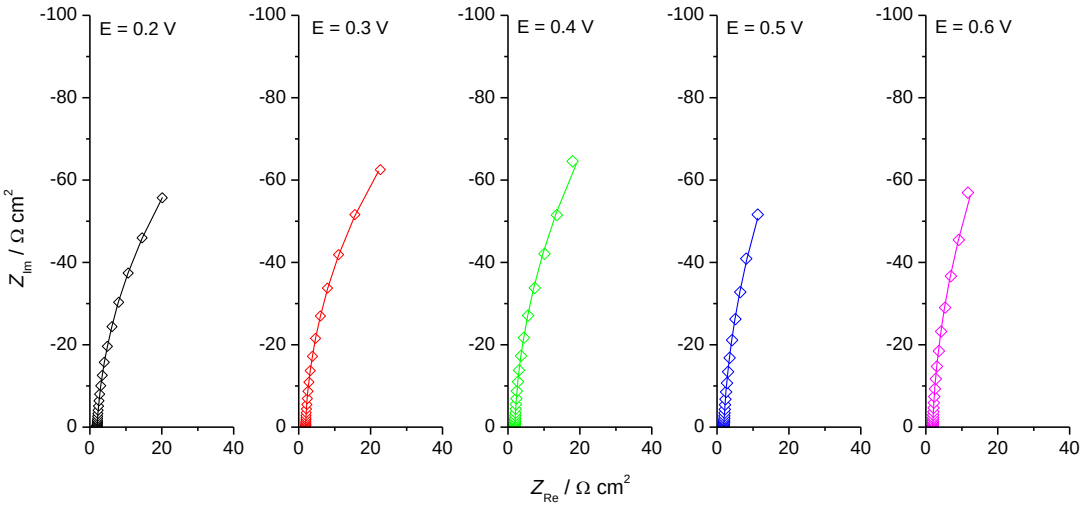

Figure 38. Complex plane plots of Pani/Ni/100 measured in 0.5 mol L^{-1} H_2SO_4 solution at different electrode potentials.

Table 16. Charge transfer and capacitance values of Pani/Ni films obtained by fitting EIS data.

Sample	R_{ct} [Ω cm^2]					T [F cm^{-2} s$^{(n-1)}$]				
	0.2 V	0.3 V	0.4 V	0.5 V	0.6 V	0.2 V	0.3 V	0.4 V	0.5 V	0.6 V
Pani/Ni/10	3.47	1.44	1.14	**1.03**	1.37	0.268	0.255	0.261	0.318	0.288
Pani/Ni/25	3.13	1.15	0.82	**0.74**	1.05	0.100	0.095	0.095	0.123	0.110
Pani/Ni/50	11.2	3.50	2.97	3.11	4.67	0.046	0.042	0.041	0.052	0.047
Pani/Ni/100	231	237	301	387	392	0.026	0.023	0.023	0.030	0.027

The impedance data from Table 16 indicate that the charge transfer resistance of Pani/Ni samples obtained at a potential scan rate of 10, 25 and 50 mV s^{-1} decreases up to an electrode potential of 0.4 – 0.5 V, where polyaniline is in its conductive form, emeraldine, and increases again at more positive potentials. The lowest values of charge transfer resistance and highest values of capacitance are obtained for Pani/Ni/25 and Pani/Ni/10, with a highly porous, nanofibrilar morphology, whereas for Pani/Ni/100 the charge transfer resistance values are two orders of magnitude higher, corresponding to a much lower conductivity, explained by its compact morphology.

The lower resistance and higher capacitance of Pani films obtained at low scan rates are a result of different morphology. It has been shown that conductivity and apparent charge carrier mobility are enhanced for nanofibrilar Pani as compared to granular Pani having the same oxidation levels [119]. In fibrilar morphology the chains are extended, more ordered and allow the existence of delocalized states along the chain length direction. In granular

morphology the chains are coiled up which tends to localize the electronic states [120], thus explaining the higher conductivity of polyaniline nanofibers.

The morphology changes induce different properties of polyaniline films. Thus, films deposited at lower scan rates show high values of surface related capacitances, due to the increase of both thickness and electrochemically active surface area. However, comparing mass related capacitances, the best results are obtained for Pani/Ni/25. The optimum scan rate applied for deposition of Pani in this work, leading to best performances in terms of specific capacitance and charge transfer resistance, was found to be 25 mV s^{-1} and it is supposed to originate from an optimum combination of intrachain and interchain transport of charge carries.

2.2.3. Effect of temperature

Temperature is one of the synthesis parameter that can be varied in both chemical and electrochemical synthesis of polyaniline. It has been reported that polyaniline obtained at sub-zero temperatures should exhibit a higher conductivity, therefore several studies have been conducted at low temperatures [121-123]. Another study indicated that polyaniline with high conductivity can be prepared if the chemical oxidative polymerization of aniline is carried out at temperatures above room temperature with an optimum between 50 and 60°C [124]. In case of electrochemical synthesis the effect of temperature is to increase the rate of the electrochemical polymerization. In case of the electrochemical polymerization of substituted anilines a 4.2% per degree increase of the polymer rate formation is obtained [125] although ortho-coupling and degradation reactions are also favored by temperature.

Another aspect is related to the effect of thermal treatment on the conductivity of polyaniline. It has been reported that the conductivity of electrochemically prepared polyaniline films increases at moderately high temperatures up to 70°C [126] or even 100°C [127]. At elevated temperatures a marked decrease of the conductivity is observed generally due to molecular structure changes such as deprotonation, oxidation, chain scission and cross-linking reactions [128-131]. Other studies on the thermal stability of polyaniline films have shown that 80°C is the minimum temperature at which a noticeable decrease on the electrochemical activity was observed [132].

The aim of our study was to investigate the effect of moderately high temperatures on the electrochemical synthesis of polyaniline and to determine the electrochemical properties of Pani films obtained at different temperatures. Cyclic voltammetry has been applied to study the redox reactions of Pani/Pt films and to evaluate their pseudocapacitances in dependence of the synthesis temperature. Electrochemical impedance spectroscopy was the method of choice for studying electrical resistance, double layer capacitance and pseudocapacitance of polyaniline films.

The electrochemical polymerization of aniline was carried out by cyclic voltammetry using an Autolab PGSTAT 302N. All measurements were performed in a conventional one-compartment, three-electrode electrochemical cell equipped with a Pt disc working electrode

(A = 0.1963 cm^2), a Pt counter electrode (A = 1 cm^2) and a saturated calomel electrode (SCE) as reference electrode. Cyclic voltammograms were recorded at a scan rate of 50 mV s^{-1} from 0.1 mol L^{-1} aniline in 0.5 mol L^{-1} H_2SO_4 solutions. For the first three cycles the potential range was from –0.200 V to 1.200 V to allow the initiation of the polymerization process, afterwards the reversal potential was decreased to 0.800 V to avoid the overoxidation reactions of the polymer chain and seven consecutive cycles were recorded. Polyaniline films obtained at three different working temperatures (25, 40 and 60°C) are denoted as Pani/Pt/25, Pani/Pt/40 and Pani/Pt/60, respectively.

Cyclic voltammograms obtained for the electro-oxidation of aniline on platinum electrode at different temperatures are given in Figure 39. The first three scans correspond to the initiation of polymerization and the consecutive seven scans to the growth of Pani film on the surface of the platinum electrode.

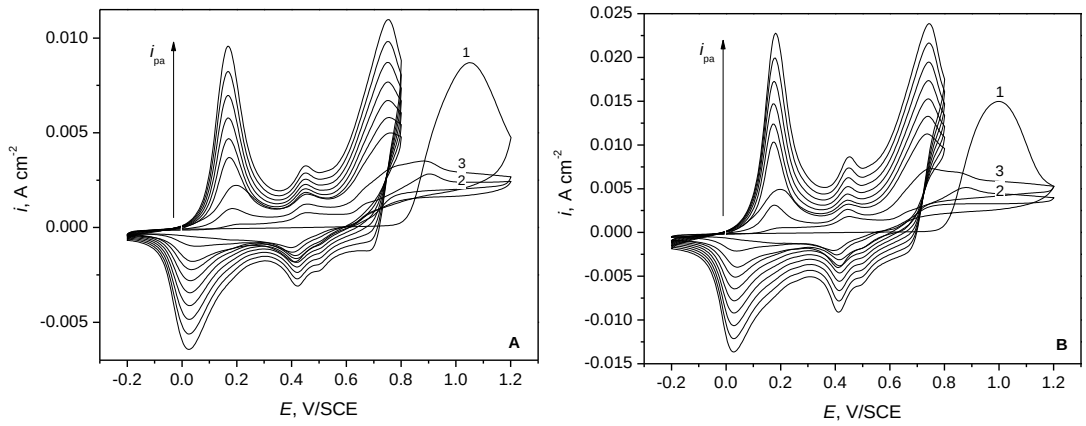

Figure 39. Potentiodynamic deposition of Pani/Pt samples from a solution of 0.1 mol L^{-1} aniline in 0.5 mol L^{-1} H_2SO_4 at different temperatures: 25°C (a) and 40°C (b). Scan rate 50 mV s^{-1}.

The appearance of an anodic peak in the first positive potential scan is assigned to the oxidation of aniline with the formation of the anilinium radical-cation. The characteristics of this peak are temperature dependent, i.e. the onset potential decreases (0.80 V at 25°C, 0.77 V at 40° and 0.72 V at 60°C) and the peak potential shifts to more negative values (1.07 V at 25°C to 0.98 V at 40°C and 0.96 V at 60°C) as the temperature increases. This behavior indicates that the initiation step is favored by temperature.

In the following 4 to 10 scans, the cyclic voltammograms obtained at different temperatures are rather similar in shape, with differences concerning the peaks position and their intensity. The first anodic peak is related to the formation of radical-cations in the polymer chain, the second peak is attributed to degradation processes in the polymer chain due to the oxidation of intermediary compounds or secondary oxidation products. The third anodic peak may be attributed to the oxidation of aniline on the platinum electrode covered with polyaniline, with the exception of the first cycle where the oxidation takes place on a clean platinum surface.

A comparison of the last cycle recorded during the electrochemical deposition of Pani/Pt samples is given in Figure 40, together with the dependence of the charge corresponding to the first anodic peak versus the number of scans.

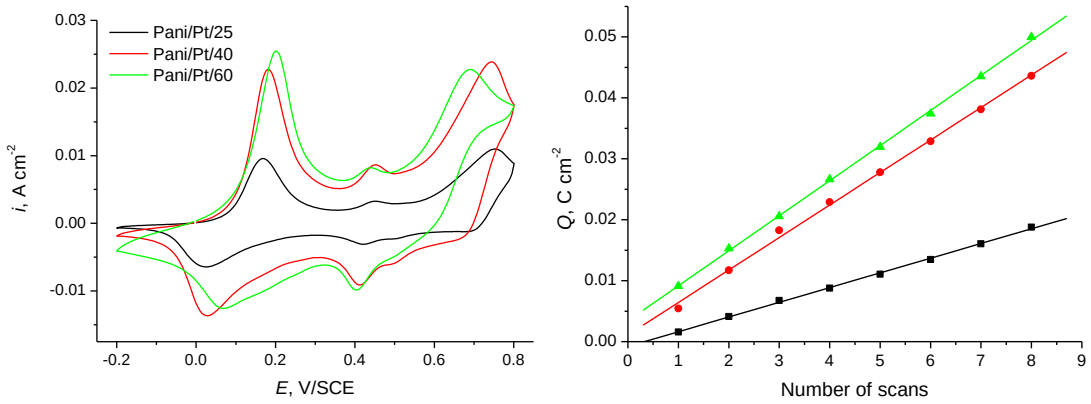

Figure 40. Last scan of the cyclic voltammograms during electrochemical deposition of Pani/Pt samples at different temperatures(a) and dependence of the charge on the number of scans (b).

An overview of the three anodic peak potentials and currents as a function of temperature is given in Table 17.

Table 17. Characteristics of the anodic peaks of Pani/Pt films obtained at different temperatures.

Sample	E_{aI} [V]	E_{aII} [V]	E_{aIII} [V]	i_{aI} [mA cm^{-2}]	i_{aII} [mA cm^{-2}]	i_{aIII} [mA cm^{-2}]	Q_I [mC cm^{2}]
Pani/Pt/25	0.170	0.450	0.750	7.7	0.9	3.3	18.8
Pani/Pt/40	0.175	0.450	0.740	20.2	2.2	5.4	43.6
Pani/Pt/60	0.190	0.440	0.690	22.0	1.2	8.2	50.0

The obtained data indicate a shift of the first peak potential to slightly more positive values as the temperature increases and a marked increase of peak current as the temperature increases from 25 to 40°C. The second anodic peak corresponding to degradation processes in the polymer film is less influenced by temperature concerning its position and height.

The charge corresponding to the first anodic peak increases linearly with the number of cycles, as shown in Figure 40, indicating a continuous growth of the polymer film on the electrode surface. Increasing the temperature from 25 to 40°C leads to a doubling of the slope, pointing to a higher reaction rate, while further increasing the temperature up to 60°C during the electropolymerization has only a slight effect on the charge involved in the process.

The effect of temperature on the electrochemical polymerization of aniline has been discussed before for temperatures between 0 and 40°C [121]. The authors reported that the polymerization rate increased strongly from 0°C to 20°C but it was followed by a decrease at

temperatures higher that 25°C. They explained this behavior due to the formation of a polymer film with lower conductivity and poorer electroactivity as the temperature of synthesis increased. A similar behavior has been observed in case of polyaniline synthesized by the pulse galvanostatic method [97]. In this case the increase of the synthesis temperature leads to the increase of the anodic current peak for the first redox transition of PANI up to 20°C followed by a decrease at higher temperatures.

Our results doesn't indicate a decrease of the polymerization rate, neither a higher rate of decomposition at moderately high temperatures. This facts are supported by the increase of the charge corresponding to the first anodic peak and by the ratio between the height of the first and second anodic peaks. This ratio is an indicator of the rate of polymer film growth versus its degradation. The highest value is obtained for Pani/Pt/60 pointing out to the formation of a polymeric film with improved electroactive properties.

The redox behavior of Pani/Pt samples was studied by cyclic voltammetry in monomer free electrolyte solution. A classical behavior for conducting polyaniline is observed, as seen in Figure 41. The anodic peaks are roughly centered at 0.16 V and 0.75 V for Pani/Pt/25, at 0.19 and 0.73 V for Pani/Pt/40 and respectively 0.24 V and 0.66 V for Pani/Pt/60.

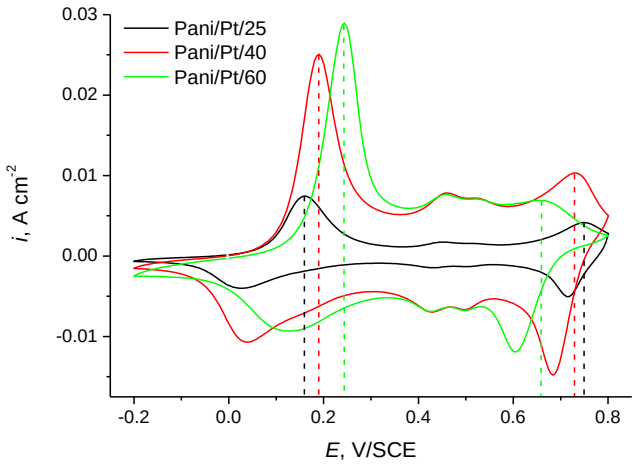

Figure 41. Cyclic voltammograms of Pani/Pt samples in monomer free 0.5 mol L^{-1} H_2SO_4 solution. Scan rate 50 mV s^{-1}.

The intensity of the first anodic peak corresponding to the reversible transition from leucoemeraldine (LE) to emeraldine (EB) is dependent on the synthesis temperature and the peak potential shifts to more positive values as the synthesis temperature increases. The peak corresponding to the emeraldine / pernigraniline (PE) redox transition is also temperature dependent, showing a shift to more negative values for higher synthesis temperatures. This shift of the first and third anodic peaks points out to a narrower region of electroactivity for polymers synthesized at higher temperatures, as it has been also observed from impedance measurements. Also, two pairs of less defined redox peaks situated at about 0.45 and 0.5 V, independently on the temperature of synthesis, correspond to the redox transitions of degradation products formed during the electropolymerization of aniline. Usually these

intermediate products are identified as *p*-quinone/*p*-hydroquinone and *p*-quinoneimine/*p*-aminophenol redox couples.

The electrochemical properties of Pani/Pt samples obtained at different synthesis temperatures were investigated by cyclic voltammetry and electrochemical impedance spectroscopy in monomer free H_2SO_4 solution. The mass specific capacitance was determined using equations (30) and (31) and the corresponding values are given in Table 18.

Table 18. Capacitance values of Pani/Pt films determined from CV and EIS data.

Sample	Pani/Pt/25	Pani/Pt/40	Pani/Pt/60
C_{CV} [F cm^{-2}]	0.0301	0.072	0.096
C_{EIS} [F cm^{-2}]	0.0342	0.066	0.110
$C_{S,\,CV}$ [F g^{-1}]	636	611	697
$C_{S,\,EIS}$ [F g^{-1}]	723	560	799
δ [μm]	0.34	0.84	0.98

It can be observed that, as expected, the capacitance of Pani films increases proportionally with the synthesis temperature, due to the increase of film thickness and mass of deposited Pani.

Electrochemical impedance measurements were conducted to determine the effect of temperature of synthesis on the charge transfer resistance and specific capacitance of Pani/Pt samples. EIS measurements were carried out in the frequency range from 0.1 Hz to 100 kHz and AC voltage amplitude of 10 mV. For each spectrum 60 points were collected, with a logarithmic distribution of 10 points per decade. Figures 42-44 show impedance spectra of Pani/Pt samples at different electrode potentials in the range of 0.2 to 0.6 V.

The complex plane plots of Pani/Pt/25 shown in Figure 42 point out to a typical behavior of conducting polyaniline films, characterized by a pure resistive response at high frequencies and a pure capacitive response at low frequencies.

The complex plane plots of Pani/Pt/40 and Pani/Pt/60 films at 0.1 V show the presence of a depressed semi-circle in the high frequency part of the spectrum followed by a vertical line at low frequencies. This is an indication that at 0.1 V the polyaniline films are not completely conductive, showing an intermediate behavior, between conducting and insulating state. These findings are in good agreement with the cyclic voltammograms of Pani/Pt/40 and Pani/Pt/60 shown in Figure 41, where it can be seen that the onset potential and respectively the peak potential corresponding to the oxidation of leucoemeraldine to emeraldine are shifted to more positive potential as compared to Pani/Pt/25. Increasing the electrode potential, the high frequency semicircle disappears for both Pani/Pt/40 and Pani/Pt/60, but appears again starting from 0.6 V for Pani/Pt/60. This points out to a restriction of the electroactivity range for polymers synthesized at higher temperatures.

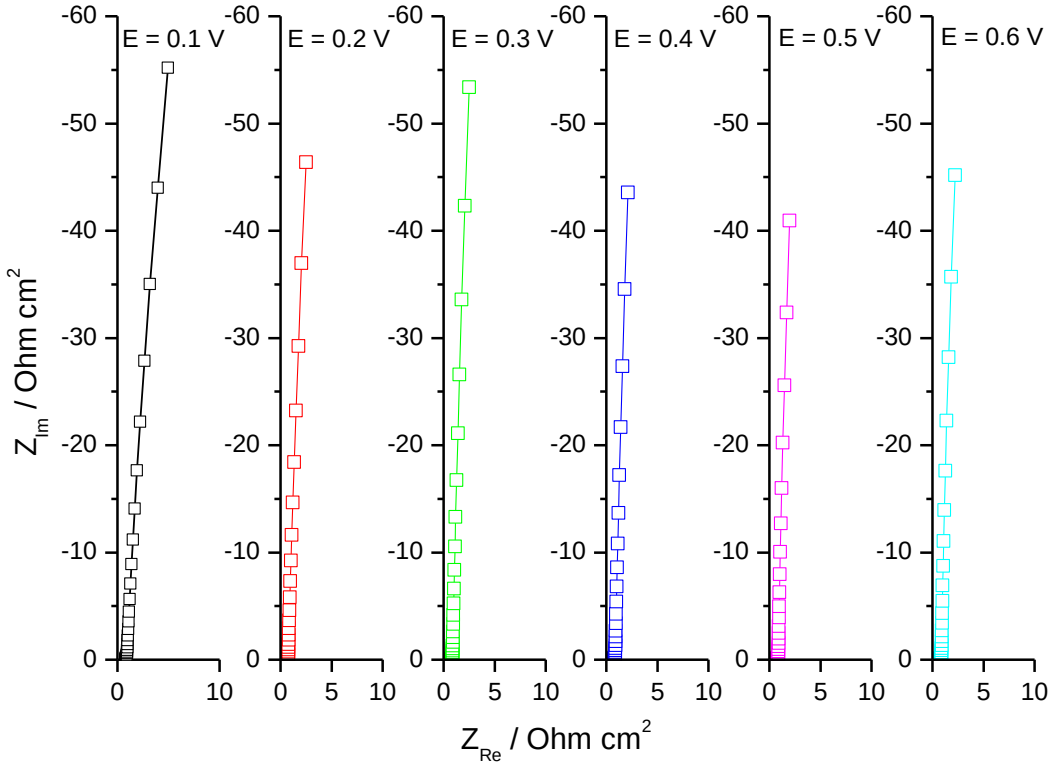

Figure 42. Complex plane plots of Pani/Pt/25 measured in 0.5 mol L^{-1} H_2SO_4 solution at different electrode potentials.

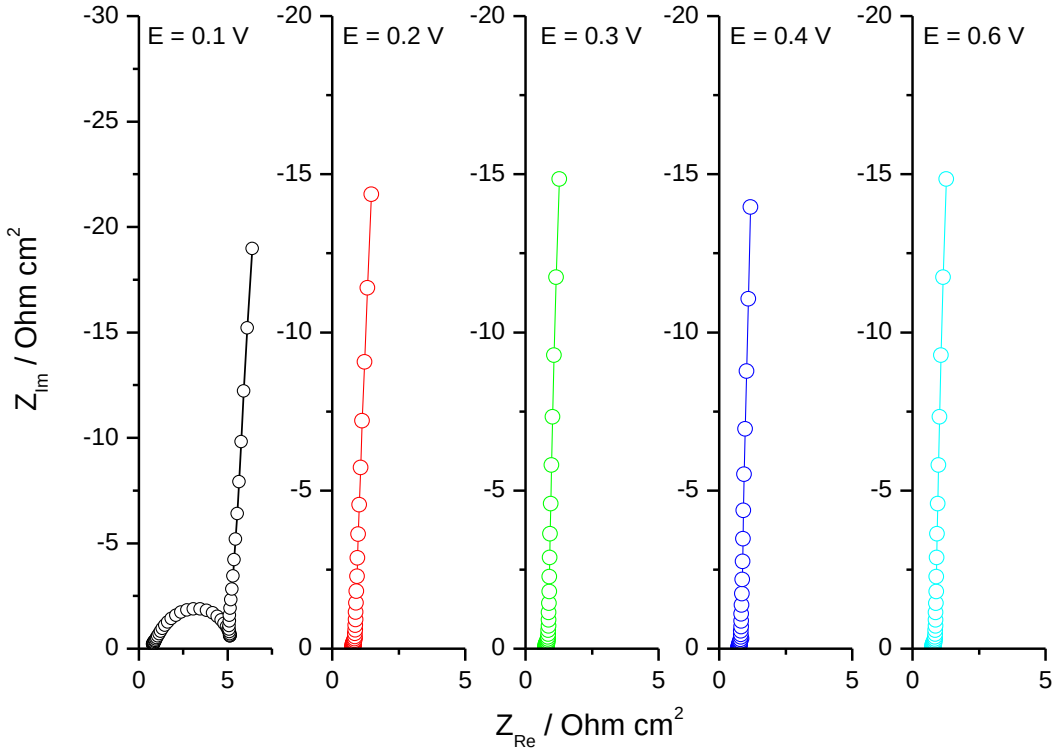

Figure 43. Complex plane plots of Pani/Pt/40 measured in 0.5 mol L^{-1} H_2SO_4 solution at different electrode potentials.

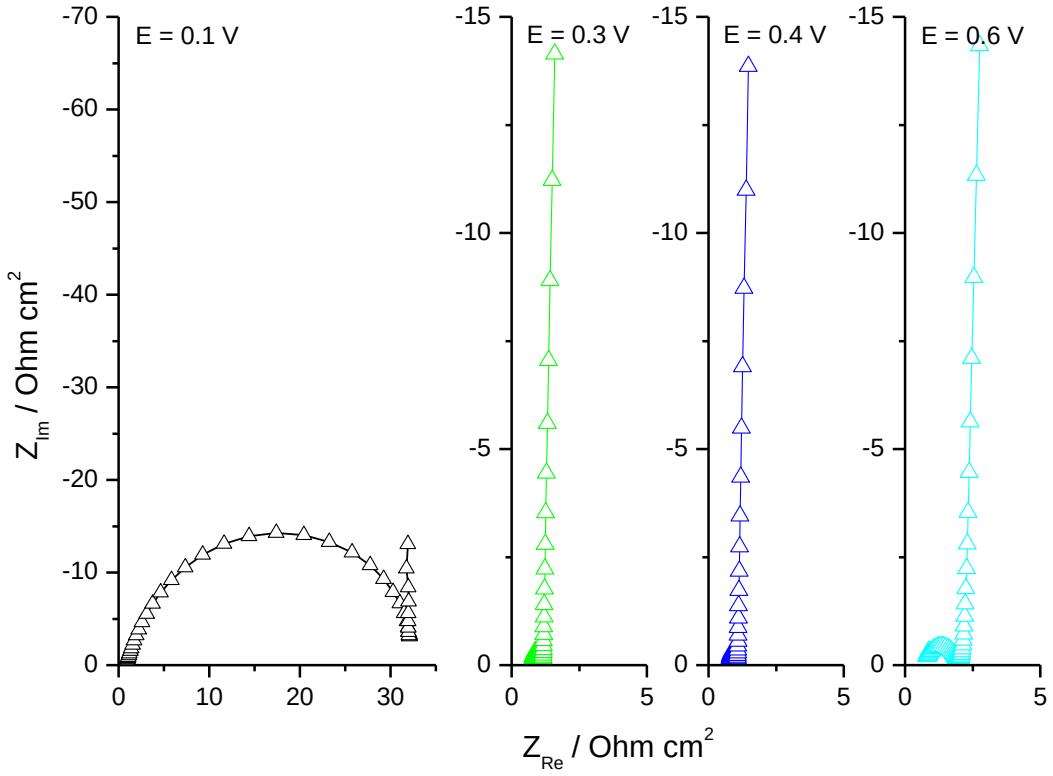

Figure 44. Complex plane plots of Pani/Pt/60 measured in 0.5 mol L^{-1} H_2SO_4 solution at different electrode potentials.

The impedance data were fitted to an electrical equivalent circuit characteristic for the intermediate form of Pani and some of the electrical parameters (charge transfer resistance and capacitance of polymer films) obtained after fitting are given in Table 19.

Table 19. Charge transfer and capacitance values of Pani/Pt films obtained by fitting EIS data.

Sample	R_{ct} [Ω cm^2]					T [F cm^{-2} s$^{(n-1)}$]				
	0.1 V	0.2 V	0.3 V	0.4 V	0.6 V	0.1 V	0.2 V	0.3 V	0.4 V	0.6 V
Pani/Pt/25	0.26	0.36	0.38	0.40	0.31	0.022	0.017	0.015	0.017	0.022
Pani/Pt/40	4.34	0.19	0.22	0.21	0.19	0.079	0.063	0.053	0.062	0.069
Pani/Pt/60	33.1	1.37	0.52	0.36	1.42	0.098	0.127	0.111	0.114	0.112

The electrochemical impedance measurements showed that the synthesis temperature has an effect on the electrical properties of the films. Pani/Pt/25 is in the conductive state over the entire studied potential range although the anodic charge passed until 0.1 V is low. This may be explained by the property of Pani films to give a fully conducting response even if only a small fraction of Pani is oxidized. For Pani/Pt/60 the conductive range is restricted to 0.3 to 0.5 V. The best results in term of film resistance, capacitance and conductivity range were obtained for Pani/Pt/40.

2.2.4. Effect of substrate

It is generally accepted that the substrate plays a special role in the formation and growth of polyaniline nanofibers, however there are only scarce studies regarding the effect of electrode material on the formation and growth of electrochemically deposited polyaniline nanofibers. Generally, the electrochemical synthesis of polyaniline nanofibers is carried out on conventional substrates such as platinum, gold or stainless steel. The electrochemical deposition of granular polyaniline is reported on a large variety of electrode materials including nickel, graphite, glassy carbon, carbon fibers, and indium tin oxide.

In our studies we have tried to elucidate the mechanism of polyaniline nanofiber growth on niobium. Niobium is a transitional metal with hydrogen overpotential much higher than platinum, which is the usual substrate used for polyaniline deposition. This offers the possibility to extend the cathodic potential limit to more negative values during the synthesis and characterization of polyaniline films. This is not possible for polyaniline films deposited on platinum, since at negative potentials the hydrogen evolution reaction interferes with polymer deposition. Also, niobium shows the property to form vertically aligned nanofibers of niobium oxide, when subjected to thermal treatment [133], which lead to the question if niobium oxide formed during electrochemical oxidation of niobium can play a role in the nucleation and growth of polyaniline nanofibers.

The electrochemical oxidation of niobium in sulfuric acid leads to the formation of a passive layer of niobium oxide. Figure 45 shows cyclic voltammograms obtained on niobium, revealing a typical shape for anodic passivation curves, with three distinct regions.

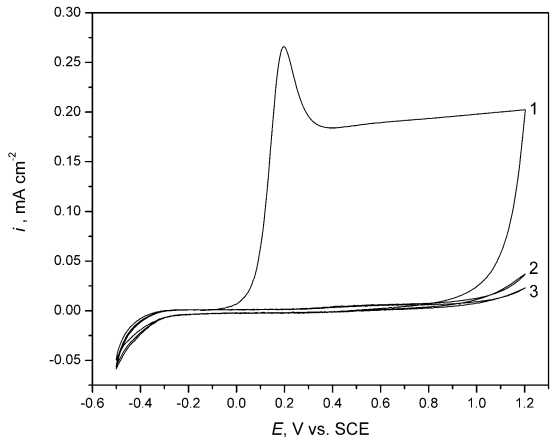

Figure 45. Cyclic voltammogram of Nb in 0.5 M H_2SO_4, scan rate 50 mV s^{-1}.

The first region is the so-called active region, where the current density increases exponentially with the applied potential and an oxidation peak is formed at 0.2 V, corresponding to the dissolution of Nb. The second or passive region, where the anodic current reaches a plateau and is independent of the applied potential, corresponds to the electrochemical passivation of Nb according to the reaction [134]:

$2Nb + 5H_2O \rightarrow Nb_2O_5 + 10H^+ + 10e^-$

The third region (here not shown) corresponds to the oxygen evolution reaction which takes place on the passivating oxide layer. In the following scans, the current has a constant value closed to zero and neither additional oxidation nor reduction peaks can be seen since Nb is covered by a passivating layer of niobium oxide.

Literature data indicate different chemical composition of the passive oxide film formed on niobium, depending on the environment and treatment conditions. It seems that, for the electrochemical passivation of Nb in acidic aqueous solution, the main component of the passivating oxide film is Nb_2O_5 [134,135].

The three dimensional morphology of the electrochemically passivated niobium surface was examined by atomic force microscopy using a Nano surf® EasyScan 2 Advanced Research AFM. A comparison has been made to the surface of niobium oxidized in air.

The surface roughness is calculated using the equation (32) for the mean square root roughness:

$$S_{rms} = \sqrt{\frac{1}{MN}\sum_{k=0}^{M-1}\sum_{l=0}^{N-1}\left(z\left(x_k, y_l\right)\right)^2} \qquad (32)$$

where N and M are the number of crystal axes x and y respectively;
z is the average height of crystallites;
x_k and y_l are maximum and minimum deviations from the average crystallite.

The AFM images of the niobium surface oxidized in air and of the niobium surface after electrochemical passivation are given in Figures 46-48.

The value of the root mean square (RMS) surface roughness decreases from 70 nm for Nb oxidized in air to 7 nm for passivated Nb. The average surface grain size of niobium oxide is higher than 200 nm for Nb oxidized in air and lower than 100 nm for electrochemically passivated Nb. This surface with smaller grain size could explain the growth of polyaniline nanofibers on electrochemically passivated Nb. This conclusion is also supported by the SEM analysis, which shows that the mean diameter of the polyaniline nanofibers is about 100 nm.

Polyaniline was electrochemically deposited on the passivated niobium substrate from sulfuric acid solutions of 0.5 and respectively 1 mol L^{-1} concentrations and different aniline/acid molar ratios, as described in section 2.2.1. The morphology of the obtained polyaniline films was analyzed by scanning electron microscopy, as seen in Figure 29 and reveals a granular structure of polyaniline films obtained in 0.5 mol L^{-1} sulfuric acid and a fibrilar structure in 1 mol L^{-1} sulfuric acid solution.

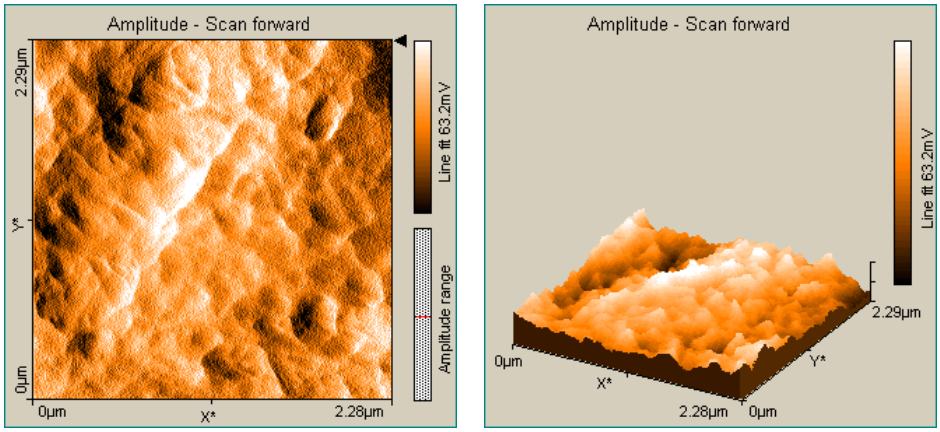

Figure 46. AFM images of the Nb electrode oxidized in air. 2D (a) and 3D image (b).

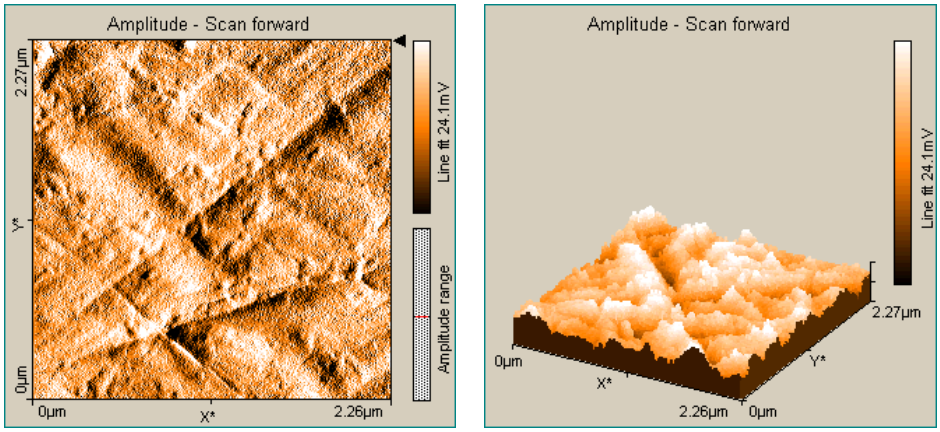

Figure 47. AFM images of the electrochemically passivated Nb. 2D (a) and 3D image (b).

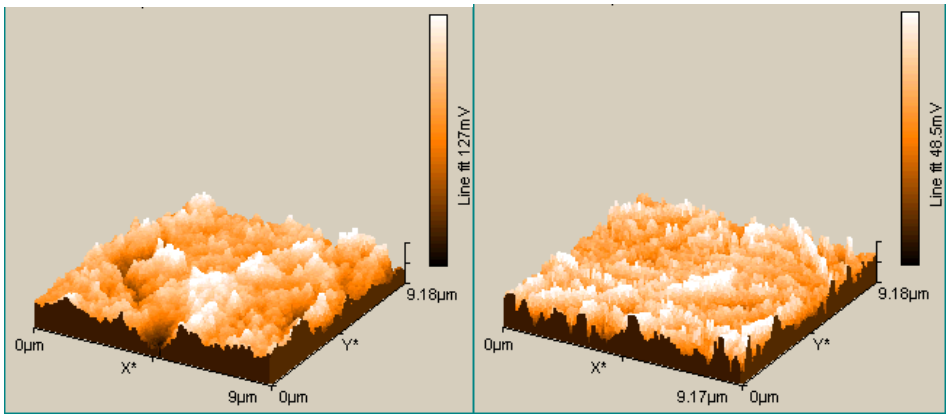

Figure 48. AFM images of Nb electrode oxidized in air (a) and electrochemically passivated (b).

Structural characterization of the polyaniline nanofibers grown on niobium substrate was carried out by Fourier-transformed infrared (FTIR) spectroscopy using an IFS 66v spectrometer (Bruker Optics, Germany) equipped with a DTGS detector working at room temperature. For each spectrum 100 interferograms with a resolution of 4 cm^{-1} were sampled. Figure 49 shows FTIR spectra of polyaniline electrochemically synthesized on passivated

niobium and platinum, in identical conditions regarding solution concentration, scan rate and number of scans, together with FTIR spectra of a commercial emeraldine base (EB) with a weight average molecular weight of 50.000. The main vibrations observed in the mid-infrared region, along with their assignments are presented in Table 20.

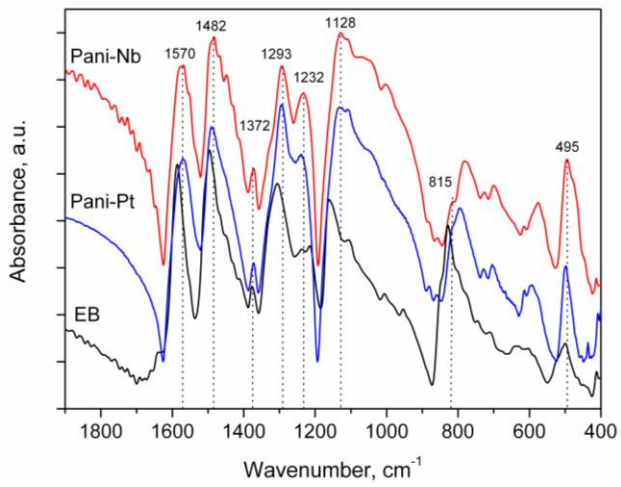

Figure 49. FTIR spectra of electrochemically synthesized Pani/Nb and Pani/Pt and of commercial emeraldine base.

FTIR studies conducted on Pani nanotubes [136,137], nanofibers [94,138,139], nanowires and nanorods, revealed that the backbone structure of all nanostructured Pani samples is similar to that of conventionally prepared granular Pani [140]. However, in case of nanostructured Pani there are indications that phenazine units may initiate the growth of Pani nanotubes [141] and hydrogen bonding between neighboring Pani chains may play an important role in stabilizing the supramolecular nanotubular structure [136,137,141].

Table 20. Main FTIR bands of Pani/Nb and Pani/Pt and their assignments.

Pani/Nb	Pani/Pt	EB	Assignment [136-141]
-	3426 s	3430 s	free ν(N–H)
1570 s	1570 s	1588 s	ν(C=C) in N=Q=N
1482 s	1490 s	1495 s	ν(C=C) in N–B–N
1467 m	-	1466 w, sh	**ν(C=N) in Phz**
1448 m	1450 vw, sh	1447 w, sh	**ring stretching in Phz-type ring**
1414 w, sh	-	1413 w, sh	
1372 m	1372 m	1375 m	ν(C–N) in QBQ
1293 s	1295 s	1305 s	ν(C–N) in QBQ, QBB, BBQ
1232[1] m	1239[1] m	1238[2] m	[1] ν(C–N$^{\bullet+}$) in polaron lattice / [2] ν(C–N) in BBB
1128 s	1130 s	1160 s	δ(C–H) in 1,4-subst B ring
1040 b	1040 b	-	ν(SO_3^-)
815 m	817 m	828 s	γ(C–H) in 1,4-subst B ring
495 m	498 m	500 m	out-of-plane ring def vib in 1,4-disubst ring

ν, stretching; δ, in-plane bending; γ, out-of-plane bending; B, benzene ring; Q, quinoid ring; Phz, phenazine; s, strong; m, medium; w, weak; vw, very weak; sh, shoulder; b, broad.

Structural characterization of Pani/Nb samples carried out by FTIR spectroscopy revealed the presence of similar vibrations to that of conventional polyaniline but also additional vibrations at 1448, 1414 and 780 cm^{-1} related to phenazine-like units, which are known to play an important role in the formation of polyaniline nanotubes.

The formation of Pani nanofibers on the surface of oxidized niobium may be explained based on the theory of phenazine nucleates, considering also the hydrophobicity of niobium oxide. For chemically prepared Pani, the model of phenazine nucleates [142] proposes that in the first stages of polymerization oligomers are produced that may contain phenazine rings formed by *ortho*-coupling followed by intramolecular cyclization reactions. Such oligomers are called nucleates, they are hydrophobic and adsorb preferentially on hydrophobic surfaces. The nucleates self-assemble to produce stacks stabilized by π-π interaction between phenazine units and the growth of Pani nanostructures starts from this pre-organized nucleates [142].

The hydrophobic surface of passivated niobium favors the aniline adsorption and concentration on the niobium oxide grains. The formation of nucleates (oligomers), involves neutral aniline molecules, and not the anilinium cations. In the initial stage of oxidation the aniline molecules link in *ortho* or *para*-positions with the formation of dimers, trimers or phenazine-containing oligomers, depending on acid concentration. The trimer can add a molecule of aniline, with the formation of a tetramer containing the phenazine unit. At high acid concentration it will be protonated and converts to an initiation center. This fragment starts the growth of Pani chains. The propagation step involves anilinium cations that are added to the growing chains exclusively in *para*-positions but only at sufficiently high acidity (1 mol L^{-1}). At low acid concentration the *ortho*-linkage of anilinium cations is present and this leads to a heterogeneous growth resulting in a prevalence of granular particles.

Similar findings have been reported for electrochemically synthesized Pani on hydrophobic nanodiamond ultradispersed particles [143] which also promotes the formation of π-stacked oligomer aggregates and induces the production of one-dimensional nanostructures.

Therefore, it is proposed that the niobium oxide particles formed during electrochemical oxidation of niobium act as hydrophobic interfaces for the adsorption of phenazine nucleates which play a key role in the growth of polyaniline nanofibers.

2.3. Applications of electrochemically synthesized polyaniline films

2.3.1. Electrochemical sensors

Conducting polymers have a high application potential in chemical and biological sensors [144]. In case of polyaniline, the only conducting form is the oxidized form, emeraldine salt, which is obtained in acidic conditions. Deprotonation results in a decrease of charge carriers along the polymer chains and leads to lower conductivities, this effect is very strong in case of polyaniline [144]. This kind of pH sensitivity of electrical and optical properties is

unfavourable for application in biosensors, because most bioassays must be performed in neutral or slightly acidic conditions. In order to overcome this disadvantage, functionalization strategies were adopted. In some studies *N*-substituted anilines were used instead of aniline and it was found that the alkyl chain, which is covalently bonded to the nitrogen atom, prevents the formation of the emeraldine base (EB) form, and finally the obtained polymer is not pH sensitive [145]. Other studies revealed that polymerization of aniline monomers functionalized with a boron moiety lead to poly(aniline boronic acid) PABA [146], a polymer which exhibits redox activity also in solutions with neutral pH [147]. Electrochemically synthesized PABA was used in the detection of fluoride [148,149], iodide [150], saccharides [151,152], butylamine [153] and dopamine [154,155] based on the analyte interactions with the boronic acid functionality. Most of the papers investigate the electropolymerization of aminophenylboronic acid (APBA) on noble electrodes (platinum or gold) and most of the developed sensor are either amperometric or potentiometric sensor.

In our studies we have developed a method to prepare a sensitive electrode based on PABA, which we have tested for the detection of dopamine. Our method consists in the electrochemical deposition of two layers of conducting polymers, first a polyaniline layer deposited on smooth or skeleton nickel electrodes and then a sensitive PABA layer. This approach has been also used for the preparation of an amperometric protein sensor, obtained by the application of two separate polymer layers, one of polypyrrole and one of poly-aminophenylboronic acid on screen-printed platinum electrodes [156]. In our work, we have used a skeleton nickel substrate for the deposition of polymer films, which ensures an active area much larger than the geometric surface area. This kind of surface offers at the same time high area and also highly active catalytic centres. Similar porous metallic matrices have been used in our group before for the electrodeposition of Pani films [157]. The use of such substrates is beneficial for dopamine sensor design, since a high surface area will lead to a higher concentration of boronic groups and to a better sensitivity.

The skeleton nickel electrodes were prepared from a smooth nickel plate, immersed in a bath of molten zinc (at 450°C) for 30, 60 and respectively 90 minutes. The skeleton structure was obtained by dissolving the zinc from the Ni-Zn alloy formed during thermal diffusion using a 30% NaOH solution at 70-80°C until complete reaction.

The skeleton electrodes were used for the two-step deposition of Pani (10 initiation cycles and 10 growth cycles) from 0.1 mol L^{-1} aniline in 0.5 mol L^{-1} H_2SO_4 solution at a scan rate of 100 mV s^{-1}. Paba was then electrochemically generated on top of the Pani layer from 0.02 mol L^{-1} aminophenylboronic acid in 0.5 mol L^{-1} H_2SO_4 for 30 cycles. For comparison a similar Pani-Paba layer was deposited on smooth nickel substrate.

The prepared electrodes with two layers of conducting polymers are further referred to as Ni/0/Paba on smooth nickel and Ni/30/Paba, Ni/60/Paba and Ni/90/Paba on skeleton nickel.

Cyclic voltammograms recorded during the two-step synthesis of Pani-Paba electrodes are given in Figure 50.

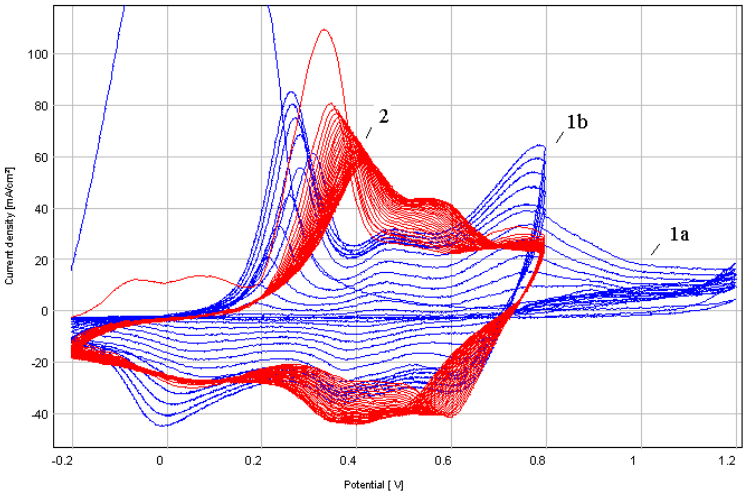

Figure 50. Two-step potentiodynamic deposition of Pani/60/Paba sample, consisting of Pani initiation and growth (1a and 1b) followed by Paba growth (2).

The nature of substrate had a strong impact on the structure and electrochemical properties of Paba films. Cyclic voltammetry and electrochemical impedance spectroscopy showed that for Paba films deposited on the skeleton substrate about 2.5 times higher current densities and lower charge transfer resistances have been obtained, indicating a higher surface area.

The morphology of Paba films was investigated by SEM using a FEI Inspect S microscope. Typical SEM images of granular polymer are shown in Figure 51.

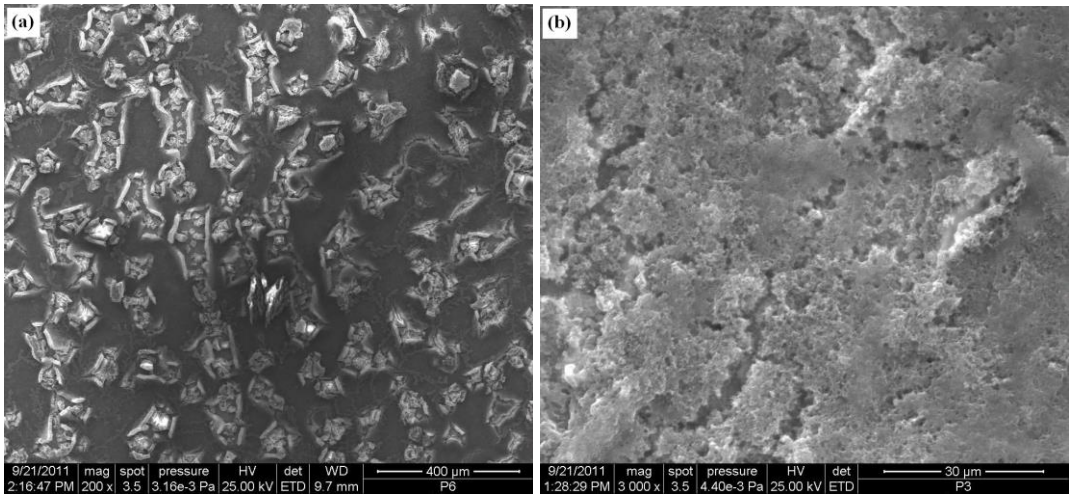

Figure 51. SEM images of Paba modified electrodes: Ni/0/Paba (a) and Ni/30/Paba (b).

The morphology of Paba film obtained on smooth Ni reveals a compact structure, consisting of an inner barrier layer and an outer porous layer. The outer layer contains microscopic pores with a closed cell structure, and the barrier layer is compact (Figure 51(a)) and it is associated to a very large charge transfer resistance, as obtained from EIS data. Using skeleton nickel as substrate affects the morphology of deposited Paba films. Thus, the outer

porous layer becomes predominant (Figure 51(b)) and so the boronic groups are exposed to the interaction with dopamine, which is a prerequisite to enhance the sensitivity of sensor.

The modified skeleton Ni/Paba films have been tested for the detection of dopamine at neutral pH. It is generally accepted that the detection mechanism of dopamine on Paba modified electrodes does not rely on direct oxidation of dopamine on electrodes but on the high affinity binding of dopamine to the boronic acid groups, due to the boronic acid – diol complexation [158] that leads to the formation of an anionic ester, as shown in Figure 52.

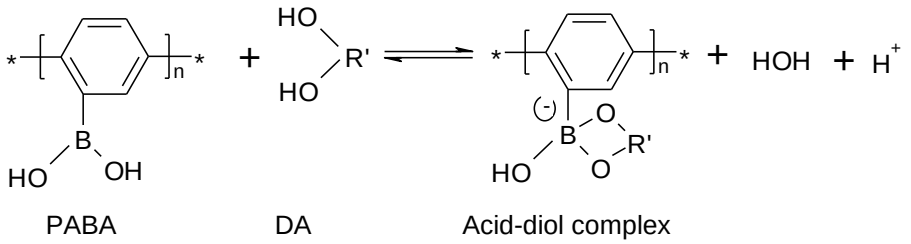

Figure 52. Selective binding of dopamine by Paba and formation of boronate ester.

It is expected that the involvement of boronic acid moiety in the complexation equilibrium will decrease the electroactivity of the Paba film and this will affect the impedance values. Also, the resulting boronate ester sterically hinders the conformational changes of the polymer backbone during oxidation/reduction, leading to a decrease of the electrochemical activity, which is in agreement with the results of Ali *et al.* [159]. Accordingly, Paba modified electrodes can be used in the development of non-oxidative sensors for dopamine, because binding the dopamine molecules changes the properties of the polyaniline backbone (i.e. conductivity) thus providing signal transduction for molecular detection.

The impedance spectra were recorded for Ni/0/Paba and Ni/30/Paba in phosphate buffer at pH = 7.4 in the presence of various concentrations of dopamine, between 10^{-4} and 10^{-10} mol L^{-1} as shown in Figure 53.

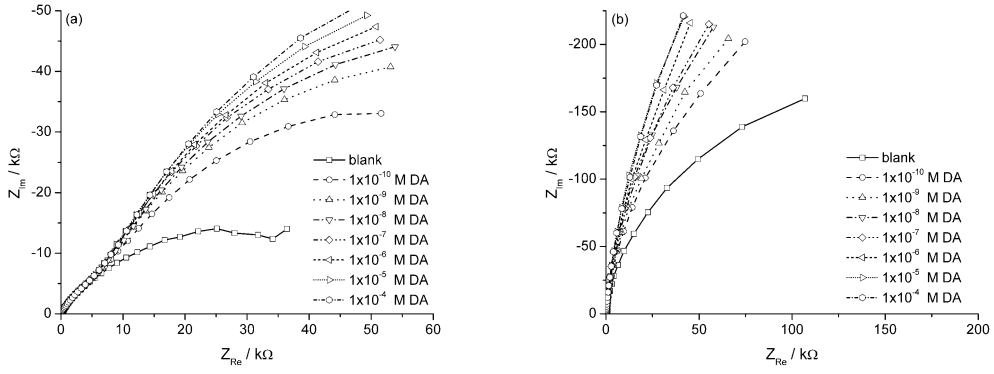

Figure 53. Complex plane plots for Ni/0/Paba (a) and Ni/30/Paba (b) in phosphate buffer solution at pH = 7.4 and different concentrations of dopamine.

A gradual increase of the impedance with dopamine concentration is observed, due to immobilization of dopamine by the boronic acid units available at the interface. This leads to an increase of the charge transfer resistance which can be determined form the impedance data as a function of dopamine concentration. Calibration curves of R_{ct} versus concentration have been constructed, given in Figure 54.

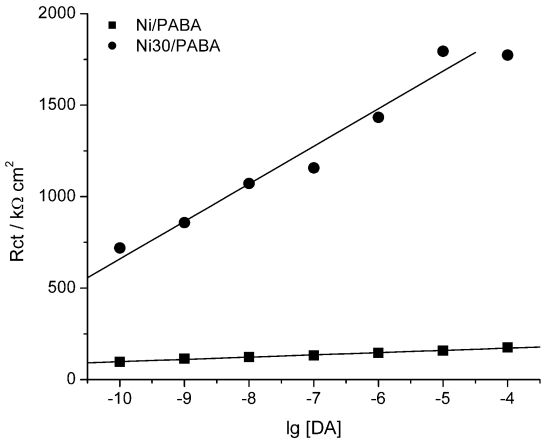

Figure 54. Calibration curves of R_{ct} versus dopamine concentration for Ni/0/Paba and Ni/30/Paba modified electrodes.

A linear response has been obtained for DA concentrations between 10^{-5} and 10^{-10} mol L^{-1}, with a correlation coefficient of 0.994 for Ni/0/Paba and 0.980 for Ni/30/Paba and a detection limit of 1×10^{-10} mol L^{-1}. The sensitivity obtained from the slope of the calibration curves was 12.3 kΩ mol^{-1} for Ni/0/Paba film and increased to 205.4 kΩ mol^{-1} for Ni/30/Paba film.

Amperometric detection tests of dopamine have been also carried out on the Ni/Paba modified electrodes showing a linear response in the concentration range of 10^{-5} to 10^{-9} mol L^{-1} DA for Ni/0/Paba and between 10^{-6} and 10^{-9} mol L^{-1} DA for Ni/30/Paba.

We have found that the redox current decreases with the DA concentration, suggesting that DA is not oxidized but is bonded to the boronic acid groups forming the boronate ester, which reduces the electrochemical activity of the polymer backbone. However, because the differences in current are quite reduced using amperometric detection, the impedimetric detection seems to be more favourable. Significantly large differences are usually obtained by EIS technique, based on the inverse relation of the impedance with the current, *i.e.*, $\Delta R(Z) = \Delta V/\Delta I$ [160]. It has been demonstrated that EIS measurements can provide significantly more sensitive responses than cyclic voltammograms for the detection of several biomolecules [161,162]. Our results have shown that EIS technique allowed the extension of the concentration ranges for detection of dopamine with one order of magnitude in both high and low concentration ranges.

Both smooth and skeleton modified electrodes give a linear response for DA concentrations between 10^{-5} and 10^{-10} mol L^{-1} in aqueous phosphate buffer solution at pH = 7.4. However, the slope of the calibration curves is higher for the Paba-skeleton nickel electrodes, showing that a larger specific surface area, where the density of boronic groups is higher, improves the sensorial response.

2.3.2. Adsorption of dyes

Synthetic dyes generally present a complex aromatic molecular structure, are stable and hard to biodegrade, so the presence of dye toxic wastes in aquatic environments remains nowadays a real problem. As a consequence, an important subject of researches in this field is related to the removal of these compounds from the environment. Various technologies have been proposed for the treatment of dye-containing effluents, such as ion exchange, adsorption, precipitation, biodegradation, membrane filtration, coagulation, flocculation, etc. Different types of adsorbents have been used for the removal of dyes, among them are also conducting polymers, such as polyaniline. Nanostructured conducting polymers present an increasing interest, due to their enhanced properties, which might be completely different from the properties of corresponding macroscopic form [76,77]. Nanomaterials based on conducting polymers offer a large surface area and an improved electrical conductivity.

The removal of organic pollutants from wastewaters using conducting polymers is based on chemical and physical interaction of dye molecules with conducting polymers. Several reports have shown the possibility to use nanostructured polyaniline for the removal of both anionic sulphonated dyes and cationic dyes [163-166] from aqueous solutions. Also, nanocomposites of polyaniline with starch [167] chitosan [168] but also hybrid organic-inorganic composites [169-171] have been successfully used for the removal of dyes from synthetic effluents.

In our studies we have used nanostructured polyaniline films electrochemically deposited on niobium, for the adsorption of an azo dye. The adsorption process was studied by electrochemical impedance spectroscopy, which was used to evaluate the values of surface coverage θ at different dye concentrations and to obtain the adsorption isotherms. Impedance was chosen as measurement technique for this study because it is quantitative, non-destructive and allows to determine the dielectric properties of an insulating layer present on the surface of a working electrode.

The studied dye is a diazo dye derived from 4,4'-diaminobenzanilide and its chemical structure is given in Figure 55.

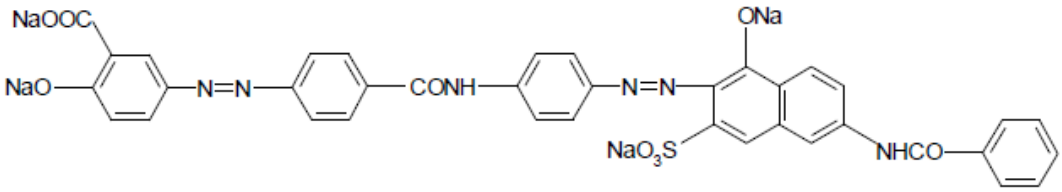

Figure 55. Chemical structure of azo red dye.

The values of surface coverage θ, corresponding to different concentrations of dye were used to get best linearity isotherms. The values of surface coverage θ were obtained from impedance measurements according to equation (33):

$$\theta = (C_o - C_i)/C_o \qquad (33)$$

where C_o is the capacitance at time $t = 0$ and C_i is the capacitance at any moment.

The adsorption of azo red dye was studied under open circuit potential conditions and the adsorption profile in time was investigated. The impedance plots for PANI electrode in solutions containing different concentrations of azo dye red are shown in Figure 56.

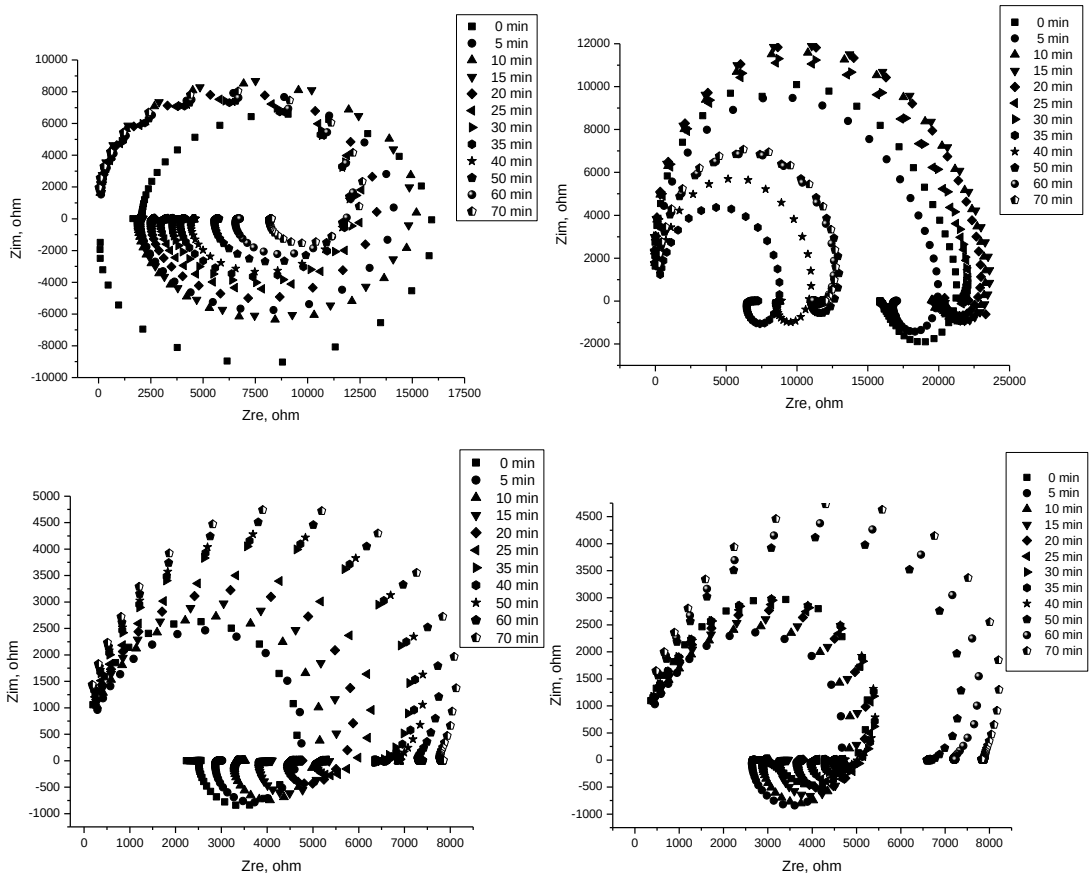

Figure 56. Complex plane plots of Pani/Nb electrode as a function of time for different concentrations of azo dye: (a) 1×10^{-5} mol L^{-1}; (b) 2×10^{-5} mol L^{-1}; (c) 3×10^{-5} mol L^{-1} and (d) 5×10^{-5} mol L^{-1}.

The impedance spectra show the presence of a high frequency semicircle attributed to the electrode-solution interface and a low frequency inductive loop usually attributed to physical phenomena such as adsorption.

The impedance data were modeled by an electrical equivalent circuit and parameters such as double layer capacitance have been determined. The evolution of double layer capacitance of Pani/Nb electrode and of surface coverage degree during the adsorption of azo dye is presented in Figure 57.

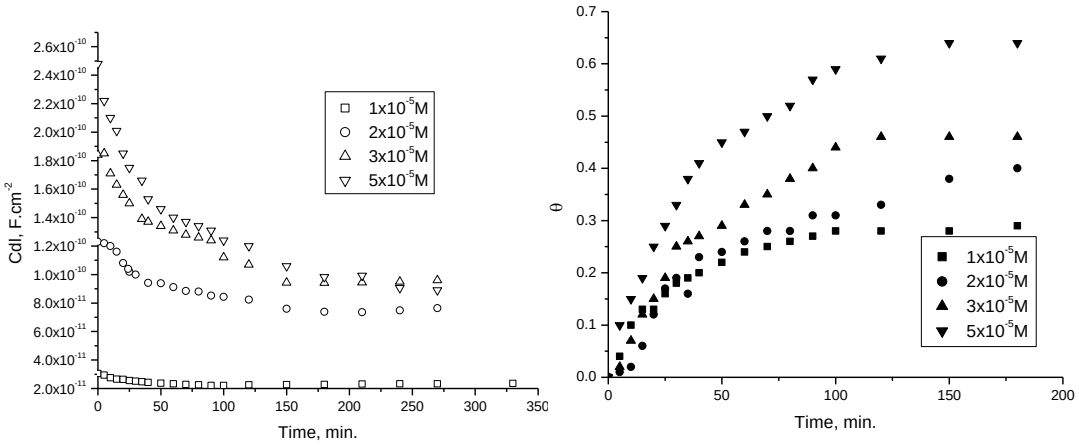

Figure 57. Dependence of double layer capacitance (a) and surface coverage (b) as a function of adsorption time for different dye concentrations.

The double layer capacitance decreases in time due to the adsorption of organic molecules on the Pani/Nb surface, because adsorption causes a decrease of the local dielectric constant, since water molecules are replaced by dye molecules. The decay of double layer capacitance in time shows two distinct regions: a first region of adsorption up to 40 minutes where double layer capacitance decreases exponentially in time, followed by a plateau region from 40 min to 270 min. The variation of the surface coverage is reciprocal of capacitance decay and complete saturation appears after 40 minutes.

Attempts have been made to fit the surface coverage values using several isotherms, including Langmuir, Temkin, Frumkin, and Flory-Huggins isotherms, expressed by equations (34) – (37) given below:

$$\frac{C}{\theta} = \frac{1}{K_{ads}} + C \qquad \text{(34a) (Langmuir isotherm)}$$

$$R_L = \frac{1}{1 + K_{ads} C} \qquad \text{(34b) (Langmuir isotherm)}$$

$$\theta = \frac{1}{a}\left(\ln C + \ln K\right) \qquad \text{(35) (Temkin isotherm)}$$

$$\ln\left(\frac{\theta}{C(1-\theta)}\right) = \ln K + a\theta \qquad \text{(36) (Frumkin isotherm)}$$

$$\log\left(\frac{\theta}{C}\right) = \log(xK) + x\log(1-\theta) \qquad \text{(37) (Flory–Huggins isotherm)}$$

where θ is the surface coverage, $C = C_{dye}$ is the dye concentration, K_{ads} is the adsorption equilibrium constant and a is the molecular interaction constant expressing the interaction between adsorbed and adsorbing molecules. In Flory–Huggins isotherm x represents the number of adsorbed water molecules replaced by one molecule of dye and y is the number of dye molecules occupying one active site. The linear plots obtained using the five adsorption isotherms are given in Figure 58.

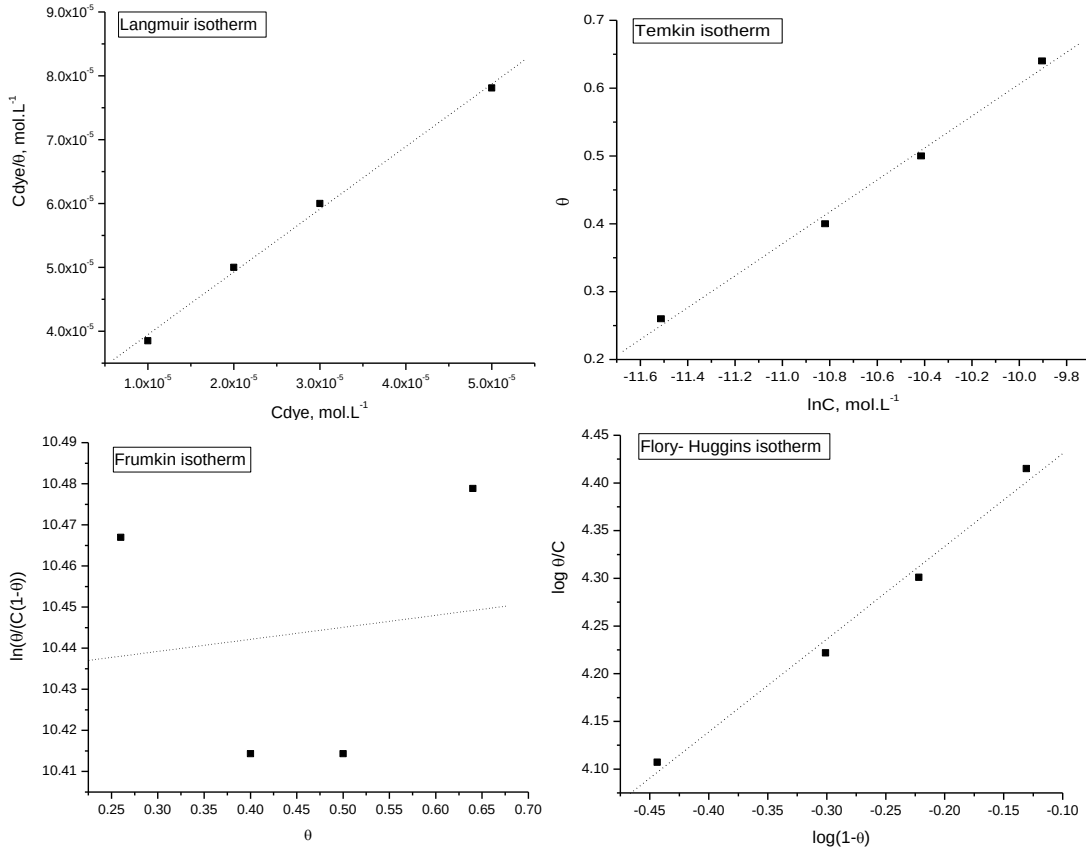

Figure 58. Langmuir (a), Temkin (b), Frumkin (c) and Flory–Huggins (d) isotherms for adsorption of azo red dye on Pani/Nb electrode.

The Langmuir adsorption isotherm ($R^2 = 0.998$) was found to be suitable for our experimental data and based on the value obtained for the adsorption equilibrium constant the Gibbs free energy of adsorption (ΔG^o_{ads}), was calculated using equation (38):

$$\Delta G^{\circ}_{ads} = -RTLn(55.5K_{ads}) \quad (38)$$

where R is the universal gas constant (8.314 J mol^{-1} K^{-1}) and T is the absolute temperature in Kelvin, K_{ads} is the adsorption equilibrium constant, ΔG^o_{ads} is the standard free energy of adsorption, 55.5 is the concentration of water in the solution expressed in mol dm^{-3}.

The value of ΔG^o_{ads} gives indications about the nature of interactions between adsorbate and adsorbent. Values lower than -20 kJ mol^{-1} usually indicate a physical adsorption based on

electrostatic interactions between charged molecules and a charged surface, whereas value higher than -40 kJ mol^{-1} indicate chemisorption, which takes place due to charge sharing or transfer from the molecules to the surface as a coordinate type of bond.

The values of ΔG^{o}_{ads} and K_{ads} obtained from Langmuir isotherm (ΔG^{o}_{ads} ~ - 36.38 kJ mol^{-1} and K_{ads} ~33.7 $kmol^{-1}$) indicate that adsorption of azo red dye on Pani/Nb is a spontaneous process and takes place via a combination of physical and chemical adsorption but mainly due to physical adsorption.

2.4. Conclusions

The electrochemical synthesis of polyaniline nanofibers has been studied in regard of influence of synthesis conditions on the structure, morphology and electrochemical properties of the resulting polyaniline films. The results obtained have shown that polyaniline nanofibers can be obtained by electrochemical synthesis on different electrode materials under specific conditions of each substrate.

The originality of our work is related to the following aspects:

(i) we have investigated the electrochemical polymerization of aniline on a novel transitional metal substrate such as niobium and we have established the optimum conditions in terms of acid concentration and monomer / acid ratio to obtain polyaniline nanofibers with a mean diameter of 70 nm. Since niobium shows a hydrogen overpotential much higher than platinum, which is the conventional substrate for polyaniline deposition, this gave us the possibility to extend the cathodic potential limit to more negative values during the synthesis and characterization of polyaniline films without interference of hydrogen evolution reaction.

(ii) we have explained the growth of polyaniline nanofibers on passivated niobium surface by the theory of phenazine nucleates. Electrochemical passivation results in the formation of hydrophobic niobium oxide particles with an average surface grain size bellow 100 nm as determined by AFM measurement, which closely matches the diameter of polyaniline nanofibers determined by SEM. We have proposed that hydrophobic niobium oxide induces the preferential adsorption of phenazine nucleates and promotes the nucleation of polyaniline nanofibers and we have found evidence about the presence of phenazine-like units in the structure of polyaniline nanofibers as indicated by characteristic FTIR vibrations.

(iii) we have found that capacitance values, which indicate the ability of polyaniline films to store electrical charges, are much higher for nanostructured polyaniline films as compared to those with granular structure.

(iv) we have developed a method for the preparation of an impedimetric sensor for dopamine, using a two-step electrochemical deposition, first a polyaniline layer and then a sensitive poly(aminophenyl boronic acid) layer and demonstrated that the high porosity of the skeleton nickel substrate leads to a higher concentration of available boronic acid groups and to a better sensitivity.

3. Contributions on the study of charge transport mechanism in conducting polymer films

The results presented within this chapter have been obtained in the frame of an international collaboration with the *Center of Spectroelectrochemistry from the Leibniz Institute for Solid State and Materials Research Dresden, Germany* during a number of 5 post-doctoral research stages.

The results have been published in 5 ISI indexed papers, as follows:

- **A. Kellenberger**, E. Jähne, H.J. Adler, T. Khandelwal, L. Dunsch, *In situ* FTIR spectroelectrochemistry of poly[2-(3-thienyl)ethyl acetate] and its hydrolyzed derivatives, *Electrochimica Acta* 53 (2008) 7054-7060.
- L.F. Chazaro-Ruiz, **A. Kellenberger**, E. Jähne, H.J. Adler, T. Khandelwal, L. Dunsch, *In situ* ESR-UV-Vis-NIR spectroelectrochemical study of the p-doping of poly[2-(3-thienyl)ethyl acetate] and its hydrolyzed derivatives, *Physical Chemistry Chemical Physics* 11 (2009) 6505-6513.
- L.F. Chazaro-Ruiz, **A. Kellenberger**, L. Dunsch, *In situ* ESR-UV-Vis-NIR and ATR-FTIR spectroelectrochemical studies on the p-doping of copolymers of 3-methy-lthiophene and 3-hexylthiophene, *Journal of Physical Chemistry B* 113 (2009) 2310-2316.
- **A. Kellenberger**, E. Dmitrieva, L. Dunsch, The stabilization of charged states at phenazine-like units in polyaniline under p-doping. An *in situ* ATR-FTIR spectroelectrochemical study, *Physical Chemistry Chemical Physics* 13 (2011) 3411-3420.
- **A. Kellenberger**, E. Dmitrieva, L. Dunsch, Structure dependence of charged states in "linear" polyaniline as studied by *in situ* ATR-FTIR spectroelectrochemistry, *Journal of Physical Chemistry B* 116 (2012) 4377-4385.

3.1. Background

Conducting polymers are widely investigated due to their practical and potential applications which include rechargeable battery electrodes, electrochromic devices, chemical and optical sensors, light-emitting diodes, molecular based devices such as microelectrochemical amplifiers, field-effect transistors and supercapacitors [172-176]. A considerable number of theoretical and experimental works have been focused on the electronic properties and conduction mechanism of conducting polymers.

One of the most important features of conducting polymers, which also presents increased interest for practical applications, is the possibility to enhance their electrical conductivity by doping [177]. The doping process consists in the chemical or electrochemical oxidation / reduction of the polymer. Accordingly, *p*-doping corresponds to the injection of positive charges and *n*-doping to the injection of negative charges in the polymer chain. The

advantage of electrochemical doping consists in the precise and reproducible tuning of the doping level by controlling the electrochemical parameters such as electrode potential. An essential characteristic of the doping process is its reversibility, i.e. conducting polymers can be switched repeatedly between their conducting (doped) and insulator (undoped, pristine) state. The doping process modifies in the electronic band structure of the polymer, by generating new electronic states in the energy gap. Also, the doping process induces color changes that enable conducting polymers to be used in advanced optical devices, such as multichromic displays or "smart" electrochromic windows.

The chemical and electrochemical oxidation and reduction of such conjugated systems leads to the formation of charge carriers denoted as positive/negative polarons (radical cations/anions) delocalized along the polymer chain with very special electronic, vibrational and charge transport properties. Vibrational spectroscopy has proved to be a powerful technique to investigate the formation of charge carriers and the charge transport mechanism [178-182] because the infrared spectra of conjugated polymers in their conducting (doped) state are characterized by the appearance of very intense infrared active vibration (IRAV) bands. These bands generally appear between 1600 and 700 cm^{-1} and are related to the strong electron-phonon coupling. They provide not only structural but also electronic information. Usually they are accompanied by broad IR absorption bands with maxima at higher energies (around 1500 to 5000 cm^{-1}) related to the formation of free charge carriers during charging of the polymer film.

The idea to perform simultaneously different spectroscopic and electrochemical measurements lead to the development of spectroelectrochemistry, which offers a new way to investigate and unequivocally identify intermediates and products in electrochemical reactions. By using different *in situ* spectroelectrochemical methods, formation and stabilization of charged species, follow-up processes, and mechanism of the electron transfer reaction can be investigated [183]. The basic principle of each spectroelectrochemical technique is that a change in the electrode potential will determine a change of the structure and this will lead to a change of the spectra. The advantage of spectroelectrochemistry consists in its applicability in the study of electrochemical systems, as both the solid and liquid phases are accessible to a detailed spectroscopic study. However, disadvantages are related to the need to construct special spectroelectrochemical cells, the type and size of which are adjusted to the requirements of the spectroscopic method, which might contradict the requirements of the electrochemical method in terms of electrode geometry, electrolyte composition, and volume [184].

One of these methods is *in situ* attenuated total reflection Fourier transform infrared (ATR-FTIR) spectroelectrochemistry.

ATR-FTIR spectroscopy is a technique based on the internal reflection of the infrared beam down the length of an internal reflection element, usually Ge or ZnSe. The most important fact is that at each internal reflection point the evanescent wave will penetrate a short distance outside from the crystal inside the sample which is in contact with the crystal. So, when a sample is placed in optical contact with the reflection element it will absorbs infrared energy and one can obtain the infrared spectra of the sample. This penetration depth is usually

between 0.5 and 2 µm and depends on several factors such as the angle of incidence, wavenumber and the reflection indices of both ATR crystal and sample.

ATR-FTIR spectroelectrochemistry can be applied for *in situ* studies of polymer or copolymer film growth on the electrode surface, for *in situ* evidence of counterions incorporation into the polymer film and for *in situ* studies of the charge transfer mechanism during doping and dedoping of polymer films.

A spectroelectrochemical cell is based on the cell construction described in [185]. The cell consists of a Teflon body provided with openings for the platinum counter electrode and for the Ag/AgCl pseudo-reference electrode. Details about the construction of the spectroelectrochemical cell are given in Figure 59.

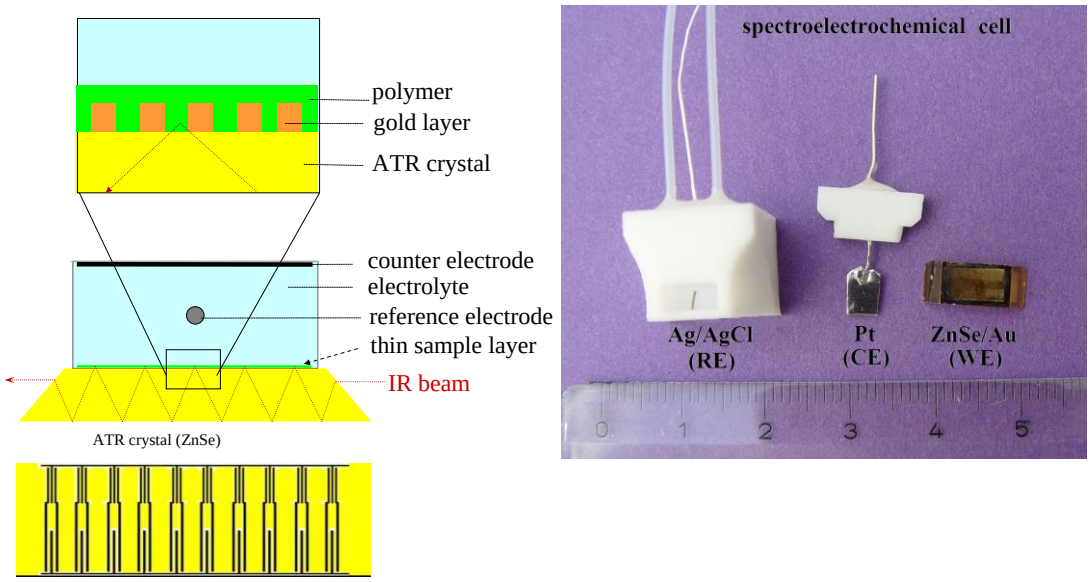

Figure 59. ATR-FTIR **s**pectroelectrochemical cell. Schematic view of cell and of Au interdigitated structure deposited on top of the ZnSe crystal (left) and disassembled cell (right).

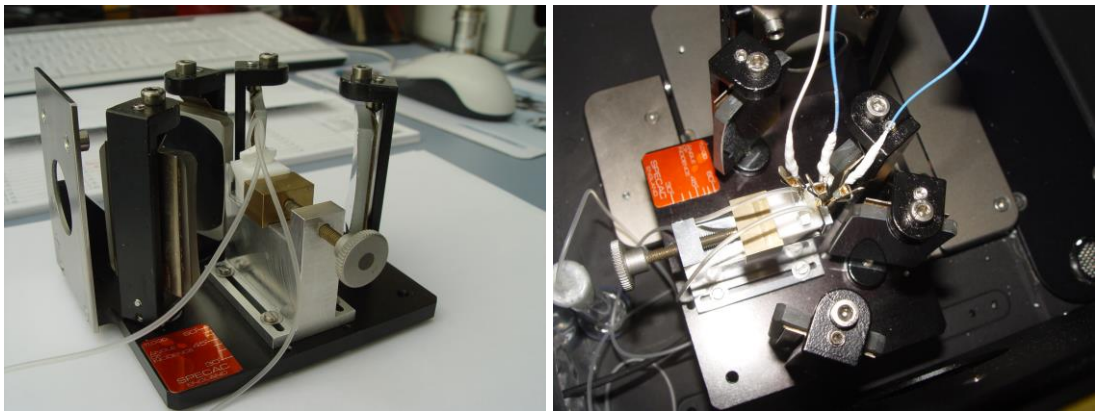

Figure 60. Pictures of the experimental setup. Reflection unit with spectroelectrochemical cell installed (left) and complete cell installed and connected to the potentiostat (right).

To assure a reasonable conductivity, but to maintain at the sample time optical transparency, the zinc selenide internal reflection element was covered with a fine gold interdigitated structure by photolithography. The gold layer had a thickness of 50 nm with an intermediate chromium layer with a thickness of 5 nm applied to improve the adhesion of the gold layer. To provide electrical connection to the potentiostat, a gold strip is pressed against the Au/ZnSe working electrode.

The polymer film can be deposited on the crystal by electropolymerization or by drop coating technique. The spectroelectrochemical cell is then assembled and mounted in the reflection unit of the FTIR spectrometer and the three electrodes are connected to a potentiostat. Pictures of the experimental setup are given in Figure 60.

3.2. Charge transport mechanism in polyanilines

The chemical structure of polyaniline is often given as a linear model with three oxidation states, shown in Figure 61. Leucoemeraldine base is the completely reduced form having only benzenoid rings, emeraldine base is the half-oxidized form having both benzenoid and quinoid ring and pernigraniline base is the completely oxidized form having only quinoidic nitrogen.

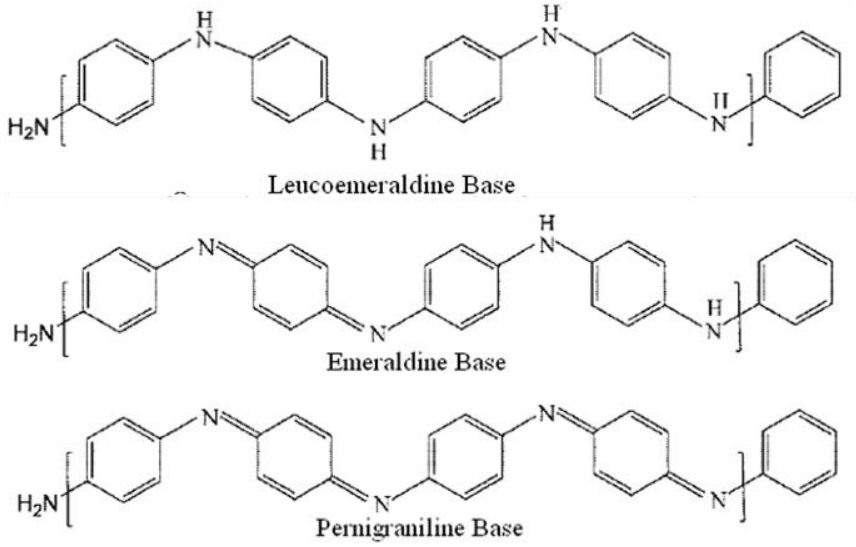

Figure 61. Structure of linear Pani and its different oxidation states.

Switching between the three different oxidation states of polyaniline can be realized by chemical or electrochemical doping/dedoping. The electrochemical doping has the advantage of a precise and reproducible tuning of the doping level by adjusting the electrode potential. In a typical cyclic voltammogram of polyaniline, two pairs of reversible redox peaks appear, the first one is assigned to the transformation of leucoemeraldine to emeraldine and the second one to further oxidation of emeraldine to pernigraniline.

Based on these structures, the well-accepted polaron-bipolaron model for polyaniline (Figure 62) is interpreted as follows: the polaron (radical cation) is the singly oxidized form of a polymer segment with spin s = 1/2 and two optical transitions and the bipolaron (dication) is a doubly oxidized form, which is diamagnetic and has one optical transition [186].

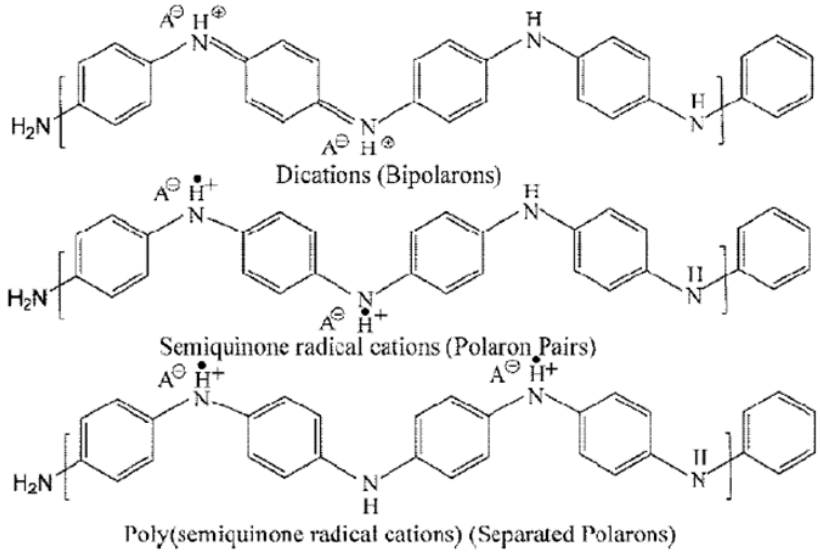

Figure 62. Structure of charged states in polyaniline.

It is generally accepted that polyaniline consists preferably by a linear arrangement of the monomers [187]. However, since the early studies on chemically synthesized Pani [188, 189] and the latter studies on electrochemically prepared Pani [190] it became obvious that phenazine rings have to be considered as part of the polymer chain. Phenazine rings may appear by intramolecular cyclization of branches that occur by aniline coupling reaction in the *ortho*-position, as seen in Figure 63. Therefore, the linear structure of the Pani is an idealized structure model and does not represent the real polymer structure.

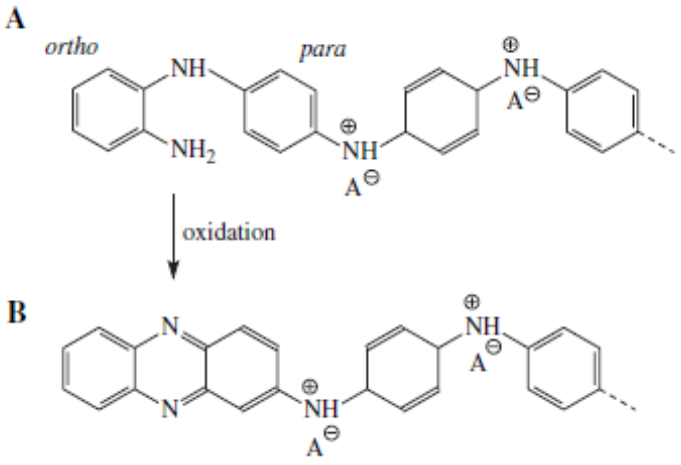

Figure 63. Formation of phenazine rings in the structure of polyaniline. (*Reprinted from Polymer 47 (2006) 8253-8262, J. Stejskal, I. Sapurina, M. Trchová, E. Konyushenko, P. Holler, The genesis of polyaniline nanotubes, Copyright (2006), with permission from Elsevier*)

.
The existence of phenazine structural units has been identified by the appearance of characteristic FTIR bands at 1623, 1414, 1208, 1144, 1136, 1108 cm^{-1} and Raman bands at 1645–1630, 1420–1400, 1380–1365, ~575, and ~415 cm^{-1} [141,191,192]. It has been also shown that phenazine-like units are involved in the formation of Pani nanotubes and nanofibers [141,193-195] so it is obvious that phenazine units play an important role in defining the structure, morphology and properties of Pani.

3.2.1. Charged states in electrochemically prepared polyanilines and copolymers

In our work we have investigated the role of phenazine-like units in the formation and stabilization of charged states in polyaniline using *in situ* ATR-FTIR spectroelectrochemistry. To obtain a high proportion of phenazine-like unit in the structure of polyaniline we have electrochemically prepared copolymers of aniline with different ratios of phenosafranine (Phsafr). The chemical structure of phenosafranine and the obtained copolymer are given in Figure 64.

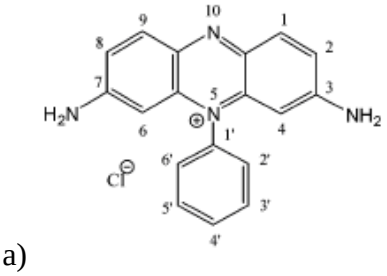

a)

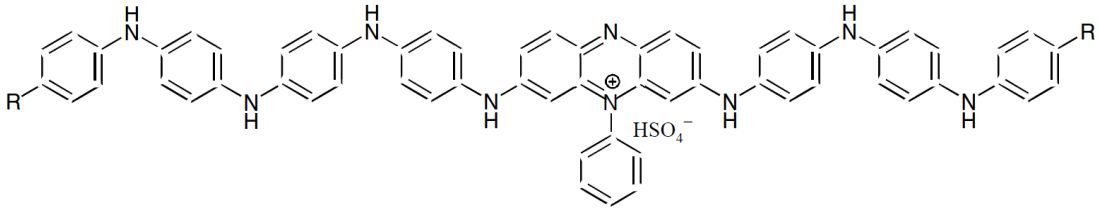

b)

Figure 64. Chemical structure of Phsafr (a) and An-Phsafr copolymer (b).

Electrochemical measurements were carried out using a PG 284 potentiostat/galvanostat (HEKA Electronic, Lambrecht, Germany). Electrochemical synthesis of polyaniline and copolymers was carried out by cyclic voltammetry in a conventional three-electrode one-compartment glass cell, using a Au band as working electrode, a Pt wire as counter electrode and a silver-silver chloride pseudoreference electrode. Polyaniline was prepared from an aqueous solution of 50 mM aniline in 0.1 M H_2SO_4 with 0.01 M sodium p-toluenesulfonate. Three different copolymers (Pani-PPS1, Pani-PPS2 and Pani-PPS3) were prepared similarly, keeping the concentration of aniline constant at 50 mM and varying the concentration of phenosafranine from 1 mM to 5 mM and 20 mM. To initiate the polymerization the potential

was swept from 0 to 1.0 V in the first scan. Afterwards, to allow the homo- and copolymer film growth, the anodic limit was lowered to 0.5 V and the potential was cycled between -0.5 and 0.5 V for the next 20 scans at a scan rate of 25 mV/s. Polyphenosafranine films (PPS) were electrochemically prepared from a 5 mM phenosafranine solution in supporting electrolyte by potential cycling between -0.5 and 1.2 V. All solutions were deaerated with nitrogen 10 min prior to the electrochemical measurements. The polymer films obtained potentiodynamically were thoroughly rinsed in monomer free electrolyte solution and carefully dried. For ATR-FTIR studies the polymers were dissolved in dimethyl sulfoxide.

Cyclic voltammograms obtained during electrochemical polymerization of phenosafranine, aniline and their copolymer are given in Figure 65.

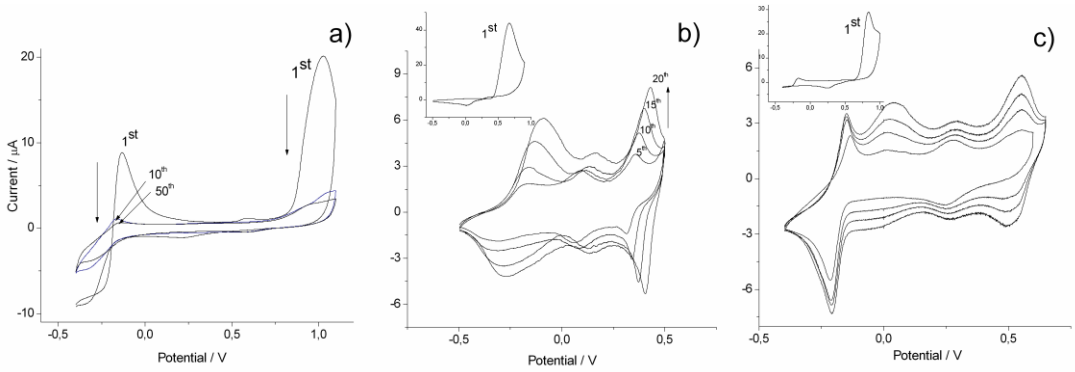

Figure 65. Cyclic voltammograms on gold electrode during oxidation of 5 mM Phsafr (a) 50 mM An (b) and 50 mM An + 5 mM Phsafr (c) in 0.1 M sulfuric acid and 0.01 M sodium p-toluenesulfonate, scan rate 25 mV s^{-1}.

It can be observed that the cyclic voltammogram recorded for electropolymerization of aniline in the presence of phenosafranine has an additional reversible peak at ca. -0.15 V, which is close to the potential of the reversible peak for phenosafranine and points to the copolymerization of aniline with phenosafranine.

Ex situ ATR-FTIR spectra of commercial emeraldine base and of electrochemically synthesized polyaniline and aniline-phenosafranine copolymer are given in Figure 66. The major vibrations found in Pani and copolymers correspond to those from emeraldine base. However, there are some weak intensity peaks or shoulders, that appear only and Pani and copolymers and not in EB. A key vibration for the structure of Pani and copolymers, which cannot be seen in EB is a shoulder at 1537 cm^{-1} in the spectrum of Pani which shifts to lower wavenumbers in the copolymers. A similar band with medium intensity appears at 1534 cm^{-1} in the spectrum of PPS. This vibration has been also found in aromatic diamine polymers, such as poly(o-phenylendiamine), obtained by electrochemical polymerization and it was attributed to the C=N and C=C stretching vibrations in the phenazine ring [200,201]. In the same time, the band at ca. 1530 cm^{-1} also appears in phenosafranine, pyridinium salts, 1-(4-pyridyl) pyridinium chloride hydrochloride, phenazine methosulfate and safranine O, which have a central charged nitrogen atom in their structures, but it is shifted in pyridine and phenazine to ca. 1510 cm^{-1} [199,202] We propose that this peak can be attributed to the –$C=N^{+}$– stretching vibration in a phenosafranine unit in the Pani structure.

Another proof about the branched structure of the polymers relies in the C–H in-plane and out-of-plane deformation vibrations of 1,2,4-trisubstituted benzene ring. A summary of the vibrational bands corresponding to phenazine / phenosafranine units is given in Table 21, however, since the C=N and C–N stretching vibrations of aromatic amines appear at closed wavenumbers in both linear polyaniline and phenazine it is difficult to make a clear distinction between them. These findings have been explained by the presence of phenazine / phenosafranine units in the structure of electrochemically synthesized polymers.

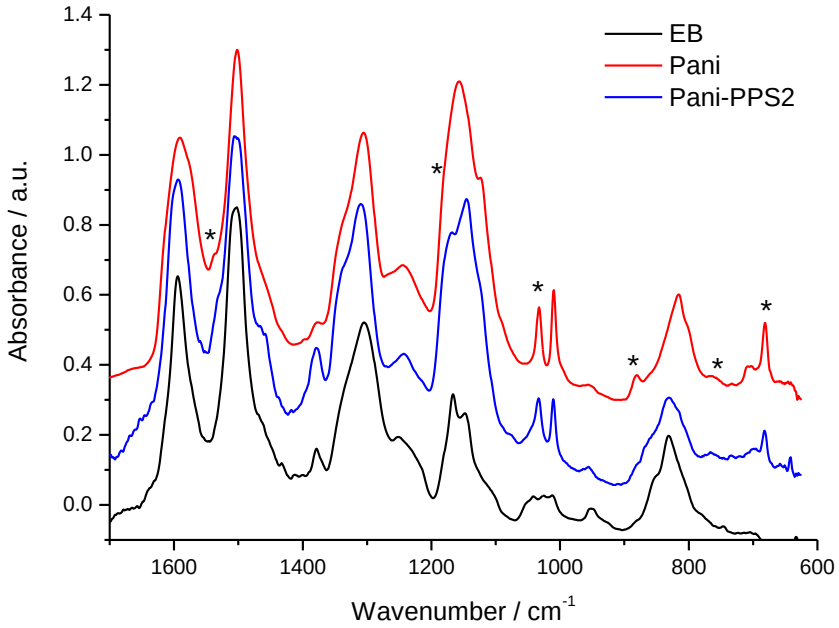

Figure 66. ATR-FTIR spectra of emeraldine base, polyaniline and aniline-phenosafranine copolymer.

The obtained results suggest that Pani and its copolymers with phenosafranine have a crosslinked structure, consisting not only of closed phenazine rings, but a combination of linear and phenazine-like units, according to the structure proposed in Figure 64(b).

Table 21. FTIR bands of EB, Pani, Pani-PPS1, Pani-PPS2, Pani-PPS3 and PPS.

EB	Pani	Pani-PPS1	Pani-PPS2	Pani-PPS3	PPS	Assignment [196-206]
a	**1537sh**	**1535sh**	**1532sh**	**1532sh**	**1534s**	***ν(C=N), ν(C=C) in Phsafr***
1464sh[1]	1454sh[1,2]	1454sh[1,2]	1458sh[1,2]	1454sh[1,2]	1455s[2]	[1] ν(C=C) and ν(C=N) or [2] *ν(C=N) in Phz*
1378w[1]	1378w[1,2]	1382w[1,2]	1378[1,2]	1380w[1,2]	1375m[2]	[1]ν(C–N) in QBQ or [2]*ν(C=N) in Phz*
1251w,b[1]	1245w,b[1,2]	1245w,b[1,2]	1243w,b[1,2]	1249w,b[1,2]	1240w[2]	[1] ν(C–N) in BBB or [2] *ν(C–N) in Phz*
a	**1179sh,vw**	**1170sh**	**1169s,sh**	**1182sh**	**1182m-s**	***δ(C–H) in Phsafr***
a	**-**	**1131m,sh**	**-**	**1131m,sh**	**1132m-s**	***δ(C–H) in Phsafr***
950w[1]	957w[1,2]	957w[1,2]	955w[1,2]	951w[1,2]	952w[1,2]	[1]ring def or [2]*δ(C–H) in Phz*
a	**880w**	**880w**	**880w,sh**	**880w**	**880w**	**γ(C–H) in 1,2,4-trisubst B ring (1H)**
a	-	-	-	869w,sh	871w,sh	γ(C–H) in 1,2,4,5-tetrasubst ring (1H)
					842m	*skeletal vibr of Phz*
a	**766w**	**769w**	**767w**	**767w**	**a**	**γ(C–H) in 1,2,4-trisubst ring (2H)**
					752w	*γ(C–H) in Phz*
a	**681m**	**681m**	**682m**	**681m**	**682w,sh**	**γ(C–H) 1,2,4-trisubst ring (2H)**

ν, stretching; δ, in-plane bending; γ, out-of-plane bending;
s, strong; m, medium, w, weak; sh, shoulder; b, broad;
a, absent; B, benzene ring; Q, quinoid ring; SQ; Phz, phenazine; Phsaf, phenosafranine.

The *in situ* ATR-FTIR measurements were performed with the attenuated total reflection (ATR) technique, using a BRUKER IFS 66v spectrometer working with a DTGS detector at room temperature. Polymer films were prepared on the ZnSe-Au working electrode by drop casting from dimethyl sulfoxide solution, followed by solvent evaporation. The potentials were controlled with a HEKA PG 284 potentiostat/galvanostat. The cyclic voltammograms were recorded at low scan rate (1 mV s^{-1}) in 0.1 M H_2SO_4 – 0.01 M sodium *p*-toluenesulfonate solution, purged for 10 minutes with nitrogen prior to the determinations. FTIR spectra with a resolution of 4 cm^{-1} and 100 accumulated interferograms were measured in dependence of the applied potential and are given in Figure 67 for Pani and its copolymers.

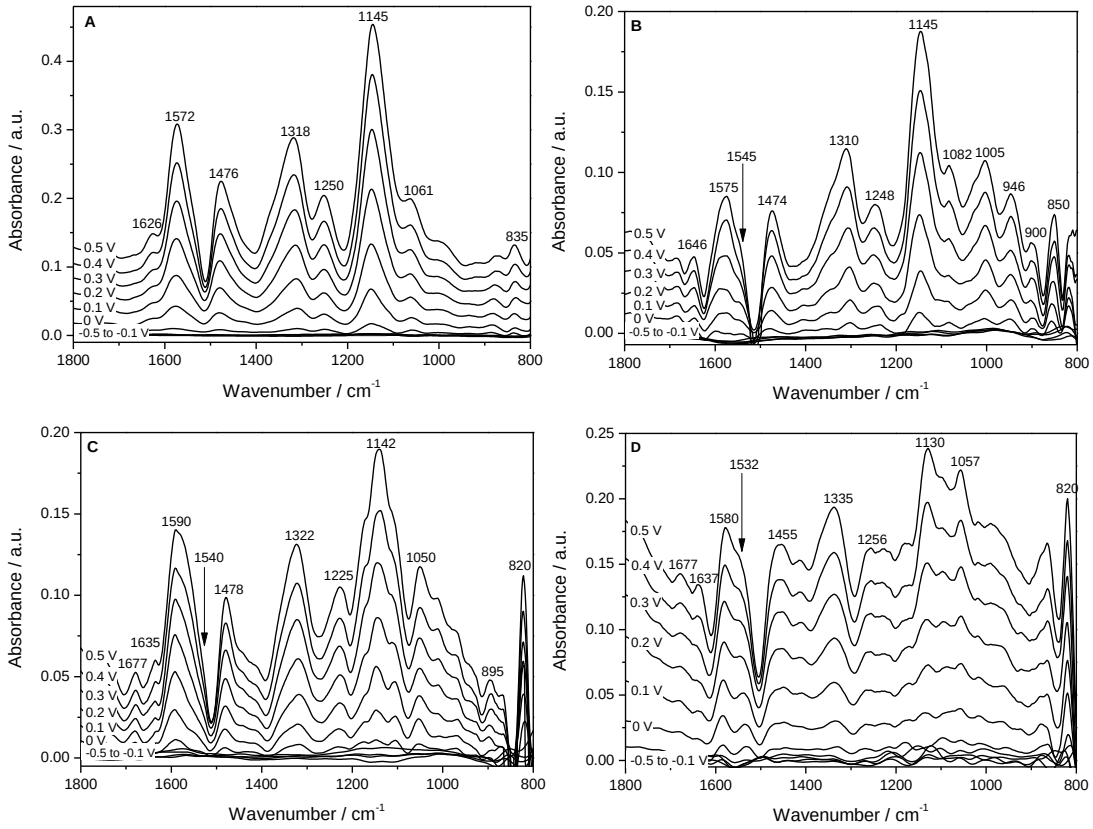

Figure 67. *In situ* ATR-FTIR spectra during oxidation of Pani (a); Pani-PPS1 (b); Pani-PPS2 (c) and Pani-PPS3 (d) between -0.5 and 0.5 V with reference state at -0.5 V.

The main changes in the *in situ* spectra induced by doping during electrochemical oxidation are the decrease of the vibration bands from 1600, 1510, 1200 and 814 cm^{-1} together with the increase of new vibrations at 1572, 1476, 1318, 1250 and 1145 cm^{-1} for both Pani and its copolymers with phenosafranine.

The decrease and of the vibrations at 1510 cm^{-1} attributed to the C=C stretching vibration and at 814 cm^{-1} corresponding to C–H vibration in 1,4-substituted benzene ring is equivalent to a loss of the benzenoid ring structure which is transformed during oxidation into semiquinoid or quinoid structure.

The appearance of new vibrations at 1572, 1476, 1318 and 1145 cm^{-1} in Pani and shifted to slightly different wavenumbers in copolymers are usually related to the transition to a semiquinoid structure [205-208]. The vibration band at 1250 cm^{-1} is often attributed to the polaron lattice structure [128,129,206,209-211] based on the analogy with Raman spectroscopic studies, which showed the presence of a Raman band around 1250 cm^{-1} attributed to the C–$N^{\bullet+}$ stretching mode in the semiquinone radical cations [204,212].

The *in situ* spectra of copolymers Pani-PPS1, Pani-PPS2 and Pani-PPS3 show additionally a broadening of the vibration at 1575 cm^{-1} which is not obvious in the *in situ* spectra of Pani, probably because it is hidden by the strong absorption at 1572 cm^{-1}. This band has been also observed at 1530 cm^{-1} in the *in situ* spectra of PPS as well as in the ex situ spectra of the polymers around 1532-1537 cm^{-1} and could be related to the increase of the quinoidic character of the phenosafranine units in the copolymers. As the ratio of phenosafranine units in the copolymers ratio increases, the band at 1572 cm^{-1} splits in two distinct vibrations at 1580 and 1532 cm^{-1}.

By comparing the potential dependency of IR bands and ESR signal it has been established that IR bands reach their maxima at higher potentials than the ESR signal (Figure 68(a)), therefore they cannot be attributed to the formation of polarons. This points to the formation of diamagnetic species such as polaron pairs or π-dimers after polaron formation in the polymer structures. On the other hands, the potential dependencies of IR band at 1535 cm^{-1} and of NIR band at 1300 nm are in close agreement (Figure 68(b)). As the band at 1535 cm^{-1} was associated with the phenazine units in the polymer / copolymer structures, we propose that the π-dimers are stabilized on the linear segments of the polymer chains linked to the phenazine-like units. The π-dimer is formed as a face-to-face complex of two polarons interacting through their π-orbitals provided by planar structure of the phenazine segments of two polymer chains.

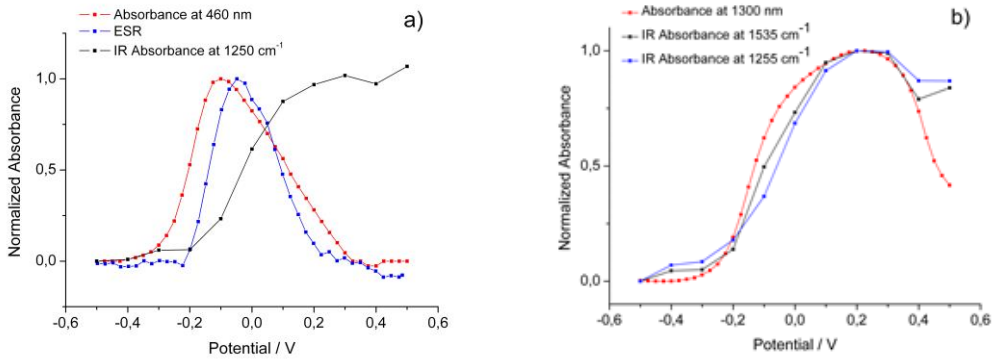

Figure 68. Comparison of UV-Vis-NIR absorbance, selected IR absorbance and ESR signal intensity during oxidation of: Pani (a) and Pani-PPS3 (b).

At higher oxidation levels two new peaks appear at 1628 and 1375 cm^{-1} which start to increase from 0.3 V up to the reversal potential of 0.5 V, then decrease in the backward scan

and disappear at 0 V. The band at 1628 cm^{-1} is attributed to a fully quinoid structure [205-208,213]. The band at 1375 cm^{-1} is attributed to the ring=N=ring mode in the quinoid form of the polymer. As shown in a previous work [203], the UV-Vis-NIR spectra of the polyaniline at high oxidation level present a peak at 620 nm, which corresponds to a π-π*-transition of the diimine groups in the polymer [214] and can be associated to the bipolaron structures of polyaniline. The potential dependence of the IR peaks at ca. 1630 and 1375 cm^{-1} in the spectra of Pani coincides with the potential dependence of the absorption peak at 620 nm. Therefore, these IR peaks are attributed to a bipolaron structure in Pani at high potentials.

3.2.2. Charged states in "linear" polyanilines

It has been shown by FTIR spectroscopy, that even in commercially available emeraldines small amounts of phenazine units are present [215] and branching of the polymer chain increases with the increasing of the weight average molecular weight of such emeraldines.

In our work we have investigated the formation of charge carriers during p-doping in so-called "linear" emeraldines by *in situ* ATR-FTIR spectroelectrochemistry pointing to the role of phenazine structure in the stabilization of charged states.

We have used commercially available emeraldine base with different average molecular weights (average Mw ≈ 5,000; 50,000 and 300,000 Aldrich) and emeraldine salt (average Mw > 15,000 Aldrich). The polymer powders were dissolved in dimethyl sulfoxide (puriss., Aldrich) and deposited on the ATR crystal by drop coating, followed by solvent evaporation under nitrogen flow. The obtained polymer film are denoted as EB1, EB2, EB3, and ES, respectively. The polymer films were initially equilibrated in the spectroelectrochemical cell containing the supporting electrolyte solution (0.1 M sulfuric acid and 0.01 M sodium p-toluenesulfonate) at the starting potential of -0.5 V and a spectrum was taken for reference. Then, 22 IR spectra were collected during one cyclic voltammogram measured at a scan rate of 4 mV/s, each spectrum covering a range of about 80 mV in the potential scan.

Examples of *in situ* spectra obtained for EB1 and EB3 are given in Figure 69. The changes in the *in situ* spectra can be divided in two regions: the near infrared region, between 7000 and 1800 cm^{-1} where a broad band appears with maxima around 5000 cm^{-1} characteristic for the intermediate oxidized metallic form of Pani and the mid infrared region, between 1700 and 700 cm^{-1} where four infrared active vibration (IRAV) modes are increasing at around 1570, 1490, 1300 and 1150 cm^{-1}. These IRAV modes are a result of local symmetry breaking caused by the introduction of charge carriers onto the backbone of a conjugated polymer and their intensity is proportional to charge carrier density, or the doping level.

In the same time with the increase of the IRAV bands, four major peaks are decreasing around 1600, 1500, 1200 and 814 cm^{-1} during the oxidation of polyaniline structures. A more detailed overview of the potential dependence of these band is given in Figure 70 and their assignment is presented Table 22.

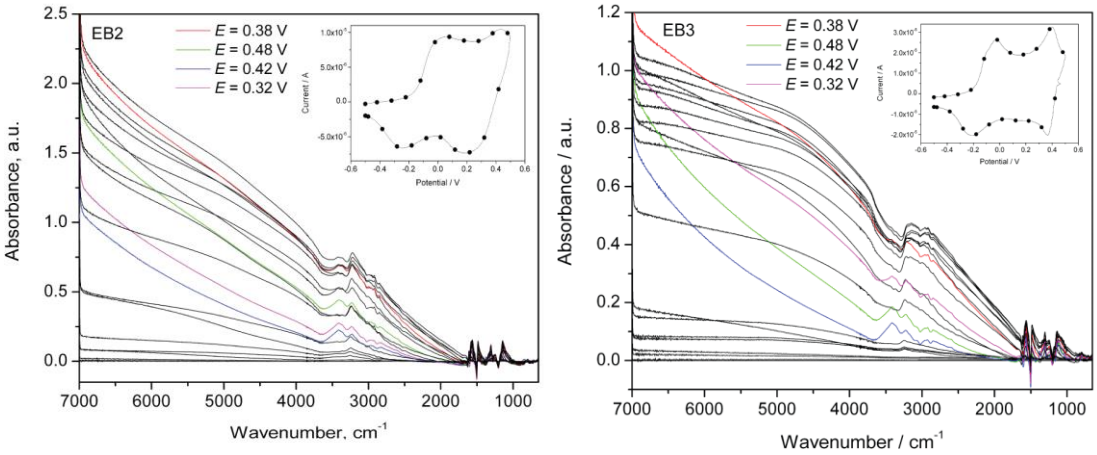

Figure 69. *In situ* ATR-FTIR spectra of different PANI structures upon charging. Inset shows the simultaneous CVs with triggers marked with points.

The decreasing peaks in the *in situ* FTIR spectra are the correspondent of the vibrations of emeraldine bases observed in the ex situ FTIR spectra at 1600, 1500, 1300 and 820 cm^{-1}. The decrease of the vibration bands around 1500 cm^{-1} attributed to the stretching mode of carbon-carbon covalent bond in benzene ring and of the vibration at 814 cm-[1| corresponding to the out-of-plane bending of carbon-hydrogen bond in 1,4-substituted benzene ring is consistent with a loss of the benzenoid ring structure, which is transferred into semiquinoid or quinoid ones. The decrease of the band around 1200 cm^{-1} corresponding to the C–N stretching in aromatic amines is indicative for the transformation of amino groups into imino groups upon oxidation of the polymer structures.

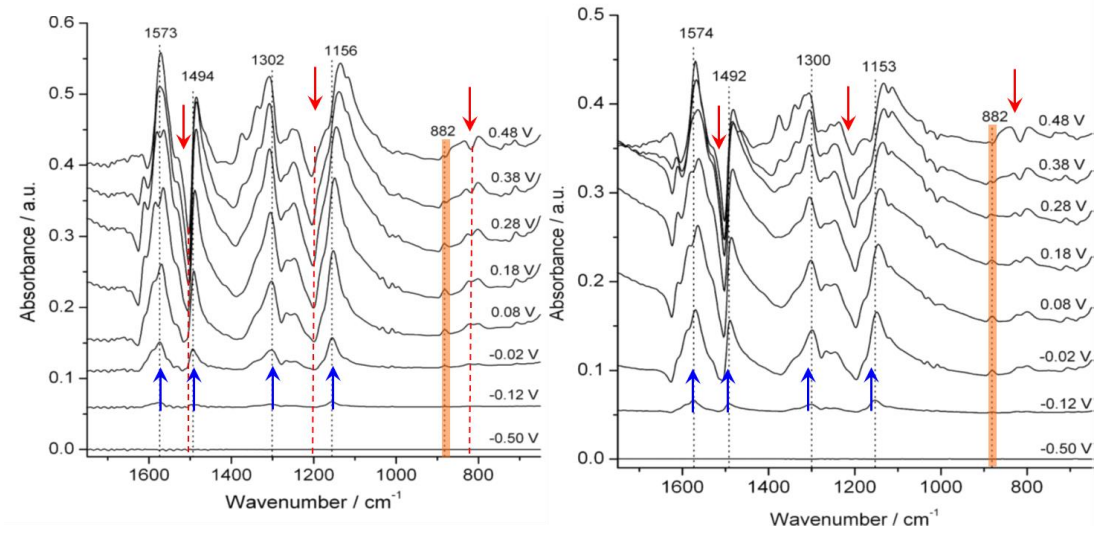

Figure 70. Mid infrared region of *in situ* ATR-FTIR spectra of different PANI structures upon charging, EB2 (left) and EB3 (right).

Table 22. Mid-IR region vibrations of *in situ* FTIR spectra of different PANI structures.

EB1	EB2	EB3	ES	Assignment [196, 204-212, 216-219]
1571	1573	1574	1571	ring stretching in SQ (↗ up to 0.3 V than ↘)
1481	1494	1492	1490	ring stretching in SQ (↗ up to 0.3 V than ↘)
1292	1302	1300	1297	ν (C-N) in SQ ring (↗ up to 0.3 V than ↘)
1151	1156	1153	1145	δ (C-H) in SQ or ν (HSO_4^-) (↗ up to 0.3 V than ↘)
882	882	882	878	γ (C-H) in 1,2,4-trisubstit B ring (2-substit phenazine ring) (↗ up to 0.3 V than ↘)
1598	1605	1604	1600	ν (C-C) in Q ring (↘ in the forward scan)
1502	1507	1506	1505	ν (C-C) in B ring (↘ in the forward scan)
1197	1197	1196	1193	ν (C-N) in aromatic amine (↘ in the forward scan)
814	818	816	810	γ (C-H) in 1,4 substit B ring (↘ in the forward scan)

. ν, stretching mode; δ, in-plane bending mode; γ, out-of-plane bending mode; B, benzene ring; Q, quinoid ring; SQ, semiquinoid structure. ↗ increasing peak intensity; ↘ decreasing peak intensity.

The potential dependence of the four IRAV bands in the mid infrared region is the same for all Pani structures under study. Two other vibrations found at 5000 and 880 cm^{-1} show a similar potential dependence. They all start to increase at potentials around −0.22 V and reach a maximum at around 0.28 V in the forward scan. In the backward scan they increase and again reach a maximum at around 0 V, according to Figure 71.

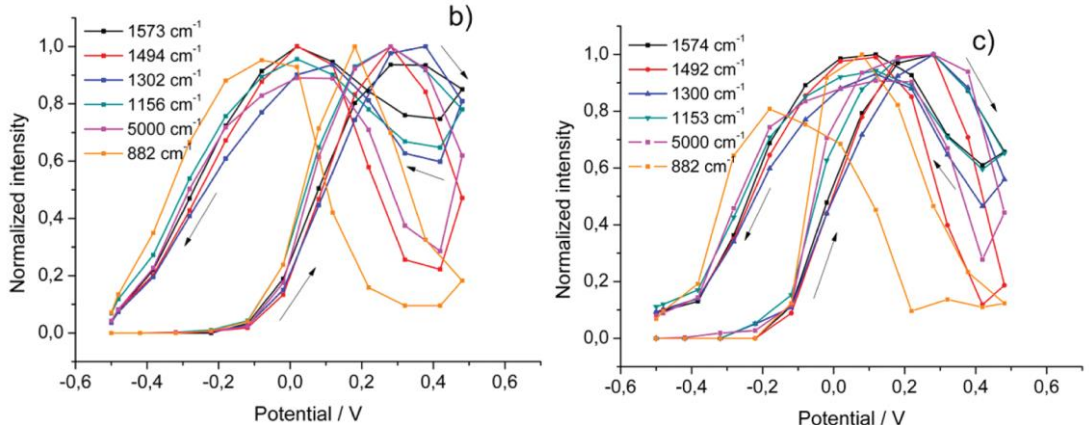

Figure 71. Potential dependence of semiquinoid bands and of the free charge carries band for the PANI structures EB2 (b) and EB3 (c).

The potential dependence of these bands has been compared to the potential dependence of the *in situ* electron spin resonance (ESR) signal which is attributed to polarons (Figure 72(a)). Because the two dependences does not coincide, it has been concluded that the semiquinoid bands at 1570, 1490, 1300 and 1150, usually attributed to the polaron lattice, correspond in

fact to the formation of spinless doubly charged species, such as π-dimers, which are face-to-face complexes of two polarons.

Additionally, the *in situ* spectra show the presence of a weak intensity vibration around 880 cm^{-1}, which was attributed in a previous IR study of polyaniline, phenazine polymer and aniline-phenazine copolymer to a 2-substituted phenazine ring [215]. Because the potential dependence of the band at 882 cm^{-1} which is associated with the branches in the polymer is similar to the potential dependence of the bands attributed to the π-dimer, it has been proposed that the π-dimers are stabilized at the phenazine-like units of the polymer chain.

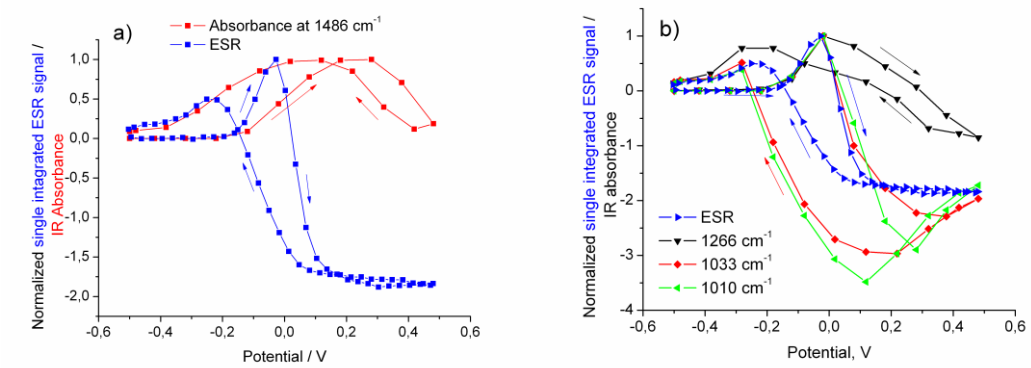

Figure 72. Potential dependence of spectroscopic data of Pani-EB3 during doping / dedoping: single integrated ESR signal together with one selected semiquinoid IR band (a) and with polaronic bands at 1266, 1033 and 1010 cm^{-1} (b).

Moreover, it has been found that IR vibrations at 1266, 1033 and 1010 cm^{-1} start to increase at potentials above −0.22 V and have a similar potential dependence with the π-dimer bands at low oxidation levels, but they show a completely different potential dependency at high doping levels. The shape of the potential dependence of these bands matches that of the ESR signal (Figure 72(b)), therefore these bands could be ascribed to polarons.

The band at 1266 cm^{-1} is attributed to C–$N^{\bullet+}$ stretching in semiquinone radical cations in agreement with Raman spectroscopic studies, which showed a band at around 1250 cm^{-1} attributed to the polaron lattice structure [212,216]. The bands at 1010 and 1033 cm^{-1} could be ascribed to the C–H in-plane deformation vibration of 1,4-disubstituted or 1,2,4-trisubstituted benzene rings or 2-substituted phenazine ring. This demonstrates that polarons are stabilized on the linear polymer segments close to the branches by phenazine-like units in the polymer chains.

By going to higher oxidation levels, the polaron and π-dimer bands start to decrease because the semiquinoid structure is further oxidized to a quinoid structure. As a result, new bands are arising at 1630, 1375, 1338 and 1238 cm^{-1} in the *in situ* spectra. The band at 1630 cm^{-1} is assigned to the C=N stretching in quinoid rings and the bands at 1375 and 1338 cm^{-1} to C-N stretching in the neighbourhood of quinoid rings. These bands are observed to appear only after the first redox peak of Pani, they increase in intensity during the second redox peak (Figure 73) and correspond to the formation of bipolarons as protonated quinoid structures.

Additionally, a weak intensity IR vibration at 734 cm^{-1} attributed to in-plane-bending of C–H in phenazine ring shows the same potential dependence to that of bipolaronic bands, suggesting that bipolarons are also stabilized near the phenazine units.

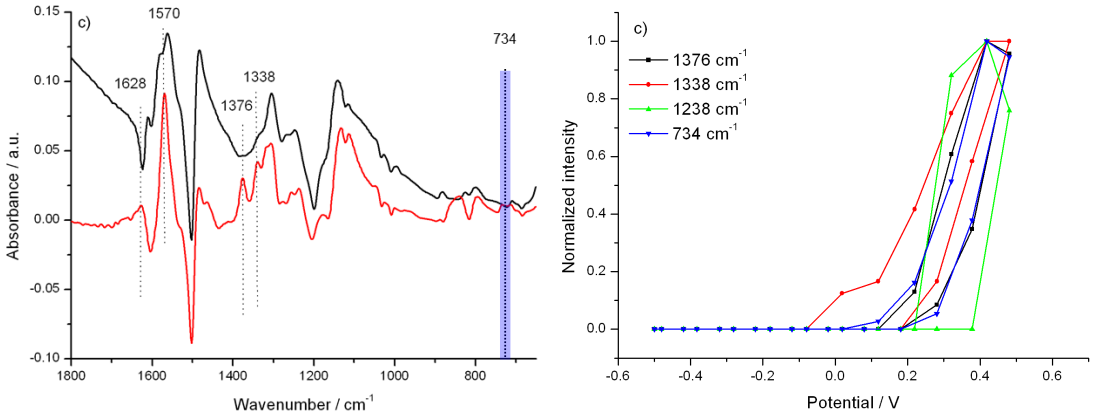

Figure 73. *In situ* FTIR spectra of EB3 after the first and the second redox peak (black and red line) and potential dependence of bipolaronic bands in EB3.

The potential dependence of bipolaronic bands is opposite to that of bands assigned to π-dimers. The π-dimer bands start to decrease above potentials of 0.28 V where the bipolaronic bands start to increase and reach again a maximum at 0 V in the backward scan, where the bipolaronic bands completely disappear. This allowed us to propose the following mechanism for the formation of charged states in polyaniline upon p-doping (Figure 74).

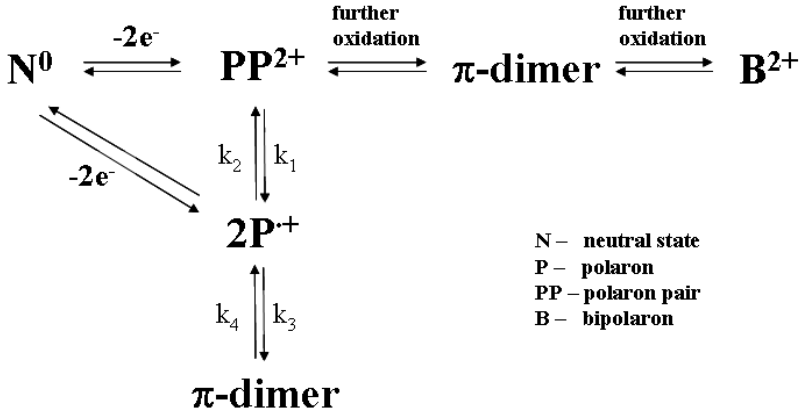

Figure 74. Scheme for formation of charged states upon electrochemical oxidation of polyaniline.

At the early stage of charge injection into the polymer a polaron pair is formed, which can dissociate into two polarons at higher potentials. Polarons and π-dimers are formed at the same potential. At that potential where the concentration of π-dimers is at its maximum no ESR signal is observed. This behaviour points to the fact that the polarons are converted into

π-dimers at higher oxidation level. The further p-doping of the PANI leads to the transfer of π-dimers into bipolarons.

In conclusion, the combined use of different *in situ* spectroelectrochemical methods allowed us to establish the complete reaction mechanism of the formation of charged states in Pani upon electrochemical doping.

3.3. Charge transport mechanism in polythiophenes

Polythiophene (PT) is a conjugated polymer intensively studied due to its environmental stability, good conduction properties and wide range of potential applications. It shows semiconducting properties in the neutral form and metallic conductivity in the p-doped form [220]. Polythiophene, like many other linear polyaromatic compounds, is insoluble in organic solvents due to its rigid backbone. A major challenge in the field of conducting polymers is to obtain materials with improved solubility and processability without affecting the electrical properties, i.e. conductivity.

For polymers like polythiophene one of the methods suggested for this purpose is the introduction of a substituent in the 3- and/or 4-position of the thiophene ring. High conductivities were obtained for electrochemically synthesized poly(3-methylthiophene) and poly(3-ethylthiophene) [221]. However, appropriate solubility in common organic solvents has been achieved only with an alkyl side chain of more than four carbon atoms [222]. In addition to improved solubility and crystallinity, the introduction of side chains in the 3- or 4-position also decreases the probability of defects during polymerization (2,4 linkages or α–β coupling) since at least one of the β position is already occupied [223]. Beside alkyl substituents, various other substituents were grafted in the 3-position of the thiophene ring, in order to achieve tailored properties.

Poly(3-alkylthiophenes) (P3AT) have been further functionalized by different chemical groups at the end of the alkyl chain in order to modify their solubility, their spatial arrangement and electrical properties. Such examples are thiophenes functionalized with ω-alkyl-phosphonic acid [224,225] and ω-alkyl-trichlorosilane groups [226] that have been successfully prepared and used in the formation of self-assembled monolayer with potential applications as protective coatings, sensors, electronic semiconductors or adhesive systems.

Poly(3-alkylthiophenes) functionalized with hydroxyl groups are valuable in obtaining immobilized enzymes for sensor systems. However, thiophene monomers with functionalized with hydroxyl groups can only be polymerized after the protection of the reactive –OH group by etherification or esterification. After polymer formation, the protected –OH group can be recovered by ether or ester cleavage via acidic or basic hydrolysis. This approach lead to the electropolymerization of 3-(2-methoxyethyl)thiophene [227] but gave no result for the homopolymerization of various esters of 2-(3-thienyl)ethanol [228], revealing the importance of the alkyl side chain. Recently, the electrochemical polymerization of 2-(3-thienyl)ethyl acetate has been reported at high monomer concentrations and relatively low electrode potentials [229]. One of the attractive properties of the ester-functionalized

polyalkylthiophenes is their good solubility in common organic solvents resulting in the casting of homogeneous, free-standing films [230].

Despite their interesting properties, the doping mechanism of ester-substituted polyalkylthiophenes was not investigated.

The doping process of polythiophene and poly(3-methylthiophene) has been investigated in detail. It has been shown that both chemical, electrochemical and photo-induced doping generally induces the same changes in the FTIR spectra: the appearance of very intense infrared active vibration (IRAV) bands, usually in the range between 1600 and 700 cm^{-1}, accompanied by broad IR absorption bands with maxima at higher energies (around 1500 to 5000 cm^{-1}) related to the formation of free charge carriers [231-236]. This behaviour was explained in terms of local breaking of the symmetry around the injected charge carrier, and transition from the aromatic to a quinoid structure, so that the polymer chain becomes highly polarized and some initially silent modes become infrared active. The IRAV bands are therefore related to the charge transport along the polymer chain and do not depend on the type of doping and on the nature of the dopant anion

In case of polythiophene four doping induced bands are observed at around 1330, 1200, 1120 and 1020 cm^{-1} [237-239]. Chemical and photo-induced doping of poly(3-methylthiophene) leads also to four doping induced bands at around 1308, 1203, 1165 and 976 cm^{-1}, comparable to the those obtained by electrochemical doping (1300, 1160, 1100 and 975 cm^{-1}) [231-233]. The electrochemical oxidation of poly(3-methylthiophene) in different solvent-electrolyte systems allowed to obtain evidence of the counterion diffusion into the polymer film, as shown by vibrations at 1075 cm^{-1} and 1060 cm^{-1}, originating from the incorporation of perchlorate, and respectively tetraflouroborate anions. A comparison between chemical and photo-induced doping of poly(3-methylthiophene) showed that in both cases the charge carrier configuration is similar and charge is stored predominantly in form of bipolarons which is equivalent to a quinoid like structure [231,232].

Poly(3,4-ethylenedioxithiophene) (PEDOT) was also subject to numerous studies regarding the doping/dedoping process. Upon electrochemical p-doping in different electrolytes, generally four new IRAV bands were found (1290, 1205-1189, 1090, 977 cm^{-1} in $TBAPF_6$), their position slightly depending on the electrolyte, due to small differences in the film structure [178]. The incorporation of the counterion (hexafluorophosphate) from the electrolyte is evident from the strong band at 839 cm^{-1}. *In situ* FTIR analysis also showed that the doping/dedoping process is reversible. If the film thickness exceeds 2 μm the process becomes partly irreversible. Another study presents a comparison between IRAV modes obtained during p- and n-doping of PEDOT films. IRAV bands intensities in n-doping are lower than those of p-doped polymer, indicating that a lower degree of n-doping compared with p-doping has been obtained. The p- and n-doping induced IRAV bands (1513, 1319, 1195, 1090, 1060 and 980 cm^{-1} for p-doping; 1285, 1245, 1195, 1090 and 1060 cm^{-1} for n-doping) are not identical, meaning that different electronic structures are formed by positive and negative charging [179].

3.3.1. Charged states in poly(3-alkylthiophenes)

3-methylthiophene (3MT) and 3-hexylthiophene (3HT) are intensively used starting monomers to obtain poly(3-alkylthiophenes) by copolymerization reaction with thiophene or thiophene derivatives. The copolymerization path is frequently used to combine desirable properties of two polymers, such as desired electrochromic properties and high electrical conductivities. It has been found that the copolymerization of 3-alkylthiophene derivatives leads to a higher thermal stability of doped P3ATs [240] which is a tremendous problem for their application [241]. The copolymer of 3MT and 3HT is a material which still has excellent solubility together with high electrical conductivity, even higher than the conductivity of p3HT [242], due to the presence of 3MT moieties which show an exceedingly high conductivity among the polythiophenes [243].

In our work we have investigated the influence of the random distribution of the long side alkyl chain of 3HT on the formation and stability of the charge carriers in a copolymer of 3MT and 3HT. The use of several *in situ* spectroelectrochemical techniques allowed us to detect both the paramagnetic and diamagnetic species formed during electrochemical p-doping of homo- and copolymers (p3MT, p3HT and p3MT-co-3HT).

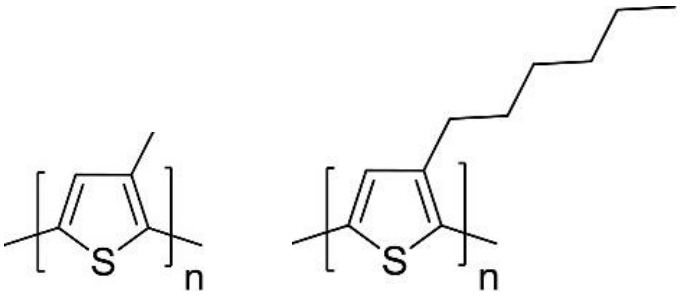

Figure 75. Chemical structure of p3MT and p3HT.

Homo- and copolymers have been prepared by electrochemical pulse deposition. This method implies that the electrode potential is increased from an initial value where no faradaic current is observed, up to a positive value where the oxidation of monomers take place and then lowered and maintained constant to allow growth of homo- and copolymer films but avoid their overoxidation. Homo- and copolymer films have been synthesized on ITO electrodes in acetonitrile solution with 0.1 M *n*-$BuNPF_6$ as supporting electrolyte at concentration of 20 mM 3MT and 40 mM 3HT. The electrochemical synthesis of the copolymer was achieved using a molar ratio of 3MT:3HT of 1:2, taking into account that the electrochemical oxidation of 3MT occurs at lower potential than that of 3 HT [242].

For *ex situ* FTIR measurements the polymer films obtained on ITO were carefully peeled off and transferred to the ZnSe internal reflection element. For *in situ* FTIR studies, the polymers were synthesized in the spectroelectrochemical cell on the ZnSe-Au working electrode and their p-doping behavior was studied in 0.1 M tetrabutylammonium-hexaflourophosphate (*n*-$BuNPF_6$) acetonitrile solution. *In situ* FTIR spectra were taken at equidistant time intervals during electropolymerization and also during the electrochemical p-doping.

An important characteristic of poly(3-alkylthiophenes) is regioregularity which denotes the percentage of stereoregular head-to-tail (HT) attachments of the alkyl side chains to the 3-position of the thiophene ring. It has been reported that FTIR studies can give information on the degree of regioregularity of polymer chains in P3ATs [244-246]. Side chains of adjacent rings in P3ATs can be in head to tail (HT) or in head to head (HH) conformation, resulting in four triad regioisomers: HT-HT, HT-HH, TT-HT, and TT-HH triad. P3ATs with only HT-HT triad (regioregular P3ATs) lead to a minimal steric hindrance and an extended π-conjugation length as a result of self-organization of P3AT main chains, whereas the HH or TT junctions result in spatially disordered polymer chains with limited conjugated segments [247].

For the qualitative analysis of the FTIR spectra of substituted polyalkylthiophenes two criteria have been proposed, namely the position of the aromatic C-H out-of-plane vibration [244,246] and the intensity ratio of the symmetric and antisymmetric ring stretch modes [245]. The main vibrations of electrochemically synthesized homo- and copolymer are given in Table 23 together with their assignments.

Table 23. Characteristic IR bands of p3MT, p3HT and p3MT-co3HT and their structural assignments.

Polymer	**p3MT**	**p3HT**	**p3MT-co-3HT**
aromatic C-H stretch	3059	3053	3053
aliphatic C-H stretch	2957, 2918, 2849	2951, 2918, 2850	2950, 2918, 2850
ring stretch	1503, 1468	1510, 1456	1510, 1456
$-CH_3$ def	1388	1372	1388
aromatic C-H out-of-plane	827	829	822
$-CH_3$ rock	-	723	716

According to the first criterion the band position of the aromatic C-H out-of-plane vibration is shifted to lower wavenumbers for regioregular P3ATs (820–822 cm^{-1}) and to higher wavenumbers for regiorandom P3ATs (827–829 cm^{-1}). For p3MT and p3HT this band is situated at 827 and 829 cm^{-1} respectively, which points to a random structure. For p3MT-co-3HT the same band appears at 822 cm^{-1} indicating a more ordered polymer chain. A measure of the conjugation length in the polymer backbone is given by the ration I_{sym}/I_{asym}, lower ratios being associated with longer conjugated segments. The calculated ratios are 4.8 for p3HT and about half of this value for p3MT (2.6) and p3MT-co-3HT (2.2). These results are consistent with a higher conjugation length of the copolymer in accordance with its regioregular structure. In contrast, the FTIR data suggest that the parent homopolymers p3HT and p3MT have a regiorandom structure.

In situ ATR-FTIR spectra taken during the copolymerization by the potential pulse method are given in Figure 76. A spectrum taken before the start of the electrochemical polymerization for the cell containing the monomers solution was used as a reference spectrum. Thus, only changes induced by the copolymer film deposition on the surface of the electrode and by its simultaneous doping can be seen.

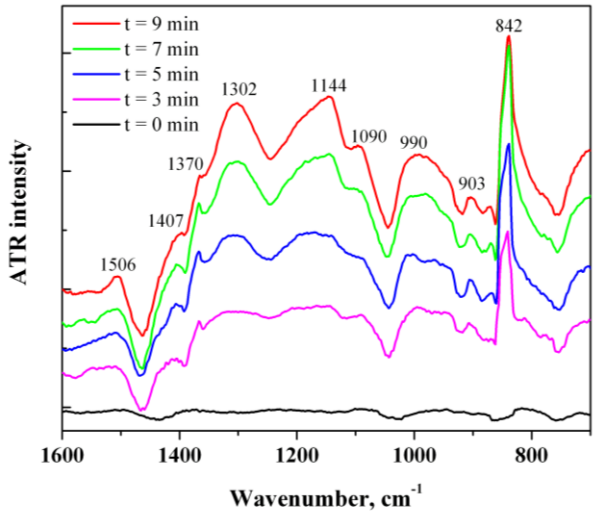

Figure 76. *In situ* ATR-FTIR spectra during copolymerization of 20 mM 3MT with 40 mM 3HT in 0.1 M *n*-BuNPF_6 acetonitrile solution.

The shape of *in situ* FTIR spectra is characterized by some broad absorption bands which develop in three absorption peaks centered at 1302, 1144 and 990 cm^{-1} with bandwidth larger than 100 cm^{-1}. These are doping induced bands, similar to those observed for polythiophene [237-239] and poly(3-methylthiophene) [231-233]. Additionally, a sharp peak is at 842 cm^{-1} is ascribed to the PF_6^- anions incorporated into the copolymer film to compensate the positive charge created during the oxidative polymerization. Beside the doping induced bands, some additional bands have been attributed to the formed copolymer film. Vibrations at 1506 and 1407 cm^{-1} originate from the thiophene ring stretching and vibrations at 1370, 990 cm^{-1} are assigned to the side alkyl chain [231-233,235].

In situ ATR-FTIR measurements during p-doping of p3MT-co-3HT show a typical profile for P3ATs, characterized by the development of two distinct vibrational patterns: the range 1600-700 cm^{-1} where some very intense infrared active vibration (IRAV) bands appear and that above 1600 cm^{-1} where the electronic absorption of free charge carriers is found with a maximum around 5000 cm^{-1}. The FTIR spectra also give evidence about the inclusion of the counterion PF_6^- indicated by a very intense peak at 842 cm^{-1}. The results of FTIR spectroelectrochemical study point to a high concentration of the positive charge carriers, but gives no information about their nature, which is to be clarified by simultaneous ESR and UV-Vis NIR spectroelectrochemistry.

Characteristic examples of ESR and UV-Vis-NIR *in situ* spectra of p3MT-co3HT are given in Figure 77. The ESR signal starts to increase in the forward scan and reaches a maximum at a potential close to the anodic peak from the cyclic voltammogram, corresponding to the highest concentration of polarons. Then, both current and ESR signal start to decrease, indicating that a fraction of polarons are transformed into diamagnetic species (polaron pairs or bipolarons). In the same time with the ESR signal, the optical spectra show two absorption bands at 850 and 1650 nm corresponding to polarons. As the ESR signal decreases, the UV-Vis absorptions further increase and shift to higher energies. These two bands are more

intense than the polaronic bands and correspond to the formation of spinless polaron pairs with a similar absorption pattern to that of polaron. Therefore only the simultaneous use of both the ESR and the UV-Vis-NIR spectroscopy enables the differentiation of polarons (paramagnetic) and polaron pairs (diamagnetic).

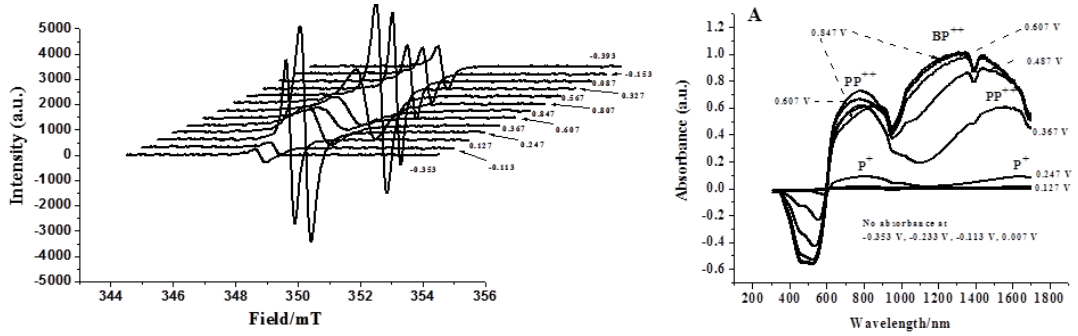

Figure 77. *In situ* ESR (left) and UV-Vis-NIR (right) spectra of p3MT-co3HT.

In addition, by going to higher potentials, a single broad absorption band is formed at 1310 nm, in the middle of the two polaronic transitions, which is attributed to the formation of bipolarons. Thus in this potential range both the polaron pair and the bipolaron are coexistent and being in equilibrium with the polaron. The development of the optical absorption signal consisting of the three absorption peaks (polaron pair and bipolaron) together with a decrease of the ESR signal indicates the transformation of polarons into polaron pairs and bipolarons, as found in previous studies on the p-doping of 3MT [248,249]. At higher doping levels, literature data indicate that the predominant charge carriers in polythiophene and p3MT films are expected to be bipolarons [250-253] which is consistent with our results obtained for the copolymer of 3MT and 3HT.

3.3.2. Charged states in functionalized poly(3-alkylthiophenes)

The aim of our studies was to investigate the effect of the functional group attached to the alkyl chain (acetyl, hydroxyl and a combination of both functional groups) on the *p*-doping behavior of these conjugated polymers, using a combination of *in situ* spectroelectrochemical techniques, such as ATR-FTIR and ESR-UV-Vis-NIR spectroelectrochemistry.

Spectroelectrochemical measurements were carried out on three polymers with the structures given in Figure 78. The first structure poly[2-(3-thienyl)ethyl acetate] (PTEtAc) was chemically synthesized by polymerization of the corresponding monomer and contains an acetyl functional group attached to the alkyl chain. The third structure, poly[2-(3-thienyl)ethanol] (PTEtOH) has been obtained by complete hydrolysis of the parent polymer and contains a hydroxyl group attached to the alkyl chain. The second structure, PTEtAcOH was obtained by partial hydrolysis and contains both acetyl and hydroxyl functional groups

and may be regarded as a copolymer of PTEtAc and PTEtOH. This modification altered the solubility and the spatial arrangement of the polymers in the resultant films.

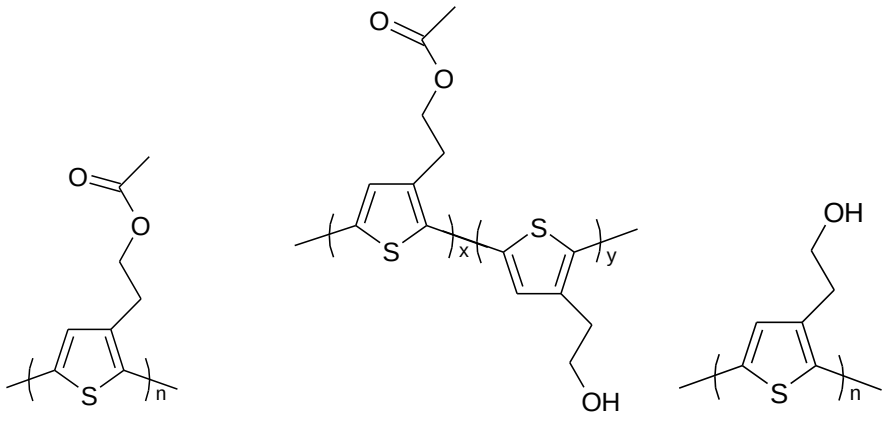

PTEtAc PTEtAcOH PTEtOH

Figure 78. Chemical structure of the studied polyalkylthiophene derivatives.

Electrochemical and spectroelectrochemical measurements were carried out for PTEtAc and PTEtAcOH films deposited on the working electrode surface by drop casting from a dichloromethane solution. PTEtOH film was prepared by drop casting from a dimethylsulfoxide solution and dried at 50°C. The electrolyte was a 0.1 M tetrabutylammonium-hexaflourophosphate ($TBAPF_6$) – acetonitrile solution, purged with nitrogen.

The cyclic voltammograms of the three conducting polymer, shown in Figure 79, reveal a stable and reversible redox behaviour for both PTEtAc and the copolymer PTEtAcOH, characterized by a pair of oxidation/reduction peaks at 0.78 / 0.52 V and respectively 0.89 / 0.70 V which remain stable during consecutive cycling. The completely hydrolyzed polymer, PTEtOH, shows a loss of the redox activity during consecutive scans, explained by the presence of interchain hydrogen bonds which are responsible for a cross-linked structure, which obstructs the counter-ions from leaving the polymer film during the reduction step. In the following doping-dedoping cycles a lower number of sites are available for oxidation/reduction and the redox activity of the polymer film decreases gradually.

All the three structures showed electrochromic behaviour, during *p*-doping they changed their colour from orange to green at lower doping levels and to dark blue at higher doping levels.

The presence and nature of hydrogen bonds in the structure of both PTEtAcOH and PTEtOH was confirmed by ATR-FTIR spectroscopy. Generally, hydrogen bonds affect the shape and position of the hydroxyl stretching vibration, producing a significant band broadening and a shift to lower wavenumbers. This effects can be observed in the spectra of PTEtOH, were the OH stretching vibration appears as a broad band at 3300 cm^{-1}, indicating strong intermolecular interaction between neighbouring polymer chains, rather than intramolecular

bond within the same chain. The spectra of PTEtAcOH shows the presence of both functional groups, acetyl and hydroxyl, as indicated by the carbonyl group absorption at 1738 cm^{-1} and the OH stretching vibration at 3460 cm^{-1}. The hydrogen bonds are weaker than for PTEtOH, since the band position is shifted to higher wavenumbers. Also, there is no proof for associations between the hydroxyl and carbonyl group, since the carbonyl band position is the same for PTEtAcOH and PTEtAc

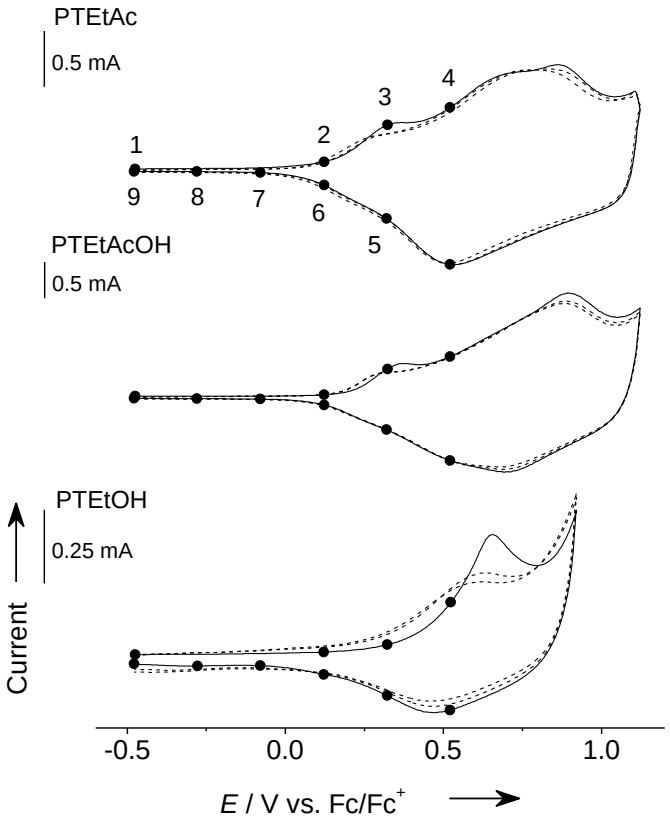

Figure 79. Cyclic voltammograms of PTEtAc, PTEtAcOH and PTEtOH films on a Pt working electrode in a $TBAPF_6$ (0.1 M) – acetonitrile solution at 100 mV s^{-1}.

The IRAV bands start to appear around 0.12 V for PTEtAc and at 0.22 V for PTEtAcOH, as seen in Figure 80, which corresponds to the potential values where the Faradaic current starts to increase in the cyclic voltammograms. The changes observed in the *in situ IR* spectra correspond to the fading of the bands corresponding to the neutral state, as seen by decreasing IR vibrations at 1448, 1378, 1245, 1040 and 847 cm^{-1}, accompanied by the appearance of some new IR bands with intensities increasing in dependence of the applied electrode potential.

The new absorption pattern observed during oxidation is characterized by four major IR absorptions, with bandwidth larger than 100 cm^{-1}, and relative position depending on the polymer structure. The pattern is quite similar for PTEtAc and PTEtAcOH, which show

increasing IR bands at 1396, 1330, 1150 and 970 cm^{-1} and shifted for PTEtOH at 1394, 1340, 1130 and 990 cm^{-1}. The band at 1150 cm^{-1} is accompanied by two shoulders at 1204 and 1090 cm^{-1}, which are more pronounced at lower doping levels and tend to merge with the main band as the doping level increases. These doping induced bands are very similar to those observed for the doping of polythiophene [235-237] and poly(3-methylthiophene) [231-233]. The doping induced changes are reversible, i.e. they disappear during de-doping, for PTEtAc and PTEtAcOH but not for PTEtOH. During the reversal scan the intensity of the IRAV bands in PTEtOH does not completely decrease with the potential and we propose that this behaviour is due to the "trapping" of the charge inside the polymer chains cross-linked by hydrogen bridges.

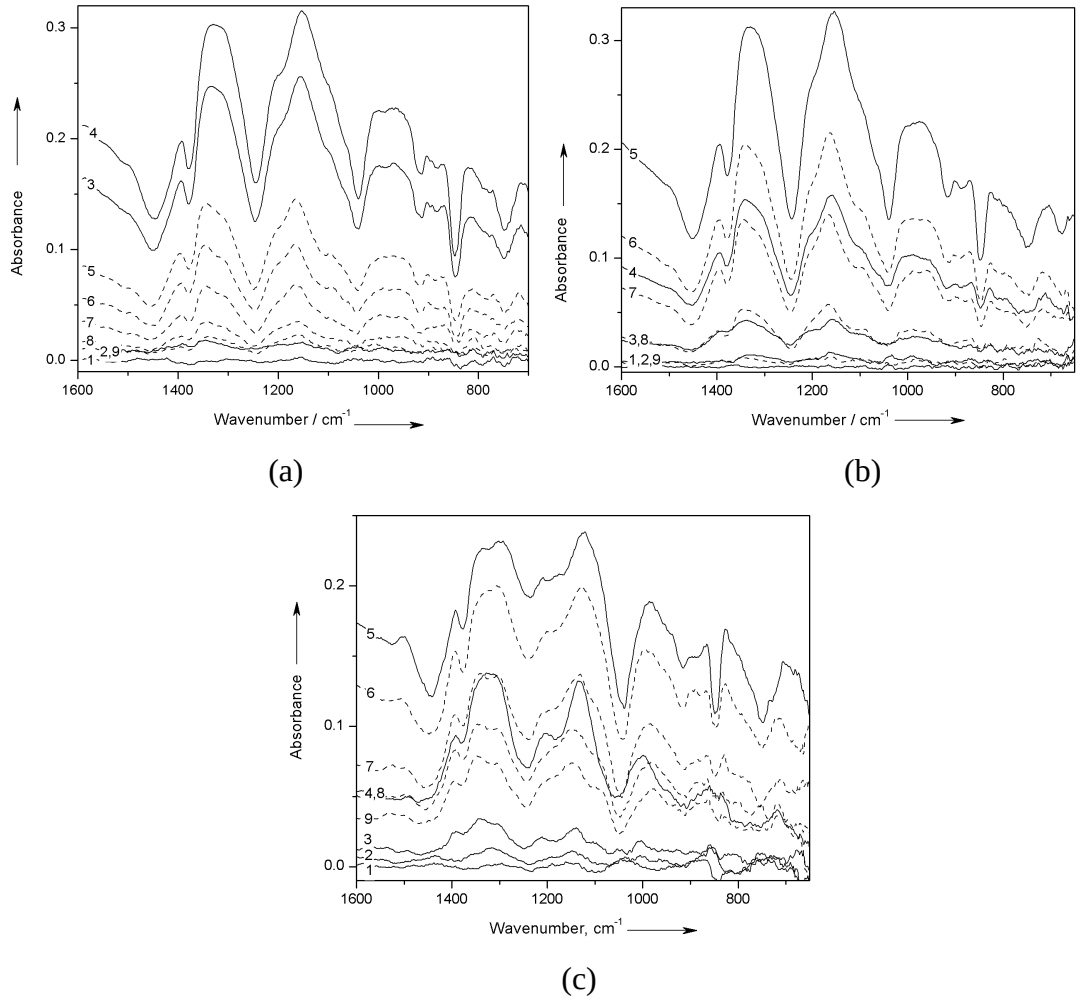

Figure 80. *In situ* ATR-FTIR spectra during p-doping (solid lines) and de-doping (dashed lines) of PTEtAc (a), PTEtAcOH (b) and PTEtOH (c). Numbers correspond to potential values from Fig. 79.

The lower intensity of the electronic absorption of free charge carriers (between 1500 and 500 cm^{-1}) and that of the IRAV bands (between 700 and 1500 cm^{-1}) in case of PTEtOH as compared with PTEtAc and PTEtAcOH indicate a lower charge density and less

delocalization of the charged states created upon electrochemical doping and a smaller effective conjugation length in the polymer backbone. Although the charges are generated more easily in PTEtOH, the interchain hydrogen bonds may cause a deviation from coplanarity, which affects the conjugation and cannot stabilize the charged states to a larger extent. Another important finding is the irreversible change of the hydroxyl group starting around 0.32 V, confirmed by the downward pointing absorption band at 3320 cm^{-1} corresponding to the stretching vibration of the –OH group in the polymer chain.

The appearance of doping induced modes similar to those for other substituted polythiophenes indicate the presence of delocalized charge carriers but doesn't offer information about the nature of the charges generated by the electrochemical doping of these polymers. To differentiate between the charged states, further *in situ* ESR and UV-Vis-NIR spectroelectrochemical studies have been carried out.

In situ ESR and UV-Vis-NIR spectroelectrochemical measurements have shown that the doping process is reversible only up to a potential of 0.45 V, at low doping levels. Beyond this potential value, at high doping levels, irreversible changes take place in the polymer structures.

For PTEtAc at low doping levels an ESR signal appears and increases in the forward scan, pointing to the formation of polarons. The intensity of the ESR signal reaches a maximum and starts to decrease before the reversal potential of the cyclic voltammogram, indicating that the concentration of polarons start to decrease since they are transformed into spinless species, such as polaron pairs. In the same time the UV-Vis-NIR spectra show two absorptions at 750 nm and 1695 nm associated with the formation of polarons during the doping of polythiophenes [249]. With increasing potential, the NIR transition at 1695 nm reaches a maximum and shifts to lower wavelength. The blue shift of the NIR band from 1695 to 1560 nm indicates the formation of polaron pairs [249,254] which are diamagnetic species, therefore ESR silent.

For PTEtAcOH and PTEtOH the potential dependence of the ESR signal shows a high hysteresis between doping and de-doping caused by the presence of OH groups. Even with a degree of hydrolysis of about 30% for PTEtAcOH, the formation of hydrogen bonds in this (partially) hydrolyzed polymer reduces the diffusion of the counterions incorporated during doping, and thus, controls the de-doping kinetically via the removal of the counterions. The NIR transition of PTEtAcOH appears at 1670 nm with a maximum at 1590 nm and that of PTEtOH at 1633 nm with a maximum shifted to 1525 nm. Here the degree of hydrolysis might change the conformation of the polymer chain completely, because the side chains are shortened from 5 (PTEtAc) to 3 (PTEOH) atoms and fixed by the formation of the hydrogen bonds.

At high doping levels the ESR signal appears at 0.02 V (Figure 81), reaches a maximum at 0.51 V and then starts to decrease, indicating that a certain amount of polarons is transformed into spinless species, which can be either polaron pairs or bipolarons. The UV-Vis-NIR spectra collected simultaneously at different potentials allowed the differentiation between the paramagnetic species (detected by ESR spectroscopy) and the diamagnetic species generated during the electrochemical p-doping. It has been found that the decrease of the

ESR signal is correlated with the appearance of both the two new optical bands at 930 nm and 1460 nm as well as that at 1290 nm. The last one appears between the two polaronic bands and dominates the spectra at high doping levels. This is in accordance with the formation of bipolarons, which have been discussed for conducting polythiophenes with absorption maxima at this wavelength [248]. The key difference between bipolarons and polaron pairs is their optical absorption: bipolarons give rise of a single absorption band from dipole-allowed transition in the UV-Vis-NIR spectrum, while polaron pairs show two absorption bands, according to theoretical and experimental studies of thiophene based conducting polymers [254-258]. Therefore, the existence of both the bipolaron, absorbing at 1290 nm, and the polaron pair with absorptions at 930 and 1460 nm is demonstrated in our case.

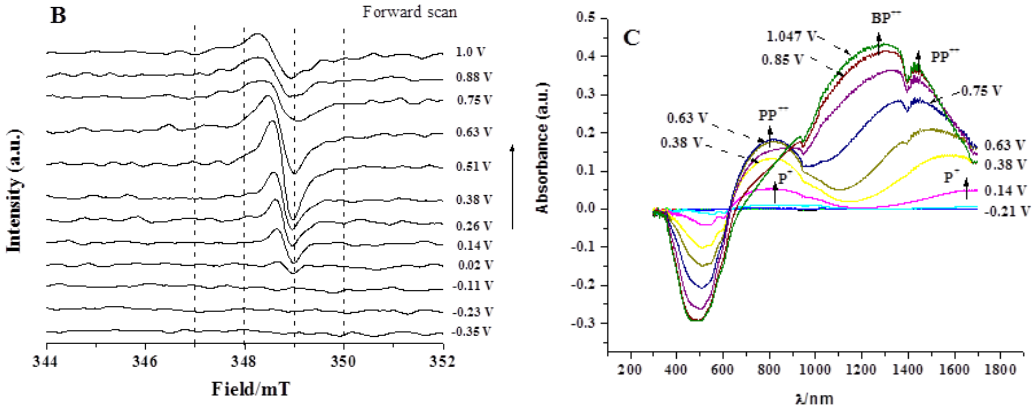

Figure 81. *In situ* ESR (left) and UV-Vis-NIR (right) spectra at high doping levels of PTEtAc.

This is the rare case in a polymer where both the bipolaron and the polaron pair are stable at higher doping levels. Using the electron spin resonance in parallel to absorption measurements it is possible to attribute the new double absorption peak at 930 and 1460 nm to the ESR-silent polaron pair. Both dicationic species coexist with the polaron which is demonstrated in the backscan where the polaron is reformed under symproportionation of both the polaron pair and the bipolaron.

As a conclusion, only by the combined use of *in situ* ESR and UV-Vis-NIR spectroelectrochemistry it has been demonstrated that at low doping levels polarons and polaron pairs are formed, while at high doping levels the bipolarons and polaron pairs are the dominating charged species. The presence of OH groups leads to the formation of hydrogen bonds, which alter both the formation of charged species and the facility of the doping process to return to the initial neutral state of the film.

3.4. Conclusions

The charge transport mechanism in several conducting polymers has been investigated by *in situ* spectroelectrochemical methods. It has been shown that only the combined application of several spectroelectrochemical techniques, such as *in situ* infrared spectroscopy, electron spin resonance spectroscopy, and ultraviolet and visible spectroscopy, allows the differentiation of paramagnetic and diamagnetic species and the unambiguous assignment of adsorption bands to various charge carriers, such as polarons, bipolarons or polaron pairs.

Based on the obtained results we could conclude that in the case of polyaniline phenazine-like structures play an important role in the formation and stabilization of the charge carriers. In the case of substituted polythiophene derivatives, it has been shown that polarons and polaron pairs are the main charge carriers at low doping levels, respectively, bipolarons and polaron pairs at high doping levels.

The originality of our work is related to the following aspects:

(i) we have electrochemically prepared copolymers of aniline with different ratios of phenosafranine to deliberately introduce a high proportion of phenazine units in the structure of the resultant polymer film. The presence of phenazine units has been evidenced by characteristic FTIR vibrations.

(ii) by comparing the potential dependence of IR vibrations and ESR signal we have demonstrated that bands usually attributed to a semiquinoid polaron lattice correspond in fact to diamagnetic species such as π-dimers which are face-to-face complexes formed by two polarons.

(iii) we have found three different potential dependencies of the IR bands and ascribed them to the formation of π-dimers, polarons and bipolarons. We have demonstrated that π-dimers are stabilized at the link of the phenazine units to the linear Pani segments, as shown by the same potential dependence of vibrations corresponding to substituted phenazine rings and those of semiquinoid structure. We have identified bands corresponding exclusively to polarons and found evidence that polarons are predominantly stabilized on the linear segments at the branches in the polymer chain. We have shown that bipolarons are also stabilized near the phenazine units.

(iv) in case on polythiophene derivatives we have shown that the side chain plays an important role in the formation and stabilization of charge carriers. Thus, introduction of a longer alkyl side chain such as hexyl stabilizes bipolarons and polaron pairs in contrast to short alkyl chain such as methyl which stabilizes only bipolarons at high doping levels. At low doping levels polaron formation in copolymer occurs at higher potentials than in p3MT and at lower potentials than in p3HT, as an effect of the distribution of long and short side alkyl chains. p3HT with a high density of long alkyl chains has a dense structure and does not allow the dopants to enter and leave the film, thus electrochemical oxidation requires a higher energy. In contrast, the presence of short methyl substituent in the copolymer contributes to a reduction of the side-chain interactions by separating the long chains from each other, so dopants may easily enter and leave the film during doping and dedoping.

PART II. Carrier evolution and development plan

The short term objective in my carrier is to become a PhD advisor. This step will allow to expand the research team of Electrochemistry, Corrosion and Electrochemical Processes by attracting future PhD students to carry out researches in the field of electrochemistry. Working in a team will enable us to obtain valuable scientific results which will be published in ISI indexed papers. This will contribute to the fulfilment of necessary criteria to become a professor.

Conducting research activity also implies writing grant applications for funding. Considering my previous experience as principal investigator and project manager in 3 national research grants, I intend to submit funding applications also in the forthcoming calls for proposals.

Interdisciplinary collaboration is also a key aspect for a successful research activity. For instance, our long term collaboration with the Westphalian University of Applied Sciences has led to a proposal for HORIZON 2020, call FCH-02-1-2017, topic: Game changer Water Electrolyzers, title: *Novel modular stack design for high pressure PEM water electrolyzer technology with wide operation range and reduced cost* – **PRETZEL**.

For this project a consortium of 9 partners from 5 countries has been set up, which comprises two technically oriented universities, two research institutes, one large industrial partner and four small and medium enterprises. The aim of PRETZEL is to develop a 25 kW PEM water electrolyzer system using a patented technology of hydraulic compression, capable to generate 4.5 m^3 H_2 per hour at rated power, at an output pressure of 100 bar and feed water temperature of maximum 90° C. The electrolyzer will dynamically operate between 4 and 6 A cm^{-2} with an efficiency of 70%, for more than 2000 h of operation. Moreover, the capital cost of stack components will be largely reduced by the use of non-precious metal coatings and advanced ceramic aerogel catalyst supports. The construction of the water electrolyzer system requires the optimization of stack components such as the membrane electrode assemblies (MEA), the porous current collector (CC) and the bipolar plates (BPP) which need to be mass productive and low-cost designed for an effective use of expansive raw materials. Due to the novel stack design based on hydraulic compression, modified requirements are necessary for the inner cell components. New, planar and highly conductive BPPs will be developed with anti-corrosive protection layer. The CCs are responsible for distribution of feed water and removal of produced gas, therefore new CCs with internal porosity gradient will be developed. The side in contact with the BPP will have a large pore radii to achieve the function of water distribution, while the side in contact with the electrode will have small pore radii of 6-15 μm to support the gas removal. MEAs will be also optimized by reducing the catalyst loading by using highly porous electro ceramic support materials, such as antimony doped tin oxide aerogel (ATO).

Within this project Politehnica University Timisoara represented by our research group will be coordinator of the work package "Compliance testing and characterization" which has the objective to characterize and to evaluate the developed materials and components and to provide reliable feedback for possibly necessary adjustments. The main activities will comprise: (i) Corrosion resistance evaluation of materials and components; (ii) Evaluation of

catalytic efficiency for oxygen evolution reaction (OER) and hydrogen evolution reaction (HER); (iii) Morphology, structure and physical characterization and (iv) Evaluation of MEAs and coated PCD in small area (25-100 cm^2) PEM electrolyzer tests. UPT will also participate in definition of specifications and requirements for the cell and stack components and also in processing the data obtained for long term testing of the stack system.

The research direction I intend to develop are derived from the two directions pursued in my activity after PhD and include:

- Development of new electrocatalysts for hydrogen / oxygen evolution reaction
- Development of new biosensors using carbon based materials such as conducting polymers and carbon nanotubes
- Development of supercapacitors for electrochemical energy storage using conducting polymers

Regarding the development of new electrocatalysts for hydrogen / oxygen evolution reaction one of the main goals is the reduction of the precious metal catalyst loading. This can be achieved using two main strategies: (i) increasing the electrocatalytic activity by designing bi-functional catalysts and (ii) by depositing noble metals on highly porous structures such as carbon nanofibers and antimony doped tin oxide aerogel. In both strategies it is important to deposit nanoparticles with a high degree of monodispersity and narrow particle size distribution. This will be achieved by pulse current electrodeposition, a very efficient electrochemical deposition method which is able to generate nanosized catalyst particles in very short times of only a few seconds. This method has been already applied for the preparation of nanostructured platinum catalysts used in PEM fuel cells [259-261] and for the electrodeposition of nanocatalysts of Pt, Pt-Co, Pt-Ru [64,262-264] for different applications. The electrodeposition parameters such as pulse time and current, off time and duty cycle will be optimized to obtain desired dispersion, size and electrocatalytic efficiency of bi-functional and noble metal catalysts. Part of research within this direction will be carried out in the frame of the future PRETZEL project.

Regarding the development of new biosensors using carbon based materials such as conducting polymers and carbon nanotubes the ambition is to obtain sensitive and selective sensors for dopamine (DA). Dopamine is a key neurotransmitter molecule and its detection in the ultra-low concentration range is still subject of research. The main interferents for dopamine are ascorbic acid (AA) and uric acid (UA) which are usually found together in physiological fluids at different concentration levels, therefore it is highly desired to design detection methods which are able to differentiate and simultaneously detect these molecules. One approach is to take advantage of the ability of boronic acid groups to selectively bind dopamine by the boronic acid - diol complexation reaction [158] which leads to the formation of an anionic ester. This can be achieved by using conducting polymers such as poly(aniline boronic acid) (PABA) and its derivatives. PABA is known to selectively bind 1,2 and 1,3 diols and this property has been exploited for the construction of different electrochemical biosensors [265-267]. In my research I intend to apply a newly developed electrochemical procedure for deposition of poly(3,4-ethylendioxithiophene), which uses a sinusoidal voltage superimposed on a d.c. potential. Compared to other electrochemical methods like cyclic

voltammetry, potentiostatic and galvanostatic deposition, this new method facilitates the preparation of conducting polymer matrices characterized by higher porosity [268,269]. Poly(aniline boronic acid) modified electrodes will be obtained by electrochemical deposition using the sinusoidal voltage method and their sensing properties for dopamine will be determined and compared to those of electrodes obtained by cyclic voltammetry deposition. The electrodeposition parameters such as frequency, amplitude of the sinusoidal voltage will be optimized to obtain the highest porosity. Thus, a large number of the boronic groups will be available for the interaction with dopamine, which is a prerequisite to enhance the sensitivity. It is expected that the PABA sensor for dopamine developed using the sinusoidal voltage deposition method will show improved performances.

A second approach aims to develop amperometric sensors based on electrode materials which are capable to separate the oxidation potentials of DA, AA and UA, since they have very close oxidation potentials. Different types of electrochemical biosensors have been designed, usually based on carbon nanomaterials such as carbon nanofibers, nanotubes and fullerenes decorated with metal nanoparticles [268-272]. It is well known that catalytic activity of noble metals nanoparticles is drastically affected by particle size and its distribution. Therefore, in my research in intend to apply the pulse current electrodeposition method to obtain highly dispersed and with controllable size Pt or Au nanoparticles on multi-walled carbon nanotubes (MWCNT) as a potential electrode material in the development of amperometric sensors for dopamine.

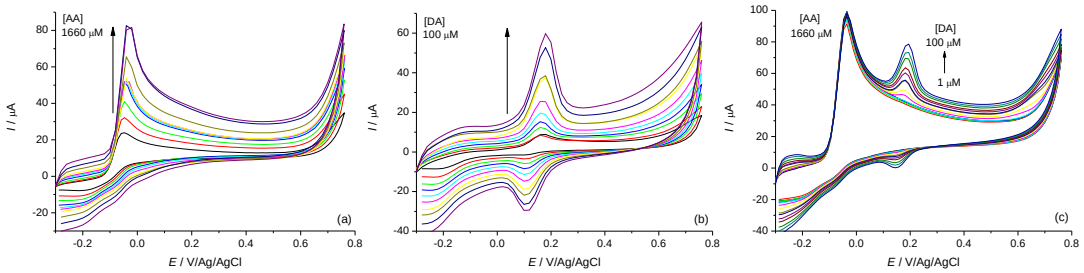

Figure 82. CV curves in 0.1 M PBS solution (pH 7.4) of 1660 μM AA (a); 100 μM DA (b) and a mixture of 1660 μM AA with different concentrations of DA (c) on GC-MWCNT electrode.

In fact, preliminary results given in Figure 82 show that the difference between the oxidation potentials of DA and AA is about 225 mV on MWCNT electrodes. It is expected that the electrodeposition of noble metal catalyst particles such as Pt or Au will further increase the gap between the oxidation potentials and improve the sensibility and selectivity of the developed biosensor. The optimization of pulse electrodeposition parameters such as pulse time and current, off time and duty cycle can further contribute to resolve DA and AA simultaneously.

Also, several electrochemical techniques such as square wave voltammetry and differential pulse voltammetry will be also used to determine and compare the sensitivity, selectivity and limit of detection of the developed electrochemical sensors.

Regarding the development of supercapacitors for electrochemical energy storage based on conducting polymers the researches are justified by the exponential growth in demand for portable electric systems and hybrid motors. Electrochemical supercapacitor act differently from conventional dielectric capacitor as concerns the way energy is stored. Thus, electrochemical capacitors can be classified according to the two different ways of storing energy in: double-layer capacitors which store energy in the electric double layer and faradaic capacitors which store energy in the form of a redox reaction. In the case of the double layer capacitors, the electrical energy is stored as charge aggregates at the surface of the electrode material therefore porous materials with a high specific surface area are highly effective for this type of storage. In the case of redox reactions, electricity is usually generated by electron transfer between the electrode and the electrolyte solution. The materials used for this type of supercapacitors include metal oxides and conductive polymers. Asymmetric supercapacitors combine the double layer storage with the cathode redox reaction to obtain the highest energy density and power. Galvanostatic charge-discharge curves

As far as teaching is concerned, I will continue to constantly improve the content of my lectures and laboratory works to make them clear, accessible and with an appropriate scientific level for all the students. As previously, I will use interactive teaching methods, so that the students have the opportunity to present their views, to argue and to ask questions. I will also encourage team work to develop the students ability to exchange ideas and work together to accomplish the assigned tasks. I will offer support to students during the laboratory works in the use of specialized software for data acquisition and processing and I will be constantly preoccupied in upgrading and equipping laboratories with specific equipment intended for teaching purposes. Additionally, based on the experience gained in research I intend to write a new lecture "Processes and materials in electrochemical energy systems" which could be a new subject for Master students.

References

1. **A. Kellenberger**, N. Vaszilcsin, W. Brandl, N. Duteanu, Kinetics of hydrogen evolution reaction o skeleton nickel and nickel-titanium electrodes obtained by thermal arc spraying technique, *International Journal of Hydrogen Energy* 32 (2007) 3258-3265.
2. **A. Kellenberger**, N. Vaszilcsin, W. Brandl, Roughness factor evaluation of thermal arc sprayed skeleton nickel electrode, *Journal of Solid State Electrochemistry* 11 (2007) 84-89.
3. **A. Kellenberger**, N. Vaszilcsin, N. Duteanu, M.L. Dan, W. Brandl, Structure, morphology and electrochemical properties of high surface area copper electrodes obtained by thermal spraying techniques, *Studia Universitatis Babes Bolyai, Chemia* 53 (2008) 89-96.
4. **A. Kellenberge**r, N. Vaszilcsin, Determinarea factorului de rugozitate al electrozilor pe bază de nichel scheletat prin voltametrie ciclică, *Revista de Chimie* 56 (2005**)** 712-715.
5. C.C. Vaduva, N. Vaszilcsin, **A. Kellenberger**, M. Medeleanu, Catalytic enhancement of hydrogen evolution reaction on copper in the presence of benzylamine, *International Journal of Hydrogen Energy* 36 (2011) 6994-7001.
6. C.C. Vaduva, N. Vaszilcsin, **A. Kellenberger**, Aromatic amines as proton carriers for catalytic enhancement of hydrogen evolution reaction on copper in acid solutions, *International Journal of Hydrogen Energy* 37 (2012) 12089-12096.
7. R. Cretu, **A. Kellenberger**, N. Vaszilcsin, Enhancement of hydrogen evolution reaction on platinum cathode by proton carriers, *International Journal of Hydrogen Energy* 38 (2013) 11685-11694.
8. R. Cretu, **A. Kellenberger**, M. Medeleanu, N. Vaszilcsin, Cathodic Hydrogen Evolution Reaction on Gold Catalyzed by Proton-Carriers, *International Journal of Electrochemical Science* 9 (2014) 4465-4477.
9. N. Plesu, **A. Kellenberger**, M. Mihali, N. Vaszilcsin, Effect of temperature on the electrochemical synthesis and properties of polyaniline films, *Journal of Non-crystalline Solids* 356 (2010) 1081-1088.
10. N. Plesu, **A. Kellenberger**, I. Taranu, B.O. Taranu, I. Popa, Impedimetric detection of dopamine on poly(3-aminophenyl boronic acid) modified skeleton nickel electrodes, *Reactive & Functional Polymers* 73 (2013) 772-778.
11. **A. Kellenberger**, N. Plesu, M. Tara Lunga Mihali, N. Vaszilcsin, Synthesis of polyaniline nanostructures by electrochemical deposition on niobium, *Polymer* 54 (2013) 3166-3174.

12. **A. Kellenberger**, D. Ambros, N. Plesu, Scan rate dependent morphology of polyaniline films electrochemically deposited on nickel, *International Journal of Electrochemical Science* 9 (2014) 6821-6833.

13. M. Tara Lunga Mihali, N. Plesu, **A. Kellenberger**, G. Ilia, Adsorption of an Azo dye on polyaniline/niobium substrate, *International Journal of Electrochemical Science* 10 (2015) 7643-7659.

14. **A. Kellenberger**, E. Jähne, H.J. Adler, T. Khandelwal, L. Dunsch, *In situ* FTIR spectroelectrochemistry of poly[2-(3-thienyl)ethyl acetate] and its hydrolyzed derivatives, *Electrochimica Acta* 53 (2008) 7054-7060.

15. L.F. Chazaro-Ruiz, **A. Kellenberger**, L. Dunsch, *In situ* ESR-UV-Vis-NIR and ATR-FTIR spectroelectrochemical studies on the p-doping of copolymers of 3-methylthiophene and 3-hexylthiophene, *Journal of Physical Chemistry B* 113 (2009) 2310-2316.

16. L.F. Chazaro-Ruiz, **A. Kellenberger**, E. Jähne, H.J. Adler, T. Khandelwal, L. Dunsch, *In situ* ESR-UV-Vis-NIR spectroelectrochemical study of the p-doping of poly[2-(3-thienyl)ethyl acetate] and its hydrolyzed derivatives, *Physical Chemistry Chemical Physics* 11 (2009) 6505-6513.

17. **A. Kellenberger**, E. Dmitrieva, L. Dunsch, The stabilization of charged states at phenazine-like units in polyaniline under p-doping. An *in situ* ATR-FTIR spectroelectrochemical study, *Physical Chemistry Chemical Physics* 13 (2011) 3411-3420.

18. **A. Kellenberger**, E. Dmitrieva, L. Dunsch, Structure dependence of charged states in "linear" polyaniline as studied by *in situ* ATR-FTIR spectroelectrochemistry, *Journal of Physical Chemistry B* 116 (2012) 4377-4385.

19. R. Banica, D. Ursu, P. Svera, C. Sarvas, S.F. Rus, S. Novaconi, **A. Kellenberger**, A.V. Racu, T. Nyari, N. Vaszilcsin, Electrical properties optimization of silver nanowires supported on polyethylene terephthalate, *Particulate Science & Technology*, 34 (2016) 217-222

20. R. Banica, D. Ursu, T. Nyari, **A. Kellenberger**, Polyol synthesis of silver nanowires in the presence of silver chloride, *Journal of Optoelectronics and Advanced Materials*, 19 (2017) 266-271.

21. R. Banica, D. Ursu, T. Nyari, **A. Kellenberger**, Two step polyol-solvothermal growth of thick silver nanowires, *Materials Letters*, 194 (2017) 181-184.

22. V.A. Goltsov, T.|N. Veziroglu, L.F. Goltsova, Hydrogen civilization of the future – A new conception of the IAHE, *International Journal of Hydrogen Energy* 31 (2006) 153-159.

23. R.J. Press, K.S.V. Santhanam, J.M. Massoud, A.V. Bailey, G.A. Takacs, *Introduction to Hydrogen Technology*, John Wiley, Hoboken, New Jersey, 2009, p. 196.

24. A. Züttel, A. Borgschulte, L. Schlapbach, *Hydrogen as a Future Energy Carrier*, Wiley-VCH Verlag, Weinheim – Germany, 2008, p. 154.

25. P. Millet, Hydrogen production by polymer electrolyte membrane water electrolysis, in V. Subramani, A. Basile and T.N. Veziroglu (Ed.) *Compendium of Hydrogen Energy, Vol. 1: Hydrogen production and Purification*, Elsevier, Amsterdam, 2015, p.255-286.

26. M. Carmo, D.L. Fritz, J. Mergel, D. Stolten, A comprehensive review on PEM water electrolysis, *International Journal of Hydrogen Energy* 38 (2013) 4901-4934.

27. P. Millet, N. Mbemba, S.A. Grigoriev, V.N. Fateev, A. Aukauloo, C. Etievant, Electrochemical performances of PEM water electrolysis cells and perspectives, *International Journal of Hydrogen Energy* 36 (2011) 4134-4142.

28. S. Trasatti, Work function, electronegativity, and electrochemical behaviour of metals: III. Electrolytic hydrogen evolution in acid solutions, *Journal of Electroanalytical Chemistry and Interfacial Electrochemistry* 39 (1972) 163-184.

29. A. Eftekahri, Electrocatalysts for hydrogen evolution reaction, *International Journal of Hydrogen Energy* (2017) in press.

30. S.S. Tong, X.-J. Wang, Q.-C. Li, X.-J. Han, Progress on Electrocatalysts of Hydrogen Evolution Reaction Based on Carbon Fiber Materials, *Chinese Journal of Analytical Chemistry* 44 (2016) 1447-1457.

31. J.B. Yadav, J.-W. Park, Y.-J. Cho, O.-S. Joo, Intermediate hydroxide enforced electrodeposited platinum film for hydrogen evolution reaction, *International Journal of Hydrogen Energy* 35 (2010) 10067-10072.

32. A. Kiani, S. Hatami, Fabrication of platinum coated nanoporous gold film electrode: A nanostructured ultralow-platinum loading electrocatalyst for hydrogen evolution reaction, *International Journal of Hydrogen Energy* 35 (2010) 5202-5209.

33. Q. Ding, M. Liu, Y.-E. Miao, Y. Huang, T. Liu, Electrospun nickel-decorated carbon nanofiber membranes as efficient electrocatalysts for hydrogen evolution reaction, *Electrochimica Acta* 159 (2015) 1-7.

34. N.K. Mahale, S.T. Ingle, Electrocatalytic hydrogen evolution reaction on nano-nickel decorated graphene electrode, *Energy* 119 (2017) 872-878.

35. L. Wang, Y. Li, M. Xi, Z. Li, Z. Chen, Z. Ma, X. Qin, G. Shao, Ni nanoparticles supported on graphene layers: An excellent 3D electrode for hydrogen evolution reaction in alkaline solution, *Journal of Power Sources* 347 (2017) 220-228.

36. P. Häussinger, R. Lohmüller, A.M. Watson, Hydrogen, 2. Production, in Ullmann's Encyclopedia of Industrial Chemistry, Wiley-VCH Verlag GmbH & Co. KGaA, 2000.

37. M.S. Faber, R. Dziedzic, M.A. Lukowski, N.S. Kaiser, Q. Ding, S. Jin, High-performance electrocatalysis using metallic cobalt pyrite (CoS_2) micro- and nanostructures, *Journal of the American Chemical Society* 136 (2014) 10053–10061.

38. L.-L. Feng, G. Yu, Y. Wu, G.-D. Li, H. Li, Y. Sun, T. Asefa, W. Chen, X. Zou,, High-index faceted Ni_3S_2 nanosheet arrays as highly active and ultrastable electrocatalysts for water splitting, *Journal of the American Chemical Society* 137 (2015) 14023–14026.

39. X R.V. Digraskar, B.B. Mulik, P.S. Walke, A.V. Ghule, B.R. Sathe, Enhanced Hydrogen Evolution Reactions on Nanostructured Cu_2ZnSnS_4 (CZTS) Electrocatalyst, *Applied Surface Science* 412 (2017) 475-481.

40. X. Dai, K. Du, Z. Li, H. Sun, Y. Yang, W. Zhang, X. Zhang, Enhanced hydrogen evolution reaction on few–layer MoS2 nanosheets–coated functionalized carbon nanotubes, *International Journal of Hydrogen Energy* 40 (2015) 8877–8888.

41. E.J. Popczun, J.R. McKone, C.G. Read, A.J. Biacchi, A.M. Wiltrout, N.S. Lewis, R.E. Schaak, Nanostructured nickel phosphide as an electrocatalyst for the hydrogen evolution reaction, *Journal of the American Chemical Society* 135 (2013) 9267–9270.

42. P. Xiao, M.A. Sk, L. Thia, X. Ge, R.J. Lim, J.-Y. Wang, K.H. Lim, X. Wang, Molybdenum phosphide as an efficient electrocatalyst for the hydrogen evolution reaction, *Energy and Environmental Science* 7 (2014) 2624–2629.

43. H. Du, S. Gu, R. Liu, C.M. Li, Highly active and inexpensive iron phosphide nanorods electrocatalyst towards hydrogen evolution reaction, *International Journal of Hydrogen Energy* 40 (2015) 14272–14278.

44. C. Tang, A. Sun, Y. Xu, Z. Wu, D. Wang, High specific surface area Mo_2C nanoparticles as an efficient electrocatalyst for hydrogen evolution, *Journal of Power Sources* 296 (2015) 18–22.

45. C. Tang, W. Wang, A. Sun, C. Qi, D. Zhang, Z. Wu, D. Wang, Sulfur-decorated molybdenum carbide catalysts for enhanced hydrogen evolution, *ACS Catalysis* 5 (2015) 6956–6963.

46. P. Wang, J. Qi, X. Chen, C. Li, T. Wang, C. Liang, New insights into high-valence state Mo in molybdenum carbide nanobelts for hydrogen evolution reaction, *International Journal of Hydrogen Energy* (2017) in press.

47. Y. Zheng, Y. Jiao, Y. Zhu, L.H. Li, Y. Han, Y. Chen, A. Du, M. Jaroniec, S.Z. Qiao, Hydrogen evolution by a metal-free electrocatalyst, *Nature Communications* 5 (2014).

48. S.G. Mairanovskii, The theory of catalytic hydrogen waves in organic polarography, *Journal of Electroanalytical Chemistry* 6 (1963) 77-118.

49. M. Heyrovsky, Catalytic Hydrogen Evolution at Mercury Electrodes from Solutions of Peptides and Proteins. In: E. Paleček, F. Scheller, J. Wang (editors): *Electrochemistry of Nucleic Acids and Proteins*, Vol 1, Elsevier, Amsterdam, 2005, p. 657-687.

50. M. Živanović, M. Aleksić, V. Ostatná, T. Doneux, E. Paleček, Polylysine-Catalyzed Hydrogen Evolution at Mercury Electrodes, *Electroanalysis* 22 (2010) 2064-2070.

51. M. Heyrovsky, Early polarographic studies on proteins, *Electroanalysis* 16 (2004) 1067-1073.

52. M. Heyrovsky, Research Topic – Catalysis of Hydrogen Evolution on mercury electrodes, *Croatica Chemica Acta* 17 (2006) 1-4.

53. A.N. Frumkin, Hydrogen Overvoltage and Adsorption phenomena. In: P. Delahay, C.W. Tobias (editors): *Advances in Electrochemistry and Electrochemical Engineering*, Vol. 3, Interscience Publishers Inc, New York, 1963, p.65-122.

54. V. Mirčeski, S. Skrzypek, W. Ciesielski, A. Sokołowski, Theoretical and experimental study of the catalytic hydrogen evolution reaction in the presence of an adsorbed catalyst by means of square-wave voltammetry, *Journal of Electroanalytical Chemistry* 585 (2005) 97-104.

55. E. Dayalan, R. Narayan, The acceleration of the hydrogen evolution reaction from acid solutions by sulfur compounds: Part I. Mercury electrode, *Journal of Electroanalytical Chemistry* 179 (1984) 167–-178.

56. J. Bukowska, K. Jackowska, Influence of thiourea on hydrogen evolution at a silver electrode as studied by electrochemical and SERS methods, *Journal of Electroanalytical Chemistry* 367 (1994) 41-48.

57. C.C. Vaduva, N. Vaszilcsin, **A. Kellenberger**, M. Medeleanu, Inhibition effect of some aromatic amines on copper electrodeposition from acidic baths, *Journal of Applied Electrochemistry* 42 (2012) 217-224.

58. N. Pentland, J.O.M. Bockris, E. Sheldon, Hydrogen evolution reaction on copper, gold, molybdenum, palladium, rhodium and iron, *Journal of the Electrochemical Society* 104 (1957) 182-194.

59. A.K. Khanova, L.I. Krishtalik, Kinetics of the hydrogen evolution reaction on gold electrode. A new case of the barrierless discharge, *Journal of Electroanalytical Chemistry* 660 (2011) 224-229.

60. C.H. Hamann, A. Hammett, W. Vielstich, *Electrochemistry*, Wiley VCH Verlag, Weinheim, 2007.

61. R. Muntean, U. Rost, G. Marginean, N. Vaszilcsin, Optimisation of the electrodeposition parameters for platinum nanoparticles on carbon nanofibers support, *Solid State Phenomena* 254 (2016) 153-158.

62. K.E. Ayers, J.N. Renner, N. Danilovic, J.X. Wang, Y. Zhang, R. Maric, H. Yu, Pathways to ultra-low platinum group metal catalyst loading in proton exchange membrane electrolyzers, *Catalysis Today* 262 (2016) 121-132.

63. B. Devadas, T. Imae, Hydrogen evolution reaction efficiency by low loading of platinum nanoparticles protected by dendrimers on carbon materials, *Electrochemistry Communications* 72 (2016) 135-139.

64. R.D. Armstrong, M. Henderson, Impedance plane display of a reaction with an adsorbed intermediate, *Journal of Electroanalytical Chemistry and Interfacial Electrochemistry* 39 (1972) 81-90.

65. A. Lasia, Applications of the Electrochemical Impedance Spectroscopy to Hydrogen Adsorption, Evolution and Absorption into Metals, In: *Modern Aspects of Electrochemistry*, B.E. Conway and R.E. White (editors), Kluwer/Plenum, New York, vol. 35, p. 1-49 (2002).

66. A. Lasia, On the mechanism of hydrogen absorption reaction, *Journal of Electroanalytical Chemistry* 593 (2006) 159-166.

67. M. Stackelberg, H. Fassbender, Untersuchungen zur Katalyse der Wasserstoffabscheidung an der Quecksilberkathode durch organische Stoffe I. Allgemeine Untersuchungen über den Strom und die Strömungen an der Elektrode, *Zeitschrift für Elektrochemie, Berichte der Bunsengesellschaft für Physikalische Chemie* 62 (1958) 834-839.

68. M. Stackelberg, W. Hans, W. Jensch, Untersuchungen zur Katalyse der Wasserstoffabscheidung an der Quecksilberkathode durch organische Stoffe II. Die konstitutionellen Voraussetzungen für die katalytische Wirksamkeit, *Zeitschrift für Elektrochemie, Berichte der Bunsengesellschaft für Physikalische Chemie* 62 (1958) 839-850.

69. S.G. Mairanovskii, Theory of catalytic hydrogen waves in organic polarography, *Russian Chemical Reviews* 33 (1964) 38-55.

70. A. G. MacDiarmid, A. J. Epstein, Polyanilines: A novel class of conducting polymers, *Faraday Discussions of the Chemical Society* 88 (1989) 317-332.

71. W. S. Huang, B. H. Humphrey, A. G. MacDiarmid, Polyaniline, a novel conducting polymer. Morphology and chemistry of its oxidation and reduction in aqueous electrolytes, *Journal of the Chemical Society Faraday Transactions 1* 8 (1986) 2385.

72. G. Inzelt, Conducting Polymers. A New Era in Electrochemistry, Springer-Verlag Berlin, Heidelberg, 2012.

73. Z. Cai, C.R. Martin, Electronically conductive polymer fibers with mesoscopic diameters showed enhanced electronic conductivities, *Journal of the American Chemical Society* 111 (1989) 4138-4139.

74. C.R. Martin, R. Parthasarathy, V. Menon, Template synthesis of electronically conductive polymers – A new route for achieving higher electronic conductivities, *Synthetic Metals* 55 (1993) 1165-1170.

75. C.R. Martin, R. Parthasarathy, V. Menon, Template synthesis of electronically conductive polymers – preparation of thin films, *Electrochimica Acta* 39 (1994) 1309-1313.

76. D. Li, J. Huang, R.B. Kaner, Polyaniline Nanofibers: A Unique Polymer nanostructure for Versatile Applications, *Accounts of Chemical Research* 42 (2009) 135-145.

77. L. Xia, Z. Wei, M. Wan, Conducting polymer nanostructures and their application in biosensors, *Journal of Colloid and Interface Science* 341 (2010) 1-11.

78. D.M. Sarno, S.K. Manohar, A.G. MacDiarmid, Controlled interconversion of semiconducting and metallic form of polyaniline nanofibers, *Synthetic Metals* 148 (2005) 237-243.

79. X. Zhang, W.J. Goux, S.K. Manohar, Synthesis of Polyaniline Nanofibers by „Nanofiber Seeding", *Journal of the American Chemical Society* 126 (2004) 4502-4503.

80. R.Chan-Yu-King, F.Roussel, Morphological and electrical characteristics of polyaniline nanofibers, *Synthetic Metals* 153 (2005) 337-340.

81. S. Xing, C. Zhao, S. Jing, Z. Wang, Morphology and conductivity of polyaniline nanofibers prepared by „seeding| polymerization, *Polymer* 47 (2006) 2305-2313.

82. N.-R.Chiou, A.J.Epstein, A Simple Approach to Control the Growth of Polyaniline Nanofibers, *Synthetic Metals* 153 (2005) 69-72.

83. J. Chen, Y. Xu, Y. Zheng, L. Dai, H. Wu, The design, synthesis and characterization of polyaniline nanophase materials, *Comptes Rendus Chimie* 11 (2008) 84-89.

84. Z. Zhang, J. Deng, M. Wan, Highly crystalline and thin polyaniline nanofibers oxidized by ferric chloride, *Materials Chemistry and Physics* 115 (2009) 275-279.

85. A. Rahy, D.J. Yang, Synthesis of highly conductive polyaniline nanofibers, *Materials Letters* 62 (2008) 4311-4314.

86. S.P. Surwade, S.R. Agnihotra, V. Dua, N. Manohar, S. Jain, S. Ammu, S.K. Manohar, Catalyst-free synthesis of Oligoanilines and Polyaniline Nanofibers Using H_2O_2, *Journal of the American Chemical Society* 131 (2009) 12528-12529.

87. J. Huang, R.B. Kaner, A General Chemical route to Polyaniline Nanofibers, *Journal of the American Chemical Society* 126 (2004) 851-855.

88. J. Huang, R.B. Kaner, The intrinsic nanofibrillar morphology of polyaniline, *Chemistry Communications* (2006) 367-376.

89. D. Li, R.B. Kaner, Shape and Aggregation Control of Nanoparticles: Not Shaken, Not Stirred, *Journal of the American Chemical Society* 128 (2006) 968-975.

90. X. Zhang, R. Chan-Yu-King, A. Jose, S.K. Manohar, Nanofibers of polyaniline synthesized by interfacial polymerization, *Synthetic Metals* 145 (2004) 23-29.

91. S. Mu, Novel properties of polyaniline nanofibers coated with polycathecol, *Synthetic Metals* 156 (2006) 202-208.

92. D. Wei, C. Kvarnström, T. Lindfors, A. Ivaska, Polyaniline nanotubules obtained in room-temperature ionic liquids, *Electrochemistry Communications* 8 (2006) 1563-1566.

93. S. Mu, Y. Yang, Spectral Characteristics of Polyaniline Nanostructures Synthesized Using Cyclic Voltammetry at Different Scan Rates, *Journal of Physical Chemistry B* 112 (2008) 11558-11563.

94. Y. Guo, Y. Zhou, Polyaniline nanofibers fabricated by electrochemical polymerization: A mechanistic study, *European Polymer Journal* 43 (2007) 2292-2297.

95. N.T. Kemp, J.W. Cochrane, R. Newbury, Characteristics of the nucleation and growth of template-free polyaniline nanowires and fibrils, *Synthetic Metals* 159 (2009) 435-444.

96. H. Zhang, J. Wang, Z. Wang, F. Zhang, S. Wang, Electrodeposition of polyaniline nanostructures: A lamellar structure, *Synthetic Metals* 159 (2009) 277-281.

97. H.H. Zhou, S.Q. Jiao, J.H. Chen, W.Z. Wei, Y.F. Kuang, Relationship between preparation conditions, morphology and electrochemical properties of polyaniline prepared by pulse galvanostatic method (PGM), *Thin Solid Films* 450 (2004) 233-239.

98. H. Zhou, J. Wen, X. Ning, C. Fu, J. Chen, Y. Kuang, Electrosynthesis of polyaniline films on titanium by pulse potenstiostatic method, *Synthetic Metals* 157 (2007) 98-103.

99. A.G. MacDiarmid, A.J. Epstein, The concept of secondary doping as applied to polyaniline, *Synthetic Metals* 65 (1994) 103-116.

100. S.K. Jeong, J.S. Suh, E.J. Oh, Y.W. Park, C.Y. Kim, A.G. MacDiarmid, Preparation of polyaniline free standing film by controlled processing and its transport property, *Synthetic Metals* 69 (1995) 171-172.

101. C. Zhou, J. Han, R. Guo, Controllable Synthesis of Polyaniline Multidimensional Architectures: Form Plate-like Structures to Flower-like Superstructures, *Macromolecules*, 41 (2008) 6473-6479.

102. C.A. Amarnath, J. Kim, K. Kim, J. Choi, D. Sohn, Nanflakes to nanorods and nanospheres transition of selenious acid doped polyaniline, *Polymer* 49 (2008) 432-437.

103. H. Wang, Y. Lu, Morphological control of self-assembly polyaniline micro/nano-structures using dichloroacetic acid, *Synthetic Metals* 162 (2012) 1369-1374.

104. W. Zhao, L. Ma, K. Lu, Facile Synthesis of Polyaniline Nanofibers in the Presence of Polyethylene Glycol, *Journal of Polymer Research* 14 (2007) 1-4.

105. Y. Li, Y. Wang, X. Jing, R. Zhu, Early stage pH-profile: the key factor controlling the construction of polyaniline micro/nanostructures, *Journal of Polymer Research* 18 (2011) 2119-2131.

106. P. Singh, R.A. Singh, Preparation and characterization of polyaniline nanostructures via a interfacial polymerization method, *Synthetic Metals* 162 (2012) 2193-2200.

107. X.-Y. Peng, F. Luan, X.-X. Liu, D. Diamond, K.-T. Lau, pH-controlled morphological structure of polyaniline during electrochemical deposition, *Electrochimica Acta* 54 (2009) 6172-6177.

108. A. Cot, S. Lakard, J. Dejeu, P. Rougeot, C. Magnenet, B. Lakard, M. Gauthier, Electrosynthesis and characterization of polymer films on silicon substrate for applications in micromanipulation, *Synthetic Metals* 162 (2012) 2370-2378.

109. N. Li, YH. Xiao, CZ. Xu, HH. Li, XD. Yang, Facile Preparation of Polyaniline Nanoparticles via Electrodeposition for Supercapacitors, *International Journal of Electrochemical Science* 8 (2013) 1181-1188.

110. G.T. Andrade, M.J. Aguirre, S.R. Biaggio, Influence of the first potential scan on the morphology and electrical properties of potentiodynamically grown polyaniline films, *Electrochimica Acta* 44 (1998) 633-642.

111. M. Žic, The effect of PANI-free volume on impedance response, *Journal of Electroanalytical Chemistry* 610 (2007) 57-66.

112. M.J. Rodriguez Presa, H.L. Bandey, R.I. Tucceri, M.I. Florit, D. Posadas, A.R. Hillman, Film thickness and electrolyte concentration effects on the EIS response of Poly-(*o*-toluidine) in the conducting state, *Electrochimica Acta* 44 (1999) 2073-2085.

113. V. Horvat-Radošević, K. Kvastek, M. Kraljić Roković, Impedance spectroscopy of oxidized polyaniline and poly(*o*-ethoxyaniline) thin film modified Pt electrodes, *Electrochimica Acta* 51 (2006) 3417–3428.

114. M. Žic, The influence of the PANI structure on the conductive mechanism and on the electrical equivalent circuit analysis, *Journal of Electroanalytical Chemistry* 653 (2009) 29-38.

115. C.-C. Hu, C.-H. Chu, Electrochemical impedance characterization of polyaniline-coated graphite electrodes for electrochemical capacitors – effects of film coverage/thickness and anions, *Journal of Electroanalytical Chemistry* 503 (2001) 105-116.

116. D.H. Zhou, Y.H. Li, J.Y. Wang, P. Xu, X.J. Han, Synthesis of polyaniline nanofibers with high electrical conductivity from CTAB-SDBS mixed surfactants, *Materials Letters* 65 (2011) 3601-3604.

117. HL. Li, JX. Wang, QX. Chu, Z. Wang, FB. Zhang, SC. Wang, Theoretical and experimental specific capacitance of polyaniline in sulfuric acid, *Journal of Power Sources* 190 (2009) 578-586.

118. J.B. Zang, Y.H. Wang, X.Y. Zhao, G.X Xin, S.P. Sun, X.H. Qu, S.B. Ren, Electrochemical synthesis of polyaniline on nanodiamond powder, *International Journal of Electrochemical Science* 7 (2012) 1677-1687.

119. Y. Zhang, X. Jiang, R. Zhang, P. Sun, Y. Zhou, Influence of the nanostructure on charge transport in polyaniline films, *Electrochimica Acta* 56 (2011) 3264-3269.

120. R. Kiebooms, R. Menon, K. Lee, Synthesis, Electrical and Optical Properties of Conjugated Polymers, in: H.S. Nalwa (Ed.), *Handbook of Advanced Electronic and Photonic Materials and Devices*, Vol. 8. Conducting Polymers, Academic Press, New York, 2001, pp. 1-102.

121. M. Gholamian, A.Q. Contractor, Effect of the temperature of synthesis on the conductivity and electrochemical behavior of polyaniline, *Journal of Electroanalytical Chemistry* 252 (1988) 291-301.

122. P.M. Beadle, Y.F. Nicolau, E. Banka, P. Rannou, D. Djurado, Controlled polymerization of aniline at sub-zero temperatures, *Synthetic Metals* 95 (1998) 29-45.

123. C.-C. Hu, J.-Y. Lin, Effects of the loading and polymerization temperature on the capacitive performance of polyaniline in $NaNO_3$, *Electrochimica Acta* 47 (2002) 4055-4067.

124. G. Boara, M. Sparpaglione, Synthesis of polyanilines with high electrical conductivity, *Synthetic Metals* 72 (1995) 135-140.

125. M.R. Nateghi, M. Zahedi, M.H. Mosslemin, S. Hashemian, S. Bezhad, A. Minnai, Autoacceleration/degradation of electrochemical polymerization of substituted anilines, *Polymer* 46 (2005) 11476-11483.

126. M. Probst, R. Holze, Time and temperature-dependent changes of the *in situ* conductivity of polyaniline and polyindoline, *Electrochimica Acta* 40 (1995) 213-219.

127. R. Ansari, W.E. Price, G.G. Walace, Effect of thermal treatment on the electroactivity of polyaniline, *Polymer* 37 (1996) 917-923.

128. M. Trchová, I. Šeděnková, E. Tobolková, J. Stejskal, FTIR spectroscopic and conductivity study of the thermal degradation of polyaniline films, *Polymer Degradation and Stability* 86 (2004) 179-185.

129. I. Šeděnková, M. Trchová, J. Stejskal, Thermal degradation of polyaniline films prepared in solutions of strong and weak acids and in water – FTIR and Raman spectroscopic studies, *Polymer Degradation and Stability* 93 (2008) 2147-2157.

130. S. Bhadra, D. Khastgir, Extrinsic and intrinsic structural change during heat treatment of polyaniline, *Polymer Degradation and Stability* 93 (2008) 1094-1099.

131. K. Luo, N. Shi, C. Sun, Thermal transition of electrochemically synthesized polyaniline, *Polymer Degradation and Stability* 91 (2006) 2660-2664.

132. S.K. Mondal, N. Munichandraiah, The effect of low temperature treatment on electrochemical activity of polyaniline, *Journal of Electroanalytical Chemistry* 595 (2006) 78-86.

133. J.H. Lim, J. Choi, Formation of niobium oxide nanowires by thermal oxidation, *Journal of Industrial and Engineering Chemistry* 15 (2009) 860–864.

134. I. Arsova, P. Abdurauf, T. Grčev, Lj. Arsov, Electrochemical characterization of the passive films formed on niobium surfaces in H_2SO_4 solutions, *Journal of the Serbian Chemical Society* 71 (2006) 177–187.

135. D.B. Camovska, M.Lj. Arsov, T.P. Grčev, Electrochemical and impedance characterization of passive films on niobium in alkaline and acidic solutions, *Macedonian Journal of Chemistry and Chemical Engineering* 26 (2007) 95–101.

136. L. Zhang, Y. Long, Z. Chen, M. Wan, The Effect of Hydrogen Bonding on Self-Assembled Polyaniline Nanostructure, *Advanced Functional Materials* 14 (2004) 693-698.

137. M. Trchová, E.N. Konyushenko, J. Stejskal, J. Kovářová, G. Ćirić-Marjanović, The conversion of polyaniline nanotubes to nitrogen-containing carbon nanotubes and their

comparison with multi-walled carbon nanotubes, *Polymer Degradation and Stability* 94 (2009) 929-938.

138. H. Guan, L.Z. Fan, H. Zhang, X. Qu, Polyaniline nanofibers obtained by interfacial polymerization for high-rate supercapacitors, *Electrochimica Acta* 56 (2010) 964-968.

139. D.S. Dhawale, R.R. Salunkhe, V.S. Jamadade, D.P. Dubal, S.M. Pawar, C.D. Lokhande, Hydrophilic polyaniline nanofibrous architecture using electrosynthesis method for supercapacitor application, *Current Applied Physics* 10 (2010) 904-909.

140. D. Zhang, Y. Wang, Synthesis and applications of one-dimensional nano-structured polyaniline: An overview, *Materials Science and Engineering B* 134 (2006) 9-19.

141. J. Stejskal, I. Sapurina, M. Trchová, E. Konyushenko, P. Holler, The genesis of polyaniline nanotubes, *Polymer* 47 (2006) 8253-8262.

142. J. Stejskal, I. Sapurina, M. Trchová, Polyaniline nanostructures and the role of aniline oligomers and their formation, *Progress in Polymer Science* 35 (2010) 1420-1481.

143. E. Tamburri, S. Orlanducci, V. Guglielmotti, G. Reina, M. Rossi, M.L. Terranova, Engineering detonation nanodiamond – Polyaniline composites by electrochemical routes: Structural features and functional characterizations, *Polymer* 52 (2011) 5001-5008.

144. U. Lange, N.V. Roznyatovskaya, V.M. Mirsky, Conducting polymers in chemical sensors and arrays, *Analytica Chimica Acta* 614 (2008) 1-26.

145. T. Lindfors, A. Ivaska, Potentiometric and UV-Vis characterization of *N*-substituted polyaniline, *Journal of Electroanalytical Chemistry* 535 (2002) 65-74.

146. M. Nicolas, B. Fabre, G. Marchand, J. Simonet, New boronic-acid- and boronate-substituted aromatic compounds as precursors of fluoride responsive conjugated polymer films, *European Journal of Organic Chemistry* (2000) 1703-1710.

147. M.S. Freund, B.A. Deore, Boronic Acid Substituted Self-Doped Polyaniline, in *Self-Doped Conducting Polymers*, John Wiley & Sons, Ltd, Chichester, UK, (2007) 156-218.

148. H. Çiftçi, Y. Oztekin, U. Tamer, A. Ramanavicine, A. Ramanavicius, Development of poly(3-aminophenylboronic acid) modified graphite electrode suitable for fluoride determination, *Talanta* 126 (2014) 202-207.

149. S. Wu, T. Han, J. Guo, Y. Cheng, Poly(3-aminophenylboronic acid)-reduced graphene oxide nanocomposite modified electrode for ultrasensitive electrochemical detection of fluoride with a wide response range, *Sensors and Actuators B* 220 (2015) 1305-1310.

150. H. Çiftçi, U. Tamer, Electrochemical determination of iodide by poly(3-aminophenyl-boronic acid) film electrode at moderately low pH ranges, *Analytica Chimica Acta* 687 (2011) 137-140.

151. E. Shoji, M.S. Freund, Potentiometric saccharide detection based on the pKa changes of poly(aniline boronic acid), *Journal of the American Chemical Society* 124 (2002) 12486-12493.

152. Y. Ma, X. Yang, One saccharide sensor based on the complex of the boronic acid and the monosaccharide using electrochemical impedance spectroscopy, *Journal of Electroanalytical Chemistry* 580 (2005) 348-352.

153. J.T. English, B.A. Deore, M.S. Freund, Biogenic amine vapour detection using poly(anilineboronic acid) films, *Sensors and Actuators B* 115 (2006) 666-671.

154. B. Fabre, L. Taillebois, Poly(aniline boronic acid)-based conductimetric sensor of dopamine, *Chemical Communications* (2003) 2982-2983.

155. J. Li, N. Zhang, Q. Sun, Z. Bai, J. Zheng, Electrochemical sensor for dopamine based on imprinted silica matrix- poly(aniline boronic acid) hybrid as recognition element, *Talanta* 159 (2016) 379-386.

156. J. Rick, T.-C. Chou, Amperometric protein sensor – fabricated as a polypyrrole, poly-aminophenylboronic acid bilayer, *Biosensors and Bioelectron*ics 22 (2006) 329-335.

157. N. Plesu, **A. Kellenberger**, N. Vaszilcsin, I. Manoviciu, Electrochemical polymerization of aniline on skeleton nickel electrodes, *Molecular Crystals and Liquid Crystals* 416 (2004) 127-135.

158. E. L. Muetterties, *The chemistry of boron and its compounds*, Wiley, New York, 1967, pp. 495-500.

159. S.R. Ali, R.R. Parajuli, Y. Balogun, Y. Ma, H. He, A nonoxidative electrochemical sensor based on a self-doped polyaniline/carbon nanotube composite for sensitive and selective detection of the neurotransmitter dopamine: A Review, *Sensors* 8 (2008) 8423-8452.

160. J.Y. Park, S. M. Park, DNA hybridization sensors based on electrochemical impedance spectroscopy as a detection tool, *Sensors* 9 (2009) 9513-9532.

161. Y. Park, B.Y. Chang, H. Nam, S.M. Park, Selective electrochemical sensing of glycated hemoglobin (HbA1c) on thiophene-3-boronic acid self-assembled monolayer covered gold electrodes, *Analytical Chemistry* 80 (2008) 8035-8044.

162. J.Y. Park, Y.S. Lee, B.H. Kim, S.M. Park, (*R*)-Lipo-diaza-18-crown-6self-assembled monolayer as a selective serotonin receptor, *Analytical Chemistry* 80 (2009) 4986-4993.

163. V. Sharma, P. Rekha, P. Mohanty, Nanoporous hypercrosslinked polyaniline: An efficient adsorbent for the adsorptive removal of cationic and anionic dyes, *Journal of Molecular Liquids* 222 (2016) 1091-1100.

164. S.M. Ahmed, F.I. El-Dib, N.Sh. El-Gendy, W.M. Sayed, M. El-Khodary, A kinetic study for the removal of anionic sulphonated dye from aqueous solution using nano-polyaniline and Baker's yeast, *Arabian Journal of Chemistry* 9 (2016) S1721-S1728.

165. M. Saad, H. Tahir, J. Khan, U. Hameed, A. Saud, Synthesis of polyaniline nanoparticles and their application for the removal of Crystal Violet dye by ultrasonicated adsorption process based on Response Surface Methodology, *Ultrasonics Sonochemistry* 34 (2017) 600-608.

166. M. Bhaumik, R.I. McCrindle, A. Maity, S. Agarwal, V.K. Gupta, Polyaniline nanofibers as highly effective re-usable adsorbent for removal of reactive black 5 from aqueous solutions, *Journal of Colloid and Interface Science* 466 (2016) 442-451.

167. V. Janaki, K. Vijayaraghavan, B.-T. Oh, K.-J. Lee, K. Muthuchelian, A.K. Ramasamy, S. Kamala-Kannan, Starch/polyaniline nanocomposite for enhanced removal of reactive dyes from synthetic effluent, *Carbohydrate Polymers* 90 (2012) 1437-1444.

168. V. Janaki, B.-T. Oh, K. Shanthi, K.-J. Lee, A.K. Ramasamy, S. Kamala-Kannan, Polyaniline/chitosan composite: An eco-friendly polymer for enhanced removal of dyes from aqueous solution, *Synthetic Metals* 162 (2012) 974-980.

169. S. Agarwal, I. Tyagi, V.K. Gupta, F. Golbaz, A.N. Golikand, O. Moradi, Synthesis and characteristics of polyaniline/zirconium oxide conductive nanocomposite for dye adsorption application, *Journal of Molecular Liquids* 218 (2016) 494-498.

170. S. Debnath, N. Ballav, H. Nyoni, A. Maity, K. Pillay, Optimization and mechanism elucidation of the catalytic photo-degradation of the dyes Eosin Yellow (EY) and Naphthol blue black (NBB) by a polyaniline-coated titanium dioxide nanocomposite, *Applied catalysis B: Environmental* 163 (2015) 330-342.

171. V.K. Gupta, D. Pathania, N.C. Kothiyal, G. Sharma, Polyaniline zirconium (IV) silicophosphate nanocomposite for remediation of methylene blue dye from waste water, *Journal of Molecular Liquids* 190 (2014) 139-145.

172. M. Granström, M.G. Harrison, R.H. Friend, Electro-optical Polythiophene Devices, in D. Fichou (Ed.) *Handbook of Oligo- and Polythiophenes*, Wiley VCH, Weinheim, 1999, pp. 405-458.

173. H.E. Katz, A. Dodabalapur, Z. Bao, Oligo- and Polythiophene Field Effect Transistors, in D. Fichou (Ed.) *Handbook of Oligo- and Polythiophenes*, Wiley VCH, Weinheim, 1999, pp. 459-490.

174. G. Kossmehl, G. Engelmann, Application of electrically Conductive Polythiophenes in in D. Fichou (Ed.) *Handbook of Oligo- and Polythiophenes*, Wiley VCH, Weinheim, 1999, pp. 491-517.

175. C. Kvarnström, A. Ivaska, Characterization and Applications of Poly(p-phenylene) and Poly(p-phenylenevinylene), in H.S. Nalwa (ed.) *Handbook of Organic Conductive Molecules and Polymers*, Vol. 4, John Wiley & Sons, 1997, pp. 487.

176. Arbizzani, M. Mastragostino, B. Scrosati, Conducting Polymers for Batteries, Supercapacitors and Optical Devices in H.S. Nalwa (ed.) *Handbook of Organic Conductive Molecules and Polymers*, Vol. 4, John Wiley & Sons, 1997, pp. 595-619.

177. H. Shirakawa, E.J. Louis, A.G.Mac Diarmid, C.K. Chiang, A.J. Heeger, Synthesis of electrically conducting organic polymers: halogen derivatives of polyacetylene, (CH)x, *Journal of the Chemical Society, Chemical Communications* 16 (1977) 578-580.

178. C. Kvarnström, H. Neugebauer, S. Blomquist, H.J. Ahonen, J. Kankare, A. Ivaska, *In situ* spectroelectrochemical characterization of poly(3,4-ethylenedioxythiophene), *Electrochimica Acta* 44 (1999) 2739-2750.

179. C. Kvarnström, H. Neugebauer, A. Ivaska, N.S. Sariciftci, Vibrational signatures of electrochemical p- and n-doping of poly(3,4-ethylenedioxythiophene) films: an *in situ* attenuated total reflection Fourier transform infrared (ATR-FTIR) study, *Journal of Molecular Structure* 521 (2000) 271-277.

180. H. Neugebauer, C. Kvarnström, A. Cravino, T. Yohannes, N.S. Sariciftci, Photoexcited spectroscopy and *in situ* electrochemical spectroscopy in conjugated polymers: a comparative study, *Synthetic Metals* 116 (2001) 115-121.

181. H. Neugebauer, A. Cravino, S. Luzzati, M. Catellani, A. Petr, L. Dunsch, N.S. Sariciftci, Spectral signatures of positive and negative charged states in doped and photoexcited low band-gap polydithienithiophenes, *Synthetic Metals* 139 (2003) 747-750.

182. H. Neugebauer, Infrared signatures of positive and negative charge carriers in conjugated polymers with low band gaps, *Journal of Electroanalytical Chemistry* 563 (2004) 153-159.

183. https://www.ifw-dresden.de/de/institute/institut-fuer-festkoerperforschung/nanoscale-chemistry/ - accessed on 06.03.2017.

184. P. Rapta, E. Dmitrieva, A.A. Popov, L. Dunsch, *In situ* spectroelectrochemistry of Organic Compounds, in O. Hammerich and B. Speiser (Ed.), Organic Electrochemistry, Fifth Edition, CRC Press, Taylor & Francis Group, Boca Raton, 2016, pp. 169-190.

185. R.-M. Latonen, C. Kvarnström, A. Ivaska, *In situ* UV–vis and FTIR attenuated total reflectance studies on the electrochemically synthesized copolymer from biphenyl and 3-octylthiophene, *Journal of Electroanalytical Chemistry* 512 (2001) 36–48.

186. S. Stafström, J.L. Brédas, A.J. Epstein, H.S. Woo, D.B. Tanner, W.S. Huang, A.G. MacDiarmid, Polaron lattice in highly conducting polyaniline: Theoretical and optical study, *Physical Review Letters* 59 (1987) 1464-1467.

187. W.R. Salaneck, I. Lundström, B. Rånby. Conjugated polymers and related materials. The interconnection of chemical and electronic structure. Proceedings of the Eighty-first Nobel Symposium. Oxford, New York: Oxford University Press, 1993.

188. R. Willstätter, C.W. Moore, Über Anilinschwarz. I., *Berichte der Deutschen Chemischen Gesselschaft* 40 (1907) 2665-2689.

189. A.G. Green, S. Wolff, Anilinschwarz und seine Zwischenkörper. III., *Berichte der Deutschen Chemischen Gesselschaft* 46 (1913) 33-49.

190. L. Dunsch, Dissertation, Bergakademie Freiberg, 1973.

191. G. Ćirić-Marjanović, M. Trchová and J. Stejskal, The chemical oxidative polymerization of aniline in water: Raman spectroscopy, *Journal of Raman Spectroscopy* 39 (2008) 1375-1387.

192. M. Trchová, I. Šeděnková, E. N. Konyushenko, J. Stejskal, P. Holler and G. Ćirić-Marjanović, Evolution of polyaniline nanotubes: the oxidation of aniline in water, *Journal of Physical Chemistry B* 110 (2006) 9461-9468.

193. G.M. Do Nascimento, C.H.B. Silva, C.M.S. Izumi, M.L.A. Temperini, The role of cross-linking structures to the formation of one-dimensional nano-organized polyaniline and their Raman fingerprint, *Spectrochimica Acta Part A* 71 (2008) 869-875.

194. G.M. Do Nascimento, C.H.B. Silva, M.L.A. Temperini, Spectroscopic characterization of the structural changes of polyaniline nanofibers after heating, *Polymer Degradation and Stability* 93 (2008) 291-297.

195. G.M. Do Nascimento, M.LA. Temperini, Studies on the resonance Raman spectra of polyaniline obtained with near-IR excitation, *Journal of Raman Spectroscopy* 39 (2008) 772-778.

196. G. Socrates. Infrared and Raman characteristic group frequencies. Table and charts, ed. John Wiley and Sons, Ltd, Chichester, 3rd edn., 2001, 107-113, 123, 157-167, 176-177, 220-222.

197. G. Ćirić-Marjanović, N. Blinova, M. Trchová and J. Stejskal, Chemical Oxidative Polymerization of Safranines, *Journal of Physical Chemistry B* 111 (2007) 2188-2199.

198. J. Tang, X. Jing, B. Wang, F. Wang, Infrared spectra of soluble polyaniline, *Synthetic Metals* 24 (1988) 231-238.

199. C. Stammer, A. Taurins, Infrared spectra of phenazines, *Spectrochimica Acta* 19 (1963) 1625-1654.

200. X.-G. Li, M.-R. Huang, W. Duan, Y.-L. Yang, Novel Multifunctional Polymers from Aromatic Diamines by Oxidative Polymerizations, *Chemical Reviews* 102 (2002) 2925-3030.

201. K. Chiba, T. Ohsaka, Y. Ohnuki, N. Oyama, Electrochemical preparation of a ladder polymer containing phenazine rings, *Journal of Electroanalytical Chemistry* 219 (1987) 117-124.

202. C.J. Pouchert, The Aldrich Library of FT-IR Spectra. Ed. 2, Aldrich Chemical Company, USA, 1985.

203. E. Dmitrieva, Y. Harima, L. Dunsch, Influence of Phenazine Structure on Polaron Formation in Polyaniline: *In Situ* Electron Spin Resonance−Ultraviolet/Visible−Near-Infrared Spectroelectrochemical Study *Journal of Physical Chemistry B* 113 (2009) 16131-16141.

204. S. Quillard, G. Louarn, S. Lefrant, Vibrational analysis of polyaniline: A comparative study of leucoemeraldine, emeraldine, and pernigraniline bases, *Physical Review B* 50 (1994) 12496-12508.

205. Z. Ping, G. E. Nauer, H. Neugebauer, J. Theiner, A. Neckel, Protonation and electrochemical redox doping processes of polyaniline in aqueous solutions:

Investigations using *in situ* FTIR-ATR spectroscopy and a new doping system, *Journal of the Chemical Society, Faraday Transactions* 93 (1997) 121-129.

206. N.S. Sariciftci, H. Kuzmany, H. Neugebauer, A. Neckel, Structural and electronic transitions in polyaniline: A Fourier transform infrared spectroscopic study, *Journal of Chemical Physics* 92 (1990) 4530.

207. Z. Ping, H. Neugebauer, A. Neckel, FTIR ATR spectroelectrochemical investigations of polyaniline with perrhenate as a new doping system, *Electrochimica Acta* 41 (1996) 767-772.

208. Z. Ping, *In situ* FTIR–attenuated total reflection spectroscopic investigations on the base–acid transitions of polyaniline. Base–acid transition in the emeraldine form of polyaniline, *Journal of the Chemical Society, Faraday Transactions* 92 (1996) 3063-3067.

209. M. Trchová, I. Šeděnková, J. Stejskal, In-situ polymerized polyaniline films 6. FTIR spectroscopic study of aniline polymerization, *Synthetic Metals* 154 (2005) 1-4.

210. M. Trchová, J. Stejskal, J. Prokeš, Infrared spectroscopic study of solid-state protonation and oxidation of polyaniline, *Synthetic Metals* 101 (1999) 840-841.

211. I. Šeděnková, M. Trchová, N. Blinova, J. Stejskal, *In-situ* polymerized polyaniline films. Preparation in solutions of hydrochloric, sulfuric, or phosphoric acid, *Thin Solid Film*s 515 (2006) 1640-1646.

212. Y. Furukawa, F. Ueda, Y. Hyodo, I. Harada, T. Nakajima, T. Kawagoe, Vibrational spectra and structure of polyaniline, *Macromolecules* 21 (1988) 1297-1305.

213. Z. Ping, G. E. Nauer, H. Neugebauer, J. Theiner, *In situ* Fourier transform infrared attenuated total reflection (FTIR-ATR) spectroscopic investigations on the base—acid transitions of different forms of polyaniline. Base—acid transition in the leucoemeraldine form, *Journal of Electroanalytical Chemistry* 420 (1997) 301-306.

214. M. Inoue, R.E. Navarro, M.B. Inoue, New soluble polyaniline: Synthesis, electrical properties and solution electronic spectrum, *Synthetic Metals* 30 (1989) 199-207.

215. E. Dmitrieva, L. Dunsch, How Linear Is "Linear" Polyaniline?, *Journal of Physical Chemistry B* 115 (2011) 6401-6411.

216. S. Quillard, G. Louarn, J. P. Buisson, M. Boyer, M. Lapkowski, A. Pron, S. Lefrant, Vibrational spectroscopic studies of the isotope effects in polyaniline, *Synthetic Met*als 84 (1997) 805-806.

217. G. Louarn, M. Lapkowski, S. Quillard, A. Pron, J.P. Buisson, S. Lefrant, Vibrational Properties of Polyaniline. Isotope Effects, *Journal of Physical Chemistry* 100 (1996) 6998-7006.

218. M.I. Boyer, S. Quillard, G. Louarn, G. Froyer, S. Lefrant, Vibrational Study of the $FeCl_3$-Doped Dimer of Polyaniline; A Good Model Compound of Emeraldine Salt, *Journal of Physical Chemistry B* 104 (2000) 8952-8961.

219. A. Zimmermann, L. Dunsch, Investigation of the electropolymerization of aniline by the *in situ* techniques of attenuated total reflection (ATR) and external reflection (IRRAS) *Journal of Molecular Structure* 410-411 (1997) 165-171.

220. G. Tourillon, F. Garnier, New electrochemically generated organic conducting polymers, *Journal of Electroanalytical Chemistry* 135 (1982) 173-178.

221. M. Sato, S. Tanaka, K. Kaeriyama, Electrochemical preparation of highly conducting polythiophene films, *Journal of the Chemical Society, Chemical Communications* 11 (1985) 713-714.

222. R. Elsenbaumer, K.W. Jen, R. Oobodi, Processible and environmentally stable conducting polymers, *Synthetic Metals* 15 (1986) 169-174.

223. R.J. Waltman, J. Bargon, A.F. Diaz, Electrochemical studies of some conducting polythiophene films, *Journal of Physical Chemistry* 87 (1983) 1459-1463.

224. E. Jähne, D. Ferse, G. Busch, H.-J. P Adler, A. Singh, I. K. Varma, Synthesis of adhesion promoters for grafting polythiophene onto metal oxides, *Designed Monomers and Polymers* 5 (2002) 427-443.

225. B. Adolphi, E. Jähne, G. Bush, X. Cai, Characterization of the adsorption of ω-(thiophene-3-yl alkyl) phosphonic acid on metal oxides with AR-XPS, *Analytical and Bioanalytical Chemistry* 379 (2004) 646-652.

226. D. Appelhans, D. Ferse, H.-J.P. Adler, W. Plieth, A. Fikus, K. Grundke, F.-J. Schmitt, T. Bayer, B. Adolphi, Self-assembled monolayers prepared from ω-thiophene-functionalized n-alkyltrichlorosilane on silicon substrates, *Colloids and Surfaces A* 161 (2000) 203-212.

227. H.-P. Welzel, G. Kossmehl, J. Schnieder, W. Plieth, Reactive Groups on Polymer-Covered Electrodes. 2. Functionalized Thiophene Polymers by Electrochemical Polymerization and Their Application as Polymeric Reagents *Macromolecules* 28 (1995) 5575-5580.

228. H.-P. Welzel, G. Kossmehl, H. Boettcher, G. Engelmann, W.-D. Hunnius, Reactive Groups on Polymer-Covered Electrodes. 5. Synthesis and Cyclovoltammetric Analysis of 3-Substituted Thiophene Derivatives, *Macromolecules* 30 (1997) 7419-7426.

229. A. Das, S. Mulik, C. Sotiriou-Leventis, N. Leventis, Protection of 2-(3-thienyl)ethanol with 3-thienylacetic acid and hard cross-linked conducting films by electro-polymerization of the ester, *Synthetic Metals* 156 (2006) 966-972.

230. M. Lanzi, P.C. Bizzari, L. Paganin, G. Cesari, Highly processable ester-functionalized polythiophenes as valuable multifunctional and post-functionalizable conjugated polymers, *European Polymer Journal* 43 (2007) 72-83.

231. Y.H. Kim, S. Hotta, A.J. Heeger, Infrared photoexcitation and doping studies of poly(3-methylthienylene), *Physical Review B* 36 (1987) 7486-7490.

232. V. Hernandez, F.J. Ramirez, T.F. Otero, J.T. Lopez Navarrete, An interpretation of the vibrational spectra of insulating and electrically conducting poly(3-methylthiophene) aided by a theoretical dynamical model, *The Journal of Chemical Physics* 100 (1994) 114-129.

233. H. Neugebauer, G. Nauer, A. Neckel, G. Tourillon, F. Garnier, P. Lang, *In situ* investigations of the 3-methylthiophene polymer with attenuated total reflection Fourier transform infrared spectroscopy, *Journal of Physical Chemistry* 88 (1984) 652-654.

234. J. Guay, P. Kasai, A. Diaz, R. Wu, J.M. Tour, Le H. Dao, Chain-length dependence of electrochemical and electronic properties of neutral and oxidized soluble α,α-coupled thiophene oligomers, *Chemistry of Materials* 4 **(**1992) 1097-1105.

235. S. Hotta, M. Soga, N. Sonoda, Infrared dichroic studies of polythiophenes, *Journal of Physical Chemistry* 93 (1989) 4994-4998.

236. A. Cravino, H. Neugebauer, S. Luzzati, M. Catellani, A. Petr, L. Dunsch, N.S. Sariciftci, Positive and Negative Charge Carriers in Doped or Photoexcited Polydithieno-thiophenes: A Comparative Study Using Raman, Infrared, and Electron Spin Resonance Spectroscopy, *Journal of Physical Chemistry B* 106 (2002) 3583-3591.

237. H.E. Schaffer, A.J. Heeger, Infrared activity of photoexcitations in polythiophene, *Solid State Communications* 59 (1986) 415-421.

238. A.J. Heeger, S. Kivelson, J.R. Schrieffer, W.-P. Su, Solitons in conducting polymers, *Reviews of Modern Phys*ics 60 (1988) 781-850.

239. P.A. Christensen, A. Hamnett, D.C. Read, Morphology and charge conduction in polythiophene, an *in situ* FTIR study, *Electrochimica Acta* 39 (1994**)** 187-196.

240. Q. Pei, O. Inganäs, G. Gustafsson, M. Granström, M. Andersson, T. Hjertberg, O. Wennerström, J. E. Österholm, J. Laakso, H. Järvinen, The routes towards processible and stable conducting poly(thiophene)s, *Synthetic Metals* 55 (1993) 1221-1226.

241. G. Gustafsson, O. Inganäs, J. O. Nilsson, B. Liedberg, Thermal undoping in poly(3-alkylthiophenes), *Synthetic Metals* 26 (1988) 297-309.

242. S. Hotta, M. Soga, N. Sonoda, Novel organosynthetic routes to polythiophene and its derivatives, *Synthetic Metals* 26 (1988) 267-279.

243. S. Hotta, Electrochemical synthesis and spectroscopic study of poly(3-alkylthienylenes), *Synthetic Metals* 22 (1987) 103-113.

244. T. A. Chen. X. Wu, R. D. Rieke, Regiocontrolled Synthesis of Poly(3-alkylthiophenes) Mediated by Rieke Zinc: Their Characterization and Solid-State Properties, *Journal of the American Chemical Society* 117 (1995) 233-244.

245. A. Buzarovska, L.Arsov, N. Hebestreit, W. Plieth, Synthesis and characterization of thiophene/3-alkylthiophene random cooligomers, *Journal of Solid State Electrochemistry* 7 (2002) 49-54.

246. R. Singh, J. Kumar, R.K. Singh, A. Kaur, K.N. Sood, R.C. Rastogi, Effect of thermal annealing on surface morphology and physical properties of poly(3-octylthiophene) films, *Polymer* 46 (2005) 9126-9132.

247. F. Costanzo, D. Tonelli, G. Scalmani, J. Cornil, Theoretical investigation of the electronic and optical properties of oligothiophenes upon methyl, thiol, and thiomethyl substitutions, *Polymer* 47 (2006) 6692-6697.

248. J. Tarábek, P. Rapta, E. Jähne, D. Ferse, H.-J. Adler, M. Maumy, L. Dunsch, Spectroelectrochemical and potentiometric studies of functionalized electroactive polymers, *Electrochimica Acta* 50 (2005) 1643-1651.

249. P. Rapta, J. Lukkari, J. Tarábek, M. Salomäki, M. Jussila, G. Yohannes, M.-L. Riekkola, J. Kankare, L. Dunsch, Ultrathin polyelectrolyte multilayers: *in situ* ESR/UV-Vis-NIR spectroelectrochemical study of charge carriers formed under oxidation, *Physical Chemistry Chemical Physics* 6 (2004) 434-441.

250. Y. Kunugi, Y. Harima, K. Yamashita, N. Ohta, S. Ito, Charge transport in a regioregular poly(3-octylthiophene)film, *Journal of Materials Chemistry* 10 (2000) 2673-2677.

251. Y. Harima, Y. Kunugi, K. Yamashita and M. Shiotani, Determination of mobilities of charge carriers in electrochemically anion-doped polythiophene film, *Chemical Physics Letters* 317 (2000) 310-314.

252. Y. Harima, T. Eguchi and K. Yamashita, Enhancement of carrier mobilities in poly(3-methylthiophene) by an electrochemical doping, *Synthetic Metals* 95 (1998) 69-74.

253. Y. Harima, T. Eguchi, K. Yamashita, K. Kojima, M. Shiotani, An *in situ* ESR study on poly(3-methylthiophene): charge transport due to polarons and bipolarons before the evolution of metallic conduction, *Synthetic Metals* 105 (1999) 121-128.

254. J. A. E. H. van Haare, E. E. Havinga, J. L. J. van Dongenn, J. L. R. A. J. Janssen, J. Cornil, J. L. Brédas, Redox States of Long Oligothiophenes: Two Polarons on a Single Chain, *Chemistry A European Journal* 4 (1998) 1509-1522.

255. G. Paasch, Transmission line description for doped conjugated polymers with polarons, bipolarons and counterions as charged species, *Electrochimica Acta* 47 (2002) 2049-2053.

256. G. Paasch, Transport in doped conjugated polymers with polarons and bipolarons forming complexes with counter ions, *Solid State Ionics* 169 (2004) 87-94.

257. G. Paasch, S. Scheinert, A. Petr, L. Dunsch, Bipolarons or polaron pairs in conducting polymers: Equilibrium and kinetics, *Russian Journal of Electrochemistry* 42 (2006) 1161-1168.

258. M.G. Hill, K.R. Mann, L.L. Miller, J.F. Penneau, Oligothiophene cation radical dimers. An alternative to bipolarons in oxidized polythiophene, *Journal of the American Chemical Society* 114 (1992) 2728-2730.

259. N. Rajalakshmi, K.S. Dhathathreyan, Nanostructured platinum catalyst layer prepared by pulsed electrodeposition for use in PEM fuel cells, *International Journal of Hydrogen Energy* 33 (2008) 5672-5677.

260. H. Kim, N.P. Subramanian, B.N. Popov, Preparation of PEM fuel cell electrodes using pulse electrodeposition, *Journal of Power Sources* 138 (2004) 14–24

261. S. Karimi, F.R. Foulkes, Pulse electrodeposition of platinum catalyst using different pulse current waveforms, *Electrochemistry Communications* 19 (2012) 17-20.

262. R. Muntean, D.T Pascal, G. Marginean, N. Vaszilcsin, Carbon Nanofibers Decorated with Pt-Co Alloy Nanoparticles as Catalysts for Electrochemical Cell Applications. I. Synthesis and Structural Characterization, *International Journal of Electrochemical Science* 12 (2017) 4597-4609.

263. M.-C. Tsai, T.-K. Yeh, C.-H. Tsai, Methanol oxidation efficiencies on carbon-nanotube-supported platinum and platinum–ruthenium nanoparticles prepared by pulsed electrodeposition, *International Journal of Hydrogen Energy* 36 (2011) 8261-8266.

264. H.-Y. Chou, C.-K. Hsieh, M.-C. Tsai, Y.-H. Wei, T.-K. Yeh, C.-H. Tsai, Pulse electrodeposition of Pt and Pt–Ru methanol-oxidation nanocatalysts onto carbon nanotubes in citric acid aqueous solutions, *Thin Solid Films* 584 (2015) 98-102.

265. J. Li, N. Zhang, Q. Sun, Z. Bai, J. Zheng, Electrochemical sensor for dopamine based on imprinted silica matrix- poly(aniline boronic acid) hybrid as recognition element, *Talanta* 159 (2016) 379-386.

266. J. Anzai, Recent progress in electrochemical biosensors based on phenylboronic acid and derivatives, *Materials Science and Engineering C* 67 (2016) 737-746.

267. M. Dervisevic, M. Senel, E. Cevik, Novel impedimetric dopamine biosensor based on boronic acid functional polythiophene modified electrodes, *Materials Science and Engineering C* 72 (2017) 641-649.

268. S. Lupu, F.J. del Campo, F.X. Muñoz, Sinusoidal voltage electrodeposition and characterization of conducting polymers on gold microelectrode arrays, *Journal of Electroanalytical Chemistry* 687 (2012) 71–78.

269. C. Lete, B. Lakard, J.-Y. Hihn, F.J. del Campo, S. Lupu, Use of sinusoidal voltage with fixed frequency in the preparation of tyrosinase based electrochemical biosensor for dopamine electroanalysis, *Sensors and Actuators B: Chemical* 240 (2017) 801-809.

270. X. Zhang, L.-X. Ma, Y.-C. Zhang, Electrodeposition of platinum nanosheets on C60 decorated glassy carbon electrode as a stable electrochemical biosensor for simultaneous detection of ascorbic acid, dopamine and uric acid, Electrochimica Acta 177 (2015) 118–127.

271. F.R. Caetano, L.B. Felippe, A.J.G. Zarbin, M.F. Bergamini, L.H. Marcolino-Junior, Gold nanoparticles supported on multi-walled carbon nanotubes produced by biphasic modified method and dopamine sensing application, *Sensors and Actuators B* 243 (2017) 43–50.

272. C. Wang, J. Du, H. Wang, C. Zou, F. Jiang, P. Yang, Y. Du, A facile electrochemical sensor based on reduced graphene oxide and Au nanoplates modified glassy carbon electrode for simultaneous detection of ascorbic acid, dopamine and uric acid, *Sensors and Actuators B* 204 (2014) 302–309.

273. D.N. Oko, S. Garbarino, J. Zhang, Z. Xu, M. Chaker, D. Ma, D. Guay, A.C. Tavares, Dopamine and ascorbic acid electro-oxidation on Au, AuPt and Pt nanoparticles prepared by pulse laser ablation in water, *Electrochimica Acta* 159 (2015) 174–183.

274. A.K. Bhakta, R.J. Mascarenhas, O.J. D'Souza, A.K. Satpati, S. Detriche, Z. Mekhalif, J. Dalhalle, Iron nanoparticles decorated multi-wall carbon nanotubes modified carbon paste electrode as an electrochemical sensor for the simultaneous determination of uric acid in the presence of ascorbic acid, dopamine and L-tyrosine, *Materials Science and Engineering C* 57 (2015) 328–337.

List of Figures

Figure 1. Electrocatalytic enhancement of electrode reactions without mechanism change (left) and by changing the mechanism (right). 16

Figure 2. Steady-state polarization curves (left) and Tafel plots (right) for hydrogen evolution reaction on copper electrode in 1 mol L^{-1} H_2SO_4 solution in the absence and presence of various concentrations of benzylamine. 19

Figure 3. Steady-state polarization curves (left) and Tafel plots (right) for hydrogen evolution reaction on copper electrode in 1 mol L^{-1} H_2SO_4 solution with 5 10^{-2} mol L^{-1} benzylamine at different temperatures. 21

Figure 4. Experimental Nyquist (a) and Bode (b) plots at E = –0.75 V, for HER on copper in 1 mol L^{-1} H_2SO_4 solution in the absence and presence of various concentrations of benzylamine. 22

Figure 5. Molecular dipole moment (arrow) of protonated benzylamine molecule. 23

Figure 6. Chemical structure of aniline derivatives used as proton carriers for HER on copper. 24

Figure 7. Steady-state polarization curves for hydrogen evolution reaction on copper electrode in 0.5 mol L^{-1} H_2SO_4 solution with 10^{-4} mol L^{-1} of different aniline derivatives. 24

Figure 8. Tafel plots for hydrogen evolution reaction on copper electrode in 0.5 mol L^{-1} H_2SO_4 solution with 10^{-4} mol L^{-1} of different aniline derivatives. 25

Figure 9. Complex plane plots for HER on copper in 0.5 mol L^{-1} H_2SO_4 in the presence of 10^{-4} mol L^{-1} aromatic amines. Inset: electrical equivalent circuit used to model impedance data. 26

Figure 10. Chemical structure of aliphatic/aromatic amines used as proton carriers for HER on gold. 28

Figure 11. Linear voltammograms on gold electrode in 0.5 mol L^{-1} H_2SO_4 solution at 25°C, concentration of amines: 10^{-3} mol L^{-1}, scan rate: 10 mV s^{-1}. 28

Figure 12. Linear polarization curves for HER on gold in 0.5 mol L^{-1} H_2SO_4 at different temperatures for a concentration of the selected amines of 10^{-6} mol L^{-1} (upper row) and 10^{-3} mol L^{-1} (lower row). 29

Figure 13. Tafel plots for HER on gold electrode in 0.5 mol L^{-1} H_2SO_4 at different temperatures for a concentration of the selected amines of 10^{-6} mol L^{-1} (upper row) and 10^{-3} mol L^{-1} (lower row). 29

Figure 14. Molecular dipole moment (arrow) of protonated aniline, 4-chloro-aniline and methylamine. 31

Figure 15. Complex plane and Bode plots plots for HER on gold in 0.5 mol L^{-1} H_2SO_4 at η = -200 mV. 32

Figure 16. Complex plane plots for HER on gold in 0.5 mol L^{-1} H_2SO_4 at η = -200 mV in the presence of AH^+ and $4ClAH^+$ at concentrations of 10^{-6} mol L^{-1} (upper row) and 10^{-3} mol L^{-1} (lower row). 33

Figure 17. Electrical equivalent circuits used to model impedance data for HER on gold in the absence of proton carriers (left) and in the presence of proton carriers (right). 34

Figure 18. Catalytic effect of aniline, 4-chloro-aniline and methylamine on HER on gold electrode. 35

Figure 20. Linear voltammograms for HER on platinum electrode in 0.5 mol L^{-1} at 25°C and different concentrations of benzylamine (left) and aniline (right). Scan rate 5 mV s^{-1}. . 36

Figure 21. Equivalent electrical circuits for HER without absorption (a) and HER with indirect absorption (b). 38

Figure 22. Complex plane plots for HER in blank 0.5 mol L^{-1} H_2SO_4 solution, η = -15 mV (a) and η = -45 mV (b). Open symbols are experimental data and continuous line is simulated by CNLS fitting. 39

Figure 23. Complex plane plots for HER in 0.5 mol L^{-1} H_2SO_4 solution with 10^{-5} mol L^{-1} BA (a) and 10^{-2} mol L^{-1} BA, η = -15 mV. Open symbols are experimental data and continuous line is simulated by CNLS fitting. 39

Figure 24. Phase angle plots for HER at increasing overpotentials in blank 0.5 mol L^{-1} H_2SO_4 solution. 39

Figure 25. Phase angle plots for HER at increasing overpotentials in 0.5 mol L^{-1} H_2SO_4 solution with 10^{-5} mol L^{-1} BA (a) and 10^{-2} mol L^{-1} BA (b). 40

Figure 26. Phase angle plots for HER at increasing overpotentials in 0.5 mol L^{-1} H_2SO_4 solution with 10^{-5} mol L^{-1} A (a) and 10^{-2} mol L^{-1} A (b)..... 40

Figure 19. Mechanism of HER in the presence of proton carriers..... 43

Figure 27. Potentiodynamic deposition of Pani/Nb samples from a solution of 0.2 mol L^{-1} aniline in 0.5 mol L^{-1} H_2SO_4 (a) and 0.4 mol L^{-1} aniline in 1 mol L^{-1} H_2SO_4 (b). Scan rate 50 mV s^{-1}. 48

Figure 28. Cyclic voltammograms of Pani/Nb samples in monomer free 0.5 mol L^{-1} H_2SO_4 solution. Scan rate 50 mV s^{-1}..... 49

Figure 29. SEM images of polyaniline nanofibers electrodeposited on Nb by cyclic voltammetry in 0.5 mol L^{-1} H_2SO_4: (a) Pani/Nb/1, (b) Pani/Nb/2, (c) Pani/Nb/3 and in 1 mol L^{-1} H_2SO_4: (d) Pani/Nb/4, (e) Pani/Nb/5, (f) Pani/Nb/6. 50

Figure 30. Complex plane plots of (a) Pani/Nb/1, (b) Pani/Nb/2, (c) Pani/Nb/3, (d) Pani/Nb/4, (e) Pani/Nb/5 and (f) Pani/Nb/6 films measured in 0.5 mol L^{-1} H_2SO_4 solution at E = 0.4 V. 52

Figure 31. Dependence of the diffusional capacitance on film thickness for granular and fibrilar Pani films obtained on Nb. 53

Figure 32. Potentiodynamic deposition of Pani/Ni samples from a solution of 0.1 mol L^{-1} aniline in 0.5 mol L^{-1} H_2SO_4. Last scan of the cyclic voltammograms (a) and dependence of the charge on the number of scans (b). 54

Figure 33. Cyclic voltammograms of Pani/Ni samples in monomer free 0.5 mol L^{-1} H_2SO_4 solution. Scan rate 50 mV s^{-1}..... 55

Figure 34. FE-SEM images of polyaniline films: Pani/Ni/10 (a), Pani/Ni/25 (b), Pani/Ni/50 (c) and Pani/Ni/100 (d). 56

Figure 35. Complex plane plots of Pani/Ni/10 measured in 0.5 mol L^{-1} H_2SO_4 solution at different electrode potentials. 57

Figure 36. Complex plane plots of Pani/Ni/25 measured in 0.5 mol L^{-1} H_2SO_4 solution at different electrode potentials. 58

Figure 37. Complex plane plots of Pani/Ni/50 measured in 0.5 mol L^{-1} H_2SO_4 solution at different electrode potentials. 58

Figure 38. Complex plane plots of Pani/Ni/100 measured in 0.5 mol L^{-1} H_2SO_4 solution at different electrode potentials. 59

Figure 39. Potentiodynamic deposition of Pani/Pt samples from a solution of 0.1 mol L^{-1} aniline in 0.5 mol L^{-1} H_2SO_4 at different temperatures: 25°C (a) and 40°C (b). Scan rate 50 mV s^{-1}. 61

Figure 40. Last scan of the cyclic voltammograms during electrochemical deposition of Pani/Pt samples at different temperatures(a) and dependence of the charge on the number of scans (b). 62

Figure 41. Cyclic voltammograms of Pani/Pt samples in monomer free 0.5 mol L^{-1} H_2SO_4 solution. Scan rate 50 mV s^{-1}. 63

Figure 42. Complex plane plots of Pani/Pt/25 measured in 0.5 mol L^{-1} H_2SO_4 solution at different electrode potentials. 65

Figure 43. Complex plane plots of Pani/Pt/40 measured in 0.5 mol L^{-1} H_2SO_4 solution at different electrode potentials. 65

Figure 44. Complex plane plots of Pani/Pt/60 measured in 0.5 mol L^{-1} H_2SO_4 solution at different electrode potentials. 66

Figure 45. Cyclic voltammogram of Nb in 0.5 M H_2SO_4, scan rate 50 mV s^{-1}. 67

Figure 46. AFM images of the Nb electrode oxidized in air. 2D (a) and 3D image (b). 69

Figure 47. AFM images of the electrochemically passivated Nb. 2D (a) and 3D image (b). 69

Figure 48. AFM images of Nb electrode oxidized in air (a) and electrochemically passivated (b). 69

Figure 49. FTIR spectra of electrochemically synthesized Pani/Nb and Pani/Pt and of commercial emeraldine base. 70

Figure 50. Two-step potentiodynamic deposition of Pani/60/Paba sample, consisting of Pani initiation and growth (1a and 1b) followed by Paba growth (2). 73

Figure 51. SEM images of Paba modified electrodes: Ni/0/Paba (a) and Ni/30/Paba (b). 73

Figure 52. Selective binding of dopamine by Paba and formation of boronate ester. 74

Figure 53. Complex plane plots for Ni/0/Paba (a) and Ni/30/Paba (b) in phosphate buffer solution at pH = 7.4 and different concentrations of dopamine. 74

Figure 54. Calibration curves of R_{ct} versus dopamine concentration for Ni/0/Paba and Ni/30/Paba modified electrodes. 75

Figure 55. Chemical structure of azo red dye. 76

Figure 56. Complex plane plots of Pani/Nb electrode as a function of time for different concentrations of azo dye: (a) 1×10^{-5} mol L^{-1}; (b) 2×10^{-5} mol L^{-1}; (c) 3×10^{-5} mol L^{-1} and (d) 5×10^{-5} mol L^{-1}..... 77

Figure 57. Dependence of double layer capacitance (a) and surface coverage (b) as a function of adsorption time for different dye concentrations. 78

Figure 58. Langmuir (a), Temkin (b), Frumkin (c) and Flory–Huggins (d) isotherms for adsorption of azo red dye on Pani/Nb electrode..... 79

Figure 59. ATR-FTIR spectroelectrochemical cell. Schematic view of cell and of Au interdigitated structure deposited on top of the ZnSe crystal (left) and disassembled cell (right)..... 83

Figure 60. Pictures of the experimental setup. Reflection unit with spectroelectrochemical cell installed (left) and complete cell installed and connected to the potentiostat (right). 83

Figure 61. Structure of linear Pani and its different oxidation states. 84

Figure 62. Structure of charged states in polyaniline. 85

Figure 63. Formation of phenazine rings in the structure of polyaniline [141]. 85

Figure 64. Chemical structure of Phsafr (a) and An-Phsafr copolymer (b). 86

Figure 65. Cyclic voltammograms on gold electrode during oxidation of 5 mM Phsafr (a) 50 mM An (b) and 50 mM An + 5 mM Phsafr (c) in 0.1 M sulfuric acid and 0.01 M sodium p-toluenesulfonate, scan rate 25 mV s^{-1}..... 87

Figure 66. ATR-FTIR spectra of emeraldine base, polyaniline and aniline-phenosafranine copolymer. 88

Figure 67. *In situ* ATR-FTIR spectra during oxidation of Pani (a); Pani-PPS1 (b); Pani-PPS2 (c) and Pani-PPS3 (d) between -0.5 and 0.5 V with reference state at -0.5 V. 89

Figure 68. Comparison of UV-Vis-NIR absorbance, selected IR absorbance and ESR signal intensity during oxidation of: Pani (a) and Pani-PPS3 (b). 90

Figure 69. *In situ* ATR-FTIR spectra of different PANI structures upon charging. Inset shows the simultaneous CVs with triggers marked with points. 92

Figure 70. Mid infrared region of *in situ* ATR-FTIR spectra of different PANI structures upon charging, EB2 (left) and EB3 (right). 92

Figure 71. Potential dependence of semiquinoid bands and of the free charge carries band for the PANI structures EB2 (b) and EB3 (c). 93

Figure 72. Potential dependence of spectroscopic data of Pani-EB3 during doping / dedoping: single integrated ESR signal together with one selected semiquinoid IR band (a) and with polaronic bands at 1266, 1033 and 1010 cm^{-1} (b)..... 94

Figure 73. *In situ* FTIR spectra of EB3 after the first and the second redox peak (black and red line) and potential dependence of bipolaronic bands in EB3. 95

Figure 74. Scheme for formation of charged states upon electrochemical oxidation of polyaniline. 95

Figure 75. Chemical structure of p3MT and p3HT..... 98

Figure 76. *In situ* ATR-FTIR spectra during copolymerization of 20 mM 3MT with 40 mM 3HT in 0.1 M *n*-$BuNPF_6$ acetonitrile solution. 100

Figure 77. *In situ* ESR (left) and UV-Vis-NIR (right) spectra of p3MT-co3HT. 101

Figure 78. Chemical structure of the studied polyalkylthiophene derivatives. 102

Figure 79. Cyclic voltammograms of PTEtAc, PTEtAcOH and PTEtOH films on a Pt working electrode in a $TBAPF_6$ (0.1 M) – acetonitrile solution at 100 mV s^{-1}. 103

Figure 80. *In situ* ATR-FTIR spectra during p-doping (solid lines) and de-doping (dashed lines) of PTEtAc (a), PTEtAcOH (b) and PTEtOH (c). Numbers correspond to potential values from Fig. 79. 104

Figure 81. *In situ* ESR (left) and UV-Vis-NIR (right) spectra at high doping levels of PTEtAc. 106

Figure 82. CV curves in 0.1 M PBS solution (pH 7.4) of 1660 µM AA (a); 100 µM DA (b) and a mixture of 1660 µM AA with different concentrations of DA (c) on GC-MWCNT electrode. 110

List of Tables

Table 1. Kinetic parameters for HER on copper electrode at various concentration of BA. .. 20

Table 2. Kinetic parameters for HER on copper electrode at different temperatures in 1 mol L^{-1} H_2SO_4 solution without / with 5 10^{-2} mol L^{-1} BA. 21

Table 3. Experimental values and standard errors for the EEC parameters related to HER on copper in 1 mol L^{-1} H_2SO_4 in the presence of different concentrations of BA..... 22

Table 4. Kinetic parameters for HER on copper electrode in 0.5 mol L^{-1} H_2SO_4 solution and 10^{-4} mol L^{-1} of different aromatic amines..... 25

Table 5. Charge transfer resistance for HER on copper in 0.5 mol L^{-1} H_2SO_4 in the presence of 10^{-4} mol L^{-1} amines. 27

Table 6. Kinetic parameters for HER on gold electrode in 0.5 mol L^{-1} H_2SO_4 solution in the presence of amines at different concentrations and temperatures. 30

Table 7. Molecular parameters of protonated amines. 31

Table 8. Values of the charge transfer resistance for HER on gold in 0.5 mol L^{-1} H_2SO_4 at η = -200 mV in the presence of amines at different concentrations and temperatures. 34

Table 9. Kinetic parameters for HER on platinum electrode in 0.5 mol L^{-1} H_2SO_4 solution.. 36

Table 10. Kinetic parameters for HER on platinum electrode in 0.5 mol L^{-1} H_2SO_4 solution in the presence of benzylamine and aniline at different concentrations and temperatures. 37

Table 11. EEC parameter values for HER at η = -25 V. 41

Table 12. Synthesis conditions and characteristics of the first anodic peak of Pani/Nb films obtained at different acid concentration and aniline/acid ratio. 48

Table 13. Capacitance values of Pani/Nb films determined from CV and EIS data..... 51

Table 14. Synthesis conditions and characteristics of the first peak of Pani/Ni films obtained at different scan rates..... 54

Table 15. Capacitance values of Pani/Ni films determined from CV and EIS data. 56

Table 16. Charge transfer and capacitance values of Pani/Ni films obtained by fitting EIS data. 59

Table 17. Characteristics of the anodic peaks of Pani/Pt films obtained at different temperatures. 62

Table 18. Capacitance values of Pani/Pt films determined from CV and EIS data. 64

Table 19. Charge transfer and capacitance values of Pani/Pt films obtained by fitting EIS data. 66

Table 20. Main FTIR bands of Pani/Nb and Pani/Pt and their assignments. 70

Table 21. FTIR bands of EB, Pani, Pani-PPS1, Pani-PPS2, Pani-PPS3 and PPS. 88

Table 22. Mid-IR region vibrations of *in situ* FTIR spectra of different PANI structures. 93

Table 23. Characteristic IR bands of p3MT, p3HT and p3MT-co3HT and their structural assignments. 99